Upper Critical Fields of the Superconducting Layered Compounds $Nb_{1-x}Ta_xSe_2$

A Dissertation

Presented to the Faculty of the Graduate School

of

Yale University

in Candidacy for the Degree of

Doctor of Philosophy

by

Bruce Jameson Dalrymple

December, 1983

Abstract

Upper Critical Fields of the Superconducting Layered Compounds $Nb_{1-x}Ta_xSe_2$

Bruce Jameson Dalrymple

Yale University

1983

The superconducting upper critical field $H_{c2}(T)$ has been measured for the layered compounds $Nb_{1-x}Ta_xSe_2$ ($0 \leq x \leq 0.20$) with the magnetic field oriented both parallel and perpendicular to the layer plane. The goal of this study has been to use substitutional alloying to investigate the affect that altering the composition has on the critical fields in a series of anisotropic superconductors. Single crystals of the 2H phase have been grown by the vapor-transport technique, primarily using selenium as the transporting agent.

Just below T_c, upward curvature is seen in $H_{c2}(T)$ for both field directions and for all compositions. This effect is larger with the field oriented parallel to the layer plane, and decreases with increasing Ta content. The amount of upward curvature appears not to be a function of the crystal quality. Since the charge-density wave present in $NbSe_2$ is supressed by alloying, it is also unlikely that the charge-density wave causes upward curvature. At low temperatures, $H_{c2}(T)$ displays enhanced linearity compared to the prediction of the isotropic theory, and shows no evidence of Pauli paramagnetic limiting

for the parallel field orientation.

The critical field slopes just below T_c change only slightly with composition. The perpendicular slope decreases and the parallel slope increases as the Ta content is increased. The critical field anisotropy of $NbSe_2$ is approximately three and increases with the Ta content. These effects can be qualitatively understood by incorporating the known changes in T_c, and by assuming small band structure and mean-free-path effects.

$H_{c2}(T)$ has been calculated for a series of Fermi surface models. These calculations indicate that Fermi surface anisotropy can explain the upward curvature and enhanced linearity seen in the experimental data. The calculations also show that the $H_{c2}(T)$ data are consistent with a Fermi surface which consists of open undulating cylinders and an additional smaller closed piece.

ACKNOWLEDGEMENTS

It is a pleasure to acknowledge that many people have provided important assistance with various aspects of this project. The low-temperature experimental apparatus was expertly constructed by Mr. Clifford Sneider. The glass blowing required to carry out the crystal-growth experiments was done by Mr. Edward Brosious, to whom I am indebted for many helpful discussions. A number of students assisted in the crystal-growth experiments. Ms. Janet Shapiro deserves special mention for her contributions. Mr. Bruce Hansen constructed the electronics associated with the frequency-shift-detection ac susceptibility apparatus.

Special thanks go to Dr. Stanley Mroczkowski for numerous helpful discussions concerning crystal growth. I am greatful to Professors G. L. Haller, V. E. Henrich, D. E. Prober, and R. G. Wheeler for serving on my thesis committee. Professors H. Winchell and V. E. Henrich kindly provided access to x-ray equipment. I am happy to thank Mr. P. Santhanam for useful conversations and collaboration, and Mr. James Gordon for assistance in running the low-temperature experiments.

I certainly owe the largest debt of gratitude to my thesis advisor, Professor Daniel Prober, whose patient instruction and unfailing optimism have contributed immeasurably to all aspects of this project. I would also like to thank my parents for their support and confidence in me over the years.

TABLE OF CONTENTS

Frequently Used Symbols and Abbreviations

SYMBOL	MEANING
BCS	Refers to the Bardeen-Cooper-Schrieffer theory
c	Speed of light
CDW	Charge-density wave
e	Magnitude of the electronic charge
E_F	Fermi energy
f_r	Resonant frequency
f_o	Undamped resonant frequency
f_a	Driven frequency
GL	Refers to the Ginzburg-Landau theory
h	Planck's constant
$H_c(T)$	Critical field of a type I superconductor or the thermodynamic critical field of a type II superconductor
$H_{c1}(T)$	Lower critical field (type II)
$H_{c2}(T)$	Upper critical field (type II)
$H_{c2\parallel}(T)$	Upper critical field, H parallel to the layer plane
$H_{c2\perp}(T)$	Upper critical field, H perpendicular to the layer plane
$H_{c3}(T)$	Critical field for surface superconductivity
H_p	Pauli paramagnetic limiting field
H_p^0	Simple theoretical estimate for H_p
k_B	Boltzmann's constant
k	Electron wavevector
ℓ	Electron mean free path

mfp	Electron mean free path
m	Electron mass
m_e	Free-electron mass
N(0)	Electronic density of states at the Fermi level
Q	Resonant circuit quality factor
RRR	Residual-resistance ratio
TMDC	Transition metal dichalcogenide
T_o	CDW onset temperature
T_d	CDW lockin temperature
T_c	Superconducting transition temperature
t	Reduced temperature
T_m	Midpoint temperature; zero-field transition curve
T_m'	Midpoint temperature; transition in an applied field
T_{ext}	Extrapolated high-temperature end of a transition curve
v_F	Fermi velocity, rms average over the Fermi surface
$\vec{v}_F(\vec{k})$	Electron velocity at a point on the Fermi surface
W	Width of the superconducting transition
γ	Coefficient of the low-temperature electronic heat capacity
δ	Normal-state electromagnetic penetration depth
$\Delta(0)$	Zero-temperature energy gap
η_{Hc2}	Strong-coupling correction factor
θ_D	Debye temperature
κ	Ginzburg-Landau parameter

λ	Superconducting magnetic field penetration depth
$\lambda_{ep}(T)$	Electron-phonon coupling parameter
λ_{ep}	Value of $\lambda_{ep}(T)$ at low temperature
λ_{tr}	Normalized electron scattering rate, potential scattering
λ_{so}	Normalized electron scattering rate, spin-orbit scattering
$\xi(T)$	Ginzburg-Landau coherence length
ξ_0	BCS coherence length
ρ	Resistivity
σ	Conductivity
τ	Electron lifetime
Φ_0	Magnetic flux quantum
χ	Gor'kov function, susceptibility (Chapter 4)
Ψ	Ginzburg-Landau wavefunction

I. Introduction

This thesis describes a study of the upper critical field $H_{c2}(T)$ of the superconducting metallic compounds $Nb_{1-x}Ta_xSe_2$ ($0 \leq x \leq 0.20$). These compounds belong to the chemical family of transition metal dichalcogenides (TMDC). These materials adopt a layered crystal structure similar to that of graphite. Thus, they can be expected to exhibit very anisotropic physical properties. $NbSe_2$ has been very extensively studied, both in this work and in previous studies, and therefore provides a convenient reference point.

The upper critical field $H_{c2}(T)$ of very anisotropic superconductors exhibits certain characteristic features not normally found in isotropic, or nearly isotropic, systems. Specifically, positive (upward) curvature is frequently seen just below T_c and extended linearity at low temperatures has also been observed. This study was undertaken to investigate the effect that substitutional alloying of Ta into $NbSe_2$ has on the temperature dependence and the magnitude of the upper critical field. Such alloying should allow systematic control of the electron mean free path ℓ, ideally going from the clean limit ($\ell >> \xi_0$) to the dirty limit ($\ell << \xi_0$). Here ξ_0 is the BCS coherence length, a fundamental, material-specific length scale characterizing the superconducting state. Alloying will also affect the band structure of these materials.

Chapter II contains an introduction to the crystal structure and physical properties of the TMDC's generally and $NbSe_2$ specifically. The band structure is emphasized, since the electronic properties, especially the Fermi surface topology, are very important for

determining $H_{c2}(T)$. Because of the quasi-two-dimensional nature of the band structure, $NbSe_2$, like most TMDC's, has an electronic charge-density wave at low temperatures. The charge-density wave found in quasi-two dimensional materials is a manifestation of the same physical phenomenon as the Peirels instability found in in one-dimensional metallic systems. • Charge density waves are discussed here since the perturbation that the they impose on the band structure directly affects the superconducting properties.

The purpose of this study has been to investigate the effects of the introduction of impurities into the $NbSe_2$ crystal lattice. It is clear that high quality crystals are required for such a study. Of equal importance is the fact that high quality single crystals are generally required for critical field studies in very anisotropic systems. For these reasons, considerable attention has been paid to the crystal growth process. While much basic information is available in the literature concerning the growth of TMDC crystals, a number of details had to be worked out for the $Nb_{1-x}Ta_xSe_2$ system. The crystal growth work is described in Chapter III.

Chapter IV describes the experimental techniques used to measure the superconducting properties. Most of the instrumentation used to produce and measure the required magnetic fields and low temperatures is of fairly standard design. However, the circuitry used to detect the superconducting-to-normal phase transition has to be usually sensitive. This is because the better quality crystals of $Nb_{1-x}Ta_xSe_2$ we have produced are rather small, with diameters of only a few hundred micrometers (microns). The apparatus designed to measure these samples

is described in detail.

Chapter V reviews the theory of $H_{c2}(T)$ as a prelude to the discussion of our measured critical field properties in Chapter VI. A completely general theory has yet to be worked out, even within the constraints of the BCS model. However, a number of important specific models have been solved, and it is usually possible to sensibly compare experimental results to the predictions of these models.

Chapter VI is the central chapter of this thesis. The measured superconducting properties of the $Nb_{1-x}Ta_xSe_2$ crystals are reported here, as is an analysis of this data. While the critical field properties have been measured accurately, only a semi-quantitative analysis is possible due to the complex nature of these materials and the lack of values for certain "normal-state" parameters.

It will be argued that Fermi surface geometry is a primary factor in determining the form of $H_{c2}(T)$, so it is of some interest to determine what type of Fermi surface characteristics are of importance. Chapter VII is concerned with computer modeling which has been done using various Fermi surface models to calculate $H_{c2}(T)$ in anisotropic systems. Such calculations are also of interest as they allow various proposed band structures for $NbSe_2$ to be critically assessed.

Finally, the thesis will conclude with a summary of the major conclusions reached. We will also present suggestions for further work.

II. The Transition Metal Dichalcogenides

The physical and electronic properties of the TMDC's are dominated by anisotropy effects which are caused by the particular type of crystal structure and chemical bonding these materials adopt. This crystal structure and the resulting electronic band structure are described in this chapter. The band structure is important here because the Fermi-surface topology is very important for determining the upper critical field $H_{c2}(T)$.

This chapter also includes a discussion of charge-density waves (CDW), a low-temperature lattice distortion common in materials of lower dimensionality. It is important to include such a discussion since CDW's influence the superconducting properties of the $Nb_{1-x}Ta_xSe_2$ compounds via their effect on the band structure.

II.1 Crystal Structure and Bonding

Many transition metals react with the chalcogens (sulfur, selenium, and tellurium) to form compounds with a layered crystal structure similar to that of graphite, and having the general formula MX_2 (M = metal, X = chalcogen).[1,2,3] The most extensively studied TMDC's are the disulfides and diselenides of group IVB (Ti, Zr, Hf), group VB (V, Nb, Ta), and group VIB (Mo, W). Other stoichiometries are also possible in these systems; e.g., the triselenides $NbSe_3$ and $TaSe_3$, which form thin needle-like crystals, are interesting quasi-one-dimensional materials in their own right.[4,5]

The basic crystal structure of the dichalcogenides is shown schematically in Figure 2-1. These materials are composed of three-atom-thick, covalently-bonded layers with only weak van der Waals-type interlayer bonding. Each individual layer is made up of three hexagonally-close-packed (hcp) planes; a metal plane is sandwiched between the 2 chalcogen planes. There are two distinct ways of stacking these three hcp planes, and thus two kinds of layers can exist. Atoms in the top plane can either be directly above the atoms in the bottom plane (an AbA sequence), or they can be directly above holes in the bottom layer (an AbC sequence). An AbA sequence leads to trigonal-prismatic coordination of the metal atoms by the six nearest chalcogen atoms, while an AbC sequence leads to octahedral coordination.

A large number of different crystal structures, or polytypes, can be constructed by arranging the two different types of layers in different stacking sequences. Structures with unit cell repeat distances 1, 2, 3, 4, and 6 layers thick have been reported.[1,2] A nomenclature has been developed to describe these structures. It consists of a number denoting the number of layers in a unit cell, followed by a capital letter indicating the symmetry of the unit cell. The letters H (hexagonal), T (trigonal), and R (rhombohedral) are used. However, all the crystal structures can be considered to be hexagonal,[6] and unit cell parameters are universally reported as the usual hexagonal lattice parameters a and c. If necessary to avoid ambiguity, a lower case letter is added in parentheses to complete the specification.

II.1.1 Phase Diagram

The particular crystal structure adopted by a compound depends upon both composition and temperature. However, there is a basic pattern common to the phase diagrams of most TMDC's. The structure stable at the highest temperatures is the 1T, consisting entirely of octahedral layers, while the polytype stable at low temperatures consists entirely of trigonal-prismatic layers, usually a 2H structure. At intermediate temperatures a variety of polytypes are found, typically consisting of a mixture of trigonal-prismatic and octahedral layers. Generally these higher-temperature phases can be obtained at room temperature by rapid quenching.

These basic trends are followed by $NbSe_2$ and $TaSe_2$. Phase diagram information for $NbSe_2$ has been reported by several authors,[7-10] who generally agree as to the phases found, although the exact values for the temperatures of the phase boundaries are only roughly in agreement. The 1T phase is found above about 950°C (and for $NbSe_2$ this phase cannot be obtained at room temperature by quenching[10]). Between 950°C and about 850°C several 4H phases have been found; 4H(b), 4H(d_I), and 4H(d_{II}). The 2H(a) phase is stable below about 850°C, although the 4H(a) phase may also be found at the lowest temperatures if excess selenium is present during the crystal growth process.[7,8,10] Both the 2H(a) and the 4H(a) phases consist entirely of trigonal-prismatic layers.[1,2,3]

The phase diagram for $TaSe_2$ is quite similar, although not as extensively investigated. Revelli[7,8] found the 1T polytype stable above 800°C, the 4H(b) and 6R polytypes stable between 800°C and 880°C

and the 2H(a), as well as the 4H(c) and 4H(b) stable at low temperatures. The lattice parameters reported[9] for 2H $NbSe_2$ are a = 3.45 Å and c = 12.54 Å, while the parameters for the same phase of $TaSe_2$ are a = 3.43 Å and c = 12.71 Å. The similarity is caused by the very similar sizes of the Nb and Ta atoms.*

A problem with accurately determining the phase diagrams in the TMDC's is that many different structures are possible, and the energy difference between the several polytypes is small, especially where they differ only in the stacking of adjacent layers. The phase obtained in a given experiment can then depend very sensitively on crystal growth conditions, e.g., the presence of excess Se favors the production of the 4H(a) phase in $NbSe_2$ at lower temperatures, as noted above.

The $Nb_{1-x}Ta_xSe_2$ crystals used in the critical field studies reported in this thesis are all of the 2H(a) phase. The conditions used to produce them, and the work done on the phase diagram for this system will be discussed in Chapter III. For the sake of conciseness, "2H" will henceforth be taken to mean the 2H(a) phase, and "4H" will be taken to mean the 4H(a) phase.

II.1.2 Anisotropy in the Physical Properties

The anisotropy in the material properties of the TMDC's is caused by the anisotropy in the chemical bonding. Physically these compounds tend to be very soft due to the van der Waals bonding, and single crystals

---

* The similar size of the Nb and Ta atoms is caused by the well-known lanthanide contraction. Reference 11 lists the atomic diameters of both elements as 2.94 angstroms.

must be handled with great care to prevent damage. In fact, naturally-occuring MoS_2 is a commonly used lubricant. As an example of the amount of anisotropy seen in $NbSe_2$, it is useful to consider the resistivity. The resistivity for current flow perpendicular to the layer plane is greater than the resistivity measured parallel to the layer plane by a factor which is 32 at 300 K and 50 at 7 K.[12] This anisotropy is readily understandable since electrons moving perpendicular to the layer plane must pass through the weakly-bonded interlayer region.

$NbSe_2$ and the compounds $Nb_{1-x}Ta_xSe_2$ are three-dimensional, although anisotropic materials (Section VI.4.5). However, it is interesting to note that the anisotropy in some layered compounds can be increased to the point that they exhibit quasi-two-dimensional behavior. This is accomplished by the process of intercalation; certain types of organic molecules (and metal atoms) can be inserted into the van der Waals gap between the individual three-atom-thick layers, separating the layers.[13] If the thickness of the organic layer exceeds the superconducting coherence length (Chapter V), the layers essentially decouple and quasi-two-dimensional critical field behavior results.[14,15] This decoupling phenomenom has also been observed in artifically produced layered composites.[16]

II.2 Band structure Calculations

A number of band structure calculations have been carried out for $NbSe_2$. The earliest calculations were of the semi-empirical tight-binding type.[2,17] Later ab-inito calculations were performed by Mattheiss[18] using the augmented-plane-wave (APW) method, and by Wexler

and Woolley[19] using a layer method. Wexler and Woolley also considered $TaSe_2$. The empirical pseudopotential method has been used by Fong and Cohen.[20] Recently a linear combination of atomic orbitals (LCAO) approach has been used by Bullett.[21] These calculations have been reviewed by Calais[22] and Doran.[23] All of them are non-relativistic and are not self-consistent.[24]

II.2.1 Elementary Considerations

There is good agreement as to the general nature of the band structure, which can be described simply. There are two $NbSe_2$ molecular units per unit cell for the 2H phase (one per covalently-bonded layer). Since the electronic configuration of Nb is $[Kr]4d^45s^1$ and the configuration of Se is $[Ar]3d^{10}4s^24p^4$, there are a total of 34 electrons outside of the filled core levels per unit cell. It is conceptually useful to label the bands according to the atomic orbitals from which they are primarily derived. With this notation, the energy bands are, in order of increasing energy; 4 bands derived from Se s orbitals (4 Se s bands), 12 Se p bands, 10 Nb d bands, and at the highest energy the Nb s-p bands. It turns out that the 10 Nb d bands are split by a "hybridization gap" into 2 lower-energy and 8 higher-energy bands. Putting 34 electrons into these bands, the Se s and p bands are filled and the lower pair of d bands is half filled.

The theoretical calculations predict that the bands are paired in $NbSe_2$ since in any hexagonal system, in the absence of the spin-orbit interaction (neglected in all the calculations), the energy bands must be doubly degenerate at the top and bottom faces of the Brillouin zone

because of time-reversal symmetry.[25] By continuity, the bands remain approximately paired elsewhere, too. A more physical way of explaining this pairing for the 2H TMDC's is to note that if the unit cell consisted of only one three-atom-thick layer, then there would be only 5 d bands (only one $NbSe_2$ molecular unit per unit cell). These 5 levels are split into 10 in the real structure due to the interlayer interactions, which are relatively weak and thus do not produce a large splitting.[18]

II.2.2 Ab Initio Calculations

The band structure as calculated by Mattheiss is reproduced in Figure 2-2. The Fermi level is shown and passes through the lower pair of d bands. The notation for some of the the special points in the Brillouin zone is shown in Figure 2-3. (The Brillouin zone of a hexagonal lattice is itself hexagonal.) The band structure as calculated by Wexler and Woolley is very similar to the result of Mattheiss, as would be expected since both are based on muffin-tin atomic potentials, and Wexler and Woolley chose the parameters of their atomic potentials to be similar to those used by Matteheiss.[19] The main difference is that Mattheiss' calculation only produced energy eigenvalues at 6 high-symmetry points in the Brillouin zone, and an interpolation scheme was used to generate the bands. On the other hand, the layer technique used by Wexler and Woolley can generate eigenvalues for general k vectors, so no interpolation scheme is needed. The layer technique can also be used to generate constant-energy surfaces, thus allowing the Fermi surface to be accurately determined (within the

approximations used in originally setting up the calculation).

The Fermi surface determined by Wexler and Woolley consists of undulating open cylinders running along the ΓA (zone center) and KH (zone corner) axes. It is convenient to display this surface in a doubled Brillouin zone scheme. As was noted above, in a non-relativistic calculation the energy bands stick together over the top of the hexagonal Brillouin zone. In the conventional Brillouin zone each of the Fermi surface cylinders is double-walled, the two walls joining at the top surface and coming into it with equal and opposite angles, as measured normal to the top surface. Thus each double surface can be unfolded into a smoothly continuous surface in a double zone.

Figure 2-4 shows a side view of the Fermi surface in this double zone (the plane defined by the points ΓKHA) and Figure 2-5 shows a top view of the Fermi surface, looking down the ΓA axis, a plane section taken through the middle of the doubled zone, corresponding to the top of the conventional zone. These Fermi surface diagrams were generated from explicit parametrization formulas published by Wexler and Woolley.[19] Both the cylinders shown in Figure 2-5 are hole surfaces. (That is, the electron states just inside the cylinders are of higher energy than the states just outside.) There is obviously a resemblance to an ideal two-dimensional Fermi surface, (which is cylindrical),* but the undulations in the cylinder walls indicate the three-dimensionality of $NbSe_2$.

---

* The basic concepts of Fermi surfaces in lower-dimensional systems are reviewed in Appendix A.

Figures 2-4 and 2-5 also show the same views of the Fermi surface of $TaSe_2$, as calculated by Wexler and Woolley. Obviously the calculated band structures of the two materials are very similar. If this is actually the case, then rather small changes in electronic properties should be expected as the composition is varied across the series $Nb_{1-x}Ta_xSe_2$.

There are several approximations which go into the ab initio calculations by Mattheiss and by Wexler and Woolley which must be considered in trying to determine the validity of their results. Both calculations are based on similar muffin-tin potentials and the small differences in the resultant band structures have been attributed to slight differences in the atomic potentials used.[23] The use of such potentials for systems as complicated as transition metal compounds has been discussed by Calais.[22] Since the calculations are non-relativistic, the spin-orbit interaction is ignored. Including this interaction would lift the double degeneracy of the bands over the top surface of the Brillouin zone and thus alter the band structure, at least near this surface. Ta (Z = 73) is roughly twice as heavy as Nb (Z = 41). Thus the spin-orbit interaction will be more important for Ta and will probably alter to some extent the conclusion of Wexler and Woolley indicating that $NbSe_2$ and $TaSe_2$ have very similar band structures.

Neither of the above calculations is self-consistent, that is, they do not allow for charge transfer from the metal atoms to the selenium atoms, which is bound to occur due to the electronegatively differences.[23,24] (The electronegativities are Nb: 1.6, Ta: 1.5, and Se: 2.4). It appears that the major error introduced by this assumption is

to over-estimate the gap between p and d bands.[23] This is potentially important since the Fermi level lies in the lower two d bands.

Although it is difficult to exactly assess the effects the approximations listed above have on the calcalated Fermi surfaces, it is appropriate to treat the calculated band structures with some caution. This is especially true since a relatively small change in narrow d bands can have a large effect on the Fermi surface.

There have been several angle-resolved photoemission spectroscopy studies done on $NbSe_2$ which have been interpreted as directly mapping the energy bands as a function of k.[26,27] While there is generally fair agreement with the calculations, these experiments cannot claim to determine the band structure in detail, and the agreement is especially poor for the very important lower pair of d bands.

II.3 Charge-Density Waves

Before considering the results of low-temperature experiments which illuminate the actual band structure, it is necessary to take note of the fact that $NbSe_2$, $TaSe_2$, and most other TMDC's undergo structural phase transitions at low temperatures which affect the electronic energy bands. This section will discuss this new state, called the charge-density wave (CDW) state. A general introduction to the phenomenon will be followed by a more detailed look at CDW's in the $Nb_{1-x}Ta_xSe_2$ system.

II.3.1 Basic Theory

A CDW is coupled lattice-electronic distortion which occurs at low temperatures in certain materials which exhibit a specific type of Fermi surface topology, as described below. The purpose of this section is to provide a brief, physically motivated description of what CDW's are and what causes them. More detailed discussions can be found in several good review articles.[1,28-32]

Consider a simple metal, and assume that by some mechanism the originally uniform electronic charge density is given a sinusoidal modulation, becoming

$$\rho(\vec{x}) = \rho_o(\vec{x})[1 + A \sin(\vec{q} \cdot \vec{x})] \qquad (2.1)$$

where $\rho_o(\vec{x})$ is the undistorted charge density, A is the amplitude of the distortion, and $\vec{q}$ is its wavevector. The ion cores will react to this new electronic distribution by moving away from their equilibrium positions in a way which is also sinusoidal with wavevector $\vec{q}$, but which is out of phase with the electronic redistribution.[28]

To determine the stability of this new structure, it is convenient to separately consider the changes in the lattice and electronic energies. The lattice energy will be increased as the ion cores are moved from their equilibrium positions. The effect of the new ionic positions on the electronic energy bands is to open up gaps in the bands at $\vec{k} = \pm\vec{q}/2$, ($\vec{k}$ is the electron wave vector) in the same way that the ordinary ionic potential in any metal introduces gaps into the band structure at the Brillouin zone boundaries.

Electron states with $\vec{k}$ near $\vec{q}/2$ but of magnitude $k < q/2$ will have their energy lowered, while states with $\vec{k}$ near $\vec{q}/2$ but with $k > q/2$ will have their energy increased. If $\vec{q}$ is chosen to be exactly twice the Fermi wavevector, then only states unoccupied (at $T = 0$) will have their energy increased, leading to a net lowering of the electronic energy.

Whether or not this lowering of electronic energy exceeds in magnitude the increase in lattice energy depends upon the fraction of the Fermi surface over which the gap occurs. For a material with an ideally spherical Fermi surface, a particular $\vec{q}$ vector can only couple electron states at two points on opposite sides of the Fermi surface. The resultant gap will only cover a small fraction of the Fermi surface, leading to a small net lowering of the electronic energy.

The situation can be quite different in materials with non-spherical Fermi surfaces. If the Fermi surface contains parallel flat sections such that a single $\vec{q}$ vector can span large sections of the Fermi surface, and thus connect many electron states on opposite sides of the Fermi surface (or on different pieces of the Fermi surface), then a gap can be opened up over a large portion of the Fermi surface. This results in a relatively large lowering of the total electronic energy. In such cases this energy lowering can exceed in magnitude the increase in lattice energy, making the electronic CDW with its associated periodic lattice distortion the stable low-temperature state of the material. As the temperature is increased, the electron population in states above the gap increases, increasing the electronic energy, reducing the gap and lowering the CDW amplitude.

The most extreme example of the phenomenon occurs in an ideal one-dimensional metal, where the Fermi surface consists of two parallel planes at $\vec{k} = \pm\vec{k}_F$. Here one $\vec{q}$ vector can connect all the electron states to other states. This opens up a gap in the band structure over the entire Fermi surface, causing the material to undergo a metal-insulator transition. That such a transition should occur in one-dimensional metals was first noted by Peirels and the phenomenon here is usually called a Peirels transition.[33] There are a number of materials where the chemical bonding is sufficiently chain-like that their Fermi surfaces can be considered to be quasi-one-dimensional. Many of these materials do display Peirels transitions.[5]

There is a potentially serious problem with the simple picture of a CDW described above. The CDW wavevector $\vec{q}$ was shown to be related to Fermi surface topology and, in general, is not in any way related to the original lattice periodicity. Such a CDW is incommensurate with the lattice. Strictly speaking there is no translational symmetry left in the crystal. Thus familiar ideas such as the concept of a Brillouin zone, the labelling of electronic states by $\vec{k}$ vectors, etc., should in principle be abandoned.

Fortunately, this doesn't have to be done in order to gain a physical understanding of CDW's in the TMDC's. This is primarily because the structure of the incommensurate CDW state is somewhat more complicated than has been described above. In the TMDC's the wavelength of the CDW is always within a few percent of being commensurate; it is always very close to being some integral multiple of the undistorted lattice constant. Taking cognizance of the fact that the displacements

of the ions from their non-CDW-state equilibrium positions are typicaly a small fraction of an angstrom, this means that there are relatively large distances over which a sinusoidal CDW will be roughly in-phase with the lattice, followed by similar distances over which it will be approximately out-of-phase.[34] Here "in-phase" means that the electronic density is shifted in such a way that the bonding energy between adjacent ions is optimized. As noted by Moncton, Axe, and DiSalvo,[35] and by McMillan,[34] in a real system the CDW is altered from a simple sinusoidal shape so as to stretch the regions over which there is an energetically optimum matching of the CDW and the lattice. This can be accomplished by adding a spacially varying phase to the argument of the sine function in Equation 2.1. The picture that thus emerges for the incommensurate state is that it consists of regions where the CDW wavelength is effectively commensurate with the underlying lattice connected by smaller regions where the phase changes rapidly and the CDW amplitude is suppressed.[30,31]

If the temperature is increased, starting in the incommensurate state, the CDW amplitude will decrease, vanishing at an onset temperature T_o. If the temperature is decreased, the amplitude will increase. As the amplitude increases it becomes more energetically favorable for the CDW to be commensurate with the crystal lattice. Usually a second transition occurs to a completely commensurate state at a lower temperature T_d.[1] In real materials it is possible for the wavevector to shift slightly without sacrificing all the energy the electrons originally gained by forming the CDW, since in these systems the parallelism between different parts of the Fermi surface is never perfect.

II.3.2 CDW's in the $Nb_{1-x}Ta_xSe_2$ System

CDW's exist in both $NbSe_2$ and $TaSe_2$.[1,36] However, as will be discussed below, alloying Ta into $NbSe_2$ suppresses the CDW, so in the composition range studied ($0 \leq x \leq 0.20$), only $Nb_{1-x}Ta_xSe_2$ compounds with compositions near pure $NbSe_2$ have CDW's. $NbSe_2$ undergoes a second-order phase transition to an incommensurate CDW state at an onset temperature T_o = 33.5 K as determined by neutron diffraction[29,35] and transmission electron diffraction.[1,36,37] $NbSe_2$ has the lowest T_o of any TMDC which has a CDW. To the lowest temperatures studied (4.5 K by neutron scattering,[35] 0.3 K by heat capacity[38]) $NbSe_2$ does not display a lock-in transition to a commensurate state as the other TMDC's do.[1] In contrast, $TaSe_2$ undergoes a second-order transition at T_o = 122 K, and subsequently undergoes a first-order transition to the commensurate CDW state at 90 K.[1,35] As was noted in the last section, the incommensurate-to-commensurate transition is driven by the commensuration energy, which increases with the CDW amplitude.[30] Thus the lack of a lock-in transition, along with the relatively low T_o implies that the CDW amplitude is relatively small in $NbSe_2$. The amplitude of the atomic displacements in the accompanying lattice distortion is largest in the plane of the Nb atoms.[35] The amplitude of the modulation in this plane is 0.05 Å at 4.2 K.[28]

In $NbSe_2$, as in the other TMDC's, there are actually three symmetry-related CDW's, all lying in the basal plane with their wavevectors at 120° angles from each other. Just below T_o the average wavelength of the distortion is very close to being 3 times the hexagonal unit cell parameter a, $\lambda = 3.08a$, as determined by neutron diffraction[35]. This

wavelength shrinks toward 3a as the temperature decreases, but apparently never becomes exactly commensurate. Thus in the CDW state $NbSe_2$ almost adopts a real space supercell with unit cell parameters a' = 3a, c' = c where a, c are the undistorted hexagonal lattice parameters.

A number of experiments have been performed which indicate the effects the CDW has on the properties of $NbSe_2$. Since the CDW and its associated periodic lattice distortion affect both the band structure and the crystal structure, in principle almost every material property should be affected. Harper, Geballe, and DiSalvo[39] measured anomalies in the resistivity and heat capacity at T_o, which take the form of bumps. They found a rise of 6.5% in the specific heat and a rise of 3% in the resistivity from which they concluded that only a few percent of the Fermi surface is affected by the transition to the CDW state. Long[40] has also measured the bump in resistance and found a rise of 5.5% in a crystal of unusually high quality. It is interesting to note that although there is a small rise in R(T) at T_o, dR/dT is greater below T_o than above. Therefore, the resistance in the CDW state is lower than that obtained by extrapolating R(T) from above T_o to temperatures somewhat below T_o.*

Nuclear magnetic resonance studies have been performed on $NbSe_2$ using the ^{93}Nb nucleus, the only naturally occurring isotope, by Berthier, Jerome, and Molinie[41] Such studies are of interest since the resonance phenomena are sensitive to the electronic environment of the individual Nb atoms. The data indicate that the Nb nuclei see a

---

* This phenomena is not generally seen in CDW systems.

continuous distribution of local electronic densities, as would be expected for an incommensurate CDW. It has been claimed that the details of the line shapes are consistent with the picture of the incommensurate state as consisting of domains of effective commensurability separated by discommensurations.[30] From their data, Berthier, Jerome, and Molinie estimated that the maximum redistribution of electron density caused by the CDW in $NbSe_2$ is less than 9%, and they place an upper limit on the possible decrease in density of states at the Fermi level at 10%. This decrease in density of states can also be roughly estimated from the superconducting transition temperature to be about 1-3% (Chapter VI).

One parameter which does change dramatically at T_0 is the Hall coefficient, which is positive above T_o and becomes negative at lower temperatures.[42,43] Such a change indicates a switch from predominantly hole-like charge carriers above T_o to predominately electron-like carriers below T_o.[25] In this connection it is worth recalling that the high-temperature Fermi surface, as calculated by Wexler and Woolley, consists entirely of hole surfaces. The Seebeck coefficient also changes sign at T_0.[44]

There is considerable evidence that introducing disorder into $NbSe_2$ crystals suppresses the CDW. Substitutionally alloying in another metal to replace Nb has been shown to reduce T_o as measured by the bump in the resistivity.[38,40] Also, such doping suppresses the sign change in the Hall coefficient. In a study involving a large number of crystals, Huntley and Frindt[42] showed that the Hall coefficients of $NbSe_2$ samples with higher residual-resistance ratios changed sign at a higher

temperature and were larger in magnitude at low temperatures. Indeed, those samples with the smallest residual-resistance ratio, indicative of the poorest sample quality, had Hall coefficients which remained positive at low temperatures, indicating a suppressed CDW transition.

The CDW in $NbSe_2$ is likely caused by a parallelism in the Fermi surface. According to the usual nesting model, traditionally used to describe CDW's in the TMDC's,[1] a single $\vec{q}$ vector can connect many pairs of states on different parts of the Fermi surface. This means that if two cross-sectional diagrams of the Fermi surface in the plane containing $\vec{q}$ are superimposed with one shifted relative to the other by $\vec{q}$, then the two Fermi surfaces should at least partially lie on top of each other, that is they should "nest". The Wexler and Woolley Fermi surface exhibits a rather weak nesting when this procedure is carried out.[23]

An alternative to the nesting model for CDW formation has been proposed by Rice and Scott.[45] They showed that a two-dimensional band structure with saddlepoints at the Fermi energy would be unstable against CDW formation, and suggest that such a model might apply to the 2H layered compounds. If saddle points were to exist at the Fermi energy, the density of states as a function of energy would be very large at those points. Thus, a significant decrease in electronic energy would result not from $\vec{q}$ spanning a large portion of the Fermi surface area, but from $\vec{q}$ spanning a small portion of the Fermi surface which has a very large density of states. Such a CDW would affect only a relatively small fraction of the Fermi surface. Furthermore, the states removed at the saddle points have a small velocity. Such points can act

as scattering sinks, and Rice and Scott argued that such a material might actually be a better conductor in the CDW state, as is seen experimentally in the 2H materials $TaSe_2$[1], TaS_2,[1] and $NbSe_2$.[48] In the nesting model, if a gap opened up over a large part of the Fermi surface the conductivity would generally be expected to decrease. Another attractive feature of the Rice and Scott model is that it can easily explain the sign reversal of the Hall coefficient. The Fermi surface alterations they envision cause the K-centered and Γ-centered Fermi surface cylinders to merge or connect along the Γk axis. This will change the connectivity of the Fermi surface from consisting of hole surfaces to consisting of electron surfaces. Such an alteration would cause the sign of the Hall coefficient to become negative.

There is a saddle point along the Γk axis of the Wexler and Woolley band structure, however it is not exactly at either the correct energy (E_F) or the right wavevector to account for the CDW in $NbSe_2$.[46] The two CDW models, nesting and saddlepoint, are really quite similar, and since the density of states must vary over the Fermi surface, it is quite plausible to assume that the truth may lie in a combination of these two explainations. However, it appears that the available band structure calculations are not of sufficient accuracy to quantitatively explain the CDW in $NbSe_2$.

II.4 Low-Temperature Band Structure of $Nb_{1-x}Ta_xSe_2$

The band structures calculated for CDW-free (room-temperature) $NbSe_2$ and $TaSe_2$ show a Fermi surface dominated by open cylinders oriented perpendicular to the basal plane. At low temperatures these materials

have CDW's which alter the band structure. However, the CDW is fairly weak in $NbSe_2$, and thus may affect the band structure of this compound only slightly.

Several experiments have been performed which provide information concerning the low-temperature band structure. In a de Haas-van Alphen study, Graebner and Robbins[47] were able to explain their results by assuming that a small pancake-shaped Fermi surface piece exists lying in the basal plane. If one assumes for simplicity that the CDW in $NbSe_2$ is a commensurate 3x3 distortion, then to a first approximation the band structure in the CDW state can be obtained by folding the non-CDW band structure back into the new Brillouin zone, which is 1/9 the volume of the original.[46] Such a procedure was tried without success to explain the de Haas-van Alphen results.[47] However, Graebner and Robbins pointed out that a small modification of the d bands near the Fermi level could produce a pancake-shaped Fermi surface piece.

It was mentioned above that failure to allow for charge transfer from the metal atoms to the Se atoms in the band structure calculations has the primary effect of exaggerating the gap between the p and d bands. Allowing for such charge transfer could possibly raise the p bands to the point where they intersect the Fermi level (Figure 2-2). It appears that such a change could cause a pancake-shaped Fermi surface piece to appear.[23]

Magnetoresistance as a function of orientation has been measured by Hambourger and Lewis[48] at temperatures both above (35 K) and below (9.3 K) T_o. Their data indicates that the Fermi surface is composed of one or more at least highly elongated, and possibly open, pieces running

perpendicular to the basal plane. The data at 35 K are noisier, but otherwise similar to the data in the CDW state, implying that no large-scale Fermi surface changes occur at T_o. According to Hambourger and Lewis, the de Haas-van Alphen and magnetoresistance results may be complimentary rather than contradictory, given the different sensitivities to Fermi surface topology of each probe.

The picture that results from the band structure calculations and the experiments discussed above is that the Fermi surface of $NbSe_2$ is dominated by open cylinders parallel to the c axis, although it is very possible for at least one small flat closed piece to exist. It also appears that the CDW doesn't drastically alter the band structure, although it probably does affect the connectivity of the Fermi surface, as evidenced by the change in the sign of the Hall coefficient.

It is difficult to speculate on the band structure of the alloys at low temperatures. However, since the CDW is suppressed by alloying, and since the room-temperature (no-CDW) band structure calculations show similar theoretical results for $NbSe_2$ and $TaSe_2$, it is possible that the actual $Nb_{1-x}Ta_xSe_2$ band structures at low temperatures resemble the calculated (room-temperature) $NbSe_2$ band structure, possibly more then $NbSe_2$ itself does at low temperatures.

III. Crystal Growth

This chapter discusses the the techniques which have been developed to grow single crystals of the compounds $Nb_{1-x}Ta_xSe_2$. Although certain details had to be worked out, most of the procedures used were adapted from previously developed techniques for growing crystals of $NbSe_2$ and other TMDC's.

There are 39 crystal growth batches in all. The earlier batches were grown by several other researchers, as noted in the Acknowledgements. The author's involvement with the details of the crystal growth effort began with Batch 12.

The compounds $Nb_{1-x}Ta_xSe_2$ can be formed by simply reacting the elements in an evacuated, sealed quartz tube at temperatures ≈ 500°C or higher. Although crystals form during this process, they tend to be small and intergrown. Generally it is necessary to use the vapor-transport technique to grow reasonably sized, more perfect crystals. In addition, it is necessary to grow or anneal the crystals at the proper temperature to get the desired 2H polytype. To determine these temperatures, it was necessary to work out part of the phase diagram for the $Nb_{1-x}Ta_xSe_2$ system. This was done using x-ray analysis and measurements of the superconducting transition temperature.

This chapter is concerned with the details of these processes. First the basic concepts of vapor-transport crystal growth are outlined. The following sections then contain details of the laboratory procedures and a discussion of the results.

III.1 Vapor-Transport Crystal Growth

The compounds $Nb_{1-x}Ta_xSe_2$ have in all cases been formed by direct reaction of the elements, which is the standard method used for TMDC's. However, as will be discussed in more detail in Section III.2.4, the result of such a direct reaction, carried out at a constant temperature, is a large number of small, highly intergrown hexagonal platelets with diameters in the range of 10 to 100 μm. The size of these crystals is at the lower end of the range which can be conveniently measured with our transition temperature apparatus (Chapter IV). However, the real problem with these crystals is the intergrowth of adjacent crystallites, which makes such samples generally unacceptable for orientation-dependent $H_{c2}(T)$ measurements where high quality single crystals are required. Another technique for growing single crystals is therefore needed. The TMDC's do not melt or sublimate at any reasonable temperature,[6] so that many standard techniques for producing single crystals are inapplicable.

The standard technique for the growth of TMDC crystals is the vapor-transport technique.[49,50] The method involves sealing some prereacted powder (e.g., $NbSe_2$) along with a transporting agent such as iodine in a quartz tube. (Usually 5 mg of I per cm^3 of tube volume are used.[6,51]) This tube is then placed in a tube furnace where a temperature gradient can be maintained, the prereacted powder being at the hot end of the tube. For these materials, the hot end may be at e.g., 760°C, while the cooler end is held at 740°C. The following reversible reaction then occurs between the powder and the vaporized transport agent[52,53]

$$NbSe_2 + 2I_2 \rightleftarrows NbI_4 + Se_2 \,. \qquad (3.1)$$

The products of this reaction (those shown on the right hand side of Equation 3.1) are gaseous. The gaseous products diffuse to the cooler end of the tube, where the reaction tends to go in the reverse direction because of the temperature dependence of the equilibrium constant governing Reaction 3.1. The original material is re-formed and the iodine is released, allowing it to diffuse back to the hot end of the tube and react again. In this way the powder is slowly transfered to the cooler end of the tube. When the reverse reaction occurs, the re-formed $NbSe_2$ would prefer to condense onto an already existing crystal rather than nucleate a new one. Therefore, the result can be that a few large crystals form at the cooler end of the tube.

If the crystal growth tube is placed in the furnace and the temperature gradient is immediately turned on, a relatively large amount of material will start to be transported to the cooler end. A few crystals will start to grow, nucleating either on small tube-wall imperfections or on small crystallites from the starting powder which are in the growth zone. However, the original flux of material will be more then these nascent crystals can absorb, due to their small surface area. Thus polynucleation will result, with several crystals growing together at each site.[51,52]

Polynucleation can be avoided by slowly turning up the temperature differential between the charge end and the growth end of the tube, starting from a constant temperature.[51] In fact, the following heating schedule is usually followed. After the crystal growth tubes have been

placed in the furnace, a reverse temperature gradient is initially turned on; the the charge end being held cooler then the crystal growth end. This is done to remove (by vapor transport) any small particles of the charge which have become stuck to the tube wall in the crystal growth zone.[51,54] Such small particles usually exist, having come into contact with the tube wall at some point during the tube filling and handling procedures. It is desirable to remove them because they would provide an excessively large number of nucleation sites which would result in a large number of small crystals being produced.

The reverse gradient is typically left for 3-4 days. The furnace is then set to a uniform temperature and the desired growth profile is slowly turned on, the temperature difference being increased at the rate of 1-2 degrees per hour. The temperature of the charge end is increased; the temperature in the crystal growth zone is held as constant as possible. During the crystal growth phase the temperature difference between the hot and cold ends of the tube is typically 20°C. Larger temperature differentials have frequently been used.[6,49,51] However, a smaller temperature difference, and thus a slower rate of crystal growth has been used here in the hope that it will produce higher quality crystals. The crystals are left to grow for about one week.

Vapor-transport crystal growth depends upon the temperature dependence of the equilibrium constant governing Reaction 3.1. There is no fundamental reason why the transport should go from the hot end to the cold end, and in fact transport in the opposite direction occurs in some other systems.[49] It is also not necessary to use iodine as the

transport agent, although this is certainly the most popular agent used to grow TMDC crystals. Anything which reacts reversibly with the starting material to form gaseous products is potentially useful, and many other substances have found application in other systems.[49,54]

One obvious problem with iodine (or most other materials) is that a small amount of it inevitably becomes incorporated into the growing crystals. Iodine concentrations reported for vapor-transported $NbSe_2$ vary somewhat, but are typically a few hundred parts per million.[42,43,52,55] Rather high quality TMDC crystals have been reported to have been grown with the iodine-vapor-transport technique, so iodine inclusion by itself may not be a major problem.[38,56,57] Still, in several studies where a direct comparison has been made of TMDC crystals grown with and without iodine, it has been found that iodine-free crystals are of higher quality, as measured by their transport and superconducting properties.[40,58]

Iodine contamination can be avoided entirely by using one of the component elements of the starting powder as the transport agent. This is frequently refered to as "direct-vapor transport" (DVT). Chalcogen transport has been reported in several TMDC systems,[58,59] including $NbSe_2$.[40,52] We have grown a number of $Nb_{1-x}Ta_xSe_2$ crystals using Se transport. (Using approximately 5 mg Se per cm^3 of tube volume as the transport agent.) It appears that excess Se will not become incorporated into the crystal structure, but will condense out as droplets of elemental Se on the tube wall when the tube is finally cooled down.* Excess chalcogen is necessary to produce DVT crystals.

---

* The possibility that triselenides will form because of the presence

Sublimation growth is not possible at any reasonable temperature as diselenides remain solid up to 1250°C.[6]

A particular problem that arises for an alloy system such as $Nb_{1-x}Ta_xSe_2$ is that the composition of the final crystals may not be the same as that of the starting powder. Iodine will not necessarily react with Nb and Ta at the same rate, and the resultant gaseous species may not diffuse down the tube at identical rates. Generally, small compositional differences have been reported in other mixed cation TMDC systems.[59,60] This does not appear to be a serious problem for the $Nb_{1-x}Ta_xSe_2$ system. Reactivity differences are probably minimal given the very similar chemical properties of Nb and Ta. To promote the growth of homogeneous crystals, the original charge is never transported to completion; in fact, only a few percent are transported. Thus if Nb and Ta are transported at slightly different rates, the charge composition will not change signifigantly during the transport process, minimizing as much as possible compositional variations in the transported crystals.

In any event, the superconducting transition temperature T_c of the individual vapor-transported crystals can be measured and compared to that of the starting powder and that of other samples of the same composition. As is shown in Chapter VI, the transition temperature changes reasonably rapidly as composition is varied. The "correct" values of T_c for the various the compositions have been determined self-consistently by measuring a large number of samples from powder-growth experiments where transport was not involved. For these samples, T_c

---

of excess Se is discussed in Sections III.2.4, III.2.5, and III.3.

should reflect the stoichiometry implied by the ratio of the elements originally placed into the growth tube, provided that the resultant powder has homogeneous superconducting properties. Once T_c as a function of composition has been determined, the measured T_c of transported crystals can be used as an indicator of the extent to which their stoichiometry reflects that of the starting powder. Generally some spread in T_c values is observed in a given transport-growth tube, corresponding to a spread in composition of several tenths of an atomic percent. The average T_c for crystals from a given vapor transport tube is usually shifted relative to the average T_c for the starting powder by a small amount, typically 40 mK. The sign of the shift varies randomly form tube to tube.

III.2 Laboratory Procedures

This section contains a more detailed description of how the crystal growth experiments were carried out. To some extent, the discussion of the crystal growth temperatures will be delayed until Section III.3 where the phase diagram will be considered. Thirty-nine different batches of crystals have been grown, each batch consisting of several tubes. Batches 9, 12, 14, 16, and 21 are TaS_2; the rest are $Nb_{1-x}Ta_xSe_2$. The TaS_2 work will not be discussed further since these compounds were not used in the critical field work.

The experimental procedures evolved considerably over the course of this work, most notably with respect to excluding impurities from the crystal growth tubes. It is not completely obvious that small quantities of certain impurities are really harmful; fractional crystallization is

a standard classical purification technique. It appears that to a large extent, the impurities will form segregated phases and fairly high quality crystals can be grown despite their presence. Indeed, a number of very good crystals resulted from certain earlier batches (e.g., Batch 7) where certain precautions taken with the later batches were not used. Nevertheless, the philosophy adopted was that all reasonable precautions should be taken to exclude impurities from the crystal growth tubes.

For conciseness, a batch-by-batch description will not be included here. Certain details of each batch are tabulated in Appendix B. The discussion will instead be more general, emphasizing those procedures currently believed to be optimum.

The next three subsections deal with the furnaces used and the crystal growth tube preparation and sealing procedures, since these are essentially the same for both types of crystal growth. Then the details of the direct reaction of the elements (powder growth) and of the vapor-transport experiments will be considered separately.

III.2.1 Furnaces

Two furnaces have been used,* a Lindberg model 51849 box furnace[62] and a Bruce tube furnace[63]. The Lindberg is a nominally-uniform-temperature box furnace with a temperature range of 100°C to 1100°C. The Bruce furnace is a factory-modified diffusion furnance of the type used in the semiconductor industry. It has two horizontal tubes, each 1.37 m

---

* Batches 1-4 and 11 (none of which produced any useful crystals), were grown in other box furnaces.

long. Each tube has seven Bruce model 563B temperature controllers which can be set independently to provide a wide variety of temperature profiles (within the bounds 350°C to 1350°C). The Lindberg furnace has been used primarily for powder growth, while the Bruce furnace has been used primarily for vapor-transport experiments. Both furnaces were calibrated with chromel-alumel thermocouples (Omega Engineering Inc.[64]) using an Omega model MCJ-K electronic cold-junction compensator.

III.2.2 Crystal Growth Tube Preparation

All the crystal growth work has been carried out in sealed quartz tubes. For powder-growth experiments, tubes with an I.D. of approximately 10 mm were used, while tubing with an I.D. of approximately 16 mm was used for the vapor-transport work. Generally a wall thickness of 1 mm has been used. The crystal growth tubes are initially formed with one rounded, closed end and typically are 13 cm long for powder growth and 40 cm long for vapor-transport experiments.* The vapor-transport tubes have to be of a length commensurate with the temperature profiles obtainable in the Bruce furnace. Usually the open end of the tubes is constricted somewhat to facilitate the final sealing.

The tubes are cleaned by soaking for about one hour in a hydrofluoric acid-nitric acid mixture (typically 3 parts HF to 1 part HNO_3). This soak is followed by several (≈ 6) rinses with de-ionized water and a final rinse with methanol. For the earlier batches, the

---

* All glassblowing work has been done by Mr. Edward Brosious, the glassblower in the Yale University Physics Department.

tubes were air dried and then filled. However, starting with Batch 12, the tubes have been placed in one of the furnaces and heated to ≈ 1000°C for about 24 hours following the chemical cleaning. This is done to drive off water and any other volitle impurities which may be trapped in the quartz. It is known that water is present in quartz tubing and that it comes out of the quartz at temperatures around 700°C and higher.[49] In addition, there have been reports of other volitle species being evolved from quartz at high tempratures.[65]

III.2.3 Crystal Growth Tube Sealing

After the tubes are cleaned and filled, they are evacuated and sealed shut. Originally the tubes were sealed onto a quartz manifold which was then evacuated with a liquid nitrogen trapped diffusion pump system. The tubes were pumped for typically five hours and then sealed off (while the pumping continued). When the pressure was monitored, it was typically on the 10^{-5} torr scale just prior to sealoff.

However, this procedure may not be optimal. When quartz is heated to beyond its softening point and then cooled down, frequently a ring of white powder is seen around the heated area. This powder consists of small pieces of quartz which have flaked off the surface. After the earlier quartz tubes were sealed as described above, such a white ring was observed near the end which had been heated. This seemed to be almost exclusively on the outside of the tube, where the heat had been the most intense. However, to prevent any possible contamination caused by quartz flakes inside the crystal growth tubes, a modified procedure was developed which greatly reduces the amount of flaking on the crystal

growth tubes. This procedure involves attaching a section of tubing containing a graded quartz-to-pyrex seal to the open end of the growth tubes when they are fabricated. The tubes are then cleaned and filled in the usual way, and then are sealed onto a pyrex manifold. After evacuation the tubes are sealed off above the graded seal on the Pyrex section. After the tubes have been removed from the manifold, they are sealed off below the graded seal, resulting in an all-quartz tube. This second seal-off can be done in a much more uniform and efficient fashion than is possible when the tubes are attached to the manifold, and this seems to greatly minimize the amount of surface flaking which results. (This appears to be due to elimination of the local overheating which inevitably results from the awkward working conditions when the tubes are attached to the manifold.) This technique involving the graded seal was only used for Batches 36-39.

III.2.4 Powder Growth

This section describes those crystal growth experiments which involved simply sealing the elements niobium, tantalum, and selenium in a quartz tube and heating to promote a direct reaction. Most of the chemicals were purchased from the Atomergic Chemetals Corp.[66]; Se (99.9999%), Ta (99.95%), and Nb (99.8%). The Atomergic Nb and Ta are in the form of very fine powders (325 mesh). Because of the potential safety hazards associated with selenium, this element has only been used in pellet form, to avoid the possibility of inhaling any dust.[67] For the later crystal growth batches, higher purity Nb ("Specpure") was purchased from Johnson Matthey.[68] This Nb is in the form of a much

coarser powder, with grain dimensions on the order of 1 mm.

The rational for using very fine Nb and Ta powders was that such small particles would assure a complete reaction. However, experience with the Johnson Matthey Nb indicates that a complete reaction is possible with courser Nb and the proper heating schedule. The Johnson Matthey Nb is superior not only for its higher initial purity, but also because its much smaller surface area per unit mass signifigantly reduces the possibility of including adsorbed impurities in the crystal growth tube. The tendency of the fine metal powder to adsorb vapor from the atmosphere can readily be demonstrated by dumping a small amount on the pan of an electronic balance. In one test, the weight of 0.5 g of fine Nb powder increased by almost 2 mg in 2 minutes. This is presumably due to adsorption of water. To minimize problems with adsorbed water vapor, the later growth tubes have been filled in a glovebox (Batches 23-39)*.

A small amount of excess Se is always included in the growth tube. Typically 5-10 mg are used with a total charge mass of about 5 g. The motivation for this is simply that at least a slight excess of either metal or Se is inevitable, and excess metal is very detrimental, while excess Se is usually harmless. Any excess metal atoms will intercalate, or fit into the van der Waals gap between the layers.[9] This is known to drastically reduce the superconducting transition temperature.[69] On the other hand, excess Se will usually remain in elemental form, condensing out as small droplets as the crystal growth tube cools down. The use of

---

* For vapor-transport and anneal (phase diagram) experiments, which involved prereacted $Nb_{1-x}Ta_xSe_2$ powder, the tubes were not filled in the glovebox.

excess chalcogen to insure proper stoichiometry is well known.[35]

The only problem with using excess Se is that the triselenides $Nb_xTa_{1-x}Se_3$ can form if the temperature in the growth tube is low enough. Triselenides can easily be recognized as they form very thin, needle-like crystals.[4,9] Fortunately, they are only stable below a certain temperature (Section III.3), so if the growth temperature can be kept high enough they will not form.

When the tubes are being heated, the temperature should be turned up rather slowly over the interval from 400°C to 550°C. The basic reaction between the Nb and the Ta and the now molten Se occurs in this range, and it is very exothermic (the heat of reaction is 150-200 kcal/mole).[6] If the tubes are heated too rapidly, thermal runaway can occur, resulting at worst in an explosion, or at least in a reaction of the metal powders with the quartz tube. After 550°C is reached, the temperature can be turned up to 900°C in e.g., 50°C jumps over several days. The reason for heating to 900°C is to insure that the reaction has gone to completion.[6,7,9,70] However, it is not a good idea to go much beyond 900°C. This is because Nb and Ta can react with quartz at higher temeratures.[49,70] If the heating is carried out slowly enough, the metal-Se reaction should be essentially complete when 900°C is reached. However, excess Se or other transporting agents present can provide mobility to the metal atoms so that they can come into contact with the tube wall. It appears that this will not cause a problem if the maximum temperature is kept to about 900°C, but a definite reaction can occur if the tubes are heated to around 1000°C. The reaction between the metal and the quartz is catalyzed by the presence of water vapor in

the tube,[49] and thus can be minimized by proper preperation of the tube and its contents.

The tubes are kept at 900°C for about one week and then annealed at a lower temperature to get the correct phase. At 900°C, $Nb_{1-x}Ta_xSe_2$ is probably in the 4H phase (at least for most compositions) and an anneal is required to get the 2H phase. After an anneal period of 7-10 days, the furnace can be shut off and the door opened to allow the contents to cool to room temperature. If the powder is to be used in subsequent vapor transport growth, annealing to get the 2H phase is not important. However, this anneal procedure is useful since it allows transition temperature and phase diagram information to be obtained from measurements of the powder. Tubes removed from the furnace should be clear and contain a free-flowing, sparkly black powder of $Nb_{1-x}Ta_xSe_2$ crystallites, plus any excess Se condensed out on the tube wall as shiny black droplets. A frosted tube wall indicates that the contents have reacted with the quartz, and a very fine, non-sparkly powder indicates a Se deficiency.[52]

Most early crystal growth tubes contained more elemental Se than the small amount intentionally added, and also contained a small amount of white powder located primarily on top of the main mass of $Nb_{1-x}Ta_xSe_2$ crystals. The probable explanation of this is that water vapor present in the tube reacted with the contents to produce metallic oxides, H_2Se, and excess elemental Se, although it is possible that a reaction with the quartz tube was involved. For these batches, a faint H_2Se smell (similar to H_2S) was detected when the tubes were opened. The tubes are therefore opened in a fume hood.

The chemical composition of the white powder was never analysed. However, it appears to have been caused by water vapor either directly or indirectly, since any reaction with the quartz tube should be negligible without the catalytic influence of water vapor.[49] The white powder was eliminated by two procedural changes. The amount was decreased when, starting with Batch 12, the growth tubes were preheated to 1000°C, and the problem was virtually eliminated when, starting with Batch 23, the tubes were filled in the glovebox. The use of the coarser-grained Johnson Matthey Nb probably also helped.

When the Lindberg furnace was used, frequently a few larger crystals (diameters up to ≈ 1 mm) were found near the end of the tube which was closest to the door of the furnace. These crystals were apparently grown by Se-vapor transport driven by the temperature gradient naturally existing inside the furnace box. Observation of this "natural" vapor transport was what motivated us to try Se transport in a more controlled fashion in the Bruce furnace. Most of the good quality single crystals obtained from powder-growth runs appear to have been produced by Se transport. The main mass of crystals produced in such experiments consists of heavily intergrown crystallites with diameters in the range 10-100 μm. It is very difficult to find any of these with the size and especially the perfection required for $H_{c2}(T)$ measurements.

Signifigant Se vapor transport was only seen in those earlier powder-growth batches which contained additional excess Se due to the accidental inclusion of water vapor in the growth tubes. It has not been seen in those later batches where more care was taken in preparing and filling the tubes.

III.2.5 Vapor-Transport Crystal Growth

This section describes certain details of those crystal growth experiments which started with previously reacted $Nb_{1-x}Ta_xSe_2$ powder and had the goal of producing larger crystals by vapor transport, using either I or Se as the transport agent. As noted in the last section, a certain amount of vapor transport was done "accidently" during earlier powder-growth runs due to temperature nonuniformity in the Lindberg furnace and the presence of excess Se.

In terms of the quality of the crystals produced, as measured by their superconducting properties (T_c and the transition width), Se and I transport seem to be comparable.* An important difference is the ease with which the transport agent can be introduced into the growth tube. Selenium has a sufficiently low vapor pressure at room temperature so that pellets can simply be dropped into the growth tube along with the prereacted powder. The tube can then be sealed onto the manifold and evacuated as described in Section III.2.3 without any complications.

Getting iodine into an evacuated growth tube is much harder. Its vapor pressure is such that it cannot be pumped on at room temperature for any length of time without a large fraction of it being lost. A further complication is that iodine tends to pick up water vapor from the air. Several schemes were tried for introducing the iodine, the following being the most successful.

---

* Thus any small amount of I incorporated into the crystal structure appears to be an insignifigant source of crystalline imperfection in this work.

The iodine is sealed into small quartz ampules which are placed into the growth tube along with the prereacted powder. These ampules are then broken open during the tube-sealing procedure. The ampules are fabricated from 4 mm OD quartz tubing and have a squiggly, "pigs-tail" seal on one end. The ampules are filled in the glovebox using reagent-grade iodine. A quantity of iodine is pushed into the ampules and they are then connected through a liquid-nitrogen coldtrap to a mechanical vacuum pump. A valve is then opened, allowing the pump to evacuate the ampule. The pump is left running for approximately one minute, during which time some of the iodine escapes. At this point the ampule is sealed shut with an oxy-acetylene torch.

One of these sealed ampules is placed in each crystal growth tube along with the prereacted $Nb_{1-x}Ta_xSe_2$ powder and this tube is then connected to the manifold and evacuated as usual. The pig's-tail seal on the iodine ampule is broken before the growth tube is sealed and removed from the manifold. The best procedure utilizes a small iron weight sealed in a Pyrex ampule which can be raised and lowered with a small magnet. The tube is left to pump for about one minute after the ampule is broken. Then a container of liquid nitrogen is placed around the bottom of the growth tube to minimize any further iodine loss. The ampule containing the iron weight is pulled out of the crystal growth tube and it is sealed as usual.

The amount of transport agent used is not crucial. Generally about 5 mg per cm^3 of tube volume has been used (for both I and Se transport), as is standard.[6] The heating procedures were outlined in Section III.1. As a specific example, Figure 3-1 shows the temperature profile used for

Batch 20. Also included is a sketch showing the tube location and where the vapor-transported crystals were found. Transported crystals are typically found over the region shown in Figure 3-1. The temperature rises slightly at the cold end of the tube. This has been recommended to prevent nuclation of crystals on the rounded end where the resultant crowded conditions would be less then optimum.[51] Vapor-transported crystals have never been annealed after they are grown, therefore the growth temperature always determines the resultant crystal phase.

The crystals are typically left to grow for five days. The furnace is then shut off and the endplugs are removed to facilitate rapid cooling. The tube are always cooled fairly quickly to preclude the growth of triselenides caused by any excess Se present. It appears that triselenides can grow quite quickly, over the several hours it otherwise takes the furnace to cool down if it is left sealed.

III.3 $Nb_{1-x}Ta_xSe_2$ Phase Diagram

In Sections III.1 and III.2 the details of the crystal growth procedures were discussed, but the actual temperatures used for growing and annealing crystals were not considered in detail. The purpose of this section is to remedy this omission by considering the phase boundary between the desired 2H phase and the 4H phase which is stable at higher temperatures. It is also necessary to consider the problems caused by the existence of triselenides in choosing the powder-anneal and vapor-transport growth temperatures.

The presence of triselenides can easily be determined visually, as

they form long, thin, needle-like crystals. It is less easy to differentiate between the 2H and 4H phases. Frequently, though, 2H and 4H crystals adopt characteristically different morphologies. 2H crystals tend to be thin hexagonal platelets, while 4H crystals, which are also hexagonal, tend to be much thicker and have a faceted appearence.[71] However, many crystals, especially those in intergrown powders, have a morphology somewhat in between these characteristic forms. Therefore other methods of clearly differentiating between the phases are required. We have used powder x-ray analysis and superconducting transition temperature measurements.

III.3.1 X-Ray Measurements

Powder x-ray measurements have been carried out using copper K_α radiation with a nickel-foil filter to block the K_β radiation. There are actually two K_α lines, with wavelengths of 1.5405 Å and 1.5443 Å, and because of this a peak splitting is observed in our diffraction recordings at larger angles. This splitting indicates good crystal quality.

In principle, the measured line positions could be analyzed to determine the lattice constants and the line intensities could be analyzed to determine the basis-atom positions in the unit cell, thus determining which polytypes are present. However, since the lattice constants of $NbSe_2$ and $TaSe_2$ are very similar, it would require very precise measurements and accurate machine setup to use the measured lattice constants as an indicator of composition. Since other researchers have determined that only the 2H and 4H polytypes are likely

to be present (Section II.1.1), we have limited our analysis to determining whether the 2H, the 4H, or both phases are present. Such an analysis can be carried out very simply by comparing the measured diffraction patterns to calculated spectra for the two phases. The expected line positions can be easily calculated using Bragg's law in the form $\lambda = 2d\sin(\theta)$, where 2θ is the scattering angle, and d is the spacing between the relevant atomic planes.[72]

Certain of the calculated lines are systematically extinct.[7] Specifically, if $h-k = 3m$, where m is any integer, then the corresponding line will be extinct unless ℓ is an integral multiple of the number of layers per unit cell. Here h, k, and ℓ are the Miller indices of the atomic planes.

It is also important to note that for two hexagonal crystal structures which are identical except that one c-axis unit cell dimension is twice the other, the (h, k, ℓ) lines of the material with the smaller unit cell will be at the same position as the $(h, k, 2\ell)$ lines of the material with the larger unit cell. Thus a 4H line will fall very nearly on top of each 2H line. A spectrum which shows only 2H lines can be assumed to consist of only the 2H phase. However, a spectrum which displays 4H lines may be either pure 4H or a mixture of 2H and 4H polytypes. This ambiguity is not a serious inconvenience since the basic goal has been to determine the conditions under which the pure 2H phase forms. For virtually all of the samples, all of the observed lines coincide with one of the two calculated spectra.

III.3.2 Transition Temperature Measurements

Measurements of the superconducting transition temperature are also very useful in determining which phases are present in various crystal growth batches, since both the 2H and the 4H phases superconduct, but with different transition temperatures (T_c). The measurement techniques are described in detail in Chapter IV, and T_c as a function of composition is discussed in Chapter VI.

Transition temperature measurements have provided several pieces of useful information for the crystal growth work. In fact, the existence of two transitions in some samples was the original clue that the crystals were not all of the 2H phase. Subsequent x-ray work clearly showed the presence of the 4H phase in some samples. The T_c measurements complement the x-ray measurements nicely, since using our simplified data analysis technique, the latter cannot distinguish between a batch which is pure 4H and a 2H-4H mixture. Also, T_c can be measured on single crystals as well as powders.

Because of the high sensitivity of the T_c measuring apparatus, even fairly small single crystals can be examined individually. Such single-crystal measurements show that in batches where both the 2H and the 4H phases are present, some crystallites may be either phase, while other crystallites individually contain both phases. The T_c measurements indicate that virtually all of the crystal growth conditions we have used produce either pure 2H material, or a 2H-4H mixture.

Another useful feature of T_c measurements is that the width of the transition may be taken as a simple measure of crystal quality. Using

this criteria, it soon became apparent that larger, and especially thicker, crystals are not of as high a quality as relatively smaller, thinner crystals. It is possible to grow large and thick 2H crystals using vapor transport (diameters up to 2 mm or larger, and thicknesses greater then 100 μm). In fact, there is no intrinsic limit to the size crystals which can be produced by vapor transport (other than the tube diameter). However, none of these larger crystals were good enough for the critical field studies. The transition temperature was measured for 12 samples which had diameters larger then 1.5 mm. They all appeared visually to be good quality crystals, but none were acceptable for critical field measurements. The transition temperature was either incorrect or the transition was too broad or displayed some structure.

III.3.3 Experimental Phase Diagram

Figure 3-2 shows the experimental points which distinguish the phase boundary between the pure 2H and the mixed 2H-4H regions as a function of composition. These points were determined by a combination of x-ray and T_c measurements of samples where the crystal growth (or anneal) temperature could be accurately determined.

The general outline of the phase diagram was discussed in Chapter II. The 2H phase of $NbSe_2$ is stable to quite high temperatures; values in the literature range from 825°C [9] to 900°C [47]. However, the temperature of the phase boundary decreases as the Ta content increases. This increasing stabilization of the 4H phase is similar to the behavior seen in the $Nb_xTi_{1-x}Se_2$ system.[73]

It appears that the presence of excess Se increases the stability of the 4H phase.[74] The amount of excess Se used varied somewhat from batch to batch and this may account for some of the raggedness of the phase boundary defined by the experimental points in Figure 3-2. Therefore, Figure 3-2 should represent the phase boundary in the presence of a fairly small amount of excess Se; about 5-10 mg per tube.

The only data reported in the literature for the 2H-4H phase boundary in the $Nb_{1-x}Ta_xSe_2$ system is the work of Ikebe, Katagiri, Noto, and Muto.[75] They grew crystals by iodine-vapor transport at 750°C, and found that the compositions $NbSe_2$, $Nb_{.95}Ta_{.05}Se_2$, and $Nb_{.90}Ta_{.10}Se_2$ formed in the 2H phase, while both phases were present for $Nb_{.80}Ta_{.20}Se_2$, and apparently only the 4H phase was present for $Nb_{.70}Ta_{.30}Se_2$. These observations are consistent with those presented here.

The basic reason for determining the phase boundary is that if the crystals are grown at too low a temperature in the presence of excess Se, triselenides can form. Since at least a small amount of excess Se is desirable to insure stoichiometry, the crystals should be grown or annealed at as high a temperature as is commensurate with getting the 2H phase. When triselenide does form, it tend to grow in the coldest part of the tube, which is exactly where any vapor-transported crystals will be found. Thus there is a fairly high probability that the triselenide would grow on, and ruin, any transported crystals present.

The exact temperature at which triselenides form seems to depend sensitively upon the amount of Se present, and only weakly, if at all, upon composition. For the amounts of excess Se typically used in the

powder-growth tubes, (5-10 mg per tube) triselenides seem to be stable at temperatures in the range 710°C-730°C and below.

Because of the possibility of triselenide growth, an important question concerns the composition range over which 2H crystals can be grown by Se vapor transport. At higher Ta contents the growth temperature must be lowered, and the risk of triselenide formation increases. Only a partial answer can be given. The results of Batch 7 clearly indicate that Se transport of $Nb_{.80}Ta_{.20}Se_2$ is possible. However, this was an early powder-growth batch, where the amount of excess Se was only roughly known; it is estimated to be 5 mg per cm^3 of tube volume. This batch was grown in the Lindberg furnace. The temperature at the end of the tube where the transported crystals grew can be estimated to be 725°C. Thus, while it is clear that Se vapor transport can be used to produce 2H crystals for compositions up to $Nb_{.80}Ta_{.20}Se_2$, the conditions necessary for this have not been precisely determined.

III.4 Conclusions Regarding Crystal Growth

The procedures used to grow crystals of $Nb_{1-x}Ta_xSe_2$ evolved considerably over the course of this work, primarily as the result of the attempt to reduce the amount of impurities included with in the crystal growth tubes. A measure of the extent to which this succeeded in improving crystal quality is the change in the widths of the transitions to the superconducting state. Figure 3-3 shows the width of the transition for samples containing many crystallites from the various powder-growth experiments. These "bulk" samples were made by taking a

number of crystallites from each tube after the contents had been well mixed. The resultant T_c and transition width should be representative of all the crystals in that particular tube. Tubes which were partially 4H, all the vapor-transport batches, and the anneal experiments which utilized previously reacted materials have not been included here. The widths decrease for later batches implying that the efforts to improve the purity of the batches have indeed produced positive results. This diagram does not show the transition widths of selected single crystals, which are narrower than the transition widths of powder samples and also tend to be smaller for the later batches.

IV. Low-Temperature Experimental Technique

This chapter describes the experimental techniques and apparatus which have been used to measure the transition temperatures of the $Nb_{1-x}Ta_xSe_2$ samples, both in zero field and in large dc magnetic fields. First a brief summary will be made of the various methods which are available for measuring the superconducting-to-normal phase transition. Special emphasis will be placed on the requirements for measuring small samples, since as was noted in Chapter III, the highest quality $Nb_{1-x}Ta_xSe_2$ crystals produced are quite small, typically only several hundred microns in diameter and ≈ 20 μm thick. Following this introduction, the sensitive frequency-shift-detection ac susceptibility apparatus developed for this study will be described in detail. Then the thermometry and the superconducting magnet system will be discussed. The chapter will conclude with a discussion of the setup used at the National Magnet Lab at MIT, where measurements were made in fields up to 150 kG.

IV.1 Basic Techniques For Measuring T_c

The three main techniques which have been traditionally used to detect the superconducting-to-normal phase transition are measurements of the resistivity, the heat capacity, and the magnetic susceptibility or magnetization. Usually resistivity measurements are the easiest to carry out. However, since the only requirement for measuring zero resistance is one continuous superconducting path between the voltage leads, resistance measurements are the least reliable. In addition, for very small samples (with dimensions on the order of 100 μm) two problems

arise which complicate the measurements. First, connection of the voltage and current leads is obviously difficult. Second, the sample size dictates that the voltage leads be very close together. For some materials, such as high quality single crystals with a low resistivity just above T_c, the voltage in the normal state can be in the nanovolt range, given that the current must be kept low enough so that it does not unduly supress T_c.

Heat capacity measurements are in principle the most reliable method for determining the transition temperature, as they are true bulk measurements. However, heat capacity measurements of small samples require fairly complicated cryostats.[76-78] In addition, operation in large magnetic fields can be difficult, due to the effect of the magnetic field on thermal and electrical conductivities. The state-of-the-art in small-sample heat capacity measurement techniques has recently been reviewed by Stewart.[78]

Measurements of the magnetic susceptibility rely on detecting the diamagnetism of the superconducting state. All superconductors appear perfectly diamagnetic in a vanishingly small magnetic field, neglecting the field penetration into the sample a distance equal to the magnetic field penetration depth λ (typically of order 100 nm). Ideal type II superconductors are only perfectly diamagnetic below the lower critical field H_{c1}.* For fields between H_{c1} and the upper critical field H_{c2} the magnitude of the dc magnetization decreases uniformly to the normal-state value. Any attempt to determine H_{c2} by a dc susceptibility technique therefore amounts to determining the change in slope of the

---

* $H_{c1}(T)$ and $H_{c2}(T)$ are introduced in Chapter V.

magnetization curve at H_{c2}. This change can be rather small for high-κ superconductors (such as the compounds $Nb_{1-x}Ta_xSe_2$), making this sort of measurement difficult. (Here κ is the Ginzburg-Landau parameter.)

Type II superconductors have the useful property that they can remain at least partially diamagnetic to low-amplitude, low-frequency ac magnetic fields in the mixed state ($H_{c1} < H < H_{c2}$), displaying a sharp transition at the upper critical field $H_{c2}(T)$ (or depending upon the system, $H_{c3}(T)$).[79] This effect may be caused by an intrinsic barrier to flux entry, the physics of which is discussed in Chapter VI.

If a sample contains randomly distributed inhomogeneities, various sections will become superconducting at different temperatures. Thus, the supercurrents which shield the ac field will begin to flow in a disconnected fashion and a smeared out transition will be observed. For this reason ac susceptbility measurements are intrinsically more likely to sense inhomogeneities than are resistance measurements which require only a single superconducting path between the voltage leads to indicate zero resistance. While it is certainly possible to conceive of arrangements whereby interior inhomogeneities would be completely masked by a uniform surface layer, such arrangements are generally quite unlikely.**

Several techniques have been developed for measuring the ac susceptibility of small samples, including direct measurements of the self or mutual inductance of a pickup coil enclosing the sample,[80] and measurements of the resonant frquency of low-frequency resonant

---

**An example of this masking phenomenon is given in Reference 78.

circuits,[81,82] and of tunnel diode oscillators.[83] However, because of the small inductance required to couple efficiently to small samples, these other techniques face significant difficulties. Direct measurements of inductance are less sensitive by approximately a factor of Q (the resonant-circuit quality factor), if the same ac field amplitude is used. Use of a cooled resonant transformer to increase the signal amplitude is possible,[80] but would not in general be compatible with operation in large dc fields. Similar problems arise for low-frequency resonant circuits as the cable resistance severely limits the circuit Q when a room-temperature capacitor is used, as is necessary due to the large physical size of the required capacitance. Finally, the use of a tunnel diode oscillator[83] to determine the LC self-resonant frequency can offer excellent resolution and stablity,[84] but is not a simple technique for use at low ac field levels and with small inductances, as such inductors have a relatively small impedance at resonance; $Z_{LC} = Q\omega_r L$. Use of tunnel diode oscillators in large magnetic fields can also be difficult.[83] Thus none of these methods appear to be promising for measuring $H_{c2}(T)$ of small samples.

The method we have developed uses the shift in resonant frequency of a parallel LC circuit to monitor changes in the sample susceptibility, the sample being located in the coil. As will be described below, this apparatus is of simple construction, especially the low-temperature part, and is simple to operate and reliable.

IV.2 Frequency-Shift-Detection ac Susceptibility Technique

IV.2.1 Basic Principles of Operation

This section describes the basic principles of operation of the frequency-shift-detection ac susceptibility apparatus. Specific experimental details will be given in the next section. However, detailed interpretation of the observed transition shapes will be delayed until Chapter VI.

To determine changes in its ac susceptibility, the sample is placed inside a coil which is part of a high-Q parallel resonant circuit. This circuit is driven by a radio-frequency current source. In the superconducting state the ac field penetration can be negligible, being limited to the magnetic field penetration depth λ. For $NbSe_2$ λ is about 120 nm.[85,86] We consider here the case where the ac field is fully excluded from the sample volume below T_c in order to obtain a simple estimate of the sensitivity of the circuit. Consider what happens when the sample passes from the superconducting to the normal state, for instance as the temperature is raised. Below $T_c(H)$ the ac field is fully shielded. For $T > T_c(H)$, the ac field can penetrate a distance equal to the normal-state skin depth. This depth can be estimated using the usual formula[11] (mks units)

$$\delta = \left(\frac{2}{\omega\mu\sigma}\right)^{1/2} \tag{4.1}$$

Here $\omega = 2\pi f$ is the frequency, μ is the permeability, and σ is the conductivity. Using f = 3 MHz, $\mu = \mu_0 = 4\pi\times10^{-7}$ and taking $\sigma = 2.73\times10^{7}$ $(\Omega m)^{-1}$ (Appendix G), we get δ = 67 microns. While this is roughly equal

to the radius of the smallest samples used, it is somewhat less than the radius of most samples. In fact, all that is required is that δ be much larger then λ so that at the transition the effective cross-sectional area of the coil changes significantly, altering the inductance and thus shifting the resonant frequency.

This shift in resonant frequency can easily be estimated. The inductance of the coil can be written as (cgs units)

$$L = L_o(1 + 4\pi\chi\eta) \tag{4.2}$$

where L_0 is the inductance of the coil when empty, χ is the sample susceptibilty, and η is the volume filling factor. For a thin platelet sample placed in the coil so that it is normal to the coil axis, η is approximately the ratio of the volume of a sphere of diameter equal to the platelet face diameter to the volume of the coil,

$$\eta = \frac{\frac{4}{3}\pi(\frac{d_s}{2})^3}{V_{coil}} \approx \frac{d_s^3}{2\,V_{coil}} \quad . \tag{4.3}$$

Assuming for simplicity that the sample is completely diamagnetic in the superconducting state (and nonmagnetic in the normal state), the susceptibility change at the superconducting-to-normal transition will be

$$\Delta\chi = \frac{1}{4\pi} \quad . \tag{4.4}$$

Making the further assumption that the skin depth is larger than the sample radius, the change in inductance will be $\Delta L = \eta L_o$. The resonant frequency of a parallel LC circuit is given by

$$f_r = f_o \left[1 - \frac{1}{Q^2}\right]^{1/2} \tag{4.5}$$

where

$$f_o = \frac{\omega_o}{2\pi} = \frac{1}{2\pi\sqrt{LC}} \tag{4.6}$$

and Q is the quality factor of the circuit

$$Q = \frac{\omega_o L}{R} \tag{4.7}$$

R is the series resistance of the coil. For high-Q circuits, an excellent approximation is $f_r = f_o$. Differentiating, we get for small changes

$$\frac{\Delta f_r}{f_r} = \frac{\Delta f_o}{f_o} \approx - \frac{d_s^3}{4\ V_{coil}} \tag{4.8}$$

Using typical values of f_r = 3 MHz, d_s = 100 μm, and V_{coil} = 1 mm^3, Δf_r = -750 Hz.

The shift in resonant frequency is measured using a phase-sensitive-detection scheme which produces an output voltage proportional to the imaginary, or out-of-phase component of the LC circuit impedance. (We denote this as Z_2; the total impedance is given by $Z_{LC} = Z_1 + jZ_2$) This component is shown if Figure 4-1. Z_2 is zero at resonance, and varies linearly with frequency near resonance. With the circuit biased at the fixed frequency $f_a = \omega_a/2\pi$, as shown in the figure, Z_2 and thus the output voltage will change from point B to point A as the sample goes from the superconducting to the normal state.

The phase-sensitive detector used to measure Z_2 is shown, in block diagram form, in Figure 4-2. The resonant circuit is biased with a

constant current by the capacitor C_1 = 1 pF which, with the rf voltage generator, forms an rf current source since the impedance of C_1 is much larger than the impedance of the LC circuit. The rf current $I_1 \approx j\omega_a C_1 V_g$ is shifted 90° in phase relative to the generator voltage V_g. The voltage appearing across the resonant circuit is given by

$$V_{LC} = Z_{LC} I_1 = (-Z_2 + jZ_1)\omega C_1 V_g. \tag{4.9}$$

This voltage is amplified and fed to a balanced mixer. The mixer reference channel is also driven by V_g. The mixer output contains a dc voltage component proportional to any signal at its input which is in phase with V_g. From Equation 4.9, the mixer will see the component of V_{LC} due to Z_2 as being in phase with the reference voltage V_g, so the dc mixer output will be proportional to Z_2. Components at the harmonics of f_a are also present, but these are removed by a low-pass filter. The change in resonant frequency has thus been turned into a change in dc output voltage. This output voltage is fed directly to an X-Y recorder (to the Y channel), and also to a monitor oscilloscope which is used to initially tune the circuit to a point near resonance.

The slope of the imaginary component of Z_{LC} at resonance can easily be shown to be

$$\left.\frac{dZ_2}{d\omega}\right|_{\omega_r} = -2L_o Q^2. \tag{4.10}$$

Using this, the change in output voltage for a given change in resonant frequency can be calculated to be

$$\Delta V_{out} = -\beta 4\pi L_o Q^2 |I| \Delta f_r. \tag{4.11}$$

where $|I|$ is the magnitude of the rf biasing current and β is the

product of the gains of the rf amplifier, the balanced mixer and the low-pass amplifier. A typical measured slope of the output curve is -30 mV/kHz for a Q of 32 and f_r = 2.8 MHz. The Q can be easily obtained by measuring the resonant frequency and the frequencies at both the positive and negative peaks of the output signal (Figure 4-1). Q is then given by f_r divided by the difference between the two peak frequencies.

IV.2.2 Room-Temperature Electronics

The T_c-measuring apparatus consists of two major components; a dipstick variable-temperature cryostat and the room-temperature electronic detection circuitry.* The room-temperature circuitry will be described first, and is shown in detail in Figure 4-3. The radio-frequency current source is a stable rf voltage generator, Hewlett Packard Model 606A, in series with a 1 pf silvered mica capacitor. The rf voltage across the LC circuit is amplified with a Motorola MC1733 IC video amplifier with a gain = 30. The output of the video amplifier is fed into the signal (R) port of a Hewlett Packard Model 10534B balanced mixer. The rf generator voltage, V_g = 0.4 volts rms, is applied to the local oscillator (L) port of the mixer. As discussed above, because of the phase shift across the 1 pf capacitor, the mixer detects the voltage proportional to the out-of-phase component of the LC circuit impedance as being in phase with the driving voltage. To compensate for additional phase shifts due to the rf amplifier, a 1.7 m section of RG-174/U

---

* This circuitry was designed by Professor Daniel Prober and constructed by Mr. Bruce Hanson.

coaxial cable is used as a time-delay line between the generator and the L port. The voltage at the output of the mixer (X port) contains a dc component proportional to Z_2 and rf components at multiples of the generator frequency. These rf components are removed with a simple RC low-pass filter with a cutoff frequency of 16 kHz. The dc signal is finally amplified by an Analog Devices 504M low-noise operational amplifier with a gain of 100. In addition to the desired output signal V_o, a spurious 60 Hz signal having an amplitude ≈ 1 mV is also observed at the output, but can easily be removed using the line-frequency notch filter built into the X-Y recorder used to record the transitions (Hewlett Packard Model 7047A). The two IC amplifiers are powered by a ±6 volt modular power supply. With the exception of this power supply and the HP606A generator, the entire room-temperature detection circuit is mounted in a small aluminum box. The amplifiers and the balanced mixer are mounted on a copper-clad printed circuit board which also serves as a ground plane. There is also a grounded shield which separates the rf input from the MC1733 video amplifier. The electronic circuitry has a frequency range of about 50 kHz to 10 MHz. The high-frequency limit is determined by the rf amplifier, and the low-frequency limit by the balanced mixer.

IV.2.3 Cryostats

Three dipstick cryostat probes have been constructed, all of very similar design. The first cryostat, which no longer exists, held only one sample and was only used for making early zero-field transition temperature measurements. When the superconducting magnet cryostat was

constructed, this probe was dismantled, and a second, larger one was built which holds two samples and has interchangeable sample mounting bars for orienting the samples both parallel and perpendicular to the dc magnetic field. The outside diameter of the lower section of this cryostat is slightly less then 2 cm, so that it will fit into a wide-mouth liquid He storage dewar, facilitating rapid and economical T_c measurements. A third dipstick cryostat has also been constructed. This also holds two samples, but is of smaller diameter (bottom can diameter = 1.3 cm), so that it can fit into a narrow-neck He storage dewar for making zero-field T_c measurements. When slowly lowered into a He storage dewar, He consumption per cooldown is about 1 liter for the larger cryostat, and about 1/2 liter for the recently constructed smaller cryostat.

Since all the $H_{c2}(T)$ work and the vast majority of the zero-field T_c work has been done using the larger cryostat, only this apparatus will be described in detail. The design of the two smaller cryostats is quite similar with only minor differences.

A schematic diagram of the low-temperature end of the cryostat is shown in Figure 4-4. (For simplicity some details have been omitted.) The basic structure is a copper variable-temperature bar located inside a vacuum can. The copper vacuum can is held on with low-melting-point solder, Cerelow 136 (melting point 136^{0}F),[87] and can easily be installed and removed by gentle heating. Provided that the two mating surfaces are well tinned prior to being joined, a superfluid-tight joint can be routinely made by this method. A flux is used for the tinning, but not for actual installation of the bottom can.[88]

The copper variable-temperature bar is cylindrical, 0.76 cm in diameter and 10.2 cm long, and has several holes in it to accommodate a resistance heater (a 1 kΩ metal-film resistor), a calibrated germanium resistance thermometer,[89] and a capacitance thermometer[90] for use in high magnetic fields where the magnetoresistance of the Ge thermometer renders its calibration useless.

The variable-temperature section is connected by a 4-40 brass screw passing through a 0.5 cm long nylon spacer to the copper top plug, which is at the He bath temperature during experiments. The brass screw acts as a structural member and also as a weak thermal link to the bath temperature. A number of small copper wires, mostly #40, pass from the top plug to the variable-temperature bar. These wires are wrapped and heat sunk on both sides of the nylon spacer using General Electric 7031 varnish. They also contribute to the thermal link. It is the thermal conductance of this total thermal link which sets the practical upper limit to the cryostat's useful temperature range. For the wires and brass screw used, a heater power of 8 mW is required to reach a temperature of 7 K, while 150 mW is required to reach 20 K.

The minimum sample temperature is about 0.5 K above the bath temperature. This difference is due to heat leaking down the leads which are not perfectly heat sunk. This is usually only a problem during critical field measurements and can be eliminated by admitting a small pressure (10-20 mtorr) of He exchange gas to the cryostat. This produces a small error in the thermometry,* typically 20-40 mK, which

---

* Because of the extra cooling of the sample by the exchange gas, the temperature indicated by the thermometer is higher than the actual sample temperature.

can be determined and subsequently corrected for by recording several of the same transitions (i.e., at the same fields) both before and after admitting the exchange gas. These measurements establish the error at several temperatures unambiguously. The error at lower temperatures is determined by assuming that the error decreases linearly to zero at the He bath temperature. To the extent that the actual error measurements covered a spread in temperature, they are consistent with this assumed linear behavior.

The room temperature end of the dipstick contains two hermetic 10-pin electrical feedthroughs, a thermocouple pressure gauge, an overpressure release valve, and a pump line through which gas can be added to or pumped from the cryostat. The thermocouple pressure gauge is used to determine if the cryostat leaks.

IV.2.4 Sample Mounting

The samples are mounted by gluing them onto the flat end of a cylindrical single-crystal sapphire rod,[91] typically 0.04 to 0.06 inches in diameter (1.0 to 1.5 mm), although rods from 0.01 to 0.10 inches in diameter (0.25 to 2.5 mm) have been used for unusually small or large samples.* Initially, GE 7031 varnish was used to mount the samples. As will be discussed in Chapter VI, it became evident that a technique which applied less stress to the crystal on thermal cycling would be desirable, so a switch was made to rubber cement ("Grippit") diluted

---

* The mounted samples are stored in holes drilled in a block and identified by a letter (row) and number (column), e.g., C-10. This sample identification label does not indicate either the composition or the crystal-growth batch number.

with hexane.

Because the crystals are very soft and easily damaged, it is necessary to handle them very gently. The following technique was developed to transfer crystals from the petri dishes in which they are stored to the sapphire rods. A thin hyperdermic needle held in a handle is used. The needle is first dipped into some diluted rubber cement and pulled out, ideally leaving a very fine strand of cement protruding from the tip of the needle. The crystal can then be picked up by touching it with this whisker of cement. The crystal can be very gently placed just above the surface of the sapphire rod and a drop of hexane applied. This will dissolve the cement, allowing the crystal to settle down onto the surface of the rod. This step is always performed under a low-power stereo microscope. Finally a drop of diluted rubber cement can be applied to hold the crystal in place.

The sample rods are held into holes in the copper sample-rod mounting block in the cryostat using 0-80 screws (omitted from Figure 4-4) with grease to insure good thermal contact. Originally Apiezon N grease was used, but this reacts with the rubber cement. Therefore, Dow Corning Silicone Vacuum Grease has been used since the switch was made to rubber cement.

Several sample-rod mounting blocks exist for different size sample rods and for orienting the samples parallel and perpendicular to the direction of the dc field for $H_{c2}(T)$ measurements. All of these mounting blocks can hold two samples (and two LC circuits are provided), so two samples can be measured each time the cryostat is cooled down. These interchangeable mounting blocks have a pin (Figure 4-4) which fits into

the bottom of the variable-temperature bar. They are secured in place with an 0-80 screw which runs through the variable-temperature bar and the pin. Grease is used here too for good thermal contact. The accuracy with which the samples are oriented in the magnetic field can be estimated to be within 2-3 degrees of the desired orientations. From the consistency and reproducibility of the critical field data (Chapter VI), it appears that angular misorientation is not a problem.

IV.2.5 Low-Temperature Circuitry

The inductor is slipped over the end of the sapphire rod to enclose the sample at its center. Thus the ac field is always oriented perpendicular to the face of the sample. It is best to position the sample so that when it is centered in the inductor, the inductor need not be placed very close to the copper sample-mounting block. This is because if the end of the coil is within approximately 1 mm of the copper, ac losses in the copper will cause a noticeable decrease in the Q, and thus the sensitivity of the detection circuit. The inductor leads are connected to a twisted pair of #34 copper wires at a small terminal strip located on the variable-temperature bar. One side of the coil is also grounded to the variable-temperature bar at this terminal strip. This electrical connection is made via a wire which is pressed against the variable-temperature bar with a screw. This arrangement also helps to insure that the pickup coil and variable-temperature bar are isothermal. The twisted pair of #34 copper wires is heat sunk by wrapping and securing with GE 7031 varnish. This twisted pair continues up to the top plug where it connects to the capacitor. This arrangement

allows the inductors to be easily replaced without disturbing the heatsinking. The solder joints between the inductor and the twisted pair are made using "non-superconducting" solder (40% Cd, 60% Bi; T_c = 0.7 K) to avoid any spurious signals due to the superconducting transition of ordinary Pb-Sn solder which occurs at about 7 K.

The capacitor is mounted on the top plug to keep it at as constant a temperature as possible, since the capacitance is slightly temperature dependent. The tuned circuit is grounded at this point by soldering one side of the capacitor to the top plug. This also provides an effective method of heat sinking the capacitor.

The requirements on the capacitor to be used in the LC circuit are that it must have a high Q and a large self-resonant frequency, and be small enough to fit into the vacuum can. A small temperature coefficient (at liquid He temperatures) is also highly desirable. For this last requirement, silvered mica capacitors are ideal, having a virtually zero temperature coefficient. However, ceramic capacitors manufactured by American Technical Ceramics[92] have been used because their smaller size allows larger values of capacitance, 1 to 5 nF, to be used.

When the apparatus is being tuned up prior to making a measurement, that is, when the frequency is being swept manually and the output voltage is being monitored on the oscilloscope, the transfer curve may occasionally appear distorted from the form shown in Figure 4-1. The reason for this is not known in detail, but it must be related to deterioration of the coil, as the situation can invariably be remedied by replacing the coil.

The coils typically have inductances between 0.5 and 1 μH (for the usual size sample rod) and are typically wound from # 40 copper wire with about 20 turns (2 layers of 10 turns each). The inductor must be small enough to insure a reasonable filling factor, yet have enough inductance to achieve a reasonable Q. Q (= $\omega_o L/R$) increases with the coil size because while the resistance increases linearly with the total length of wire in the coil, the inductance increases faster than linearly when the radius and/or the number of turns is increased.

With the values of capacitance and inductance noted above, resonant frequencies between 2 and 4 MHz are obtained, and Q's are typically about 30. The calculated rf magnetic field is between 0.01 and 0.1 gauss. The circuit Q achieved is determined not only by losses in the coil, but also by losses in the twisted pair connecting the capacitor with the inductor and by losses in the coaxial cable going to the room-temprature electronics. Connected directly together, the capacitor and inductor have a Q of approximately 60 (at 4.2 K). Adding the twisted pair of #34 copper wires which is necessary to thermally separate the components lowers the Q to approximately 45. Losses in the coaxial cable from the low-temperature end of the cryostat to the top of the cryostat and from this point to the electronics cause a further reduction to a Q of approximately 30. A miniature coaxial cable[93] is used in the cryostat to satisfy space requirements and to minimize the heat leak to the helium bath. This miniature cable has a relatively high resistance, $R_{dc} \approx 20\ \Omega$, but this resistance has little direct effect on the operation of the circuit since 20 Ω is much less than both the input resistance of the MC1733 video amplifier (R_{in} = 20 kΩ) and the current source impedance [$(2\pi f_a C_1)^{-1} \approx 50$ kΩ]. It is rather the capacitance of

this cable (and the room-temperature cable) which discharge through the cable resistance which reduces the circuit Q. For this reason, a low-capacitance coaxial cable, type as RG-62/U is used to connect the cryostat to the room-temperature electronics.*

IV.2.6 Operation and Sensitivity

In order that the shape of the transition be accurately recorded, it is necessary to operate near the resonant frequency where the transfer curve shown in Figure 4-1 is linear. This requirement can be met by operating sufficiently near to f_r that the output voltage never exceeds 1/2 of the peak value. It is also important that losses in the sample have a negligible influence on the Q of the circuit, otherwise the measured transition curve will be distorted, since the slope of the frequency-to-voltage transfer curve is proportional to Q. For smaller samples no difficulties arise, since losses in the coil dominate and since the change in V_o at the transition is relatively small. For larger samples, however, losses in the sample can influence Q and the change in V_o can be so large that it moves completely off the linear portion of the transfer curve, as can easily be seen on the monitor oscilloscope. Both of these problems can be solved by adding a shunting resistor across the LC circuit at the room-temperature end of the cryostat to lower the Q, and thereby increasing the frequency range over which V_o is linear.

---

* Type RG-62/U has a capacitance of 46 pF/meter while standard coax, type RG-58/U, has a capacitance of approximately 95 pF/meter.

To illustrate the sensitivity of this apparatus, Figure 4-5 shows the zero-field transitions as a function of temperature for two small crystals. The first crystal, of $Nb_{.90}Ta_{.10}Se_2$, is a thin hexagonal platelet with a diameter of 50 μm and a thickness of about 10 μm (sample volume $V_s = 2\times10^{-8}$ cm^3). As can be seen, the signal-to-noise ratio of ≈ 20 is sufficient to allow the transition temperature to be determined accurately. Also shown in Figure 4-5 is the zero-field transition of a larger sample, a 110 μm diameter hexagonal crystal of $Nb_{.92}Ta_{.08}Se_2$. For a sample of this size, the noise is barely perceptable.

The slope of the trace above and below the transition seen in Figure 4-5 is due to a small instrumental background signal. This background signal increases considerably above about 8.5 K and is primarily caused by the temperature dependence of the capacitance. This background could be reduced by better thermal isolation of the capacitor or by the use of silvered mica capacitors. The instrumental background signal can also be greatly reduced by the presence of a small pressure (10-20 mTorr) of helium exchange gas in the vacuum can. In any case, the instrumental background signal is unimportant even for very small samples over the temperature range of interest here.

It is instructive to compare the performance of this ac susceptibility apparatus with that of sensitive heat capacity systems if used to detect superconductivity in small samples. To estimate the change in heat capacity which would be expected to occur at T_c for the 50 μm sample shown in Figure 4-5 (mass ≈ 0.13 μg), we assume that its jump in heat capacity at T_c is similar to the published value for $NbSe_2$,[94] ΔC = 0.25 J/K-mole. The heat capacity change for this sample

would thus be about 10^{-10} J/K at $T_c \simeq 6$ K. While the literature contains several reports of very sensitive heat capacity systems,[76-78] it appears that none of them could resolve a ΔC of this size with the signal-to-noise ratio demonstrated in Figure 4-5. The state-of-the-art in small-sample calorimetry is rapidly being advanced.[78] However, such machines will probably remain much more complicated than our apparatus and more difficult to use, especially in large magnetic fields.

The system described in this section thus provides an extremely sensitive and quite simple method for measuring transition temperatures. For measuring $H_{c2}(T)$ the cryostat can be inserted into the bore of a high-field magnet. The only way in which operation of the circuit is affected by the dc field is that the Q of the resonant circuit is decreased, because of the magnetoresistance of the copper wire in the coil. The Q decreases approximately linearly as the field increases, decreasing typically to 75% of the zero-field value at 70 kG. This decrease in Q lowers the sensitivity of the apparatus somewhat (Equation 4.11).

IV.3 Thermometry

IV.3.1 Resistance Thermometry

The purpose of this section is to describe the thermometers used in the cryostats and their associated room-temperature electronics. All the temperatures measured can be traced to one thermometer, a germanium resistance thermometer (SN 6218) which was purchased with a calibration

from Cryocal.[89] This type of thermometer is well known to be very stable with respect to repeated thermal cycling.[95]

The thermometer was calibrated by Cryocal by measuring its resistance at 35 temperatures between 1.5 K and 20 K and then fitting this data to a polynomial for interpolation to other temperatures in this range. For temperatures up to 12 K the accuracy of the basic calibration standards is claimed to be 10 mK or better. The accuracy of the polynomial fit can be tested at the calibration points, and the error is on the order of 1 mK or less at all temperatures of interest. Temperatures in the range 1.3 K to 1.5 K have been determined by simply extending the interpolation table using the same polynomial. The only checks made on the calibration, other than self-consistency and reproducibility of the T_c measurements, were occasional measurements of the transition temperatures of relatively pure samples of various elements (e.g., Pb, In) which always yielded the correct T_c.

The resistance thermometers are used in a four-terminal configuration driven by a current supply which is shown schematically in Figure 4-6. This particular circuit is a modification of a circuit originaly constructed by M. Feuer. A single op amp is used in a standard current-supply configuration. The current is determined by an Analog Devices AD580JH three-terminal precision voltage reference source and one of three switch-selectable variable resistors. Either 1, 10, or 100 μA can be provided. Each of these three resistors is actually a metal-film resistor in series with a ten-turn potentiometer for precisely adjusting the current. A connection for a DVM is provided which can be switched to read either the thermometer voltage or, in the

current position, the voltage across an accurately set 100 kΩ resistor. With the switch in the "current" position, the current actually flowing through the thermometer can be measured and adjusted to provide the precise value desired. The two silicon signal diodes (1N4446) are connected across the op amp input to protect the op amp input stage from damage if the thermometer is suddenly disconnected without the power supply first being shut off.

In principle this circuit could be operated in a floating mode without being grounded to the equipment rack (i.e., the power line ground) at any point. However this causes an appreciable 60 Hz ac voltage to appear across the thermometer. It was empirically determined that the optimum ground point is the output of the op amp, as shown in Figure 4-6. With this arrangement, the ac voltage across the thermometer is less than 1 μV ac. The circuit is powered by a modular ±15 volt supply. The heater control is also located in the thermometer box. The heater power is simply controlled by a 1 kΩ potentiometer connected directly across the power supply.

This thermometer current supply works quite reliably. As noted, there is no problem with ac pickup and once the current has been set, it will drift by at most 1 part in 10^4 over several hours. To avoid problems with thermal emf's and noise, the thermometer current should be selected to be as large as possible without causing self-heating of the thermometer. For the Ge thermometer, Cryocal recommends 10 μA above 3 K and 1 μA below 3 K, which roughly corresponds to shifting from 10 μA to 1 μA when the thermometer resistance has increased to 1 kΩ.

Thermal emf's can arise in the leads connecting a cryogenic thermometer to room-temperature electronics due to thermocouple-type effects in the leads. The thermal emf in the thermometer leads can be determined by measuring the thermometer voltage with the thermometer current shut off. With a 10 μA thermometer current the thermal emf is negligible. It is not quite negligible with a 1 μA current but in any case it can be easily measured and subtracted to determine the true thermometer voltage.

IV.3.2 Capacitance Thermometry

While Ge thermometers are very good as reproducible temperature standards, they do suffer from a large magnetoresistive effect,[95-97] which renders the zero-field calibration useless in large dc fields. For this reason a capacitance thermometer has been used for high-field work. These sensors, which were developed by Lawless,[98] have been tested in fields up to 140 kG without any field dependence being discovered.[99] The dielectric is a glass-ceramic material containing $SrTiO_3$. In the temperature region of interest, below 10 K, the change in capacitance is approximately a linear function of temperature.

The sensor used is a Lake Shore Cryotronics[90] model CS-400 GR which has a capacitance of approximately 20 nF at low temperatures and a sensitivity of approximately 200 pF/K. The main disadvantage of capacitance thermometers is that their calibration is not reproducible from run to run if the sensor is allowed to warm up to temperatures ≥ 50 K. This problem is apparently caused by small but irreversible changes in the microstructure of the dielectric, which shift the capacitance.[100]

When the thermometer is warmed up to room temperature between runs, the day-to-day shift in its calibration can be as large as 0.3 K.[101] Because of this, the capacitance thermometer is calibrated against the Ge thermometer during each experiment.

The capacitance thermometer is used in a bridge circuit, which is shown schematically in Figure 4-7. This circuit is only a slight modification of a design by Prober.[101] One leg of the bridge consists of the capacitance thermometer in series with a resistance which is a 130 Ω metal-film resistor in series with a ten-turn, 10 Ω potentiometer. The other leg consists of a 20 nF silvered mica capacitor, shunted by a 1.05 MΩ metal-film resistor to mimic losses in the thermometer, in series with a General Radio resistance decade box (usually set to about 135 Ω). A PAR model 124 lock-in amplifier with model 116 preamp is used both to power the bridge and measure the imbalance signal. The bridge activation comes from the lock-in reference output which first passes through a voltage control potentiometer and a dc blocking capacitor. The bridge imbalance voltage is increased by a Triad G-10 signal transformer (primary impedance = 500 Ω, secondary impedance = 712 kΩ) before being applied to the input terminals of the 116 differential preamp.

In the cryostat, the capacitance thermometer leads are connected to a twisted pair of #38 copper wires which run up to a hermetic 10 pin electrical connector on the top of the cryostat. From there, the two leads go to the rack-mounted bridge via two coaxial cables.

The bridge is set up and balanced in the following way. A frequency of 1 kHz is used. The phase of the lock-in amplifier is simply set to maximize its change in output for a given change in bridge balance. The

bridge can be balanced at the desired temperature by adjusting the resistance decade box and the ten-turn potentiometer in the sensor leg of the bridge. Finally, the input voltage is adjusted to provide a convenient scale on the X-Y recorder, but should be limited to 50 mV or less (as measured at the V_{in} monitor position) as the thermometer characteristics are insensitive to the magnitude of the ac voltage only for such small-amplitude excitations.[101]

During an $H_{c2}(T)$ experiment the capacitance thermometer is used as follows. After liquid helium has been transferred, the bridge is set up and balanced as detailed above. The zero-field and low-field transitions (usually up to 10 kG) are recorded using the Ge thermometer. The magnetoresistance of the Ge thermometer, which is located 9.5 cm from the center of the magnet, has been measured and is negligible at fields (at the center of the the magnet) of 10 kG. The reason for this procedure is that capacitance thermometers are known to have transient instabilities when they are first cooled down.[98,101] By making the first few measurements with the Ge thermometer, a time of ≈ 1 hour is allowed for sensor stabilization, which should be sufficient.

At this point the field is turned off and the capacitance thermometer is calibrated using the Ge thermometer. The calibration data consist of a set of lock-in amplifier output voltages at known temperatures. These data are analyzed with a simple computer program. This program uses the bridge imbalance voltages at known temperatures as input, and does a least-squares fit of the data to an equation of the form $V = b_o+b_1T+b_2T^2+b_3T^3$, which appears to be sufficient to reproduce the nearly linear relationship between the bridge imbalance voltage and

temperature. The program then plots all the data points along with the polynomial fit. The main reason that the program does the plotting is to make it obvious if any errors have been made in recording the calibration data. Finally the program prints out a calibration table listing the voltage calculated from the polynomial fit as a function of temperature.

This calibration procedure has been carried out for each experiment.* The advantages of this approach are that no precise setup of the instrumentation is required, no assumptions need be made regarding the linearity of the sensor or the bridge, and most importantly, no assumption is made regarding the day-to-day reproducibility of sensor calibration. Recording the calibration points is not time consuming, and all the fitting and plotting is done by the computer.

IV.4 Superconducting Magnet System

This section describes the superconducting magnet system used at Yale for critical field measurements at fields up to 80 kG. The higher field work done at the National Magnet Lab at MIT is described in Section IV.5. First the magnet cryostat and its associated room-temperature electronics will be described. Then the operation of the system will be discussed and finally the magnet calibration will be considered.

---

* For the first experiments using the capacitance thermometer a calibration graph was plotted by hand.

IV.4.1 Magnet Cryostat and Electronics

The superconducting magnet is a standard-type epoxy-filled Nb-Ti solenoid, manufactured by the Magnetic Corporation of America, model SC160-YU.[102] It is capable of producing a maximum field of 80 kG at a current of 31.68 amperes (2.525 kG/amp), and at the lowest helium bath temperature attainable, approximately 1.3 K. This magnet has a persistent switch which allows the power supply to be shut off once the desired field is established.

The magnet cryostat basically consists of a brass top plate, a stainless steel tube which supports the magnet at the bottom, and the wires going down to the magnet. The magnet itself has an outside diameter of 6.99 cm (2.75 inches) with a bore of 2.54 cm (1 inch). The windings are 10.16 cm (4 inches) long. Measurements made on the completed cryostat indicate that the magnet is coaxial with the stainless steel support tube to within an error of 0.3°. The cryostat fits into a 7.62 cm I.D. (3 inch) helium dewar which is connected through a standard Walker regulator to a mechanical vacuum pump which allows the helium bath to be pumped down to about 1.3 K.

When the magnet system was first constructed and tested it became apparent that a large amount of noise was present at the output of the frequency-shift-detector because of vibration of the dipstick cryostat in the magnet. This was caused by motion of the pickup coils in the slightly inhomogeneous magnetic field at the center of the magnet. The problem was solved by installing a ring of beryllium-copper fingers around the top of the magnet which hold the dipstick cryostat firmly in place in the magnet.

In the cryostat, the magnet current is carried by 18 gauge enameled copper wire which is heat sunk in two ways. First, there are two cylindrical copper heat sinks connected to the central stainless steel tube and coaxial with it. These are constructed in such a way that the helium vapor boiling off the bath is forced to flow over their outside surface around which the current leads are wrapped several times. Also there are four cooling fins soldered directly to each of the two current-carrying wires below the cylindrical heat sinks. These are oval shaped piecs of sheet copper approximately 2.5 cm by 1.5 cm and are also cooled by the helium vapor.*

The electrical system associated with the magnet cryostat is shown schematically in Figure 4-8. The system consists of the power supply, connecting cables and two rack panels, one containing the shunts used to measure the magnet current and one containing the persistent switch heater circuitry and a voltmeter (±2 volts full-scale) used to measure the magnet charging and discharging voltage.

The power supply which is usually used is a Hewlett Packard 6259B (I_{max} = 50 amps, V_{max} = 10 volts). The only modification that has been made to the supply was to replace the coarse current control potentiometer by a ten-turn potentiometer. For low-field work, less than 15 kG, usually a smaller power supply, a Hewlett Packard 6291A (I_{max} = 5 amps, V_{max} = 40 volts), is used. This smaller supply is used only because its greater current-control resolution makes it easier to obtain specific small values of current. The magnet current is determined by a 1 mV/amp shunt (1% accuracy) in the magnet-current lead.

---

* When the dewar is full of liquid He the heat sinks are immersed.

Between the power supply and the shunts there is a diode array which protects both the power supply and the magnet. 12 amp silicon diodes are used in this array. Seven diodes are connected in series across the power-supply leads in a forward-biased direction while two sets of two in series are connected across the leads in a reversed-biased direction. In normal operation none of the diodes conducts any significant current. The voltage at the power supply terminals is the sum of the IR drops in the current loads and the magnet voltage. At a current corresponding to the maximum field of 80 kG (31.68 amps), the voltage drop across the leads is slightly less than 1 volt. Since the magnet charging (and discharging) voltage is kept to less than 1 volt in accord with the manufacturer's recommendations, the total voltage at the power supply terminals should be 2 volts or less. This is not enough to turn on the forward-biased diodes. However, if a large positive voltage were to be accidentally applied to the magnet, these diodes would turn on, protecting the magnet from an excessively large charging rate.*

The function of the normally reversed-biased diodes is to protect the magnet and power supply in the event that the magnet quenches. During a quench the magnet current decays rapidly and a large negative (discharge) voltage is developed. In this situation the normally reversed-biased diodes turn on, protecting the output stage of the power supply from any harm which could be caused by a reverse-polarity volage. This magnet has been quenched several times without any apparent damage

---

* Seven diodes are probably too many. They were necessary when the magnet cryostat was first constructed since the original current leads in the cryostat were too long, leading to large IR drops under normal operating conditions. The leads have been shortened, but the number of forward-biased diodes has not been reduced.

to either the magnet or the power supply.

A modular ±15 volt power supply is used to power the persistent switch heater. Current-limiting resistors allow either 50 or 90 mA to be passed through the heater in order to drive the persistent switch normal. Below 2.17 K, when the helium bath is superfluid, the persistent switch will respond very sluggishly unless 90 mA are used.

IV.4.2 Magnet Operation

All of the $H_{c2}(T)$ measurements, both using the superconducting magnet at Yale and at the National Magnet Lab have been made by sweeping the temperature in a fixed field. Thus the magnet operation simply consists of setting the field to a succession of fixed values. The swept-temperature method has several advantages over the swept-field method, given that a variable-temperature cryostat is needed anyway since some of the relevant transition temperatures are above 4.2 K. Background effects tend to be more field-dependent than temperature-dependent, so less noise is generated. Also He consumption is reduced since changing the field dissipates energy into the He bath.

The magnetic field can be increased simply by changing the power supply current-control setting. As the current increases, a voltage = L×dI/dt will develop across the magnet, and the power supply will switch into the constant voltage mode. The magnet will charge up at a constant rate (governed by the voltage-control setting on the power supply). When the current reaches its set point the power supply will switch to a constant-current mode and the magnet voltage will drop to zero. The

actual current flowing through the magnet can be determined from the shunt voltage and any desired correction can be made. Finally the persistent-switch heater can be shut off, isolating the magnet. If desired, the power supply can be shut off after a short delay to allow the persistent switch to stabilize. The only reason for shutting off the power supply is to conserve liquid helium by halting the dissipation of heat in the magnet current leads, as operation of the power supply has no effect on the performance of the frequency-shift-detector circuitry.

There are two methods of decreasing the field in the magnet. The first is to slowly manually decrease the power supply current control knob setting, monitoring the discharge voltage on the magnet voltmeter (and keeping it to 1 volt or less). The second method of discharging the magnet, which is most useful when the field is to be completely shut off, is to gradually decrease the voltage control on the power supply which causes a slow decrease in the magnet current. The voltage setting can be lowered to zero in several steps (to keep the discharge voltage at 1 volt or less) and the current will very conveniently, if somewhat slowly, ramp down by itself.

IV.4.3 Field Calibration

The field in the magnet has always been determined during critical field experiments by measuring the current with the 1 mV/amp shunt and using the conversion factor 2.525 kG/amp supplied by the manufacturer. This technique was checked by measuring the field with two calibrated Hall probes kindly lent to us by L. G. Rubin of the National Magnet Lab,

who has studied such probes.[103] Both were F. W. Bell type 921 transverse cryogenic Hall probes calibrated at the NML at 4.2 K. For both probes the agreement with the field determined from the magnet calibration was excellent.

With probe number 891, 16 data points were taken between 5 and 60 kG at 4.2 K. The Hall probe voltage was measured at a current of 80 mA and converted to a field using the supplied conversion factor 6.87 ± 0.02 mV/T (an uncertainty of 0.3%). The average difference between the field determined this way and the field determined in the usual way was 0.31% with a standard deviation of 0.16%. With Hall probe number 889, 13 data points were taken over the same field range. Here the Hall probe conversion factor was 6.79 ± 0.03 mV/T (an uncertainty of 0.5%) and the average difference was -0.10% with a standard deviation of 0.30%. This test indicates that the field values determined from the shunt voltage using the conversion factor of 2.525 kG/amp are accurate to at least 1%.

IV.5 Measurements at the National Magnet Lab

During the week of June 25, 1979, a series of $H_{c2}(T)$ measurements were made at the Francis Bitter National Magnet Laboratory, located at the Massachusetts Institute of Technology, in fields up to 150 kG. The dipstick cryostat and all its associated room-temperature electronics were transferred intact and used there in the usual way. In essence, the only things which differed were the dewar and the magnet. The dewar, supplied by the National Magnet Laboratory was a metal dewar (Janis model 10 D.T.) designed to fit into the bore of a Bitter solenoid. A ring with 4 Be-Cu fingers was constructed which slid over the lower end

of the cryostat and could be secured with set screws. The fingers of this ring flare outward to contact the inner walls of the dewar to prevent vibration of the cryostat in the dewar.

The magnet used was a standard water-cooled Bitter solenoid, magnet 2D, capable of producing fields of up to 154 kG at a current of 22.5 kA. This magnet was calibrated before and after the experiments by L. G. Rubin, Head of Instrumentation and Operations at the NML. While the two calibrations agreed very well, the more extensive calibration performed after the experiments was used to analyze the data. It was found necessary to use a field stabilization unit to provide a sufficiently constant dc field. This is a small feedback controlled solenoid which fits into the bore of the main magnet. Without this unit the thermometer voltage kept jumping around in an erratic manor, presumably caused by eddy-current heating of the variable-temperature bar in the cryostat caused by small fluctuations in the field of the main magnet. The field stabilization unit senses such fluctuations and produces a small field which cancels the original fluctuation.

Unfortunately, there was a problem with the field calibration which was not discovered until the data were later analyzed at Yale. By some mechanism, which was not discovered, the field values recorded at the NML appear to be too large by a factor of 1.11. This figure was obtained by using low field (less than 80 kG) data for samples measured both at Yale and at the NML. Plotting the uncorrected data reveals an obvious discrepancy which can be removed by dividing all the NML field vaues by 1.11.

Obviously the measurements used to position the cryostat in the magnets both at Yale and at the NML were checked and rechecked, but no problems were found. It was at this point that L. G. Rubin loaned us the Hall probes referred to earlier to check our magnet calibration. As noted above, the magnet calibration was found to be correct. There are two other pieces of evidence that indicate that the calibration of the superconducting magnet system at Yale is correct. $H_c(T)$ was measured for a piece of 99.9% lead wire and very good agreement was found with published values.[104] Also $H_{c2}(T)$ has been measured for several samples of various TMDC's which had previously been studied by D. E. Prober[14] at Harvard. Again good agreement was obtained. In light of all the evidence, the calibration of the superconducting magnet was assumed to be correct, and the NML data was scaled accordingly, although the source of the discrepancy could not be determined. In any event, the NML data are not important for any of the quantitative conclusions which are drawn from the $H_{c2}(T)$ in Chapter VI, as is discussed in detail below.[105]

V. Theory of the Upper Critical Field

The purpose of this chapter is to examine the various theories which have been proposed to explain the upper critical field $H_{c2}(T)$ in bulk, type II superconductors. Emphasis will be placed on those aspects of the theory most relevant to the $Nb_{1-x}Ta_xSe_2$ system. Since these materials are, in spite of their anisotropy, definitely three-dimensional (Chapter VI), the theory of $H_{c2}(T)$ in lower-dimensional systems will not be discussed in detail.

Detailed comparisons with experimental results for the $Nb_{1-x}Ta_xSe_2$ system are presented in Chapter VI, although some experimental results will be presented here, especially for other systems. Chapter VII is concerned with the results of computer modeling which has been carried out to investigate the influence of various types of Fermi surface topology on $H_{c2}(T)$.

This chapter will begin with a brief introductory discussion of the critical field properties of superconductors. Considerably more detailed treatments can be found in a number of texts.[106,107] Following this introductory section, the relevent theories will be discussed in detail.

V.1 Basic Properties of Superconductors in Magnetic Fields

One of the most fundamental properties of superconductors is their complete diamagnetism to small-amplitude magnetic fields, discovered by Meissner and Ochsenfeld in 1933. Such fields are excluded from the interior of superconducting bodies except for a surface layer of

thickness approximately equal to the magnetic field penetration depth λ, which is typically 100 nm. It "costs" the superconductor a certain amount of energy to set up the surface currents which exclude the magnetic field. As the field amplitude is increased, this field-exclusion energy increases until it equals the condensation energy; the amount by which the sample's energy was lowered when it became superconducting in the first place. At this point the system becomes unstable. Unless the sample has a zero demagnetizing factor, normal and superconducting regions will form, allowing partial field penetration, and thus lowering the field-exclusion energy.

Of fundamental importance is the energy associated with the interface between the normal and the superconducting regions. The sign of this energy depends on the relative sizes of two fundamental lengths, the penetration depth λ and the coherence length ξ.* It is convenient to consider the quantity $\kappa = \lambda/\xi$, because λ and ξ have similar temperature dependencies, so κ is approximately temperature independent.

For $\kappa < 0.707$, the interface energy is positive (type I superconductivity). Because this energy is positive, the structure of the intermediate state, as it is called in type I materials, consists of alternately normal and superconducting lamina with boundries parallel to the applied field. The width of the lamina are small but macroscopic, typically 1 mm,[108] and are determined by a balance between the magnetic

---

* There are two different coherence lengths in superconductivity. $\xi(T)$ is the Ginzburg-Landau coherence length and gives, in the GL theory, the distance over which small perturbations in the pseudowavefunction describing the superconducting state die out. Typical values at $T = 0$ range from less then 10 nm up to $\approx$ 1 μm. $\xi(T)$ is a temperature dependent quantity, diverging at T_c. The BCS coherence length is ξ_0, and will be discussed later.

field energy and the interface energy. As the field is increased, the fraction of the material in the normal state increases, until all superconductivity is eliminated at the critical field H_c. Almost all of the elements (as pure crystals) are type I superconductors, and typical values of H_c at T = 0 are several hundreds of gauss.

If $\kappa > 0.707$, the surface energy is negative and radically different behavior results (type II superconductivity). In a large field it is energetically favorable to form boundries between superconducting and normal regions, so the field becomes divided into as many small regions as possible, limited only by the quantization of magnetic flux. These small field-containing regions are called vortices because of the screening currents which flow around them. Each vortex contains an total magnetic flux equal to the fundamental quantity $\Phi_0 = \hbar c/2e = 2.07 \times 10^{-7}$ gauss-cm^2. (Here $\hbar$ is Planck's constant, c is the speed of light, and e is the magnitude of the charge on the electron.)

The number of superconducting electrons is depressed near the center of the a vortex and this can be crudely modeled by assuming that the vortex has a normal core of radius ξ. Because of the small size of the vortex, the field distribution in the superconductor can adjust to minimize the field exclusion-energy and very large critical fields can result, as high as several hundred kilogauss(kG). As the applied field is increased, the number of vortices increases until finally, at $H_{c2}(T)$, the normal cores of the vortices occupy all of the material, and superconductivity vanishes. The elements Nb and V,[109] and Tc,[110] and most alloys and intermetallic compounds, including the compounds $Nb_{1-x}Ta_xSe_2$, are type II superconductors.

There are two critical fields for type II superconductors, as shown schematically in Figure 5-1. Below the lower critical field $H_{c1}(T)$ (and for a zero demagnetizing factor) the applied field is completely excluded (the Meissner state). At $H_{c1}(T)$ a second-order phase transition occurs to the mixed state where vortices enter the material.* At the upper critical field $H_{c2}(T)$, another second-order transition occurs, the material becoming completely normal.** Under some conditions superconductivity can persist at the surface of a type II material up to a higher critical field $H_{c3}(T)$. H_{c3} is briefly discussed in Section V.6.

The magnetization of a type II superconductor goes continuously to zero at $H_{c2}(T)$, so demagnetizing effects become unimportant as H approaches $H_{c2}(T)$. Thus $H_{c2}(T)$ can be determined without reference to sample shape. The field at which magnetic flux first enters is $H_{c1}(T)$ for samples with zero demagnetizing factors, but this entry field depends in general on sample geometry. $H_{c1}(T)$ is thus difficult to determine for $Nb_{1-x}Ta_xSe_2$, which grows in non-ellipsoidal shapes and is too soft to be shaped by machining.[113]

---

* For type II superconductors with values of κ only slightly greater than 0.707, the phase transition can be first order at H_{c1}. This implies an attractive vortex-vortex interaction.[111]

**The transition at the upper critical field can be first order at lower temperatures if the magnitude of the field is very large and there is little spin-orbit scattering. (Thus the field-spin interaction becomes very important in determining the upper critical field.) To date this behavior has only been observed in thin Al films (with the field parallel to the plane of the film).[112]

V.2 Introduction to the Theories of $H_{c2}(T)$

There are basically three general theoretical approaches which can be used to calculate $H_{c2}(T)$. The simplest approach is the phenomenological Ginzburg-Landau theory,[114] which, however, is only valid just below T_c. The most important approaches are those based on the BCS theory. Although the original paper by Bardeen, Cooper, and Schrieffer[115] did not contain any discussion of $H_{c2}(T)$,* theories which are based on the BCS model interaction have been proposed to explain the upper critical field. The original work based on the BCS theory contained a number of simplifing assumptions. Since then, various extensions of that work have been proposed which remove some of these restrictions. The basic BCS model interaction is retained as the cause of superconductivity, and therefore these can be considered BCS theories in a generalized sense. For application to the $Nb_{1-x}Ta_xSe_2$ system, the most important of the original assumptions is the assumption of isotropy.

The most sophisticated theories are based on the strong-coupling Eliashberg formalism.[117] For certain materials (e.g., Pb, Hg, some alloy systems) the assumption that the electron-phonon interaction is weak, essential to the quantitative results of the BCS theory, is inadequate. In principle, strong-coupling materials require a more sophisticated treatment of the electron-phonon interaction, one which includes the details of the microscopic interactions in the particular material of

---

* The original BCS paper[115] and the landmark theoetical paper by Abrikosov[116] first detailing the properties of type II superconductors were both published in 1957. BCS do not mention Abrikosov's work in their paper.

interest. However, most properties of superconductors, including the critical fields, can usefully be written as a product of the weak-coupling BCS value and a correction factor. For crystalline superconductors, the correction factor for the upper critical field usually does not differ greatly from unity and is only weakly temperature dependent. It can be obtained either from a knowledge of the relevent microscopic material parameters, or by using model calculations (Appendix E).[118-121] Strong-coupling corrections can be somewhat larger for amorphous superconductors.[122,123]

V.3 Ginzburg-Landau Theory

The Ginzburg-Landau (GL) theory is one of the most successful applications of Landau's phenomenological theory of phase transitions. Although strickly speaking it is valid only just below T_c, its relative simplicity has provided useful physical insights into many areas of superconductivity. In 1959 Gor'kov showed that the GL theory is equivalent to the BCS theory at temperatures sufficiently close to T_c.[124]

The GL result for $H_{c2}(T)$ for an isotropic superconductor is

$$H_{c2}(T) = \frac{\Phi_o}{2\pi\xi^2(T)} . \qquad (5.1)$$

$\xi(T)$ is the GL coherence length, shown here to be explicitly temperature dependent. Since $\xi(T)$ can be thought of as the radius of the normal core of a vortex, the denominator of this equation can be interpreted as

being proportional to the cross-sectional area of the vortex core. Thus, the smaller the vortex cores are, the more of them can be packed into the material before all the superconductivity is displaced, and the larger $H_{c2}(T)$ will be.

To determine the dependence on temperature and material properties which Equation 5.1 implies, it is convenient to introduce the other coherence length, the BCS coherence length:

$$\xi_o = \frac{\hbar v_F}{\pi\Delta(0)} = \frac{\hbar}{\pi 1.764 k_B} \frac{v_F}{T_c} \tag{5.2}$$

where the BCS equation for the zero-temperature energy gap

$$\Delta(0) = 1.764\ k_B T_c \tag{5.3}$$

has been used to obtain the second form. Here v_F is the Fermi velocity, and k_B is Boltzmann's constant. It is also necessary to define the important concepts of "clean" and "dirty" superconductors. This classification is based on a comparison of the intrinsic length scale ξ_0 and the electron mean free path ℓ. The dirty limit is defined as $\ell << \xi_0$ and the clean limit is defined as $\ell >> \xi_0$. Physically, ξ_0 gives, in the BCS theory, the range over which the strong electron-electron correlations responsible for superconductivity are effective, or roughly, the size of the Cooper pairs. The clean and dirty limits then correspond to ℓ being much larger or much smaller then this fundamental parameter. In terms of ξ_0, the GL coherence length can be written as

$$\xi(T) = 0.74 \frac{\xi_o}{(1 - \frac{T}{T_c})^{1/2}} \tag{5.4}$$

in the clean limit.[106] In the dirty limit[106]

$$\xi(T) = 0.855 \frac{(\xi_o \ell)^{1/2}}{(1 - \frac{T}{T_c})^{1/2}} \tag{5.5}$$

With these forms, it is clear from Equation 5.1 that the GL theory predicts that $H_{c2}(T)$ is linear in temperature just below T_c. Experimentally, $H_{c2}(T)$ for most superconductors is linear just below T_c, and an important use of the GL theory is to extract the coherence length from the measured slope dH_{c2}/dT just below T_c.

Equations 5.2, 5.4, and 5.5 predict that materials with large critical fields will have high T_c's, small Fermi velocities, and short electron mean free paths. The highest critical field materials known, such as the A-15's (e.g., Nb_3Sn, $H_{c2}(0) \approx 270$ kG[125]) and the Chreval compounds (e.g., $Pb_xMo_6S_8$, $H_{c2}(0) \approx 540$ kG[126]) are high-T_c transition metal compounds. The large number of transition metal atoms in the unit cell means that there will be many flat d bands. This implies a small v_F, since

$$\vec{v}_F(\vec{k}) = \frac{1}{\hbar} \nabla_k E \quad . \tag{5.6}$$

These materials also have rather short electron lifetimes due to strong electron-phonon interaction, and usually due also to impurity

scattering. In comparison, $H_{c2}(0)$ is about 150 kG for $NbSe_2$ with the field oriented parallel to the layers, but only about 40 kG for the field oriented perpendicular to the layer plane. Assuming that $NbSe_2$ is a relatively clean material, its high critical field in the parallel direction can be explained in the GL theory as being primarily caused by the small component of $\vec{v}_F(\vec{k})$ perpendicular to the layer plane. This is caused by the weak interlayer bonding.

The GL equations can be generalized to account, to an extent, for anisotropy effects.[127] This can be accomplished by replacing the electron mass in the GL equations by a 3x3 inverse effective-mass tensor with elements defined by[128]

$$\left(\frac{1}{m}\right)_{ij} = \frac{1}{2E_F} \langle \beta^2(\vec{k}) v_i(\vec{k}) v_j(\vec{k}) \rangle \qquad (5.7)$$

where E_F is the Fermi energy, $v_i(\vec{k})$ is the component of the electron velocity at the Fermi energy in the i direction, and $\beta(\vec{k})$ is a function which describes the anisotropy of the superconducting energy gap. β is a function of the electron mean free path and becomes 1.0 in the dirty limit. The brackets < > denote a Fermi surface average (Appendix C). The tensor of Equation 5.7 is a symmetrical, second-rank tensor, and therefore must satisfy certain symmetry requirements. For materials with cubic symmetry such tensors must be proportional to the unit tensor, so the GL theory predicts no anisotropy in such systems.[129] In fact, clean samples of cubic type II superconductors such as Nb[109,119] and Nb_3Sn[125] do exhibit anisotropy in $H_{c2}(T)$. By similar reasoning, the anisotropic GL theory predicts no basal-plane anisotropy in hexagonal

materials. While none has been found in any TMDC system (both by other researchers[14] and in this work [Chapter VI]), basal-plane anisotropy has been observed in other hexagonal materials.[130] Even so, the qualitative features predicted by the anisotropic GL equation for very anisotropic systems are found experimentally (see below).

For hexagonal systems, the GL result for $H_{c2}(T)$ can be written as[14,131]

$$H_{c2}(\theta,T) = \frac{\Phi_o}{2\pi\xi^2(T)[\cos^2\theta + \frac{m}{M}\sin^2\theta]^{1/2}} \qquad (5.8)$$

where $\xi(T)$ is the coherence length in the plane perpendicular to the c axis (this is the coherence length in the layer plane for the TMDC's), m is the effective mass for electron motion in this plane, and M is the effective mass for electron motion parallel to the c axis for (the TMDC's M > m). θ is the angle between the c axis and the direction of the applied magnetic field. The coherence length parallel to the c axis is given by

$$\xi_c = \left(\frac{m}{M}\right)^{1/2} \xi(T). \qquad (5.9)$$

Equation 5.8 predicts the same linear temperature dependence for $H_{c2}(T)$ as does the isotropic GL equation, only here the magnitude of H_{c2} varies with direction. The angular dependence implied by Equation 5.8 has been tested for various TMDC's[58,131,132] including $NbSe_2$,[14,133,134] and generally good agreement has been found.

Equation 5.8 also predicts that the ratio of the critical field parallel to the layers to the critical field perpendicular to the layers should be a temperature-independent constant. The anisotropy as a function of temperature has been measured for various TMDC's and although this ratio has been reported to be constant in some systems, usually some temperature dependence is seen.[14,133,132] A definite temperature dependence of this ratio is seen in the $Nb_{1-x}Ta_xSe_2$ system (Chapter VI).

In summary, the anisotropic GL theory has definite limitations for dealing with anisotropic superconductors, beyond the usual restriction to temperatures just below T_c. While the angular dependence predicted by Equation 5.8 has been fairly well verified by measurements of various TMDC's, the GL theory cannot explain anisotropy in cubic systems or the basal-plane anisotropy seen in other hexagonal systems. Also the anisotropic GL theory does not predict a temperature dependence of the ratio of critical fields in two different directions, as is frequently observed. The problem is in part that the GL theory uses the approximation of local electrodynamics, while the non-local electrodynamics used in the microscopic theory appears to be required for a more accurate description of the experimental data.[129]

V.4 Microscopic Theories Based on the BCS Model Interaction

The BCS theory[115,106] provides the basis of our current understanding of superconductivity. Fundamental to this theory is the notion that superconductivity is caused by an attractive, phonon-mediated, electron-electron interaction. The quantitative aspects of

the BCS theory follow by treating this attractive interaction in a very simple way. The BCS approach thus disregards most of the details of the microscopic interactions in any given material. This weak-coupling approximation is a least semi-quantitatively correct for materials where the electron-phonon interaction is weak. In this section, theories of $H_{c2}(T)$ based on the weak-coupling approximation will be discussed. Correction factors and other factors concerning $H_{c2}(T)$ in more strongly-coupled superconductors will be discussed in Section V.5. There it will be shown that to a good approximation strong-coupling corrections shift the overall magnitude of $H_{c2}(T)$ slightly, without signifigantly changing the shape of the $H_{c2}(T)$ curve, at least for crystalline superconductors.

V.4.1 Isotropic Limit

As mentioned in the introduction, the original BCS paper did not consider the critical fields of type II superconductors. In 1958, Gor'kov[135] presented a Green's function reformulation of the BCS theory. Helfand and Werthamer(HW)[136] were able to solve the Gor'kov equation for $H_{c2}(T)$. (Gor'kov himself provided a partial solution.) Their technique involves linearizing the equation, an approach which is valid if the transition is second order. Other important assumptions involved are:

1) The effect of the magnetic field on the electron motion is ignored. (The field-spin interaction is also omitted from the GL theory.)

2) The Fermi surface is assumed to be spherical. This is a somewhat questionable assumption, since most superconductors have complicated

Fermi surfaces. (The monovalent metals, which have nearly spherical Fermi surfaces, do not superconduct.) However, in dirtier materials, with rapid electron scattering over the Fermi surface, the effects of anisotropy become averaged out. This approximation of isotropy does have to be improved upon in cleaner materials, or in very anisotropic materials even if they are fairly dirty (e.g., the TMDC's).

3) The electron motion is treated in the semi-classical approximation. This requires that the spacing between Landau levels be small compared with the thermal and impurity broadening of the levels. Quantitatively, the restriction is

$$\hbar\omega_c = \hbar \frac{eH}{mc} << 2\pi k_B T + \frac{\hbar}{\tau} \tag{5.10}$$

or, using the bare electron mass ($m_e = 9.11\times10^{-28}$ g)

$$H << 47T + \frac{5.70 \times 10^{-11}}{\tau} \tag{5.11}$$

where in Equation 5.11 H is in kG. Clearly this inequality will break down for clean, high-field superconductors at low temperatures. However, it is not clear what, if anything, will happen when this semi-classical phase approximation breaks down. It has been predicted that a quantum oscillatory behavior in $H_{c2}(T)$ may result,[137] but no observations of this effect have been published, nor has any indication of such behavior been seen in this study. As discussed in Appendix F, it is possible to estimate that the low-temperature electron lifetime for $NbSe_2$ is 2.6×10^{-13} sec. for motion in the layer plane. Using this value and taking T = 1 K, the right-hand side of 5.11 equals 269 kG. Since basal plane electronic motion determines the perpendicular critical field (Section V.4.3), this number can be compared to $H_{c2\perp}(0) \approx 50$ kG.

Inequality 5.11 appears satisfied for the perpendicular field orientation. It is difficult to estimate the relevant lifetime for the parallel critical field, but it is shorter than the basal-plane lifetime.[75] Since experimentally $H_{c2\parallel}(0) \approx 150$ kG it appears that the semi-classical approximation is valid for both field orientations for $NbSe_2$. For the alloy compounds $Nb_{1-x}Ta_xSe_2$ the relevant lifetimes appear to be somewhat shorter, making the approximation also valid for these compounds.

With the approximations listed above, the linearized Gor'kov equation yields an implicit equation for $H_{c2}(T)$ which depends on T_c, v_F, and the electron lifetime, although the normalized scattering rate

$$\lambda_{tr} = \frac{\hbar}{2\pi k_B T_c \tau_{tr}} \tag{5.12}$$

is usually used.* It is useful to note that λ_{tr} can be written as

$$\lambda_{tr} = 0.882 \frac{\xi_o}{\ell} \tag{5.13}$$

showing that it is essentially the inverse of the electron mean free path measured in units of the coherence length.

$H_{c2}(T)$ for several values of λ_{tr} is shown in Figure 5-2. The plots are linear just below T_c (as in the GL theory), and bend toward the field axis at lower temperatures. Since increasing λ_{tr} means decreasing the electron lifetime, making the material dirtier increases $H_{c2}(T)$. T_c and v_F are held constant in Figure 5-2, but $H_{c2}(T)$ increases with T_c and decreases with v_F.

---

* The relevant formulas are discussed in more detail in Appendix C.

The form of $H_{c2}(T)$ depends on the Fermi velocity, a quantity which is usually not well known experimentally. Therefore, it is very common to define a dimensionless normalized field h(t) by

$$h(t) = \frac{H_{c2}(t)}{-\left.\frac{dH_{c2}}{dt}\right|_{t=1}} = \frac{H_{c2}(t)}{-T_c \left.\frac{dH_{c2}}{dT}\right|_{T_c}} \tag{5.14}$$

where the reduced temperature $t = T/T_c$ has been used. Defined in this way, h(t) has a slope of -1 just below T_c and, for the HW theory, becomes a function of only λ_{tr}. Two curves are shown in Figure 5-3. Note that when plotted in this fashion, the clean-limit curve ($\lambda_{tr} = 0$) lies above the dirty-limit curve ($\lambda_{tr} = \infty$), which is opposite to the behavior seen in the un-normalized "real" field, $H_{c2}(T)$.

$H_{c2}(T)$ is clearly linear just below T_c in Figures 5-2 and 5-3. It is possible to obtain an explicit formula for the slope in this region,*

$$\left.\frac{dH_{c2}}{dT}\right|_{T_c} = -\frac{24\pi^2}{7\zeta(3)} \frac{k_B^2 c}{\hbar e} \frac{T_c}{v_F^2} \chi^{-1}(\lambda_{tr}) \,. \tag{5.15}$$

Here ζ is the Riemann zeta function ($\zeta(3) = 1.202$). $\chi(\lambda_{tr})$ is the Gor'kov function, a monotonically decreasing function of the electron scattering rate which governs how the slope increases as the material is made dirtier. Figure 5-4 shows the inverse Gor'kov function χ^{-1} as a

---

* Slope formulas are valuable because they demonstrate explicitly the dependence of the slope on the relevent physical parameters. The complete implicit equations for the upper critical field as a function of temperature are too complicated to readily yield this sort of physical insight.

function of the electron mean free path, measured in units of ξ_0. Note that in the clean limit $\ell >> \xi_0$, changes in ℓ have a relatively small effect on the slope. χ^{-1} is approximately a linear function of the inverse electron lifetime. To a very good approximation, $\chi^{-1} = 1.032 + 0.895\lambda_{tr}$.

One of the more serious approximations in the theory as it has been presented so far is the neglect of the interaction between the electron spin and the magnetic field. In the simplest model of a BCS superconductor at T = 0, all the electrons are bound in Cooper pairs with one electron spin up and one electron spin down. It is generally energetically favorable for spins to be aligned parallel to an applied magnetic field. Since the condensation energy (the energy difference between the normal and superconducting states [with H = 0]) is fixed, in a large enough magnetic field it must become energetically favorable for the material to revert to the normal state due to the spin-field interaction. A simple limiting field at T = 0 can be calculated by assuming that only the spin-field interaction exists. This was first pointed out by Clogston[138] and Chandrasekhar.[139] To derive this limiting field, the metal in the normal state is treated as a simple free electron gas. Using relationships from the BCS theory, it can be shown that the limiting field is given by the simple expression

$$H_p^o = 18.6\ T_c \tag{5.16}$$

with H in kG.

Spin effects are only important in large fields. As a general rule, if the measured $H_{c2}(0)$ is much less than H_p^0, then spin effects can be

neglected altogther. Spin effects are also unimportant just below T_c, where $H_{c2}(T)$ is small. Thus, the neglect of spin effects in the GL theory is not a serious problem. Also, Equation 5.15 for the slope of $H_{c2}(T)$ just below T_c should remain valid for a theory where spin effects are included.

Equation 5.16 is somewhat oversimplified, and needs to be corrected by including both spin-orbit scattering and many-body corrections. There is considerable motivation for including such corrections since experimentally H_{c2} can exceed H_p^0 at low temperatures in some systems.

Implicit in the derivation is the assumption that the spin susceptibility is zero at T = 0 in the superconducting state. This is not the case for real materials, which have surfaces, impurities, and other types of crystalline disorder which can scatter electrons and may, in so doing, reorient the electron spin (a spin-orbit scattering event).* In such non-perfect crystal lattices, spin is no longer a good quantum number and the simple spin up-spin down electron pairing concept familiar from the BCS theory has to be modified to include a more general type of pairing. This was first pointed out by Anderson.[140,141] In this generalized scheme, electron states are paired with their time-reversed partner. Most properties predicted by the original BCS theory remain unchanged (one of the reasons why the BCS theory works so well), but because of this generalized pairing scheme the spin susceptibility need not be zero at T = 0. This obviously decreases the amount by which the energy of the normal state is lowered in a magnetic field relative

---

* We do not consider here spin-flip scattering by magnetic impurities which has a different effect on the critical fields.[126]

to the superconducting state which has the effect of raising H_p.

Many-body corrections also affect the value of H_p and thus the influence of spin effects on $H_{c2}(T)$. These corrections are due to both electron-electron and electron-phonon effects.

The electron-phonon interaction is conventionally quantified by the coupling constant λ_{ep}, which is determined by the phonon density of states and the matrix elements connecting the electron and phonon wavefunctions.[142,143] λ_{ep} is a well known quantity in solid state physics, describing the renormalization of many band structure** electronic properties near the Fermi surface caused by the electron-phonon interaction.[25,142] The electron-phonon coupling constant is a function of temperature, vanishing at temperatures in excess of the Debye temperature.[144] (λ_{ep} will be taken to mean the low-temperature value of $\lambda_{ep}(T)$.) λ_{ep} is also useful for quantifying what is meant by strongly-coupled and weakly-coupled superconductors. Al, a typical weakly-coupled superconductor has a $\lambda_{ep} = 0.39$. Nb is a moderately-coupled superconductor with $\lambda_{ep} = 0.95$, while strongly-coupled superconductors such as Pb ($\lambda_{ep} = 1.55$) and some alloy systems have larger coupling constants. (See Appendix E for a more complete list and references.)

That the Pauli limiting field should be renormalized by many-body corrections has only recently been recognized,[145] although the need for such corrections was discussed in the original paper by Clogston.[138] It

---

**By "band structure" is meant electronic properties which could, at least in principle, be calculated by assuming the electrons move in a rigid lattice.

now appears that the correct form is[146]

$$H_p = H_p^o (1 + \lambda_{ep} + \lambda_{spin})(1 - I') \tag{5.17}$$

where λ_{spin} and I' describe the contribution due to to electron-electron, or spin flucuation effects. The electron-phonon part of the enhancement $1+\lambda_{ep}$ will almost always exceed 1.5, even in the more weakly-coupled superconductors. This factor by itself is probably big enough so that the apparent lack of Pauli limiting in some materials (for which $H_{c2}(0) > 18.6T_c$) is in fact not a problem. However, initial estimates of the full renormalization for several transition-metal systems indicate that when spin effects are taken into account $H_p \approx H_p^0$, so that there appears to be only a small net renormalization.[146] It appears that more theoretical work, as well as better estimates of λ_{spin} and I' will be required to fully reconcile theory and experiment.

A theory of $H_{c2}(T)$ incorporating field-spin interactions and spin-orbit scattering was developed as an extension of the theory of Helfand and Werthamer by Werthamer, Helfand, and Hohenberg (WHH)[147] (before the need to renormalize H_p^0 because of many-body interactions was widely recognized). With the exception of the inclusion of spin effects, all the other approximations of the earlier theory are retained. Spin-orbit scattering is included via a normalized spin-orbit scattering rate

$$\lambda_{so} = \frac{2\hbar}{3\pi k_B T_c \tau_{so}} \quad . \tag{5.18}$$

Here τ_{so} is the electron lifetime due to scattering events which flip the spin. The theory is only valid provided that $\lambda_{tr} >> \lambda_{so}$. This is

physically reasonable, since usually the electron's spin will only be flipped in a small fraction of its scattering events. However, here it is fundamentally a mathematical requirement due to certain approximations made in the calculations.

The probability of spin-orbit scattering increases with atomic number, the approximate relation being[148,149]

$$\frac{\tau_{tr}}{\tau_{so}} = (\alpha Z)^4 \tag{5.19}$$

where α is here the fine structure constant ($\simeq 1/137$), and Z is the atomic number. This relationship appears to hold for scattering from impurities, surfaces, and lattice defects.[149]

WHH presented an implicit equation for $H_{c2}(T)$ in the dirty limit. Here the reduced field h(t) is a function of two parameters, λ_{so} and a parameter α which is defined here as

$$\alpha = \frac{3\hbar}{2mv_F^2\tau_{tr}} \quad . \tag{5.20}$$

α can be related to the slope just below T_c,

$$\alpha = -\frac{\hbar e\pi}{8ck_B m} \left.\frac{dH_{c2}}{dT}\right|_{T_c} . \tag{5.21}$$

It has recently been suggested that this definition of α can be modified

to account for the many-body renormalization of the Pauli limiting field.[145]

Figure 5-5 shows $H_{c2}(T)$ for the WHH theory for several values of α with $\lambda_{so} = 0$ (no spin-orbit scattering). As the magnitude of the field increases, Pauli limiting becomes increasingly important and $H_{c2}(T)$ bends toward the field axis faster at low temperatures. Figure 5-6 shows how spin orbit scattering effectively raises the Pauli limiting field. In Figure 5-6 α is kept constant, i.e., the initial slope just below T_c is kept constant. At $\lambda_{so} = \infty$ (no Pauli limiting) the $H_{c2}(T)$ curve is the same as the spin-free theory dirty limit curve.

V.4.2 Applicability of the Isotropic Theory

The theories of HW and WHH have been widely used since their introduction in 1966 to interpret experimental results. Usually reasonably good agreement is found.[150] However, in many systems characteristic deviations from predicted behavior have been noted.

Since the theories of HW and WHH assume isotropy, they obviously cannot account for variation of $H_{c2}(T)$ with the orientation of the sample in the magnetic field. Such behavior has been seen in many type II superconductors when prepared in single-crystal form. Some examples are the elements Tc,[110] Nb and V,[109] as well as the compounds Nb_3Sn,[125] V_3Si,[151] several of the Cheveral compounds,[126,152] the TMDC's,[14,58,131,133] as well as other compounds.[130,153,154] It is quite reasonable to assume that $H_{c2}(T)$ will display some critical field anisotropy in any superconductor that can be prepared in good quality

single-crystal form.

There are also discrepancies with the shape of the $H_{c2}(T)$ curve, which occur both with single crystals, with polycrystalline materials, and with amorphous materials. It is frequently observed that $H_{c2}(T)$ displays extended linearity at low temperatures, that is, the data doesn't bend toward the field axis at low temperatures as fast as the theoretical result does. Also, in a number of systems positive, or upward, curvature has been observed in $H_{c2}(T)$ just below T_c where the isotropic BCS and GL theories predict a linear region.* Both of these features are seen in the $Nb_{1-x}Ta_xSe_2$ system where they are undoubtedly caused by anisotropy effects. Microscopic anisotropy, primarily of the Fermi surface, can alter the temperature dependence of the $H_{c2}(T)$ curve as well as adding an angular dependence. (Section V.4.3 and Chapter VII.) However, there are other factors which can cause these effects and which are important in other systems.

Extended linearity at low temperatures can be caused by strong-coupling effects in amorphous superconductors,[122] although strong-coupling corrections in most crystalline superconductors tend to depress $H_{c2}(T)$ at low temperatures. It has recently been demonstrated that inhomogeneities can also cause both positive curvature and extended linearity.[155] Since the GL coherence length $\xi(0)$ is always much larger then atomic dimensions, the atomic-scale inhomogeneities introduced by a uniform alloying process, such as replacing Nb atoms in $NbSe_2$ with Ta atoms, can not cause an effect of this sort. Since the $Nb_{1-x}Ta_xSe_2$ samples used in this study are all high quality single crystals, it

* See Figures 6-10 through 6-12.

seems quite unlikely that the inhomogeneity effect is important here.

For completeness, it should be mentioned that positive curvature can be caused by magnetic constituents.[126] There is no reason to expect this mechanism is relevant for the $Nb_{1-x}Ta_xSe_2$ system.

It has recently been sugested by Machida, Koyama, and Matsubara[156] that positive curvature in superconductors having a CDW may be due to an interaction between the CDW and the superconductivity. However, this calculation has recently been criticized.[157] In Chapter VI it is shown that the CDW in the $Nb_{1-x}Ta_xSe_2$ system is suppressed by increasing the Ta content, while the positive curvature remains. It is thus unlikely that this mechanism is important.

V.4.3 Theory of $H_{c2}(T)$ in Anisotropic Superconductors

In the previous section the theory of $H_{c2}(T)$ in the weak-coupling limit was outlined for isotropic type II superconductors. It was pointed out that for many systems, including the $Nb_{1-x}Ta_xSe_2$ system, the normalized critical field $h_{c2}(t)$ cannot be fitted to the temperature dependence of the isotropic theoretical predictions. In addition, $H_{c2}(T)$ often is observed to depend on the orientation of the magnetic field. A number of possible reasons were discussed. However, it was argued that none of those reasons were likely to be the cause of the behavior seen in the $Nb_{1-x}Ta_xSe_2$ system.

This section will consider extensions of the BCS theory which include anisotropy effects. By including such effects it is possible to generate theoetical curves which display the same features of positive

curvature and extended linearity seen in the data for $Nb_{1-x}Ta_xSe_2$ and other systems.

Lawrence and Doniach[158] introduced a modified GL theory in which the superconducting order parameter in adjacent layers is coupled by Josephson tunneling. This model was intended to be relevant to intercalated layered compounds. A dirty-limit microscopic theory of $H_{c2}(T)$ based on this model was produced by Klemm, Luther, and Beasley.[159] The most interesting feature of these theories is the prediction that for sufficiently weak interlayer coupling adjacent layers can decouple at some temperature below T_c. Quasi-two-dimensional superconductivity results. This implies that a dramatic upturn in $H_{c2}(T)$ may be seen when the field is oriented parallel to the layer plane. This effect has been seen in intercalated layered compounds[14,15] and in artifically produced layered composites,[16] in agreement with the KLB theory.

In the KLB theory the interlayer coupling strength is measured by the parameter

$$r = \frac{4}{\pi} \left(\frac{\xi_c(0)}{s/2}\right)^2 . \qquad (5.22)$$

Here $\xi_c(0)$ is the zero-temperature GL coherence length parallel to the c axis and s is the layer repeat distance, which is equal to half the c-axis lattice constant for a 2H compound. The theory predicts that quasi-two-dimensional critical field effects can be observed for $r \leq 1$, while no decoupling of the layers will occur if $r \gg 1$. In Section

VI.4.5 it is shown that $r \geq 20$ for the compounds $Nb_{1-x}Ta_xSe_2$, indicating that theories which include such quasi-two-dimensional effects are not needed to explain the critical field behavior of these materials.

Several authors have published theories which are essentially generalizations of the weak-coupling isotropic theory of Helfand and Werthamer[136] to include an arbitrary Fermi surface geometry. These theories retain the weak-coupling (BCS) approximation, allow for an arbitrary impurity-scattering rate, but include only orbital pairbreaking; spin effects have not yet been included. The main difference with respect to the isotropic theory is that here the Fermi surface shape and the variation of the electron velocity over the Fermi surface can be ansiotropic.

The theory of Youngner and Klemm,[160] which extends earlier work by Hohenberg and Werthamer,[129] allows for anisotropy of the superconducting energy gap in addition to Fermi surface anisotropy. Youngner and Klemm present results for a model Fermi surface which is a distorted sphere and find that increasing the anisotropy in either the Fermi surface geometry or the gap (or both) causes $H_{c2}(T)$ to first become more linear at low temperatures and then develop positive curvature well below T_c as the magnitude of the anisotropy is increased. Their theoretical curves always remain linear just below T_c, however.[161] Youngner and Klemm did not consider the effects of rotating their model Fermi surface relative to the applied field direction. An interesting result of their work was the discovery that a very large electron scattering rate λ_{tr} is required to remove the the positive curvature and enhanced linearity caused by anisotropy. For one model Fermi surface a

$\lambda_{tr} \approx 50$ was needed. Recalling that $\lambda_{tr} = 0.882\xi_0/\ell$, this implies that materials may display anisotropy effects even when they are quite dirty.

Butler has presented a formalism based on the earlier work of Berthel and Pietrass,[162] and used it to calculate $H_{c2}(T)$ for Nb.[119]* Butler found that gap anisotropy was not needed to obtain a good fit to the experimental data and that strong-coupling corrections to the calculations were small. (For Nb, $\lambda_{ep} = 0.95$.) A clean-limit version of the formalism introduced by Butler has been used in this work to calculate $H_{c2}(T)$ for several Fermi surface models. The results of these calculations, and their relevence to the experimental $H_{c2}(T)$ results for the compounds $Nb_{1-x}Ta_xSe_2$ are discussed in Chapter VII.

The anisotropic theories predict that $H_{c2}(T)$ will still be linear just below T_c.[160,161] In the clean, weak-coupling limit, the slope just below T_c can be shown to be (Appendix D)

$$\left.\frac{dH_{c2}}{dT}\right|_{T_c} = -\frac{16\pi^2}{7\,\zeta(3)}\frac{ck_B^2}{e\hbar}\frac{T_c}{\langle v_\perp^2\rangle}. \qquad (5.23)$$

Here $\langle v_\perp^2\rangle$ is the Fermi surface average of the square of the component of the electron velocity in the plane perpendicular to the field direction. This equation differs from the isotropic formula (Equation 5.15) only in the replacement of v_F^2 by $\langle v_\perp^2\rangle$ and in the numerical

---

* The measured upper critical field field of high quality, single-crystal Nb depends on the field orientation relative to the crystal axes, exhibits enhanced linearity at low temperatures, and a small amount of positive curvature.[109] Nb has a transition temperature of 9.27 K, and an upper critical field at T = 0 of ≈ 4.25 kG. Thus spin effects are unimportant, since $18.6T_c$ is much greater than $H_{c2}(0)$.

factor of 2/3. This is a very reasonable generalization, since only electron motion in this plane is relevant for shielding the magnetic field (confining it to the vortex cores). For a spherical Fermi surface, one readily finds that $\langle v_\perp^2 \rangle = (2/3)v_F^2$, so the isotropic result is recovered. Here v_F will be taken to mean the square root of the Fermi surface average of the square of the electron velocity at each point on the Fermi surface (the rms average). The averaging technique is discussed in Appendix C. For a isotropic Fermi surface, v_F is also the magnitude of the electron velocity at each point on the Fermi surface. (The usual isotropic definition.)

V.5 Strong-Coupling Corrections

As noted above, the BCS theory is quantitatively valid only for superconductors where the electron-phonon interaction is fairly weak. However, all high-T_c superconductors, most materials of technological interest, as well as the compounds $Nb_{1-x}Ta_xSe_2$ are moderately- or strongly-coupled. One approach for describing these materials would be to abandon the BCS theory and calculate the relevant properties using the Eliasberg formalism, which does not include the weak-coupling approximation.[117,163]

This approach is in principle possible, but is mathematically quite difficult, relative to the corresponding BCS calculation. Also, the use of the Eliashberg formalism requires a more detailed knowledge of a material's microscopic properties than is usually available. The full strong-coupling formalism has been successfully used to calculate $H_{c2}(T)$, although to date such calculations have been confined to the

dirty limit.[123]

An alternative approach is to consider the property of interest as a product of the BCS value and a strong-coupling correction factor.[118] The upper critical field can be written as

$$H_{c2}(T) = H_{c2}^{BCS}(T)\eta_{Hc2}(T) \tag{5.24}$$

where the BCS critical field is calculated using one of the theories discussed in Section V.4. This approach is especially useful when the correction factors are close to unity and only weakly temperature dependent, as appears to be the case for the upper critical field.

The correction factors can be calculated from microscopic properties [$\alpha^2F(\omega)$]. However a very useful alternative approach is to calculate the correction factors approximately using results which can be obtained from simple models for $\alpha^2F(\omega)$. Generally, $\alpha^2F(\omega)$ has two main peaks corresponding to the transverse and longitudinal phonon peaks in the phonon density of states. However, the lower peak is more important for determining the superconducting properties. The simplest model for $\alpha^2F(\omega)$ then consists of only one peak, which can be characterized by a single parameter T_c/ω_0, where ω_0 is the frequency characterizing the single peak (in temperature units). The value of the this model is that it allows certain correction factors to be calculated explicitly as functions of only T_c/ω_0. If this parameter can be estimated from other experimental data, the correction factors can be easily calculated.

Model calculations for various enhancement factors have been carried out by Rainer and Bergmann[118] using the Eliasberg formalism. They used both experimental data for $\alpha^2F(\omega)$ and model spectra, including Debye

spectra and combinations of Debye and Einstein spectra. Their results indicate that the values of η_{Hc2} for most real superconductors match the results for simple model spectra quite well. This implies that a simple model spectrum calculation is a valid way to estimate the correction factor when $\alpha^2F(\omega)$ is not known. The values they find for η_{Hc2} are close to, but always greater then, unity; typically η = 1.3 or less even for quite strongly-coupled superconductors ($\lambda_{ep} \simeq 1.5$). Also η_{Hc2} appears to be a rather weak function of temperature. As a quantitative example, for a particular Debye spectrum, $\eta_{Hc2}(T_c) = 1.3$ and $\eta_{Hc2}(0) = 1.22$ for a fairly strongly-coupled material with $\lambda_{ep} \simeq 1.5$. In a calculation for the moderately-coupled material Nb, Butler[119] found $\eta_{Hc2} \simeq 1.11$ and also that η_{Hc2} was only very weakly temperature dependent.

Thus while strong-coupling effects cause $H_{c2}(T)$ to be enhanced, the effect is not very large. Furthermore, since η_{Hc2} is only weakly dependent on temperature, the effect of this correction factor on the shape of the $H_{c2}(T)$ curve is very slight. Since $\eta_{Hc2}(T_c)$ is usually greater then $\eta_{Hc2}(0)$, strong-coupling effects actually tend to depress $H_{c2}(T)$ slightly at low temperatures for crystalline superconductors. Finally, it appears valid, as a first approximation, to calculate η_{Hc2} and other correction factors using fairly simple models. Such calculations are discussed further in Appendix E.

V.6 Surface Superconductivity

In addition to H_{c1} and H_{c2}, type II superconductors can have a third critical field H_{c3} which must be mentioned since it appears to influence the observed transition curves (Chapter VI). It turns out that for

fields oriented parallel to the surface of a superconductor, superconductivity can nucleate at the surface at a field H_{c3}, which is larger than H_{c2}. In the GL theory, $H_{c3} = 1.69H_{c2}$.[106] Between H_{c2} and H_{c3}, superconductivity is confined to a surface sheath of thickness approximately equal to the coherence length.

The existence of surface superconductivity has been confirmed in numerous experiments, and generally H_{c3}/H_{c2} ratios near 1.69 are obtained.[164] As a function of angle between the field and the surface, H_{c3} decreases rapidly as the field moves away from a parallel orientation, becoming equal to H_{c2} at a perpendicular orientation.[165]

V.7 Conclusions

The theory of $H_{c2}(T)$ is fairly well developed, although some difficulties do remain. Most of the experimentally observed phenomena are qualitatively understood and can be explained at some level theoretically. For most superconductors a theory based on the BCS model interaction seems to be sufficient, especially when augmented by the appropriate strong-coupling correction factor.

An important need is for a theory (still based on the BCS theory) which incorporates both spin effects and Fermi-surface anisotropy. Such a theory might be very helpful in trying to understand the apparent lack of Pauli paramagnetic limiting in many high-field superconductors. In this regard, realistic estimates of the enhancement of the Pauli paramagnetic limiting field due to many-body effects and of the spin-orbit scattering rate are also needed. To date the Eliasberg equation

has only been solved for $H_{c2}(T)$ in the dirty limit. It would be very interesting to have solutions applicable for arbitrary mean free paths to compare this result with the known mean free path dependence of the weak-coupling theory.

VI. Superconducting Properties of $Nb_{1-x}Ta_xSe_2$

This chapter describes the transition temperature and critical field measurements which have been made on the compounds $Nb_{1-x}Ta_xSe_2$ and our interpretation of them. These comprise the main body of experimental results reported in this thesis. The zero-field results are discussed first. The observed transition shape is analyzed and T_c versus composition data are presented for the 2H and 4H phases.

The sections which discuss the critical field results also begin with an analysis of the experimentally observed transition curve, which is somewhat more complicated than seen in the zero-field case. The $H_{c2}(T)$ data are then presented for the field oriented both perpendicular and parallel to the layer plane (for the 2H phase) and an attempt is made to infer from the systematics of this data the changes which occur in $Nb_{1-x}Ta_xSe_2$ as a result of varying the composition. Of necessity, this latter program begins with a detailed analysis of superconductivity in $NbSe_2$ itself.

VI.1 Zero-Field Transition

Figure 6-1 shows a typical zero-field transition, measured as described in Chapter IV.* The output signal is flat above the transition and changes smoothly and reasonably symmetrically through the transition. There is a small temperature dependence seen at

---

* No attempt was made to shield the earth's magnetic field for any of the measurements. Thus "zero-field" means here the ambient field present in the laboratory. It will be shown below that such fields produce only a negligible error.

temperatures below the transition, which may, in part, be caused by the temperature dependence of the superconducting penetration depth λ. The curve is reversible; the same X-Y recorder trace is obtained by sweeping the temperature in either direction.

VI.1.1 Definition of the Transition Temperature

The following notation will be used here; T_c shall mean the superconducting transition temperature in an idealized sense, the single temperature which determines the superconducting-normal phase boundary. Since all real materials have transitions of finite width, the temperature corresponding to some characteristic of the experimentally observed transition must be chosen to approximate T_c.

Figure 6-1 indicates how several characteristic temperatures are defined. Three straight lines are drawn as shown: one tangent to the main linear portion of the transition and two extending the output both above and below the transition. The intersection of the transition curve with (another) horizontal line drawn halfway between these latter two lines at the transition defines the midpoint transition temperature T_m. The width of the transition is defined by the intersection of the transition curve with horizontal lines drawn at 10% and 90% of the height of the transition as measured at the midpoint of the transition. Also shown is the definition of T_{ext}, a temperature corresponding to the extrapolated high-temperature end of the transition. The only uncertainty in this procedure concerns drawing the straight line tangent to the output below the transition, since the curve is not exactly flat here. However, the amount of curvature in this region is usually

sufficiently small to cause only a negligible change in T_{ext}, T_m, and W if this lower line is drawn differently.

Most researchers define T_c in terms of the midpoint of the transition, although other temperatures, such as T_{ext}, which characterize either the high-temperature or low-temperature end of the transition are also used. The the midpoint temperature T_m will be used here as it seems to be the best single number for characterizing at what temperature the transition occurs. Another reason for choosing T_m is that T_{ext} cannot always be unambiguously defined when a magnetic field is applied to the sample (Section VI.3.1).

VI.1.2 Zero-field Transition Widths

The observed transition widths vary considerably. The narrowest transitions are approximately 20 mK wide, for the highest quality crystals, while widths in excess of several tenths of a Kelvin have been recorded for crystals of obviously lower quality. Of the 27 crystals selected for H_{c2} measurements, the widths range from 20 mK to 100 mK, with the average width being 56 mK. The transition width is not a function of composition. There is no reason why alloying should cause the transition width to increase, provided the material remains uniform on a macroscopic length scale.

VI.2 T_c as a Function of Composition

Figure 6-2 shows the temperature T_m as a function of composition for both the 2H and 4H phases. These data are tabulated in Table 6-1. The goal of the crystal growth work was to produce good quality 2H crystals for the critical field experiments. However, a number of 4H and mixed phase crystals have been produced as a by-product of the effort to determine the optimum growth conditions for the 2H phase. The transition temperature determined for 4H $NbSe_2$, 6.31 K, agrees very well with values previously reported.[6,69,166]

For the 2H phase, T_m initially increases slightly and then gradually decreases as the Ta content is increased. An overall decrease might be expected, since the transition temperature of 2H $TaSe_2$ is only 0.15 K.[8] The initial increase is caused by suppression of the CDW found in pure $NbSe_2$, as will be discussed below. Because the CDW introduces gaps into the band structure at the Fermi energy, it decreases the total electronic density of states at the Fermi level and thus decreases T_c.* One can speculate that T_m in the absence of a CDW might vary monotonically with composition, and thus the transition temperature of $NbSe_2$ in the absence of a CDW would be between 7.5 and 8 K.

Evidence that T_c increases are correlated with CDW suppression is supplied by studies of T_c and T_o (the CDW onset temperature) in $NbSe_2$ under pressure. These studies have shown that as pressure is applied T_o is depressed.[56] T_c rises relatively rapidly until the CDW is completely suppressed, and then increases much more gradually if the pressure is

---

* See Equation 6.1, the BCS T_c equation.

further increased.[167] Extrapolating from this region of gradual change back to atmospheric pressure, it appears that T_c in $NbSe_2$ in the absence of CDW effects should be slightly less than 8 K. Since $NbSe_2$ is more compressible along the c axis,[168,169] applying pressure will move the layers relatively closer together, presumably increasing the interlayer interaction and making the material more three-dimensional. The resultant changes in the band structure apparently make CDW formation less favorable, thus causing the depression of T_o.

There is a considerable amount of evidence in the literature that the CDW in $NbSe_2$ is suppressed by disorder, either introduced by alloying, or caused by crystalline imperfections. This information, derived from studies of transport properties, was reviewed in Chapter II. Further evidence that the CDW is suppressed by disorder is provided by our observation that the experimentally observed transition curve of low-Ta-content crystals is quite sensitive to crystal damage. The initial procedure for making zero-field T_c measurements involved gluing the samples onto the sapphire sample-mounting rods with a liberal quantity of GE 7031 varnish. Before the T_c measurement, the dipstick cryostat was lowered into the liquid helium storage dewar fairly slowly to conserve the helium. However, after the T_c measurement, the cryostat was usually removed very quickly from the dewar and the sample was rapidly warmed up. With this procedure it was observed that the transition curves of $NbSe_2$ and the low-Ta-content alloy compounds were not reproducible. If the first measurement showed a smooth, narrow transition, subsequent measurements would show a degraded and widened transition with parts of the transition shifted to higher temperatures. (For $NbSe_2$, the high-temperature end of the distorted transition was

typically 7.25 K.) This type of behavior was never seen for samples with compositions to the right of the peak in the T_m vs. composition curve. It appears that the combination of rigid bonding to the sapphire rods and a rapid warmup damaged the crystals due to stress caused by a mismatch in the rates of thermal expansion. This damage appears to supress the CDW present in the low-Ta-content alloys, accounting for the shift of the transition to higher temperatures.*

Given that both band structure changes and crystalline disorder can suppress the CDW, the question remains as to which mechanism is more important in the compounds $Nb_{1-x}Ta_xSe_2$. Since both of these phenomoma occur here, it is not possible to definitely rule out one mechanism in favor of the other. However, it may be useful to note that the CDW in $TaSe_2$ is of considerably larger magnitude then in $NbSe_2$ (Chapter II). If alloying Ta into $NbSe_2$ produces a smooth and reasonably monotonic change toward the $TaSe_2$ band structure, from band structure considerations alone it might be expected that the CDW would get stronger upon alloying. To the extent that this is true, the lattice-disorder effect must be considered the more important cause of the CDW suppression.

The observed variation of T_m as a function of composition can thus be understood as resulting from the interaction of two somewhat different phenomena. Alloying both gradually changes the band structure, which in this system tends to lower T_c, and it also suppresses the CDW which tends to increase T_c. From the position of the peak in the T_m data, it appears that the CDW is largely suppressed at a composition of

---

* As discussed in Section IV.2.4, this problem was solved by slower thermal cycling and by mounting the crystals with a minimum quantity of softer rubber cement.

about $Nb_{.96}Ta_{.04}Se_2$.

It also appears that lower T_c's for $NbSe_2$ indicate a higher quality crystal. However, some caution is necessary, since it is known that T_c is also depressed in off-stoichiometry, Nb-deficient material.[69] As was discussed in Chapter III, growing the crystals in the presence of excess selenium should insure the correct stoichiometry, so lower T_c's can probably be safely taken as indicative of higher quality crystals if this precaution has been taken. T_m for our better $NbSe_2$ crystals ranges from 6.99 to 7.05 K.

VI.2.1 CDW Effect on the Electronic Density of States

Given the various estimates for the transition temperature of $NbSe_2$ in the absence of CDW effects, it is possible to crudely estimate the change in the density of states at the Fermi energy N(0) caused by the CDW. This can be done using the BCS transition temperature equation[106]

$$T_c = 1.13\theta_D \exp\left[\frac{-1}{N(0)V}\right] . \qquad (6.1)$$

Here V characterizes the strength of the attractive (phonon-mediated) electron-electron interaction, and θ_D is the Debye temperature. θ_D has been measured for $NbSe_2$ by several researchers, and it appears that the correct value is close to 220 K.[85,170] Using this value and taking T_c = 7.01 K and N(0) = 3.6 states/(eV-molecule)[170] yields V = 0.08 eV. Assuming that V and θ_D remain unchanged as the CDW is suppressed, the change in N(0) can be calculated from the change in T_c. Of course, it

is not obvious what T_c should be for this hypothetical CDW-free $NbSe_2$. The highest T_c reported for $NbSe_2$ is 7.40 K.[133,171] Assuming that this is the CDW-free-state T_c, the change in N(0) is 1.5%. Extrapolations of the pressure and composition dependence of T_c mentioned above imply that a somewhat higher CDW-free T_c, approximately 7.75 K. Using this number, a change in N(0) of 2.8% is obtained. These estimates are fairly crude, but they do imply that the CDW in $NbSe_2$ imposes a rather small perturbation on the electronic structure.

VI.2.2 Other Measurements of T_c

Given the sensitivity of T_c of $NbSe_2$ to disorder, primarily through the effect of disorder on the CDW, it is not surprising that a number of different T_c's have been reported previously. Literature values range from about 6.95[172] to 7.40[133,171] (ignoring anomalously low values which appear to be caused by off-stoichiometry or other severe crystalline imperfection). In several cases a range of T_c values are reported along with a measure of crystal quality, and lower T_c values have been shown to be correlated with higher residual-resistance ratios[40] and longer electron mean free paths,[173] again implying that lower T_c's indicate a higher quality crystal.

The critical fields of the compounds $Nb_{1-x}Ta_xSe_2$ have also been studied by Ikebe, Katagiri, Noto, and Muto.[75] Their T_c results are roughly similar to those obtained here and are included in Table 6-1. They measured the transition resistively, and took T_c to be the extrapolated temperature at which resistance first appears, the extrapolated low-temperature end of the transition. While this

measurement technique and T_c-defining criterion differ from those used here, it has been pointed out by Prober, Schwall, and Beasley[14] that in general, the low-temperature end of a resistively-measured transition approximately corresponds to the high-temperature end of a transition measured by a susceptibility technique. Thus the corresponding pairs of T_c values in Table 6-1 should ideally agree closely (within ≈ ½ the transition width). It is interesting to note that Ikebe et al. report the same T_c for both the 2H and 4H phases for the composition $Nb_{.80}Ta_{.20}Se_2$. This is contrary to our results and may be the result of their resistivity measurements being fooled by a mixed-phase crystal.*

VI.2.3 Selection of Samples for H_{c2} Measurements

Over the course of this work, the transition temperatures of several hundred crystals have been measured. The usefulness of the information obtained from these measurements for the crystal growth work was discussed in Chapter II. Transition temperature measurements have also been used as the primary tool for selecting crystals for use in the critical field experiments. Only those crystals with the narrowest and smoothest transitions were selected. It has also been required that T_c be close to the correct value for that composition, as determined self-consistently using crystals from many different crystal growth batches. Crystals displaying any structure in the zero-field transition curves have been avoided for the $H_{c2}(T)$ measurements as experience has shown that any bump, or abrupt change of slope in the zero-field transition

---

* The crystal growth conditions used by Ikebe et al. are discussed in Section III.3.3. Under their conditions it would be very difficult to grow pure 2H $Nb_{.80}Ta_{.20}Se_2$.

curve will invariably get much worse in large dc fields. Crystals selected for $H_{c2}(T)$ measurements have also been inspected carefully under a microscope. Only very flat, reasonably perfect single crystals have been used. Crystals are rejected if they show any evidence of twinning or of being bent or otherwise damaged.

VI.3 The Transition Curve in dc Fields

Figure 6-3 shows a typical transition curve recorded with a field of 21.6 kG oriented perpendicular to the layer plane.* At temperatures above the transition, the output is flat as for the zero-field case. Again the sample goes through a transition of finite width, but the signal at lower temperatures, where the sample is in the mixed state, is quite different. In the first place, the curve is not flat below the transition, indicating a partial, temperature-dependent ac field penetration into the sample in the mixed state. There is also an intrinsic hysteresis below the transition. If initially the temperature is well below the transition, and the temperature is swept up and then down again, a transition curve will be generated as shown by the solid line in Figure 6-3. If on the temperature-decreasing branch below the transition the direction of the temperature sweep is reversed (increasing the temperature), the output will move from the lower (temperature-decreasing) branch to the upper (temperature-increasing) branch, as shown by the dotted line in Figure 6-3. The hysteresis seen is independent of the speed with which the temperature is swept.**

---

* In this section and below, only the 2H phase will be discussed.
**This assumes that the sweep speed is slow enough for the sample and thermometer to remain effectively in thermal equilibrium.

Figure 6-4 shows a transition curve of a particular sample with a field of 65 kG oriented parallel to the layer plane. Only the temperature-increasing trace is shown here. This transition is quite similar to the perpendicular-field transition, except that above the main transition the output has a non-zero slope over a certain temperature interval. At higher temperatures the output is again flat. This new feature is probably caused by surface superconductivity, which certainly should be suspected since the field here is oriented parallel to the face of the crystal. If the temperature at which the output does become flat (denoted $T_{c3}(H)$) is recorded, then the field defined by this temperature behaves roughly as H_{c3} should, that is H_{c3}/H_{c2} is approximately constant. The Ginzburg-Landau theory predicts that[106] $H_{c3} = 1.695H_{c2}$. Here a value of about 1.55 is obtained.

A very similar effect is sometimes, although not always, observed in transitions where the field is oriented perpendicular to the crystal. Microscopic examination of the crystals showing this effect reveals that they all have a sloping edge, probably where they grew attached to the crystal-growth-tube wall. This phenomena associated with these crystals is probably caused by these edges and is possibly a surface superconductivity effect.[165]

VI.3.1 Definition of the Transition Temperature

Figures 6-3 and 6-4 also show how the transition temperature is defined for the transitions occurring in applied dc fields. For both field orientations the transitions always have a linear section, and a line is drawn tangent to the curve through this section. The temperature

corresponding to the middle of the region over which the straight line lies on top of the output curve is defined to be the midpoint temperature T_m'. The symbol T_m' is used since this temperature is defined in a different way than T_m is defined for the zero-field transitions. However, when T_m' is determined for a zero-field transition, it always agrees with T_m to within a few mK.* So for the zero-field case, the two definitions of the midpoint temperature are essentially equivalent.

The presence of surface superconductivity in the parallel-field transitions, and the occasional presence of a similar effect in the perpendicular-field transitions makes it very difficult to define an extrapolated transition temperature T_{ext} (as in Figure 6-1). To define T_{ext} it is necessary to draw a line tangent to the output above the transition, and the problem is with the placement of this line. For small fields, $T_{c3}(H)$ is very close to T_m', the two differing by less than the width of the main transition. Thus there is no evidence of surface superconductivity, and T_{ext} can be defined as in the zero-field case. For large fields, T_{c3} is much higher than T_m', and the only reasonable way of defining T_{ext} is to draw the "horizontal" line tangent to the slightly sloping output curve between the main transition and $T_{c3}(H)$. To draw this line tangent to the flat output above $T_{c3}(H)$ produces unreasonably high values for T_{ext}, values which clearly are at higher temperatures than any feature of the main transition. The problem therefore is that the definition of T_{ext} must be changed at some aribitrary point during the data analysis as $T_{c3}(H)$ pulls away from the

---

* Assuming a reasonably good quality crystal is used for the test; one with a smooth, structureless transition.

main transition. For this reason, no attempt has been made to record T_{ext} for the parallel-field data. It has only been recorded, where possible, for the perpendicular-field orientation. In any event, the midpoint temperature T_m' is probably the best single number for characterizing at what temperature the transition occurs.

VI.3.2 Other Published Transition Shapes

The upper critical field of $NbSe_2$ has been studied by a number of other researchers, some of whom have published their raw transition curves. Transitions measured resistively, obtained by sweeping the field at a constant temperature, have been reported by Morris, Coleman, and Bhandari,[134] and by Toyota et al.[133] In both cases no hystersis was seen in the mixed state. However, ac susceptibility measurements at 125 kHz by Leupold et al.[174] produced transitions which show a hysteretic behavior very similar to our transitions. Leupold et al. swept the temperature in a fixed dc field (as we do), in contrast to the swept-field method. Finally, the transition curve published by Foner and McNiff[171] measured with a swept-field technique using an rf loss detection scheme looks very similar to our temperature-increasing curve in that it displays a dip before the transition. It is not clear if Foner and McNiff swept the field in both directions, so it is not clear if their transition curve was hysteretic.

VI.3.3 Discussion of the Hysteresis

The hysteresis in the mixed state (at temperatures below the main transition) is apparently only seen when the transition is measured with an ac susceptibility technique. Thus it is probably caused by an interaction between the small-amplitude ac measuring field and the surface of the superconductor. It is possible to provide a tentative explaination of the hysteresis based on the concept of an intrinsic surface barrier to flux entry.

The existence of an energy barrier to flux entry at a surface was originally proposed theoretically by Bean and Livingston.[175] The basic physical idea is that a fluxoid (flux vortex) just inside the surface of a superconductor experiences two forces, which are in opposition. The vortex interacts with the diamagnetic screening currents flowing at the surface. This interaction tends to move the vortex into the body of the superconductor. This force can also be considered to arise from the field gradient present at the surface, and depends upon the magnitude of the external field. The second force arises from the interaction of the surface with the shielding currents flowing around the core of the vortex itself. This force tends to pull the vortex toward the surface. Both of these forces decay exponentially in magnitude as the vortex moves into the superconductor, but with slightly different spacial dependencies. The result of this is that there can be a potential energy barrier to flux entry. The field will not enter the superconductor at the external field strength at which it should according to an ideal magnetization curve, but only at some higher field at which the larger field gradient can overcome the barrier. Considering the Meissner state

of a type II superconductor, Bean and Livingston found that the barrier field was approximately H_c (the thermodynamic critical field, which is less than $H_{c2}(T)$ for a type II superconductor).

The theory of the surface barrier has been extended into the mixed state of a type II superconductor by Clem.[176] It is well established experimentally that surface barriers to flux motion do exist.[177,178,179] For a type II superconductor in the mixed state the barrier depends on the direction of the flux motion. The barrier for flux leaving the sample is very small, if not negligible, while the barrier for flux entry is relatively larger.[176,179,180] The magnitude of the barrier decreases with increasing dc field and appears to vanish at $H_{c2}(T)$.[178,179,181] Surface conditions are important, as small surface irregularities can produce local field variations which can significantly reduce the effective barrier field.[177]

Assuming a surface barrier exists in the compounds $Nb_{1-x}Ta_xSe_2$, the hysteresis seen in Figure 6-3 can be explained as follows. As the temperature is increased in a fixed dc field flux votices move into the sample. Assuming that a surface barrier exists a small distance inside the material, it is reasonable to assume that flux will pile up at the surface, increasing the surface magnetic field above the equilibrium value. This will reduce the superconducting order parameter at the surface, making the surface appear more normal. If the barrier to flux exit is negligible, the field distribution and surface order parameter should be close to their equilibrium values during the temperature-decreasing sweep, when vortices are moving out of the sample. If we assume that the small amplitude ac field probes (predominantly) the

surface of the sample, the temperature-increasing sweep should show an offset in the direction of a more normal-state-like frequency shift, as is seen in Figure 6-3. In this model the temperature-decreasing sweep corresponds most closely to equilibrium conditions. The dip seen in the temperature-increasing sweep just below the main transition may be caused by the vanishing of the surface barrier at T_c.

For measurements of $H_{c2\perp}(T)$, the ac and dc fields are coaxial, and the model described above is most easily visualized. However, when the dc field is oriented parallel to the layer plane, there will still be some sections of the sample where the ac field will be impinging upon a surface parallel (or nearly parallel) to the dc field.

In connection with hysteretic magnetic phenomena in type II superconductors, flux pinning is also usually considered. It is impossible to rule out some influence of flux pinning on our data. Specifically, the dip seen in the temperature-increasing sweep just below T_c may be related to the peak effect.[182] However, it is not obvious how flux pinning could produce hysteresis in the direction seen in Figure 6-3. Also, flux pinning may be relatively unimportant in reasonably clean materials at the frequencies used here.[183]

The explaination presented here for the hysteresis is only a suggestion, but it appears to be a plausible explaination of this particular feature of the transition curves. The model presented is in general agreement with the results of a tunneling study involving Nb_3Sn which showed a hysteretic suppression of the superconducting order parameter when a dc magnetic field was applied parallel to the junction. The order-parameter suppression was found to be greater when the dc

field was being increased than when it was being decreased.[184,185]

Outside of the TMDC studies refered to above,[171,174] the literature does not contain many reports of measurements of $H_{c2}(T)$ using ac susceptibility techniques where the raw transition curves have been published. However, transition curves showing hysteresis qualitatively similiar to that seen in Figure 6-3 have been reported in other systems.[186]

VI.3.4 Transition Widths in Applied dc Fields

Because the observed transition shape in a field is different from the zero-field shape, it is not possible to precisely define the width in the same manner. However, estimates are possible using essentially the same criterion. The transition widths tend to increase uniformly with the applied field. At the lowest temperatures (≈ 1.4 K), and thus at the highest fields, widths for the perpendicular-field orientation typically increase to about 0.13 K while widths in the parallel direction increase to about 0.2 K.

VI.4 $H_{c2}(T)$ as a Function of Composition and Field Orientation

The purpose of this section is to discuss the $H_{c2}(T)$ curves obtained for fields oriented parallel $H_{c2\parallel}(T)$ and perpendicular $H_{c2\perp}(T)$ to the layer plane. All the data discussed here will be based on defining H_{c2} by T_m', except where explicitly noted. Also, T_c shall mean the zero-field transition temperature unless a field dependence is shown explicitly.

Figures 6-5 and 6-6 show the perpendicular and parallel critical fields of a crystal of composition $Nb_{.01}Ta_{.99}Se_2$. These curves are representative of all the compositions studied. Also shown in each figure is the temperature dependence of the theoretical isotropic clean-limit curve, scaled by an adjustable factor for each orientation to obtain good agreement at intermediate temperatures.* To lowest order, the parallel and perpendicular critical field curves have the same shape, the main difference being that the parallel critical fields are larger by a factor of about 3. For both directions $H_{c2}(T)$ displays extended linearity at low temperatures, lying above the isotropic curve. Also, positive, or upward, curvature is observed just below T_c. In Chapter V it was pointed out that there are several mechanisms which can cause these effects. There it was argued that in the $Nb_{1-x}Ta_xSe_2$ system these effects, along with the gross dependence of H_{c2} on the orientation of the sample in the magnetic field, are caused by anisotropy, primarily anisotropy of the Fermi surface.

Figures 6-7 and 6-8 show $H_{c2}(T)$ for two more compositions, illustrating that $H_{c2}(T)$ doesn't change dramatically as the composition is varied. Figure 6-7 shows our results for $NbSe_2$, which are similar to previously published results.[133,171] Figure 6-8 shows the parallel critical field of a sample of $Nb_{.95}Ta_{.05}Se_2$, and is noteworthy because it illustrates the apparent lack of Pauli paramagnetic limiting seen in these materials.* As discussed in Chapter V, the simple Pauli limiting

---

* If the isotropic dirty-limit theoretical curve were used here, the discrepancy at lower temperatures would be even larger.

* Given the trends in the transition temperatures and the critical field slopes, the apparent lack of Pauli paramagnetic limiting is most pronounced for compositions near $Nb_{.95}Ta_{.05}Se_2$.

field is given by $18.6T_c$ kG, although many-body corrections and spin-orbit scattering will modify this number somewhat. For this sample, T_m = 6.84 K and a dashed line at 18.6×6.84 = 127 kG has been drawn in Figure 6-8. The experimental points clearly exceed this simple limit and, in fact, show no strong tendency to curve toward the field axis down to 1.53 K.

Figure 6-9 shows the perpendicular critical field data for a particular sample with H_{c2} defined by both T'_m and T_{ext}. (At each field value the higher temperature is T_{ext}.) The shape of the curve is nearly the same for both definitions; the only difference is a temperature offset approximately equal to half the width of the transition. The two sets of data points do separate somewhat more at lower temperatures as the width of the transition increases. Thus if $T_c(H)$ were defined by T_{ext}, the main difference would be that $H_{c2}(T)$ would display slightly more enhanced linearity at low temperatures. However, the basic conclusions to be drawn from the data regarding, e.g., extended linearity and positive curvature, are independent of exactly how $H_{c2}(T)$ is defined.

VI.4.1 Positive Curvature Just Below T_c

An unusual feature of all the $H_{c2}(T)$ data is the apparent absence of linearity just below T_c. In order to study $H_{c2}(T)$ in this region in more detail, it is convenient to plot the data in a way which emphasizes the deviations from the overall linear behavior seen in $H_{c2}(T)$. To do

this it is useful to define a quantity ΔH as shown in Figure 6-10.* The experimental $H_{c2}(T)$ data points always exhibit a nearly linear region at intermediate temperatures. A straight line can be fit to the data over this temperature interval (with a least-squares technique). ΔH is defined as the difference between the actually measured data points and the straight-line fit. Figure 6-10 also shows how the amount of positive curvature (PC) is quantified, as the difference between the measured and extrapolated zero-field transition temperatures.

Figure 6-11 shows ΔH for a sample of composition $Nb_{.98}Ta_{.02}Se_2$ with the field oriented both parallel and perpendicular to the layer plane. ΔH is positive just below T_c, is approximately zero at intermediate temperatures, and becomes negative at lower temperatures (not shown in this figure) as $H_{c2}(T)$ bends towards the field axis. Figure 6-12 shows ΔH for two more samples.

When looked at in this way, it appears that the critical field curves may be linear over a narrow temperature interval just below T_c, as evidenced by the apparent linearity of the highest-temperature points in Figures 6-11 and 6-12. In this respect the parallel and perpendicular critical fields behave in the same manner. This interpretation is certainly not demanded by the data, but it seems possible, and is agreeable in light of the theoretical expectations that $H_{c2}(T)$ should be linear just below T_c.[160,161] If this is correct, then the slope of $H_{c2}(T)$ just below T_c, from which the Ginzburg-Landau coherence length can be extracted, is not the slope of the main linear

---

* For clarity, the "experimental data" in this figure are represented by an exaggerated curve drawn schematically.

section of the $H_{c2}(T)$ data (the part to which the line was fit in Figure 6-10). Rather, the "correct" slope, which is smaller in magnitude, can only be determined by making measurements very close to T_c.

It is worth noting that the data presented in Figures 6-11 and 6-12 have been obtained by making very detailed measurements at low fields. It was necessary to record the transition temperatures with milliKelvin precision to avoid unnecessary scatter in the data. The relatively small amount of scatter seen in these figures tends to justify the procedure outlined above for determining T_m' as being a quite precise and reproducible way of measuring the transistion temperature, even if in principle it is a somewhat arbitrary definition.

Figure 6-13 shows the amount of positive curvature seen in the parallel and perpendicular critical field data plotted as a function of composition. Figures 6-14 shows the same thing, except here the zero-field transition width is plotted on the abscissa. The zero-field transition width may be taken as a simple measure of crystal quality. Although there is some scatter in the data, it appears that for both field orientations the amount of positive curvature seen decreases as the composition is varied, while there appears to be no correlation with the zero-field transition widths. This implies that the positive curvature is an intrinsic property and is not caused in any way by sample inhomogeneities. It is worth noting that positive curvature is seen over a temperature interval significantly larger then the transition width.

VI.4.2 Anisotropy as a Function of Temperature

Figure 6-15 shows the anisotropy in the critical fields $H_{c2\parallel}/H_{c2\perp}$ as a function of temperature for two compositions. These curves were obtained by using the actual $H_{c2\parallel}(T)$ data points and by obtaining $H_{c2\perp}$ values at the relevant temperatures by interpolating from the measured $H_{c2\perp}(T)$ data. In both cases the anisotropy is nearly constant at low temperatures, but fall off just below T_c due to the relatively greater amount of positive curvature seen in the parallel critical field data. Anisotropy data are only available to very low temperatures for those samples where $H_{c2\parallel}(T)$ was measured at the National Magnet Lab. That the ratio $H_{c2\parallel}/H_{c2\perp}$ remains almost constant to the lowest temperatures in these materials is another indication of the apparent lack of Pauli paramagnetic limiting in the parallel critical fields.

If $H_{c2}(T)$ is linear in (T_c-T) just below T_c for both field orientations, then the ratio $H_{c2\parallel}/H_{c2\perp}$ should be a constant just below T_c. As shown in Figure 6-15, for some samples the anisotropy continues to decrease as T approaches T_c, while for others it does appear to become constant close to T_c. No trend is seen as a function of composition. However, there is a relatively large amount of uncertainty for points where $T \approx T_c$ since $H_{c2\parallel}/H_{c2\perp}$ becomes the ratio of two small numbers close to T_c. Therefore, it is difficult to draw any firm conclusions regarding the behavior of the anisotropy just below T_c, although it is quite clear that $H_{c2\parallel}/H_{c2\perp}$ is almost constant at the lowest temperatures and does fall off considerably as T approaches T_c.

VI.4.3 Anisotropy in the Basal Plane

The possibility that $H_{c2}(T)$ may be anisotropic in the basal plane was explored by measuring the parallel critical field for two samples twice, the second time with the crystals rotated by 30° around their c axes relative to their position for the first measurement. Within the experimental resolution, no anisotropy was found in the basal plane. This result is consistent with other measurements of the critical fields of TMDC's[14] and is also consistent with the basal plane isotropy found in the de Haas-van Alphen work done on $NbSe_2$,[47] and the nearly circular cross-sections of the calculated Fermi surface.[19]

VI.4.4 Anisotropy as a Function of Composition

Figure 6-16 shows the anisotropy as a function of composition at a reduced temperature $t = T/T_c = 0.5$, where the anisotropy is relatively temperature independent. The anisotropy increases with increasing Ta content and is a minimum for pure $NbSe_2$. Generally it is assumed that making a material dirtier will make its properties more isotropic.[129,160] This is because as the electron mean free path (mfp) is shortened the electrons are scattered more frequently to other states on the Fermi surface. As this scattering rate increases, anisotropy effects which arise from the different properties of electron states on different parts of the Fermi surface should eventually become washed out. It will be shown below that alloying does reduce the electron lifetime in the $Nb_{1-x}Ta_xSe_2$ system (Section VI.5.3). Thus, this argument predicts that increasing the Ta content should decrease the anisotropy, contrary to the experimental result.

A mechanism has been proposed which could cause the anisotropy to increase as the electron scattering rate increases in materials which are not extremely dirty.[75] For $NbSe_2$ it appears that the electron lifetime in the layer plane exceeds the electron lifetime for motion parallel to the c axis, although quantitative estimates of the ratio are difficult (Section VI.5.2). Thus, $NbSe_2$ may be a relatively clean material for intralayer electronic motion, which determines $H_{c2\perp}(T)$, and somewhat dirtier for interlayer electron motion, which partially determines $H_{c2\parallel}(T)$. Decreasing the electron lifetime increases $H_{c2}(T)$, but the effect is of larger magnitude in materials which have shorter electron lifetimes to begin with (Figure 5-4). It is therefore possible that increasing the Ta content may reduce the electron lifetimes in such a way that $H_{c2\parallel}$ is increased faster than $H_{c2\perp}$, resulting in an increase in the anisotropy.

The observed increase in the anisotropy may also be caused partially by band structure changes. In Chapter II it was pointed out that $NbSe_2$ and $TaSe_2$ have very similar crystal structures, the main difference being that the c-axis lattice constant is slightly larger in $TaSe_2$; 12.71 Å vs. 12.54 Å for $NbSe_2$. It is reasonable to assume that alloying Ta into $NbSe_2$ increases the c-axis lattice constant in a monotonic fashion. This has the effect of increasing the separation between the planes of metal atoms, and thus may, to lowest order, have the effect of decreasing the interlayer interaction, making the material more anisotropic. This would increase the critical field anisotropy. This interpretation is supported by the observation that the CDW is much

stronger in $TaSe_2$ than in $NbSe_2$.* A more two-dimensional band structure is presumably more favorable to CDW formation, thus a stronger CDW implies that the interlayer interaction is relatively weaker in $TaSe_2$. However, the distance between the planes of metal atoms increases only by 0.085 Å in going from $NbSe_2$ to $TaSe_2$. This implies that band structure changes in the series of compounds from $NbSe_2$ to $Nb_{.80}Ta_{.20}Se_2$ may be slight.

VI.4.5 Slope as a Function of Composition

The behavior seen in the anisotropy as a function of composition can be viewed from another perspective by examining the slope of the linear section of the $H_{c2}(T)$ curve as a function of composition. As noted above, there are two slopes which can be defined. There is clearly a large linear region at intermediate temperatures, typically over a reduced temperature range of t = 0.5 to 0.8. However, it appears that $H_{c2}(T)$ may also be linear in a small region just below T_c. Assuming that this is the case, Figure 6-17 shows the slopes of these two linear sections as a function of composition for the parallel critical field data, and Figure 6-18 shows the same thing for the perpendicular critical field data. The slopes are also shown in Tables 6-2 and 6-3. Table 6-2 compares our $NbSe_2$ results with previously published values. (The slopes listed in Table 6-2 are for the main linear section of the $H_{c2}(T)$ curve, as that is what other workers generally present.) Our slopes and T_c's tend to be somewhat lower. Given the effect of the CDW on the superconducting transition temperature (Section VI.2), this may

* The CDW onset temperatures are discussed in Section II.3.2.

imply that our samples are of higher quality. Table 6-3 contains both our results for the alloys and also the results of Ikebe et al.[75]

Using these measured slopes it is possible to estimate the extent to which the "zero-field" transition temperature measurements are depressed by the presence of the earth's magnetic field. This field is approximately 1 gauss, and thus introduces a quite negligible shift of a fraction of a millikelvin. It is also possible to calculate the Ginzburg-Landau coherence length perpendicular to the layer plane from the slopes using Equations 5.8 and 5.9. Using the measured slopes (the "just-below-T_c" values) the GL coherence lengths perpendicular to the layer plane $\xi_c(0)$ are found to lie in the range 25-30 Å for the compositions studied. Since these values are considerably greater than the layer-to-layer repeat distance (6.27 Å for $NbSe_2$), it seems unlikely that the compounds $Nb_{1-x}Ta_xSe_2$ would display any quasi-two-dimensional critical field behavior. This assumption can be quantified by using the KLB theory parameter r, which measures the degree of interlayer coupling (Section V.4.3). With the values of $\xi_c(0)$ listed above, $r \geq 20$, indicative of three dimensional critical field behavior. (r must be approximately unity or less to see quasi-two-dimensional critical field behavior.)

The critical field slopes discussed above have been determined by a least-squares fit of a straight line to the data, those data points included in the fit being chosen by visual inspection. There is considerably more scatter in the data for the slopes just below T_c, because an accurate determination of this quantity requires careful measurements at very low fields. Such measurements were not made on all

the samples, since at the beginning of this investigation it was not obvious that this region would be of particular interest. In any event, the two slopes seem to behave in the same way as the composition is varied, the main difference being that the slope of the main linear section is larger in magnitude. This difference in slopes is greater for the parallel critical field data, reflecting the greater amount of positive curvature observed for this field orientation.

For both field directions the slope initially increases as the Ta content is increased. This initial increase can be ascribed to changes which accompany suppression of the CDW. At larger Ta concentrations, for $x > 0.03$, the slopes change more slowly and behave somewhat differently for the parallel and perpendicular field orientations. This change in behavior occurs at a composition of about $Nb_{.97}Ta_{.03}Se_2$. This provides another estimate of the composition at which the CDW is essentially suppressed.

For the perpendicular field orientation, the slopes at higher Ta concentrations clearly decreases, if only slightly. For the parallel orientation the slopes remain nearly constant, although they may increase slightly. To understand what causes this behavior, it is helpful to recall from Chapter V how various physical parameters affect the slope dH_{c2}/dT. While it was not possible to present a totally general formula, the qualitative behavior is clear. The magnitude of the slope should increase with T_c, increase as the electron lifetime is decreased, and increase if the Fermi surface average $\langle v_\perp^2 \rangle$ decreases.

Since T_c is an isotropic quantity, it obviously cannot explain the different behavior seen in the slopes for the two field directions.

Since all of the theoretical slope formulas listed in Chapter V depend linearly on the zero-field transition temperature, it is probably safe to assume this functional dependence on T_c is universally true. Therefore it is useful to normalize out T_c variations by plotting

$$-\frac{1}{T_c}\frac{dH_{c2}}{dT}\bigg|_{T_c} . \qquad (6.2)$$

This quantity should only be a function of the electron scattering rate λ_{tr} and the band structure. This normalization does not totally eliminate the T_c dependence since λ_{tr} depends on T_c as well as the electron lifetime (Equation 5.12). However, the dependence of the slope on T_c through λ_{tr} is weak for cleaner materials (Figure 5-4). The slopes normalized in this way are shown in Figure 6-19 for the slope of the main linear section of the $H_{c2}(T)$ curves. The quantity increases only very slightly for the perpendicular-field orientation, while the increase is somewhat more pronounced for the parallel-field data. The changes which are seen are consistent with the anisotropic electron lifetime effect discussed in Section VI.4.4. From the data it is clear that the changes seen as a function of composition are small in magnitude, especially for the perpendicular critical field data.

Because of the apparent smallness of electron lifetime effects, it is important to consider how band structure changes may affect the slopes. It is quite simple to see how a change in the band structure, and thus in the Fermi surface topology, can generally affect $H_{c2}(T)$ differently in two orthogonal directions. For an anisotropic superconductor, the calculation of $H_{c2}(T)$ depends upon a Fermi surface

average of the component of the electron velocity in a plane perpendicular to the field direction. A general Fermi surface change will alter both the magnitude and the direction of the electron velocity. The shift in direction implies that the components of $\vec{v}_F(\vec{k})$ in two orthogonal directions will be affected differently. It is therefore quite possible that the component in one direction could decrease while the component in the orthogonal direction could increase.

The the behavior seen in Figure 6-19 can be reasonably explained in a qualitative manner by including band structure and mfp effects. It appears that increasing the Ta content makes the band structure more anisotropic, which tends to increase the parallel critical field and decrease the perpendicular critical field. Alloying also shortens the mfp, which should increase $H_{c2}(T)$ for both field directions, although a greater increase should be seen in $H_{c2\parallel}(T)$. The net result could be constant behavior in the perpendicular slope and a small increase in the parallel slope as the Ta content is increased (with T_c variations largely normalized out). The effects which accompany changes in composition appear to be fairly small. The smallness of the band structure effect is consistent with the very similar crystal structures of $NbSe_2$ and $TaSe_2$, while the apparent smallness of the mfp effect is surprising, as will be discussed below.

VI.5 Analysis of the Critical Field Data

The various parameters which describe the critical fields, such as the slopes and the anisotropy, do not change greatly as the composition is varied. It was suggested above that the changes that are seen can be

explained by incorporating T_c, mfp, and band structure effects. The purpose of this section is to quantify this analysis as much as possible. It is of interest to calculate how clean $NbSe_2$ is, and to what extent varying the composition changes it into a dirty superconductor. In addition, estimates are made of several fundamental parameters of the superconducting state, including the electron-phonon coupling constant λ_{ep} and the BCS coherence length ξ_0. Emphasis will be placed on $NbSe_2$, since many of its properties have been measured, making such calculations possible. However, even for $NbSe_2$ the calculations must remain incomplete since many of its properties have only been measured for electron motion in the basal plane.

There is a unique problem which arises when attempting to calculate quantities such as ξ_0 and λ_{ep} for anisotropic superconductors. The usual definitions of these quantities contain an implicit assumption of isotropy, so the definitions must be generalized to the anisotropic case. For instance, the standard definition of the coherence length is

$$\xi_o = \frac{\hbar v_F}{\pi\Delta(0)} = \frac{\hbar}{\pi 1.764 k_B} \frac{v_F}{T_c} \tag{6.3}$$

where v_F is the Fermi velocity and $\Delta(0)$ is the zero-temperature energy gap (within the BCS theory $\Delta(0) = 1.764 k_B T_c$). This can be generalized by assuming that $\Delta(0)$ is an average gap and that v_F should be interpreted as the rms Fermi surface average of the electron velocity, as discussed in Chapter V and Appendix C. This obvious and simple way of generalizing the definition has the advantage that ξ_0 remains a scalar quantity. However, it is far from obvious that it is correct in the

sense of being an acceptable generalization for all purposes.

Similar problems arise with the electron-phonon coupling constant λ_{ep}. Fundamentally, this parameter measures the effect of the electron-phonon interaction on the electronic band structure. It is hard to imagine how this quantity could be isotropic in a material with anisotropic electronic states and anisotropic phonon dispersion curves. Further evidence for anisotropy is implied by recent theories which allow λ_{ep} to be estimated directly from transport[187] and optical[188] properties, quantities which certainly can be anisotropic.

For $NbSe_2$ it will only be possible to estimate the ξ_0 and λ_{ep} which refer to electronic motion in the basal plane. This is because the relevant normal-state properties are only available for this direction of electronic motion.

VI.5.1 Normal-State Properties of $NbSe_2$

To analyze the slope of the critical field curves of $NbSe_2$ requires a knowledge of certain normal-state parameters, such as the Fermi velocity v_F, the electron lifetime τ, and the electron-phonon coupling constant λ_{ep}. These quantities can be estimated using published experimental values for various properties such as the resistivity, the heat capacity, and the optical reflectivity. A calculation of the relevent normal-state parameters is contained in Appendix F and the results are presented in Table 6-4. There is some disagreement among the several estimates of v_F, reflecting the general difficulty of obtaining accurate estimates of this quantity. It must be stressed that

the calculations are of an approximate nature, being largely based on free-electron-type analysis, and that the values for v_F, τ, and λ_{ep} refer only to electron motion in the basal plane. However, specifically because these estimates refer only to electronic motion in the basal plane, they may be reasonably accurate. The experimental and theoretical evidence indicates that electronic motion in the basal plane is quite isotropic. Also, the chemical bonding in this plane is of a fairly normal metallic type, although of a d-band variety. Therefore the free electron approximation may be more valid when used in this restricted manner then when used in any way which, implicitly or explicitly, involves electronic motion perpendicular to the layer plane.

Also included in Table 6-4 is the Fermi velocity calculated form the $NbSe_2$ band structure proposed by Wexler and Woolley, as discussed in Chapter VII. This quantity is an average over the entire Fermi surface and does not refer only to the basal plane.

VI.5.2 Superconducting Properties of $NbSe_2$

Using our estimates of λ_{ep} and the lifetime τ it is possible to estimate the extent to which $NbSe_2$ is a clean superconductor. Fundamentally, for a clean superconductor $\xi_0 << \ell$ and for a dirty superconductor $\xi_0 >> \ell$, so the two quantities to be compared are the basal-plane mfp and the coherence length $\xi_0 = \hbar v_F/\pi\Delta(0)$. Assuming that the BCS form $\Delta(0) = 1.764 k_B T_c$ holds for the gap,* the two quantities to be compared are

---

* See Appendix F for a discussion of experimental values for $\Delta(0)$.

$$\xi_o = \frac{\hbar v_F}{\pi\, 1.764 k_B T_c} \tag{6.4}$$

and

$$\ell = v_F \tau \tag{6.5}$$

where in Equation 6.5 v_F refers only to basal-plane electronic motion. However, as a first approximation this electron velocity is probably very similar to the usual definition of v_F as used in Equation 6.4. We use Cartesian coordinates for simplicity. The full v_F involves a Fermi surface average of $v_x^2+v_y^2+v_z^2$, while the basal-plane velocity involves a Fermi surface average of $v_x^2+v_y^2$. Given the anisotropy in the transport properties (a factor of 50 in the conductivity at 7 K),[12] it is reasonable to assume that v_z is much smaller than the basal-plane components and thus will be quite negligible when the components are squared. Thus, to a good approximation, in $NbSe_2$ v_F can be taken to be equal to the Fermi surface average of the components of the electron velocity lying in the basal plane. With this assumption, the two electron velocities can be cancelled, the two quantities to be compared are τ and $\hbar/(1.76\pi k_B T_c)$. Thus, an equivalent approach is to calculate the normalized scattering rate

$$\lambda_{tr} = \frac{\hbar}{2\pi k_B T_c \tau_{tr}} \quad . \tag{6.6}$$

The proper electron lifetime τ at low temperatures is longer than the room-temperature value by a factor of the residual-resistance ratio (RRR) multiplied by $(1+\lambda_{ep})$

$$\tau = RRR(1 + \lambda_{ep})\tau_{RT} \, . \tag{6.7}$$

This equation simply follows from the Drude formula $\rho = m/ne^2\tau$ where m can be written in terms of the band structure mass as $m = m^{BS}(1+\lambda_{ep}(T))$. Equation 6.7 follows by assuming that $\lambda_{ep}(T)$ is effectively zero at room temperature. Since $\lambda_{ep}(T)$ vanishes for temperatures in excess of the Debye temperature[144] (which is about 220 K for the compounds $Nb_{1-x}Ta_xSe_2$[85,170,189]), this appears to be a good approximation.

The residual resistance ratio (RRR) is obviously very sample dependent. Extensive resistance measurements have not been done, primarily because the crystal size which appears optimum for $H_{c2}(T)$ measurements is too small for convenient attachment of electrical leads. However, one sample from Batch 27, which yielded generally good material, had a RRR = 41.* Using this value, along with $\tau_{RT} = 2.5\times10^{-15}$ sec (an average of the two very similar room-temperature values obtained in Appendix F from resistivity and optical reflectivity data), a low-temperature value of $\tau = 2.57\times10^{-13}$ sec is obtained. This yields (with $T_c = 7.01$ K)

$$\lambda_{tr} = 0.67 \quad \text{or} \quad \ell = 1.31\xi_o \,. \tag{6.8}$$

Thus this estimate, based on measured normal-state properties, implies that the mfp is approximately equal to the coherence length in the basal plane. This calculation indicates that our $NbSe_2$ is midway between being clean and dirty.

---

* Since our transition temperature and critical field measurements have shown that smaller samples are generally of higher quality then larger crystals (as are used in the resistivity measurements), it is possible some of the $NbSe_2$ crystals used for upper critical field measurements are actually of higher quality than is implied by a RRR = 41.

The electron lifetime for motion perpendicular to the basal plane is difficult to estimate. There are no optical measurements of the lifetime and effective mass for this orientation. There is one measurement of the resistivity parallel to the c axis[12] (ρ = 5100 $\mu\Omega$cm at 300 K, ρ = 500 $\mu\Omega$cm at 7 K). However, not knowing the effective mass, which probably differs greatly from the free electron value, there is no way to estimate τ directly from the resistivity.

The c-axis lifetime has been estimated by Ikebe et al.[75] Using the Drude formula, $\sigma = ne^2\tau/m$, it is easily seen that the ratio of the basal-plane (BP) lifetime to the c-axis (C) lifetime depends on the resistivities and effective masses as

$$\frac{\tau_{BP}}{\tau_c} = \frac{m_{BP}\sigma_{BP}}{m_c\sigma_c} \quad . \tag{6.9}$$

The ratio of the resistivities has been determined to be 50 at 7 K.[12] Ikebe et al. approximated the quantity m_{BP}/m_C by the quantity m/M obtained from the anisotropic GL theory (Equation 5.8) using the known anisotropy in the critical fields. They found that the basal-plane electron lifetime is greater than the c-axis lifetime by a factor of 4.5, indicating that $NbSe_2$ is cleaner in the layer plane. However, equating the GL effective mass to a band structure effective mass is a fairly crude approximation,[128] so this value for the ratio of the lifetimes should be considered an estimate only.

The Fermi velocity and the coherence length ξ_0 can be calculated form the perpendicular critial field slope below T_c. Unfortunately, a rigorously correct and complete equation for the slope incorporating both anisotropy and finite mfp effects is not available. Following

Appendix D we can write down an approximate equation for the slope of an anisotropic superconductor,

$$\left.\frac{dH_{c2}}{dT}\right|_{T_c} = \frac{16\pi^2}{7\zeta(3)}\frac{ck_B}{e\hbar}\frac{T_c}{\langle v_\perp^2\rangle}\chi^{-1}(\lambda_{tr})\eta_{Hc2}(T_c). \qquad (6.10)$$

Here $\zeta(3) = 1.202$ and $\langle v_\perp^2\rangle$ is the Fermi surface average of the square of the component of $\vec{v}_F(\vec{k})$ perpendicular to the field direction. $\eta_{Hc2}(T_c)$ is the strong-coupling correction factor for H_{c2} at T_c. As discussed in Appendix E, this factor can be estimated using a model due to Masharov[121] to be 1.14. While this is only an approximate result, it agrees quite well with values for other superconductors in the literature,[118,119,145] all of which are approximately 1.1.

In the isotropic theory the clean-limit slope formula can be formally extended to the arbitrary ℓ case simply by multiplying by $\chi^{-1}(\lambda_{tr})$, the inverse of the Gor'kov function. As emphasized in Appendix D, this simple approach cannot be rigorously correct for the anisotropic theory. Simply multiplying by χ^{-1} does not affect the angular dependence implied by Equation 6.10 (through $\langle v_\perp^2\rangle$), while in fact, increasing the electron scattering rate must ultimately decrease the anisotropy, other factors being held constant.[160]

As a first approximation, however, χ^{-1} can be included in Equation 6.10 to account for mfp effects. With $\lambda_{tr} = 0.67$, $\chi^{-1}(.67) = 1.58$. Using the slope of -5.0 kG/K, taking $T_c = 7.01$, and using the values for χ^{-1} and η_{Hc2} discussed above, Equation 6.10 yields $\langle v_\perp^2\rangle^{\frac{1}{2}} = 7.3\times10^6$ cm/sec. Using Equation 6.4, this implies that $\xi_0 = 144$ Å. In the clean

limit ($\lambda_{tr} = 0$) somewhat different numbers are obtained; $\langle v_\perp^2 \rangle^{\frac{1}{2}} = 5.8 \times 10^6$ cm/sec and $\xi_0 = 114$ Å. These estimates of the basal-plane electronic velocity are somewhat less than the values derived from the normal-state properties in Appendix F (Table 6-4). There the low-temperature basal-plane velocity was estimated to be 1.3×10^7 cm/sec. It is not unreasonable that a discrepancy of this size should exist, given the several approximations which have been used here and the free-electron-type analysis used in Appendix F.

VI.5.3 Superconducting Properties of $Nb_{1-x}Ta_xSe_2$

It is not possible to analyze the superconducting properties of the compounds $Nb_{1-x}Ta_xSe_2$ in the detail that was possible for pure $NbSe_2$. This is due to the lack of values for the normal-state properties, especially the resistivity. Some values of the basal-plane RRR have been measured and are collected in Table 6-5. The drop in RRR as the Ta content increases clearly implies that alloying increases the electron scattering rate in these materials.

The most important question concerning the critical fields of the alloys is why they change so little as the composition is varied. The changes seen in the slopes were analyzed in Section VI.4.5. There it was concluded that the changes seen in the slopes can reasonably be attributed to mfp shortening, although it is possible that band structure changes also contribute.

It is useful to estimate in an approximate way the change in slope which might be expected to occur given the observed decreases in RRR

upon alloying. To do this we focus on the composition $Nb_{.80}Ta_{.20}Se_2$, and take its RRR = 4.9.[75] The room-temperature resistivity can be written as

$$\rho = \rho_{imp} + \rho_{ep}(T) \tag{6.11}$$

separated into a temperature-dependent electron-phonon term and a temperature-independent impurity contribution. With two approximations it is possible to estimate the room-temperature resistivity. First we assume ρ_{ep} = 150 μΩcm, as occurs in $NbSe_2$. Secondly, we assume that at low temperatures (≈ 7 K) $\rho_{imp} >> \rho_{ep}(T)$. Thus, for $Nb_{.80}Ta_{.20}Se_2$ with a RRR = 4.9,

$$\frac{\rho_{RT}}{4.9} = \frac{150 + \rho_{imp}}{4.9} = \rho_{imp}. \tag{6.12}$$

This can be solved to yield ρ_{imp} = 38 μΩcm, and the room-temperature resistivity can be estimated to be 188 μΩcm. The electron lifetime can be estimated using the formula

$$\tau_{RT} = \frac{m^{BS}}{n\, e^2 \rho}. \tag{6.13}$$

Using, as for $NbSe_2$, $m^{BS} = 1.6m_e$, we get $\tau_{RT} = 2.0\times10^{-15}$ sec. The low-temperature lifetime is greater by a factor of RRR$(1+\lambda_{ep})$ (Equation 6.7). Using λ_{ep} = 1.5, $\tau = 2.46\times10^{-14}$ sec. With τ, the normalized scattering rate λ_{tr} can be calculated. Using T_c = 5.55 K, we finally get $\lambda_{tr} = 8.9$ or $\ell = 0.1\xi_0$ (in the basal plane). Thus, according to this estimate the compound $Nb_{.80}Ta_{.20}Se_2$ is a fairly dirty superconductor. Although the calculation contains a large number of approximations, the result appears to be quite plausible if we assume that $NbSe_2$ is only a

moderately clean superconductor when prepared with a RRR = 41. It is unlikely that the room-temperature resistivity decreases significantly upon alloying, so as the RRR decreases the material should rapidly become quite dirty.

It is now possible to estimate the change expected in the perpendicular slope as λ_{tr} increases from 0.67 to 8.9 and T_c decreases from 7.01 to 5.55. With the velocity term held constant, Equation 6.12 predicts that the slope should increase by a factor of 4.4. From Figures 6-17 and 6-18, it is clear that the change actually observed in going from $NbSe_2$ to $Nb_{.80}Ta_{.20}Se_2$ is much less. In fact, the slope for this field orientation actually appears to decrease slightly upon alloying, after the small initial rise caused by changes introduced by the suppression of the CDW. This discrepancy is somewhat puzzling. As has been mentioned, the slope formula used here is only approximate, but it might reasonably be hoped that it would at least have semi-qualitative validity. A possible weak spot in the above analysis concerns the calculation of the resistivity of $Nb_{.80}Ta_{.20}Se_2$. $NbSe_2$ has an unusually large room-temperature resistivity which is caused by the strength of the electron-phonon interaction. Alloying probably causes the strength of this interaction to decrease. (Since the transition temperature decreases while the lattice properties appear to remain fairly constant [as evidenced by the Debye temperatures], the McMillan equation (F.5) implies that the electron-phonon coupling constant decreases with T_c.) A decrease in the strength of the electron-phonon interaction could cause the room-temperature electron-phonon resistivity to decrease upon alloying, partially offsetting the decrease in RRR, and resulting in a less dramatic change in the low-temperature electron lifetime than

predicted above. However, it is unlikely that this sort of effect could completely remove the conflict between the experimental results and the above calculation. Nonetheless, it would be most useful to have accurate resisitivity data for the alloy compounds. This would probably require larger samples than we have grown for the $H_{c2}(T)$ work, but could provide further insights into this system.

The mean free path dependence of $H_{c2}(T)$ has been investigated in many nearly-isotropic systems, for both weakly-coupled and moderately-coupled superconductors[150,164], and also for strong-coupling superconductors.[145,190,191] Quite universally, H_{c2} has been observed to increase as the mean free path is decreased, as expected theoretically. In fact, the slope dH_{c2}/dT may increase faster in strong-coupling materials than in weak-coupling superconductors.[192]

In spite of the fact that the absolute values of λ_{tr} calculated above clearly disagree with the observed behavior of the critical field slopes, it is useful to determine if the experimental trends agree with the functional form predicted theoretically. This analysis can be carried out for the perpendicular slope as follows. Assuming that the band structure and strong-coupling factors do not change significantly as the composition is varied, the slope can be written for a given field direction as

$$\frac{dH_{c2}}{dT} = - \alpha T_c(1.03 + 0.895 \lambda_{tr}) . \qquad (6.14)$$

Here α is a constant to be determined, and the approximate form of the Gor'kov function $\chi^{-1}(\lambda_{tr}) \approx 1.03 + 0.895\lambda_{tr}$ has been used. α can be determined from the critical field data for two compositions if the

ratio of the λ_{tr}'s is known for the two compositions. Since $\lambda_{tr} = \hbar/(2\pi k_B T_c \tau)$, the the ratio of the scattering rates for the two compositions is simply

$$\frac{\lambda_1}{\lambda_2} = \frac{(T_c\tau)_2}{(T_c\tau)_1} \quad . \tag{6.15}$$

The ratio of the electron lifetimes can be obtained directly from the resistivity using the formula $\rho = m/(ne^2\tau)$ (with the assumption that m and n do not change as the composition is varied). We can apply this analysis to the compounds $NbSe_2$ and $Nb_{.80}Ta_{.20}Se_2$. As disucussed above, the room temperature resistivities can be taken to be 150 μΩcm for $NbSe_2$ and 188 μΩcm for $Nb_{.80}Ta_{.20}Se_2$. The low temperature resistivity is obtained by dividing the room-temperature resistivity by the residual resistance ratio (Table 6-5). There are several ways of choosing the slopes and T_c's to be used here. Either the slope of the main linear section of the $H_{c2}(T)$ curve or the "just below T_c" slope can be used. The slope of the main linear section will be used here, although the results are essentially independent of which slope is chosen. Another choice concerns the relatively large initial increases in T_c and the slopes caused by suppression of the CDW. These increases appear to be caused by band-structure-related effects. Therefore, it is a more accurate measure of mfp effects to define a hypothetical CDW-free $NbSe_2$. Here the slope and T_c data of $Nb_{.98}Ta_{.02}Se_2$ will be used instead of the actual $NbSe_2$ data to approximate $NbSe_2$ without the CDW. With these choices one can calculate that $\lambda_{tr} = 0.023$ for $NbSe_2$, $\lambda_{tr} = 0.31$ for $Nb_{.80}Ta_{.20}Se_2$ and that $\alpha = 1.106$.

The perpendicular critical field slope for intermediate $Nb_{1-x}Ta_xSe_2$ compositions can be calculated by assuming that $\lambda_{tr}(x) = \lambda_{tr}(NbSe_2) +$

Cx. This is equivalent to assuming that the scattering rate increases linearly with impurity concentration. (C can be calculated using the results for $Nb_{.80}Ta_{.20}Se_2$; C = 0.014.) Figure 6-20 shows the experimental slopes and the slopes calculated using this method. The overall agreement is quite good. This indicates that the trends seen in the perpendicular critical fields of the compounds $Nb_{1-x}Ta_xSe_2$ are in agreement with the functional dependence on T_c and the electron scattering rate predicted by the usual theory (Equation 6.14). The agreement between theory and experiment in Figure 6-20 is poor for $x < 0.03$. This can be explained by assuming that most of the initial jump in the slope is caused by band structure changes accompanying suppression of the CDW.

The numbers obtained for λ_{tr} quantify our conclusion that electron lifetime effects appear to be very weak in this system, i.e., that $NbSe_2$ and the alloy compounds are "clean" superconductors. These values of λ_{tr} are significantly smaller than the values inferred from the electron lifetimes obtained from the resistivities. No fully satisfactory explaination for this discrepancy can be given at this time. It is certainly tempting to assume that at least some aspect of the usual free-electron-type analysis is quantitatively inadequate when applied to this series of anisotropic, strongly-coupled, d-band metals. However, assuming that the compounds $Nb_{1-x}Ta_xSe_2$ are very clean superconductors must be considered a tentative conclusion in light of the exotic nature of these materials.

VII Model Calculations for $H_{c2}(T)$

It has been shown in detail in Chapter VI that the measured upper critical fields of the compounds $Nb_{1-x}Ta_xSe_2$ differ in several ways from the critical fields of typical isotropic or nearly-isotropic superconductors. It is quite likely that these effects are caused by anisotropy , but it is of interest to actually verify this hypothesis as completely as possible, and further to determine what specific mechanisms are responsible.

When this research was begun, there were no accessible microscopic theories for calculating $H_{c2}(T)$ in anisotropic systems. However, applicable theories have recently been developed and applied to several systems, as discussed in Chapter V. We have used one of these theories to calculate $H_{c2}(T)$ for several Fermi surface models, and the results are discussed in this chapter. There are two fundamental reasons for carrying out these calculations. First, the use of rather simple models allows insight to be gained into what specific material properties are responsible for the anisotropy effects. Second, the calculations can provide information concerning the low-temperature band structure of $Nb_{1-x}Ta_xSe_2$.

$H_{c2}(T)$ results for three different Fermi surface models will be discussed in detail. First the critical field of a simple ellipsoidal Fermi surface will be examined. This model has the advantage that it can be continuously deformed into a spherical Fermi surface, which has a known $H_{c2}(T)$. This ellipsoidal model is useful because it allows certain basic conclusions to be drawn regarding what types of Fermi surface geometry produce various types of deviations from isotropic behavior.

It is not intended as a model for explaining the critical fields of $NbSe_2$.

In Chapter II it was noted that the Fermi surface of $NbSe_2$ (and of $Nb_{1-x}Ta_xSe_2$) appears to be basically cylindrical in nature. Two relevent models have been investigated. First, the parallel and perpendicular critical fields have been calculated using the Fermi surface model for $NbSe_2$ proposed by Wexler and Woolley,[19] which consists of open, undulating cylinders. It has also been suggested that the Fermi surface of $NbSe_2$ may include another piece, a closed, flat piece lying in the basal plane.[23,47] To investigate what effects such a piece would have on the critical fields, an ellipsoidal Fermi surface piece has been added to the Wexler and Woolley Fermi surface and the critical fields have been recalculated.

All of the calculations have been performed using the formalism developed by Butler[119] and described in Chapter V and Appendix C. This formalism is an extension of the weak-coupling BCS model to include an arbitrary Fermi surface geometry. Gap anisotropy is not included. Since this is a clean-limit theory, anisotropy of the electron lifetime is also not included. Anisotropy effects are incorporated only in that the Fermi surface can be non-spherical, and that the electron velocity, the important quantity in the calculations, can vary in an arbitrary way over the Fermi surface. In this chapter, the results of the calculations will be stressed. Certain details concerning the computer programs used to calculate $H_{c2}(T)$ are discussed in Appendix G.

VII.1 Single Ellipsoid Fermi Surface Model

The simplest non-spherical Fermi surface is an ellipsoid of rotation with the magnetic field applied along the axis of rotation. Within a parabolic-band model the ellipsoidal constant-energy surfaces can be represented by

$$E = \frac{\hbar^2}{2m} \left[k_x^2 + k_y^2 + \left(\frac{k_z}{B}\right)^2\right]. \tag{7.1}$$

The electrons are assumed to have the same effective mass for motion in the k_x and k_y directions, with a scaled effective mass in the k_z direction equal to mB^2. Setting E equal to a constant generates ellipsoids of rotation about the k_z axis with intercepts at

$$k_x = \frac{\sqrt{2mE}}{\hbar} \tag{7.2}$$

$$k_y = \frac{\sqrt{2mE}}{\hbar} \tag{7.3}$$

$$k_z = \frac{\sqrt{2mE}}{\hbar} B. \tag{7.4}$$

The Fermi velocity is given by

$$\vec{v}_F = \frac{\hbar}{m} \left[k_x \hat{k}_x + k_y \hat{k}_y + \frac{k_z}{B^2} \hat{k}_z\right] \tag{7.5}$$

(evaluated at points on the Fermi surface). Here $\hat{k}_x$, $\hat{k}_y$, and $\hat{k}_z$ are unit vectors. With the magnetic field oriented parallel to the k_z axis, the component of $\vec{v}_F(\vec{k})$ perpendicular to the field direction is simply

$$v_\perp^2 = \frac{\hbar^2}{m^2} \left[k_x^2 + k_y^2\right]. \tag{7.6}$$

These quantities are all that are needed to calculate $H_{c2}(T)$ using Equation C.1.* Because of the normalizations inherent in this equation, it is not necessary to specify the electronic mass m; this quantity cancels out. Also, instead of specifing the Fermi energy as an input parameter, it is possible to specify the rms Fermi velocity v_F. (Recall that $v_F \equiv \langle \vec{v}_F(\vec{k}) \rangle^{\frac{1}{2}}$, the brackets denoting a Fermi surface average.) This latter approach has been adopted as v_F is a more familiar quantity. Therefore to calculate $H_{c2}(T)$ with this model, the required input parameters are v_F, T_c, B, and the list of temperatures at which H_{c2} is to be determined.

Figure 7-1 shows $H_{c2}(t)$ for several values of B. Here $v_F = 10^7$ cm/sec and $T_c = 5$ K. H_{c2} scales in a simple fashion with changes in T_c and v_F, so except for those calculations intended to be directly compared to experimental data, most of the calculations have been carried out with these typical values. For different values of v_F and T_c the field values are scaled by a factor of

$$\left(\frac{10^7}{v_F} \times \frac{T_c}{5} \right)^2 . \qquad (7.7)$$

(See Equation C.2, Appendix C.)

The curve in Figure 7-1 for B = 1 reproduces the isotropic clean-limit result, as it should. As B is increased from unity, the Fermi surface is drawn out along the k_z axis into a prolate ellipsoid. This causes $H_{c2}(T)$ to be depressed relative to the isotropic result. If B is decreased from unity, the Fermi surface is compressed along the field

---

* Because of the symmetry involved, the calculations are actually performed in spherical coordinates for the ellipsoid model, and in cylindrical coordinates for the cylindrical Fermi surface models.

axis, becoming an oblate spheroid. This causes $H_{c2}(T)$ to become enhanced relative to the isotropic result, increasing quite rapidly as B is reduced.

It is worth noting that the shapes of the curves also change. This point is emphasized in Figure 7-2, where the reduced field h is plotted for B = 2, B = 1, and B = 0.5. The B = 2 curve is seen to bend toward the field axis faster then the isotropic result at lower temperatures. This is in contrast to the B = 0.5 curve, which exhibits both extended linearity at low temperatures and positive curvature just below T_c, the same sort of behavior seen in the experimental data examined in Chapter VI. As B is decreased from unity, the $H_{c2}(T)$ curves first develop extended linearity and then, as B is further reduced, positive curvature develops. Figure 7-3 shows Δh (defined as in Figure 6-10) for several values of B which shows how the positive curvature and extended linearity develop. For the more anisotropic Fermi surfaces with B < 1, there is clearly some similarity to the experimental data presented in Chapter VI. In fact, H_{c2} calculated for an ellipsoidal Fermi surface can be fairly accurately fit (using an arbitrary scaling factor) to the experimental data for a single field direction.* However, the experimental data exhibit positive curvature and extended linearity for both parallel and perpendicular field orientations. When the field is rotated 90^0 into the k_x-k_y plane for one of the ellipsoid models displaying positive curvature and extended linearity, the resulting $H_{c2}(T)$ curve is depressed relative to the isotropic result, qualitatively resembling the B = 2 curves of Figures 7-1 through 7-3.

---

* This is, in essence, what was done by Youngner and Klemm,[160] although their Fermi surface model is not exactly an ellipsoid.

Thus, it is clear that a single ellipsoid is not sufficient to model the experimental results in detail.

While it is not clear why changing B should affect the shape of the $H_{c2}(T)$ curve, a simple argument can be constructed to explain the variation seen in the overall magnitude. According to the isotropic theory (Equation 5.15), H_{c2} depends inversely on the square of the Fermi velocity. However, from Equation 5.23 it is clear that in the more general anisotropic case v_F^2 must be replaced by the Fermi surface average of the square of the component of $\vec{v}_F(\vec{k})$ in the plane perpendicular to the field direction. Figure 7-4 shows schematically how this quantity is affected as the Fermi surface shape is altered for the ellipsoid model. Since $\vec{v}_F(\vec{k})$ is always perpendicular to the Fermi surface, compressing the Fermi surface along the field axis tends to decrease the perpendicular component of $\vec{v}_F(\vec{k})$, thus increasing H_{c2}. Similarly, elongating the Fermi surface along the field axis tends to increase the perpendicular component, decreasing H_{c2}.

This can be interpreted in a simple way physically. According to the Ginzburg-Landau theory, (Equations 5.2, 5.4, and 5.5) the coherence length ξ depends on some positive power of v_F (2 in the clean limit, 1 in the dirty limit). ξ determines, at least roughly, the radius of the normal core of the flux vortices. This in turn determines H_{c2}, since the smaller the vortex core is the more vortices can be packed into the material before all the superconductivity is displaced and the material is driven normal. Since only electron motion in the plane perpendicular to the magnetic field direction can shield the field, it is a very plausible generalization to assume that in anisotropic materials the

vortex radius is determined by the component of $\vec{v}_F(\vec{k})$ in the plane perpendicular to the field. Thus if the Fermi surface average of $v_\perp^2$ is smaller (larger) for a given field orientation, the relevent coherence length will be smaller (larger) and H_{c2} should be larger (smaller), as is the case for these model calculations.

Experimentally, the critical fields of anisotropic superconductors frequently display positive curvature and enhanced linearity, similar to the B < 1 model results. However, a depressed H_{c2}, as is seen in the B > 1 model results has never been seen experimentally (and attributed to anisotropy effects.) There may be a simple explaination for this. For B > 1 (and H parallel to the k_z axis), H_{c2} is depressed, but by a relatively small amount. On the other hand, decreasing B increases H_{c2} in a quantitatively much more dramatic way (Figure 7-1). Most real superconductors, especially those which are metallic compounds, generally have quite complicated Fermi surfaces. For any given field direction, there may well be portions of the Fermi surface which by themselves would produce an enhanced H_{c2}, and other portions which would produce a depressed H_{c2}. In such materials which display anisotropy effects it is possible that H_{c2} is generally dominated for each field orientation by those portions of the Fermi surface which tend to enhance H_{c2} for that field orientation.

VII.2 Fermi Surface Models For $NbSe_2$

The goal of this section is to discuss the parallel and perpendicular critical fields calculated using the Fermi surface model for $NbSe_2$ proposed by Wexler and Woolley,[19] and compare the results to

experimental data. A modification of the Wexler and Woolley (WW) Fermi surface will also be considered. As described in Chapter II, the WW Fermi surface consists of two open, undulating cylinders parallel to the k_z axis. We have calculated $H_{c2}(T)$ using this Fermi surface model for the field oriented parallel to the k_z axis, which corresponds to the experimentally measured perpendicular critical field, and for the field lying in the basal plane, which corresponds to the experimentally determined parallel critical field. This latter calculation has been carried out with the field parallel to the ΓM axis (Figure 2-3). The possibility that H_{c2} may be anisotropic in the basal plane has not been explored. However, no such anisotropy has been seen experimentally (Section VI.4.3), which is consistent with the nearly circular cross sections of the WW Fermi surface (Figure 2-5). These calculations of $H_{c2}(T)$ are possible because WW present an explicit formula for the radii of the Fermi surface cylinders (Equation 18, Reference 18). The coefficients in this formula, which is an angular Fourier expansion, are functions of energy. Knowing how the coefficients change with energy near E_F makes it possible to determine $\nabla_k E$ at E_F and thus $\vec{v}_F(\vec{k})$.* With $\vec{v}_F(\vec{k})$ determined in this manner, $H_{c2}(T)$ can be determined using the same formalism as has been discussed above for the other models. The rms band structure Fermi velocity is found to be 2.13×10^7 cm/sec. This compares fairly well with the estimates of this quantity obtained from experimental results in Appendix F (see Table 6-4). The calculated critical fields are shown in Figures 7-5 and 7-6. The calculated $H_{c2}(t)$ values have been scaled by a factor of $(1+\lambda_{ep})^2$ with $\lambda_{ep} = 1.5$ to

---

* The information concerning this energy dependence was kindly provided us by Prof. Woolley, and is detailed in Appendix G.

account for the electron-phonon renormalization of the band structure electron velocities used in the calculation, by a factor of $\eta_{Hc2} = 1.14$ to approximately account for strong-coupling corrections, and by a factor of $\chi^{-1}(\lambda_{tr}) = 1.58$ (with $\lambda_{tr} = 0.67$)) to approximately include finite mfp effects. The product of these three factors is 11.26. (The use of this scale factor for the parallel critical field direction will be discussed below.)

The critical fields scaled in this manner can be compared to experimental data which is also shown in Figures 7-5 and 7-6. Clearly the agreement is poor. The magnitude of the calculated curves is much too small, and in addition, the shape of the calculated curves is not in agreement with the experimental data. While the calculated parallel critical field displays both positive curvature and extended linearity, the calculated perpendicular critical field displays neither, in disagreement with the experimental data. In fact, the calculated h(t) lies below the isotropic result for the perpendicular field orientation.

Some of the discrepancy seen in Figures 7-5 and 7-6 may be caused by the rough estimates used for the strong-coupling and impurity correction factors, but it is unlikely that this could explain the bulk of the disagreement, especially for the perpendicular critical field data. An alternative explaination involves modifying the Fermi surface. As noted in Chapter II, the actual $NbSe_2$ Fermi surface may contain a small, flat, closed piece lying in the basal plane, in addition to the open cylinders. The existance of such a piece has been suggested to explain the de Haas-van Alphen results,[47] and such a piece could result from an improved band structure calculation which took account of charge

transfer from the Nb atoms to the more electronegative Se atoms.[23] To model the effects such an additional Fermi surface piece has on the critical fields, $H_{c2}(t)$ has been calculated for a Fermi surface model consisting of the WW cylinders and an additional ellipsoidal piece. Figures 7-5 and 7-6 also show the critical fields for this model.* The ellipsoid used here is an ellipsoid of rotation about the k_z axis. If centered at the origin, the ellipsoid intersects the k_x and k_y axes at 1.3/a, and intersects the k_z axis at 0.6 times the k_x-k_y intercept. (a = 3.45 Å is the lattice constant.) The radius of the cylinders in the WW Fermi surface is approximately 1.55/a. The electrons on the ellipsoidal Fermi surface are assumed to have an effective mass of $5m_e$ ($m_e = 9.11\times10^{-28}$ gm). As is clear from Figures 7-5 and 7-6 the overall agreement between theory and experiment is improved when this augmented Fermi surface is used. The magnitude of the calculated critical field is in better agreement with experiment, especially for the perpendicular direction. Also, here both the calculated critical fields display positive curvature and enhanced linearity, qualitatively in agreement with the experimental data.

In one respect the calculation using the model which includes the ellipsoid is not an improvment upon the results calculated using just the WW Fermi surface model. The anisotropy decreases when the ellipsoid is included. This is understandable in light of the conclusions reached in Section VII.1 concerning the single ellipsoid Fermi surface model. By itself, an ellipsoid compressed along the k_z axis would have $H_{c2\perp}$ greater than $H_{c2\parallel}$, so it is reasonable that adding such a piece to the

* The calculated curves have been scaled by the factor of 11.26 discussed above.

WW Fermi surface model would decrease the overall anisotropy. A possible resolution of this difficulty may be obtained by re-examining the scaling factor used to correct for finite mfp and strong-coupling effects. The factor used, 11.3, was determined using normal-state properties of $NbSe_2$ involving electron motion in the basal plane, and thus is only correct for the perpendicular critical field. In determing the proper scaling factor for the parallel critical field calculation, the largest difference may concern the electron lifetime. In Chapter VI it was noted that the mfp for electron motion parallel to the k_z axis is probably shorter than the basal plane mfp, although quantitative estimates are difficult. A mfp anisotropy can easily increase the critical field anisotropy by increasing the parallel critical field. For example, assuming the electron lifetime is 2.5 times shorter for electron motion parallel to the k_z axis than for basal plane motion increases the parallel critical field so that it agrees fairly well with the experimental data, as is also shown in Figure 7-6.* Of course, $H_{c2\parallel}(T)$ calculated from the WW Fermi surface can also be fit fairly well to the experimental $H_{c2\parallel}$ data using an arbitrary scaling factor. Therefore a comparison of the calculated perpendicular critical fields with experimental $H_{c2\perp}(T)$ data provides a more revealing test of the proposed Fermi surface models, since here the two models predict different shapes for $H_{c2\perp}(T)$ and also the mfp and strong-coupling correction factors can be estimated for this field orientation.

In this section we have presented a semi-quantitative explanation of the critical fields of $NbSe_2$, and by extension, the similar critical

---

* This assumes mfp effects are determined by the Gor'kov function and that the other correction factors remain unchanged.

fields of the compounds $Nb_{1-x}Ta_xSe_2$. This explanation is based on a plausible modification of the WW Fermi surface and a reasonable assumption regarding the anisotropy of the electron lifetime. Although the model contains several parameters which have been varied to obtain good agreement with experimental data, the values choosen for these parameters are physically reasonable. However, the ellipsoid used here is considerably larger then the ellipsoid determined by Graebner and Robbins.[47] They found a diameter equal to 0.344 $Å^{-1}$ and a thickness of 0.054 $Å^{-1}$, while the ellipsoid used here has a diameter of 0.754 $Å^{-1}$ and a thicknes of 0.452 $Å^{-1}$. $H_{c2}(T)$ is calculated from a Fermi surface average. Therefore, adding a small ellipsoid of the size described by Graebner and Robbins to the Wexler and Woolley Fermi surface would not significantly affect the critical fields because of the much greater surface area of the cylinders. The most probable cause for this quantitative discrepancy is that the cylindrical parts of the Fermi surface model require modification. In spite of this difficulty, we can still tentatively conclude that the experimental critical fields are more consistent with a Fermi surface which includes a flattened, closed piece than with a Fermi surface which consists entirely of undulating cylinders.

The calculations discussed in this chapter have not included gap anisotropy. It is difficult to estimate the consequences of this omission. Gap anisotropy was not needed to explain $H_{c2}(T)$ of Nb, but this material is only slightly anisotropic.[119] Youngner and Klemm[160] have shown that gap anisotropy can produce effects very similar to those produced by Fermi surface ansiotropy, and it is certainly possible that gap anisotropy should be included to obtain a definative theoretical

explaination of H_{c2} of $NbSe_2$. The calculations have also not taken into account the charge density wave present in $NbSe_2$. However, the CDW appears to impose relatively minor changes on the electronic properties of $NbSe_2$, and so can be ignored at the semi-quantitative level of the calculations presented in this chapter. Alternatively, the calculations can be assumed to be more directly relevant to compounds such as $Nb_{.97}Ta_{.03}Se_2$, which have critical fields similar to those of $NbSe_2$ and which probably have band structures very similar to the CDW-free band structure used above for $NbSe_2$.

VIII. Summary and Conclusions

The primary purpose of this thesis has been to report a study of the upper critical fields of the compounds $Nb_{1-x}Ta_xSe_2$. The goal of this concluding chapter is to present an overview of the more important results and our interpretation of them.

The results of the critical field studies can be conveniently discussed in two parts; the shape of the $H_{c2}(T)$ curve and the changes which occur upon alloying. The overall shape of the $H_{c2}(T)$ curve is similar to that seen for other anisotropic superconductors, displaying both positive curvature just below T_c and extended linearity at low temperatures. One result of the extended linearity is that the simple Pauli paramagnetic limiting field of $18.6T_c$ is clearly exceeded for some compositions. It is known that many-body interactions and spin-orbit scattering modify the value of this limiting field, and accurate estimates of these renormalizations would be of considerable interest. Although it is circumstantial evidence, the fact that the anisotropy $H_{c2\parallel}/H_{c2\perp}$ is relatively constant at all temperatures except just below T_c implies that spin effects are unimportant, since they would be expected to be most influential in determining the parallel critical field at the lower temperatures.

A detailed study has been made of $H_{c2}(T)$ at temperatures just below T_c. It has been clearly established that the positive curvature is a real effect and is not caused by sample imperfections of any sort. The positive curvature occurs over a temperature interval considerably in excess of the transition width and appears to be a function of composition but not a function of sample quality (as measured by the

zero-field transition width). Also, it is possible to generate theoretical $H_{c2}(T)$ curves for anisotropic Fermi surfaces which display positive curvature similar to that seen experimentally. It is less clear if the experimental $H_{c2}(T)$ curves are actually linear in a small temperature region just below T_c. Both the microscopic theory and the Ginzburg-Landau theory, which should be valid sufficiently close to T_c, predict linearity. However, the data are somewhat ambiguous. With the behavior just below T_c emphasized by plotting ΔH (defined in Figure 6-10), it usually appears that the positve curvature is caused by a rounded kink centered somewhat below T_c, and that there is a small region of linearity just below T_c. It is also useful here to consider the anisotropy $H_{c2\parallel}/H_{c2\perp}$ as a function of temperature. If $H_{c2}(T)$ is linear just below T_c for both field orientations, the anisotropy should be constant over this temperature interval. Experimentally, a roughly constant anisotropy is only sometimes observed (Figure 6-15). However, there is a fair amount of uncertainty in the anisotropy data just below T_c. This the situation is not clearly resolved. However, we feel that the preponderance of the evidence indicates that $H_{c2}(T)$ is linear over a very small temperature interval just below T_c.

Somewhat surprisingly, the critical field curves do not change greatly as the composition is varied. To analyse the changes that are seen, it is useful to concentrate on the critical field slopes, both the slope of the main linear section and the slope of the smaller (assumed) linear section just below T_c. These two slopes tend to behave in the same manner. A sufficiently general theoretical formula for the slope, incorporating both anisotropy and finite electron lifetime effects is not currently available. However, it should be possible to estimate the

general behavior which is expected by combining the available theories. The slope should depend upon T_c, a particular Fermi surface average of the electron velocity, and the electron mean free path. Experimentally, the slopes for the two field directions behave differently as a function of composition. This behavior can reasonably be explained as follows. After a small initial rise of 0.2 K caused by suppression of the CDW found in pure $NbSe_2$, T_c decreases, which tends to decrease both slopes. Alloying also progressively changes the band structure. However, it appears that band structure effects are relatively unimportant except that band structure changes accompanying suppression of the CDW appear to cause most of the initial rise in the slopes. It is necessary to consider the effect alloying has of shortening the mfp, which tends to increase H_{c2} for both field directions, although not by the same amount. It appears that the different behavior seen in the parallel and perpendicular slopes is largely the result of an anisotropic electron lifetime effect. For the perpendicular critical field data, we have shown that the changes occuring in the slope as the composition is varied are consistent with the functional dependence on T_c and electron lifetime predicted by theory. This analysis also indicates that the compounds $Nb_{1-x}Ta_xSe_2$ are very clean superconductors. However, this latter conclusion does not agree with simple estimates of λ_{tr} based on measured normal-state properties and obtained using a free-electron type analysis. The anisotropy increases with increasing Ta content. This increase is consistent with plausible band structure changes, although probably it is mostly the result of the anisotropic mfp effect.

We have also reported the results for a number of computer calculations of $H_{c2}(T)$ for various anisotropic Fermi surface models.

There are basically two reasons for undertaking these studies. Such calculations are interesting because the use of simple models makes it possible to determine what sort of Fermi surface geometries produce different types of $H_{c2}(T)$ curves. It appears that Fermi surfaces which are compressed along the field axis relative to a spherical Fermi surface have an enhanced $H_{c2}(T)$ and can display positive curvature and extended linearity. For some geometries and field orientations it is possible to see a depressed $H_{c2}(T)$, but the magnitude of the depression is relatively quite small. This implies that for real superconducting materials, which generally have quite complicated Fermi surfaces, those parts of the Fermi surface favoring an enhanced upper critical field may dominate for all field orientations, leading to positive curvature and extended linearity for all field orientations, as is seen experimentally for the TMDC's[14] and for other superconductors as well.[116,129] The effect of anisotropy on the magnitude of $H_{c2}(T)$ can be explained by noting that the critical field depends on the component of the electron velocity in a plane perpendicular to the field direction, a simple generalization of the isotropic dependence on v_F. This result has been demonstrated analytically by a formula which has been derived from the microscopic theory for the slope dH_{c2}/dT at T_c for anisotropic, clean-limit superconductors.

A second reason for calculating $H_{c2}(T)$ is that such a calculation can provide a test of a proposed band structure of a material. From one perspective this is a fairly stringent test, requiring not only the Fermi surface shape but also the electron velocity at all points on the Fermi surface (that is, the curvature of the energy bands at E_F). On the other hand, $H_{c2}(T)$ is calculated from a Fermi surface average, so

agreement between theory and experiment is a necessary but not sufficient requirement for a proposed band structure to be correct.

The Fermi surface of $NbSe_2$ as calculated by Wexler and Woolley[19] consists of several open, undulating cylinders. The perpendicular and parallel critical fields have been calculated for this model and for the WW Fermi surface augmented by a small closed ellipsoid. The inclusion of the ellipsoid was motivated by the interpretation of de Haas-van Alphen data,[47] as well as theoretical speculation.[23] It appears that the Fermi surface model which includes the ellipsoid provides a better explaination of the experimental critical field data, when a reasonable assumption is made concerning anisotropy of the electron mean free path.

In conclusion, the critical field properties of the compounds $Nb_{1-x}Ta_xSe_2$ have been thoroughly characterized experimentally (for $0 \leq x \leq 0.20$). In addition, it has been possible to qualitatively understand major features of the data, although quantitative analysis has been less successful. Further studies could profitably involve more detailed $H_{c2}(T)$ model calculations, specifically including gap anisotropy, and measurements of the normal-state properties of the alloy compounds, especially the resistivity.

Appendix A

Fermi Surfaces in Systems of Reduced Dimensionality

In this thesis "reduced dimensionality" means that the electronic motion in a given metal is essentially one or two dimensional, and the phrase is not meant to imply anything regarding the actual sample geometry. This appendix contains a very elementary discussion of the Fermi surfaces in such materials.

It is convenient to use an effective mass model, in which case the Fermi energy can be written as

$$E_F = \frac{\hbar^2}{2}\left[\frac{k_x^2}{m_x} + \frac{k_y^2}{m_y} + \frac{k_z^2}{m_z}\right] . \tag{A.1}$$

Here m_x, m_y, and m_z are the effective masses along the three axes in momentum space. The Fermi surface is an ellipsoid with the following intercepts along the axes:

$$k_x = \frac{\sqrt{2E_F m_x}}{\hbar} \tag{A.2}$$

$$k_y = \frac{\sqrt{2E_F m_y}}{\hbar} \tag{A.3}$$

$$k_z = \frac{\sqrt{2E_F m_z}}{\hbar} . \tag{A.4}$$

It is also useful to note that the Fermi velocity is

$$\vec{v}_F = \hbar\left[\frac{k_x}{m_x}\hat{k}_x + \frac{k_y}{m_y}\hat{k}_y + \frac{k_z}{m_z}\hat{k}_z\right] . \tag{A.5}$$

(Evaluated at points on the Fermi surface.) Here $\hat{k}_x$, $\hat{k}_y$, and $\hat{k}_z$ are unit vectors.

In an ideal two-dimensional metal, the electrons are constrained to move entirely in the (e.g.,) k_x-k_y plane. Since the electron velocity must obviously be constrained to this plane, Equation A.5 implies that $m_z = \infty$, and this in turn implies, using Equation A.4, that the Fermi surface becomes an open cylinder along the k_z axis with a generally elliptical cross-section in the k_x-k_y plane.

In an ideal one-dimensional metal, the electrons are constrained to move along the (e.g.,) k_x axis. From Equation A.5, this implies that $m_z = \infty$ and $m_y = \infty$. In this case Equations A.2-A.4 show that the Fermi surface has become two flat parallel planes located at

$$k_x = \pm \frac{\sqrt{2E_F m_x}}{\hbar} \tag{A.6}$$

on the k_x axis.

All real metals have finite conductivity in all crystallographic directions. Within the effective mass model, the Fermi surfaces of real quasi-two-dimensional metals can be modeled as elongated ellipsoids with $m_z >> m_x \approx m_y$ (a prolate spheroid if $m_x = m_y$). Similarly, real quasi-one-dimensional metals can be modeled by assuming $m_z >> m_x$ and $m_y >> m_x$ (an oblate spheroid if $m_z = m_y$). Of course, real materials are not limited by the analytical simplicity of Equation A.1, and thus can have much more complicated Fermi surfaces. However, in real systems of reduced dimensionality, the gross Fermi-surface topology is quite likely

to bear some resemblence to the results of the simple effective mass model discussed here.

Appendix B

Crystal Growth Batch Details

This appendix contains a tabulation of certain details concerning the crystal growth experiments. There are 39 batches, each consisting of several tubes. Generally, a batch consists of several tubes prepared at the same time. However, the entire batch may or may not have been heated together. Within each batch the several tubes are given numbers; 20-2 thus refers to (the contents of) Tube 2, Batch 20.

The following table lists the various batches, the compositions included, and what type of experiment each was. The following type code is used: PG stands for powder growth, IVT stands for iodine-vapor transport, DVT stands for selenium-vapor transport, and AE stands for anneal experiment (re-heating previously reacted powder to obtain phase diagram information). In addition, D (dud) signifies batches which for one reason or another were aborted at some point during the crystal growth procedures. These designations only indicate what the batch was primarily intended for, and are not in all cases mutually exclusive. (For example, both phase diagram information and selenium-vapor transported crystals have been obtained from some PG experiments.) Alloy compositions are listed as atomic percent Ta; e.g., $Nb_{.95}Ta_{.05}Se_2$ is listed as 5.

Batch	Type	Compositions ($NbSe_2$ or at. % Ta)
1	PG	$NbSe_2$
2	PG	$NbSe_2$, 1, 5, 20
3	PG	1, 2, 10

Batch	Type	Compositions ($NbSe_2$ or at. % Ta)
4	PG	15
5	PG	$NbSe_2$, 1, 2, 5, 10, 15, 20
6	PG	$NbSe_2$, $TaSe_2$, 1, 2, 5, 10, 15, 20
7	PG	2, 5, 8, 15, 25
8	IVT	$NbSe_2$, 5
9	PG	TaS_2
10	PG	$NbSe_2$, 4, 6, 10, 12, 17
11	IVT	5, 20
12	PG	TaS_2
13	PG	5, 10, 15
14	PG	TaS_2
15	IVT	5, 25
16	IVT	TaS_2
17	PG	5, 12, 20
18	PG	$NbSe_2$, 0.5, 1.5, 2
19	PG	8, 12, 20, 25
20	IVT	5, 10, 20
21	D	
22	D	
23	PG	$NbSe_2$, 1, 2, 4, 6
24	PG	3, 4, 5, 6, 7
25	D	
26	PG	15, 20, 25
27	IVT	$NbSe_2$, 1

Batch	Type	Compositions ($NbSe_2$ or at. % Ta)
28	IVT	2, 3, 5
29	IVT	3, 4, 6, 7
30	PG	$NbSe_2$, 1, 2, 3, 4
31	PG	0.5, 1, 5, 10
32	PG	$NbSe_2$, 1, 2, 3, 4, 5
33	DVT	$NbSe_2$, 1, 2, 3, 4
34	DVT	$NbSe_2$, 1, 2, 3, 4
35	DVT	$NbSe_2$, 0.5, 1, 1.5, 2
36	DVT	2, 4, 5, 6
37	AE	3, 4, 5, 6, 7, 8, 10
38	AE	$NbSe_2$, 5, 10, 15, 20
39	AE	5, 6, 7, 8, 10, 12

Appendix C

Theoretical H_{c2} Formulas

The purpose of this appendix is to discuss the theoretical formulas for $H_{c2}(T)$ which have been used at various points throughout the main text. The actual equations used to produce the curves shown in Chapters V, VI, and VII will either be tabulated or an explicit reference will be made to the original source. Only equations based on the weak-coupling BCS theory will be considered here. The phenomenological Ginzburg-Landau theory is discussed in Chapter V, Section V.3. Strong-coupling corrections are discussed in Chapter V, Section V.5 and in Appendix E. The usual cgs-gaussian electromagnetic units are used (fields are in gauss).

C.1 Isotropic Theory

Here the theories of Helfand and Werthamer[136], and of Werthamer, Helfand, and Hohenberg[147] will be discussed explicitly, although similar theories have been proposed by a number of other workers.[193-195] The Helfand-Werthamer (HW) theory gives $H_{c2}(T)$ in the isotropic BCS limit, ignoring the spin-field interaction. $H_{c2}(T)$ is given by an implicit equation; Equation 24 of Reference 136. This equation has to be solved iteratively on a computer, as was done to produce Figures 5-2 and 5-3.

The Werthamer, Helfand, and Hohenberg (WHH) theory gives $H_{c2}(T)$ for an isotropic, dirty-limit superconductor, including the spin-field interaction. Again, $H_{c2}(T)$ is given by an implicit equation; Equation 28 of Reference 147. This equation has been solved to produce Figures

5-6 and 5-7. (It is worth noting that the formula for λ_{so}, Equation 27, was misprinted in the Reference 147[196] The correct form is given in our Equation 5.20.) Reference 147 also contains a series of equations [20, 24, 25, and 26] for $H_{c2}(T)$ for an isotropic superconductor with spin-field interaction and arbitrary electron mean free path, although apparently these have not been used to date.

C.2 Anisotropic Theory

In this section the discussion will be limited to an analytically simple clean-limit formalism proposed by Butler.[119] Also of note is the formalism of Youngner and Klemm which allows arbitrary electron mean free paths.[160] Butler's equation is

$$\ln\left(\frac{1}{t}\right) = \frac{1}{x}\int_0^\infty \frac{\langle 1 - \exp(-\frac{1}{2}y^2u_\perp^2)\rangle}{\sinh(\frac{y}{x})}\,dy \qquad (C.1)$$

where

$$x = \left(\frac{e\hbar}{c}\right)^{1/2}\frac{1}{2\pi k_B}\frac{v_F}{T_c}\frac{\sqrt{H_{c2}}}{t} \quad . \qquad (C.2)$$

The brackets < > denote a Fermi surface average,

$$v_F = \langle \vec{v}(\vec{k})^2\rangle^{1/2} \qquad (C.3)$$

being the rms Fermi velocity. The quantity

$$u_\perp^2 = \frac{[\vec{v}_F(\vec{k})]^2 - [\vec{v}_F(\vec{k}) \cdot \hat{e}_H]^2}{v_F^2} \qquad (C.4)$$

is the normalized component of the electronic velocity in a plane perpendicular to the field direction, at a given point on the Fermi surface. The Fermi surface average of a quantity is generally defined as

$$\langle z \rangle = \frac{\int d^2k \, \frac{z}{|\vec{v}_F(\vec{k})|}}{\int d^2k \, \frac{1}{|\vec{v}_F(\vec{k})|}} \quad . \tag{C.5}$$

The Fermi surface average is basically an integral of a quantity over the Fermi surface, weighted by the density of states at each point on the Fermi surface. (The density of states is proportional to the reciprocal of the local electronic velocity.) The integral in the denominator is required for normalization. A clean-limit formula for dH_{c2}/dT just below T_c is derived in Appendix D, starting from Equation C.1. Equation C.1 has been solved for several Fermi surface models, and the results are discussed in Chapter VII.

Appendix D

The Slope dH_{c2}/dT for a Clean-Limit, Anisotropic Superconductor

The purpose of this appendix is to derive a formula for the slope of $H_{c2}(T)$ just below T_c in the clean limit for a superconductor with an arbitrary Fermi surface. Gap anisotropy is not included. The starting points are Equations 4 and 5 of Reference 119 which can be combined to yield a single implicit equation for H_{c2}

$$\ln\left(\frac{1}{t}\right) = \frac{1}{x}\int_0^\infty \frac{\langle 1 - \exp(-\frac{1}{2}y^2u_\perp^2)\rangle}{\sinh\left(\frac{y}{x}\right)}\,dy \,. \tag{D.1}$$

Here the brackets < > denote a Fermi surface average, and x and $u_\perp$ are defined by Equations C.2 and C.4. It is convenient to combine the constants and write x as

$$x = \frac{1}{\alpha}\,\frac{\sqrt{H}}{t} \,. \tag{D.2}$$

Here $u_\perp^2$ is the normalized square of the component of the electron velocity in the plane perpendicular to the direction of the magnetic field.

The problem is to solve Equation D.1 in the limit that $t \to 1$, and $H \to 0$. Defining

$$z = y\,\frac{\alpha t}{\sqrt{H}} \tag{D.3}$$

this equation becomes

$$\ln\left(\frac{1}{t}\right) = \int_0^\infty \frac{1 - \exp\left(-\frac{1}{2}z^2u_\perp^2\,\frac{H}{\alpha^2t^2}\right)}{\sinh(z)}\,dz \,. \tag{D.4}$$

In the small-field limit, the exponential can be expanded in the usual power series. Defining

$$\beta = -\frac{1}{2}\frac{u_\perp^2}{\alpha^2} \quad , \tag{D.5}$$

$$\ln\left(\frac{1}{t}\right) = -\int_0^\infty \frac{\langle \beta z^2 \frac{H}{t^2} + \frac{1}{2}\left(\beta z^2 \frac{H}{t^2}\right)^2 + \cdots \rangle}{\sinh(z)}\, dz. \tag{D.6}$$

The Fermi surface average is an integration. Assuming that the order of integration can be interchanged, and keeping only the lowest power of H, we get

$$\ln\left(\frac{1}{t}\right) = -\left\langle \frac{\beta H}{t^2} \int_0^\infty \frac{z^2}{\sinh(z)}\, dz \right\rangle . \tag{D.7}$$

Fortunately, the z integral can be done exactly*

$$\int_0^\infty \frac{z^2}{\sinh(z)} dz = \frac{7}{2}\zeta(3) \tag{D.8}$$

where ζ is the Riemann zeta function ($\zeta(3) \approx 1.202$).

Recalling the definition of β (Equation D.5),

---

* Gradshteyn and Ryzhik[197], Equation 3.523(1)

$$\ln(t) = -\frac{7}{4}\zeta(3)\langle u_\perp^2\rangle \frac{H}{\alpha^2 t^2} \quad . \tag{D.9}$$

Solving for H, and using the fact that $t^2 \ln t \approx t-1$ for $t \approx 1$, and restoring all the constants, we get

$$H = \frac{16\pi^2}{7\zeta(3)} \frac{ck_B^2}{e\hbar} \frac{T_c}{v_F^2\langle u_\perp^2\rangle} (T_c - T) \cdot \tag{D.10}$$

Defining

$$\langle v^2\rangle = v_F^2\langle u_\perp^2\rangle \tag{D.11}$$

the final result for the slope is

$$\left.\frac{dH_{c2}}{dT}\right|_{T_c} = -\frac{16\pi^2}{7\,\zeta(3)} \frac{ck_B^2}{e\hbar} \frac{T_c}{\langle v_\perp^2\rangle} \cdot \tag{D.12}$$

This can be compared with the isotropic formula for the clean limit[145]

$$\left.\frac{dH_{c2}}{dT}\right|_{T_c} = -\frac{24\pi^2}{7\zeta(3)} \frac{k_B^2 c}{\hbar e} \frac{T_c}{v_F^2} \cdot \tag{D.13}$$

For a spherical Fermi surface

$$\langle v^2 \rangle = \frac{2}{3} v_F^2 \tag{D.14}$$

so the two formulas agree, as they must. The new feature in the more general formula is the replacement of the isotropic Fermi velocity by a Fermi surface average of the square of the component of the electron velocity in the plane perpendicular to the field direction. This is quite a plausible change, since only this component of the electron velocity is useful for shielding the magnetic field (confining it to the vortex cores).

For arbitrary electron mean free path, the isotropic formula is

$$\left.\frac{dH_{c2}}{dT}\right|_{T_c} = -\frac{24\pi^2}{7\zeta(3)} \frac{k_B^2 c}{\hbar e} \frac{T_c}{v_F^2} \chi^{-1}(\lambda_{tr}) \tag{D.15}$$

This can be obtained formally from the clean-limit formula by multiplying by the inverse of the Gor'kov function, $\chi(\lambda_{tr})$ [$\chi(0) = 1$]. Our anisotropic clean-limit formula cannot be generalized in this manor since such an equation would predict that shortening the electron mean free path would have no effect on the angular dependence of $H_{c2}(T)$. This is not true, shortening the mean free path must reduce the anisotropy, other factors being held constant.

It is interesting to note that a relation can be derived between the slopes for two orthogonal field directions for a particular type of Fermi surface.* If the Fermi surface has rotational symmetry about the z

---

* We are indebted to Mr. P. Santhanam for pointing this out to us.

axis, then the critical field slopes can be written for H oriented parallel and perpendicular to the z axis as

$$\frac{dH_{c2z}}{dT} = \frac{\delta}{\langle v_x^2 + v_y^2 \rangle} \tag{D.16}$$

and

$$\frac{dH_{c2xy}}{dT} = \frac{\delta}{\langle v_x^2 + v_z^2 \rangle} \tag{D.17}$$

with

$$\delta = \frac{-24\pi^2}{7\zeta(3)} \frac{k_B^2 c}{e\hbar} T_c \, . \tag{D.18}$$

The denominator of Equation D.17 can be rewritten;

$$v_F^2 - \frac{1}{2} \langle v_x^2 + v_y^2 \rangle \, . \tag{D.19}$$

This last form provides the connection with Equation D.16. The relation between the two slopes is

$$\frac{dH_{c2xy}}{dT} = \left[\frac{v_F}{\delta} - \frac{1}{2} \left(\frac{dH_{c2z}}{dT} \right)^{-1} \right]^{-1} \, . \tag{D.20}$$

This equation indicates that with v_F and T_c held constant, if one slope increases, the other must decrease.

Appendix E

Model Results for Strong-Coupling Correction Factors

The purpose of this appendix is to discuss a simple model approach which can be used to calculate strong-coupling enhancement factors for certain superconducting properties. As was noted in Chapter V, a very convenient way of handling corrections to the weak-coupling (BCS) theory is to write the parameter of interest as a product of the weak-coupling result and a correction factor e.g.,

$$H_{c2}(T) = H_{c2}^{BCS}(T)\eta_{Hc2}(T) \ . \tag{E.1}$$

The various η's can be calculated knowing the proper microscopic quanties [$\alpha^2F(\omega)$]. However, such information is frequently unavailable. Specifically, quasiparticle tunneling, which has been used to determine $\alpha^2F(\omega)$ in a number of systems, may not be possible. Many systems do not form a good tunneling oxide, and in short-coherence-length transition metal systems, the inevitable surface damage and surface reconstruction makes quantitatively precise tunneling very difficult. Therefore it is very convenient to have an approximate method of estimating the enhancement factors.

Such an approach has been developed by several researchers.[120,121] Their approach is based on the observation that $\alpha^2F(\omega)$ usually has two peaks. $F(\omega)$ is the phonon density of states as a function of energy; the two peaks correspond to the transverse and longitudinal phonon branches. The lower peak is of more importance in determining the properties of a superconductor. In this regard, it is useful to note

that the quantity λ_{ep} can be written as

$$\lambda_{ep} = 2 \int_0^\infty \frac{\alpha^2 F(\omega)}{\omega} d\omega \qquad (E.2)$$

so lower frequency parts of $\alpha^2F(\omega)$ are of greater weight in determining λ_{ep}. Thus as a first approximation, it is possible to model $\alpha^2F(\omega)$ as a single peak. The advantage of this approach is that the theory of strong-coupling superconductivity can be solved analytically for such a simple model.

One potential problem with this type of model is that all superconducting compounds and some elements (e.g., Sn) have crystal structures with several atoms per unit cell, thus they have optic phonon modes. For such materials, $\alpha^2F(\omega)$ no longer has two main peaks somewhat separated in frequency, but has many smaller, closer peaks, so modeling it as one peak appears to be in principle less valid here.[198]

Using a single-peak, delta function model for $\alpha^2F(\omega)$ (an Einstein model), Kresin and Parkhomenko[120] were able to calculate the enhancement factors for the jump in heat capacity at T_c (no applied field), and for the zero-temperature energy gap

$$\frac{\Delta C}{\gamma T_c} = 1.43\left[1 + 1.8\left(\ln\left(\frac{\omega_o}{T_c}\right) + 0.5\right)\left(\frac{\pi T_c}{\omega_o}\right)^2\right] \qquad (E.3)$$

$$\Delta(0) = 1.764\, k_B T_c \left[1 + 5.3\left(\frac{T_c}{\omega_o}\right)^2 \ln\left(\frac{\omega_o}{T_c}\right)\right] . \qquad (E.4)$$

The BCS theory predicts values of simply 1.43 and $1.764k_BT_c$, respectively. Here γT_c is the normal-state electronic heat capacity at

$T = T_c$ and ω_0 is the frequency characterizing the single peak model for $\alpha^2F(\omega)$. The enhancement factors depend on the ratio T_c/ω_0, which obviously must be dimensionless, so here ω_0 can be considered to be in temperature units.

In both cases, the correction factors are larger than 1, and increase as ω_0 decreases. Thus strong-coupling effects increase the values of these thermodynamic properties. (This is generally true and is not a result limited to this model.) Unfortunately, anisotropy effects are known to decrease the value of both quantities, complicating the analysis for materials where both strong-coupling and anisotropy effects are important.[199]

These formulas for the enhancement factors can be used to estimate λ_{ep}.** For this purpose they can be combined with the Allen-Dynes[200] T_c equation

$$T_c = \frac{f_1 f_2 \omega_{log}}{1.2} \exp\left[\frac{-1.04(1+\lambda_{ep})}{\lambda_{ep} - \mu^* - 0.62\lambda_{ep}\mu^*}\right]. \qquad (E.5)$$

Here μ^* is a parameter which measures the strength of the direct electron-electron repulsive interaction, and ω_{log} is a particular average of $\alpha^2F(\omega)$.*** f_1 and f_2 are two functions, f_1 depending only on λ_{ep} and μ^* while f_2 depends on other averages of $\alpha^2F(\omega)$. However, using the numbers for several representative superconductors provided by Allen and Dynes, it appears that f_2 differs only very slightly from unity, so

---

** The work in this section was done in collaboration with Mr. P. Santhanam.

***See Reference 200. It is shown here in temperature units.

it can be dropped without a serious loss of accuracy. This T_c equation can then be solved for T_c/ω_{log} as a function of λ_{ep} and μ^*,

$$\frac{T_c}{\omega_{log}} = \frac{f_1}{1.2} \exp\left[\frac{-1.04(1+\lambda_{ep})}{\lambda_{ep} - \mu^* - 0.62\lambda_{ep}\mu^*}\right] \tag{E.6}$$

$$f_1 = \left[1 + \left(\frac{\lambda_{ep}}{2.46(1+3.8\mu^*)}\right)^{3/2}\right]^{1/2}. \tag{E.7}$$

Certainly the two frequencies ω_{log} and ω_0 are not exactly equivalent. However, each is, in a particular sense, the best single phonon frequency characterizing $\alpha^2F(\omega)$. Assuming that ω_{log} and ω_0 can be equated, the Allen-Dynes T_c equation gives T_c/ω_0 for a given λ_{ep} and μ^*. This can then be used in Equations E.3 and E.4.

An alternative choice might be to equate ω_0 and the rms average phonon frequency ω_2. This possibility was explored using the experimental data for both ω_2 and ω_{log} given in Reference 200. It was found that ω_{log} is definitely the better choice, although the difference is not great.

The result of this process is that $\Delta C/\gamma T_c$ and $\Delta(0)/k_B T_c$ can be expressed as functions of λ_{ep} with μ^* as a parameter, thus allowing λ_{ep} to be estimated from heat capacity data and experimental values for the zero-temperature energy gap. To test the validity of this idea, experimentally determined values for λ_{ep}, $\Delta C/\gamma T_c$, and $\Delta(0)/k_B T_c$ have been collected from the literature for a number of crystalline

superconductors, none of which are particularly anisotropic.** (Possible exceptions are the weakly-coupled elements Cd and Zn, both of which are hexagonal. Both thermodynamic properties are less than the BCS values for these elements, because of anisotropy effects.[199,201] They are included here for completeness.) Figure E-1 shows the experimental data for the heat capacity jump, along with the theoretical predictions for $\mu^* = 0.10$ and $\mu^* = 0.13$, the limits of the range of values usually ascribed to this parameter.[200] The theoretical results are not strong functions of μ^*.

The data points show some scatter which may originate from either of two factors. First, there is definitely some experimental uncertainty in the data. When more than one value is available for a particular quantity, there is frequently considerable disagreement. Where several results are available, an average has been used if the discrepancies are small, while in several cases where the discrepancies are large, both experimental values have been included. (See Table E-1.) This problem is compounded by the fact that values of the several quantities for a given element usually come form different sources.

More fundamentally, it is far from obvious that there should be a unique relationship between $\Delta C/\gamma T_c$ and λ_{ep}, given that strong-coupling effects are, in principle, material specific. However, the overall agreement between theory and experiment is fairly good, and it thus appears legitimate to obtain an estimate of λ_{ep} from the heat capacity jump.

**However, no attempt was made to conduct a complete literature search.

Figure E-2 shows the theory and experimental data for the zero-temperature energy gap. Here the agreement appears to be somewhat less satisfactory. In both figures, values for the elements are shown distinctly from values for alloys, since for the latter a single peak model for $\alpha^2F(\omega)$ is in principle less correct. However, the experimental points for the two types of materials do not seem to be segregated, so the distinction does not appear to be important. The experimental data are collected in Table E-1.

The enhancement factor for $H_{c2}(T)$ at T_c has been calculated by Masharov[121] to be

$$\eta_{Hc2} = 1 + \left(\frac{\pi T_c}{\omega_o}\right)^2 [0.6 \ln \left(\frac{\omega_o}{T_c}\right) - 0.26] . \qquad (E.8)$$

The only parameter here is, again, ω_0/T_c, which can be related to λ_{ep} using the Allen-Dynes equation. Equation E.8 is for the clean limit. Marharov indicates how the equation should be modified to cope with finite mean-free-path effects (Equation 29, Reference 121). According to this modification, η_{Hc2} should increase as the material gets dirtier.

Using the clean-limit formula (Equation E.8), η_{Hc2} can be estimated for $NbSe_2$. From Equation E.6, $\lambda_{ep} = 1.5$ implies $T_c/\omega_o = 0.118$. From Equation E.8, this implies that $\eta_{Hc2} = 1.14$.

Appendix F

Normal-State Properties of $NbSe_2$

This appendix is devoted to estimating values for the Fermi velocity v_F, the electron lifetime τ, and the electron-phonon coupling constant λ_{ep} for basal-plane electronic motion in $NbSe_2$. These estimates are based on published values for various material properties. The results of this appendix are summarized in Table 6-4.

The electron lifetime is an important parameter for determining sample cleanliness. Estimates can be obtained from resistivity and optical reflectivity data. In this appendix the following notation will be adopted; τ_ρ will refer to the room-temperature electron lifetime deduced from resisitivity data, and τ_{opt} will refer to the room-temperature electron lifetime obtained from optical reflectivity data.

Optical reflectivity data for $NbSe_2$, obtained at room temperature, has been published by Parkin and Beal[202] and by Bachmann et al.[203] At lower energies the reflectivity displays Drude-like behavior while at higher energies the spectrum is dominated by interband transitions. The Drude-like reflectivity edge can be analyzed in the usual manner, yielding values for the electron lifetime, the effective mass and the plasmon energy. For these quantities Parkin and Beal obtain $\tau_{opt} = 2.4\times10^{-15}$ sec, $m_{opt} = 1.4m_e$ ($m_e = 9.11\times10^{-28}$ g), and $\omega_p = 3.9$ eV. Bachmann et al. obtain very similar numbers; $\tau_{opt} = 2.6\times10^{-15}$ sec, $m_{opt} = 1.8m_e$ and $\omega_p = 4.06$ eV. These experiments were carried out in such a way that the measured quantities all refer to electron motion in the basal plane.

A number of reseachers have published measurements of the basal plane resistivity of $NbSe_2$ and the correct value appears to be approximately 150 μΩcm at room temperature.[6,12,40,43,204] It is worth noting that this is an extremely large value. Typical room-temperature elemental resistivities are in the 1-10 μΩcm range.[205] A resistivity of 150 μΩcm is also larger than the resistivity of most dirty alloys and metallic compounds.[206] Since this value is obtained using single-crystal samples with fairly high residual-resistance ratios,* it implies that the electron-phonon interaction is very strong in $NbSe_2$ since the large room-temperature resistivity is an intrinsic property.** The resistivity for current parallel to the c-axis is even larger, the one value reported in the literature being 5100 μΩcm at room temperature, and 500 μΩcm at 7 K.[12]

In the analysis below it will be necessary to relate parameters measured in several types of experiments, and it may be useful to start with a brief discussion of the way in which various quantities are renormalized by the electron-phonon interaction. The parameter λ_{ep} was introduced in Chapter V. It is used to quantify the extent to which the electron-phonon interaction causes the values of certain electronic parameters to be altered from their band structure values.[142,143] Here "band structure" refers to the values which could, in principle, be

---

* The residual-resistance ratio RRR is defined as the ratio of the room-temperature resistance to the resistance just above T_c.

**With reference to the elementary formula $\rho = m/ne^2\tau$, for $NbSe_2$ $n = 1.55\times10^{22}$ electrons/cm^3.[203] This value is slightly less than typical elemental values,[25] which tend to be in the range $2\text{-}18\times10^{22}$ (for copper, $n = 8.47\times10^{22}$). Since the electron mass does not appear to differ greatly from typical metallic values, the unusually high value of the resistivity must be primarily ascribed to an intrinsically short electron lifetime.

calculated by assuming the electrons move in a rigid lattice. Fundamentally, the electron-phonon interaction changes the electron's dispersion relation near the Fermi energy, and λ_{ep} accounts for this effect. It is also important because it allows one to classify a superconductor as being weakly-coupled, moderately-coupled, or strongly-coupled.

The electron mass, velocity, and lifetime are affected as follows:[142]

$$m = m^{BS}(1 + \lambda_{ep}) \tag{F.1}$$

$$v_F = v_F^{BS}(1 + \lambda_{ep})^{-1} \tag{F.2}$$

$$\tau = \tau^{BS}(1 + \lambda_{ep}) . \tag{F.3}$$

Here the superscript "BS" is used to denote the bare, unrenormalized quantities. The equation for the electron lifetime can be explained as follows. The electron-phonon interaction effects the electron lifetime in two ways. Phonons can scatter electrons, but the electron phonon interaction also changes the electron and phonon wavefunctions. It is this latter effect which is described by Equation F.3.[143] The electronic mass is increased and the electrons are slowed down. This makes sense physically, since the electrons must now carry a polarization cloud around with them. The density of electronic states of the Fermi level N(0) as measured in low-temperature specific heat experiments is also enhanced. The electronic specific heat can be written $C_{el} = \gamma T$ with

$$\gamma = \frac{\pi^2}{3} k_B^2 N(0) = \frac{\pi^2}{3} k_B^2 N(0)^{BS}(1 + \lambda_{ep}). \qquad (F.4)$$

As noted in Chapter V, the coupling constant λ_{ep} is a function of temperature, vanishing at temperatures in excess of the Debye temperature.[144] Since $\theta_D \approx 220$ K for the compounds $Nb_{1-x}Ta_xSe_2$, it is clear that for these materials, $\lambda_{ep}(T)$ will be significantly reduced at room temperature, and probably approximately zero.* However, it turns out that $\lambda_{ep}(T)$ at room temperature will not be needed in the following analysis.

Quantities determined from optical experiments are unrenormalized. This is because the electron-photon interaction occurs at such a high frequency that the ionic lattice cannot respond.[203]

It is obviously useful to obtain an estimate of λ_{ep} for $NbSe_2$. λ_{ep} is ideally determined from quasiparticle tunneling characteristics, but unfortunately such information is lacking for the TMDC's, primarily because of the difficulty of fabricating good quality tunnel junctions with these materials. Lacking this data, λ_{ep} can be estimated in several less-reliable ways. One way is from the superconducting transition temperature using the McMillan T_c equation.[207] This equation was derived by solving the Eliashberg equations for a simple trial solution and then determining certain numerical factors by fitting to the tunneling data

---

* λ_{ep} will be taken to mean the low-temperature value of $\lambda_{ep}(T)$.

for Nb. In spite of this specificity, it appears to be a reasonable first approximation for most weakly- and moderately-coupled superconductors ($\lambda_{ep} < 1$), and has been widely used. Of course an important reason for its popularity is its simplicity; the only information needed about the phonon spectrum is the Debye temperature. Improved T_c equations (such as that of Allen and Dynes[200]) require certain average phonon frequencies which can only be calculated knowing $\alpha^2F(\omega)$, a quantity which is usually not available.*

Using the McMillan equation to calculate λ_{ep} in a system such as $Nb_{1-x}Ta_xSe_2$ should be done only with considerable caution, since the phonon spectra and electron-phonon matrix elements in these very anisotropic materials are probably quite different than those found in Nb. Thus the quantitative accuracy of the resultant λ_{ep}'s may be rather low.

The McMillan equation is

$$T_c = \frac{\theta_D}{1.45} \exp\left[\frac{1.04(1 + \lambda_{ep})}{\lambda_{ep} - \mu^* - 0.62\lambda_{ep}\mu^*}\right] \qquad (F.5)$$

where μ^* is a quantity which parametrizes the strength of the direct electron-electron repulsive (coulombic) interaction and is usually taken to be in the range 0.10 - 0.13.[200] The Debye temperature of $NbSe_2$ is

---

* In total, three different transition temperature formulas are be used in this thesis. In order of increasing sophistication, and therefore, generally, accuracy, they are; the BCS equation (Equation 6.1), the McMillan equation (Equation F.5), and the Allen-Dynes equation (Equation E.5).

about 220 K.[85,170,189]* The Debye temperature for $TaSe_2$ has been determined to be 215 K,[189] so it appears reasonable to assume that θ_D is approximately constant in the series of compounds $Nb_{1-x}Ta_xSe_2$. Taking θ_D = 220 K, μ^* = 0.11 and using the measured transition temperatures, λ_{ep} can be estimated using Equation F.5. The result for $NbSe_2$ is λ_{ep} = 0.75. As the Ta content is increased, λ_{ep} increases slightly to 0.76 as T_m peaks, and gradually decreases to λ_{ep} = 0.67 at the composition $Nb_{0.75}Ta_{0.25}Se_2$. (T_c is a monotonically increasing function of λ_{ep}.) These values imply that the compounds $Nb_{1-x}Ta_xSe_2$ are moderately-coupled superconductors.

Given the uncertainty concerning the applicability of this formula to a material as unlike niobium as $NbSe_2$ is, it is very useful to have other estimates of λ_{ep}. This is especially true in light of the intrinsic room-temperature resistivity of 150 μΩcm, an exceedingly large value, which may well imply a much stronger electron-phonon interaction than is indicated by λ_{ep}= 0.75.

Other estimates of λ_{ep} can be obtained from both the room-temperature resistivity and the optical lifetime. Allen[187] has suggested that λ_{ep} can be estimated from the electron lifetime due to the electron-phonon interaction by using the relationship.[143]

$$\lambda_{ep} = \frac{\hbar}{2\pi k_B T \tau_\rho} . \qquad (F.6)$$

Here τ_ρ is the electron lifetime obtained from the high-temperature

* For the 2H phase. Only this phase will be considered here.

resistivity using the elementary formula

$$\tau = \frac{m}{ne^2\rho}. \qquad (F.7)$$

In Equation F.7, both τ_ρ and m contain a factor of $(1+\lambda_{ep}(T))$. This factor can be canceled from both sides of the equation and both τ_ρ and m can be considered to be bare, or band structure quantities. In formulas involving the resistivity, it is easier to work directly in mks units, so here $\rho = 1.5\times10^{-6}$ Ωm and $e = 1.60\times10^{-19}$ coulomb. Using a band structure mass of $1.6m_e$ (an average of the two optical masses), and $n = 1.55\times10^{28}$ m^{-3} as the electron density[203] (one conduction electron per Nb atom), we get $\tau_\rho = 2.52\times10^{-15}$ seconds. This is in excellent agreement with the optically determined lifetime, $\tau = 2.5\times10^{-15}$ sec. Using $\tau = 2.52\times10^{-15}$ sec and taking T = 300 K we get $\lambda_{ep} = 1.61$.

A very similar approach has been proposed by Hopfield[188] connecting λ_{ep} with the electron lifetime as determined from a Drude analysis of the reflectivity,

$$\lambda_{ep} = \frac{\hbar}{2\pi k_B T \tau_{opt}}. \qquad (F.8)$$

Using $\tau_{opt} = 2.5\times10^{-15}$ sec (an average of the two optical lifetimes) and T = 300 K, we get $\lambda_{ep} = 1.62$. This value agrees closely with the value determined using the resistivity, as it should since the two lifetimes are almost identical.

Another estimate can be obtained from the low-temperature heat capacity, although the situation is somewhat complicated here. Two useful quantities which can be obtained from the heat capacity of a superconductor are $\Delta(0)/k_BT_c$ and $\Delta C/\gamma T_c$. Here $\Delta(0)$ is the zero-temperature energy gap, ΔC is the jump in the heat capacity at the superconducting-to-normal transition, and γT_c is the normal-state electronic heat capacity at the transition temperature. From the BCS theory [106]

$$\frac{\Delta(0)}{k_BT_c} = 1.764 \tag{F.9}$$

and

$$\frac{\Delta C}{\gamma T_c} = 1.43 . \tag{F.10}$$

Both of these quantities are enhanced by strong-coupling effects, but unfortunately both are also decreased by anisotropy effects.[199] *

The normalized jump in the heat capacity at T_c $\Delta C/\gamma T_c$ has been measured for $NbSe_2$, and the value 2.14 was found, larger than the BCS value.[38,85] The normalized zero-temperature gap $\Delta(0)/k_BT_c$ has been measured by several researchers using different techniques. Garoche, Veyssie, Manuel, and Molinie[38] measured the heat capacity down to 0.3 K and found evidence for two energy gaps, $\Delta(0)/k_BT_c$ = 1.75 and 0.16. Kobayashi, Noto, and Muto[170] have also measured the heat capacity, although not to as low a temperature. For two different samples they get values of 1.54 and 1.49 respectively. The gap can also be measured

---

* Note that with respect to the heat capacity, "anisotropy" refers to anisotropy of the gap in the elementary excitation spectrum and does not refer to Fermi surface topology per se.

fairly directly spectroscopically and with tunnel junctions; these two techniques measuring the gap predominantly in one direction. Using infrared transmission spectroscopy, Clayman[208] found $\Delta(0)/k_BT_c = 1.78$ in the basal plane and $\Delta(0)/k_BT_c = 1.04$ parallel to the c-axis. Morris and Coleman[209] determined that $\Delta(0)/k_BT_c = 1.03$ parallel to the c-axis using a tunnel junction.

These various results do not all agree. However, it seems clear that the gap in $NbSe_2$ is anisotropic. The normalized magnitude of the zero-temperature gap seems to be reduced below the BCS value, although the basal plane gap may be close to BCS-like. For simplicity, we shall assume below that the BCS result $\Delta(0) = 1.764k_BT_c$ holds, at least for the basal plane.

It is possible to understand in a simple qualitative way how gap anisotropy can dominate the heat capacity at low temperatures while strong-coupling effects can dominate at higher temperatures, near T_c. Strong-coupling effects are fundamentally caused by quasi-particle damping due to the strong electron-phonon interaction. This damping is temperature dependent and becomes more pronounced at higher temperatures.[210] On the other hand, gap anisotropy should be more important at lower temperatures where the lower energy of the electrons makes the heat capacity more sensitive to slight variations of the gap in the excitation spectrum.

In Appendix E a relationship is derived between the normalized jump in the heat capacity $\Delta C/\gamma T_c$ and λ_{ep} for isotropic (or nearly isotropic) materials. This relationship is based on a simple model for $\alpha^2F(\omega)$, but appears to give quite good agreement with experimental data, as noted in

Appendix E. However, since $NbSe_2$ clearly displays anisotropy effects, λ_{ep} inferred from the experimental jump in heat capacity using the method of Appendix E, which is $\lambda_{ep} = 1.3$, must be considered to be a lower bound.

To summarize the various estimates of λ_{ep}: from the McMillan equation $\lambda_{ep} = 0.75$, from the optical reflectivity $\lambda_{ep} = 1.62$, from the resistivity $\lambda_{ep} = 1.61$, and from the specific heat $\lambda_{ep} > 1.3$. While all of these estimates are only approximate, the McMillan equation results are likely to be the least reliable, as there is certainly no reason to expect this equation to be quantitatively correct for a class of materials like the TMDC's. To get a specific number to use in the calculations, we have somewhat arbitrarily chosen $\lambda_{ep} = 1.5$.

The immediate implication of assuming $\lambda_{ep} = 1.5$ is that $NbSe_2$ is a fairly strongly-coupled superconductor. The two most strongly-coupled elemental superconductors are Pb and Hg, having $\lambda_{ep} = 1.55$ and 1.61 respectively.[200] The technically important material Nb_3Sn has $\lambda_{ep} \approx 1.7$.[200,211] A number of alloys have λ_{ep} in the range of 1-2 although values of λ_{ep} greater than 2 are rare, except in a few amorphous systems.[200,212] All previously published estimates of λ_{ep} for $NbSe_2$ have been based on a McMillan-equation analysis and give values similar to 0.75.

In addition to the electron lifetime, it is useful to have estimates of the Fermi velocity. Again estimates can be obtained from both the optical properties and the resistivity.

v_F can be estimted from the plasma frequency using the formula for

the plasma frequency

$$\omega_p^2 = \frac{4\pi}{3} e^2 N(0) v_F^2 . \qquad (F.11)$$

Equation F.11 can be derived within the free-electron approximation. However, it appears that it is considered to be somewhat more generally valid and applicable to transition-metal systems.[213,214] Since this equation involves optical properties it is written in terms of the unrenormalized band structure quantities. To apply it here we need N(0), the density of states at the Fermi level, which can be obtained from the low-temperature normal-state heat capacity using Equation F.4. The experimental value[85] of γ is 16.5 (mJ/mole K^2) and this can be converted to 4090 erg/(cm^3K^2) using the density[42] 6.41 g/cm^3 and the formula weight 240.83 g/mole. With Equation F.4 this implies that $N^{BS}(0)(1 + \lambda_{ep}) = 6.52\times10^{34}$ (erg-cm^3)$^{-1}$. Using an average of the two measured values of the plasma frequency, ω_p = 3.98 eV = 6.05×10^{15} sec^{-1}. With these values of ω_p and $N^{BS}(0)$ (and with e = 4.8×10^{-10} esu) we get $v_F^{BS} = 3.8\times10^7$ cm/sec from Equation F.11. This value refers to the (average) component of the Fermi velocity in the basal plane.

The Fermi velocity can also be estimated from the intrinsic room-temperature resistivity using the formula*

---

* This formula is for a two-dimensional metal, and can be derived from Equation 13.25, Reference 25 under this assumption. The standard formula for three-dimensional metals is obtained by replacing the 2 by a 3.

$$\sigma = \frac{e^2}{2} \tau v_F^2 N(0) \cdot \qquad (F.12)$$

From Equations F.1 - F.3, we see that the renormalization factors of (1 + $\lambda_{ep}(T)$) can be cancelled in Equation F.12. Thus τ_ρ, v_F, and N(0) can be considered to be band structure quantities, and we again escape having to come up with a number for $\lambda_{ep}(T)$ at room temperature. With ρ = 1.5x10^{-6} Ωm, e = 1.6x10^{-19} coulomb, τ_ρ = 2.51x10^{-15} sec and** $N^{BS}(0)$ = 2.61x10^{47} (Jm^3)$^{-1}$, we get v_F^{BS} = 2.82x10^7 cm/sec. The two values of the Fermi velocity, from the plasma frequency and from the resistivity are quite similar, although the agreement between optically and resistively determined values is not as good as it was for the lifetime.

**This value is calculated form the value N(0) = 6.52x10^{34} (erg-cm^3)$^{-1}$ with λ_{ep} = 1.5.

Appendix G

Details of the Computer Programs; $H_{c2}(T)$ Modeling

The purpose of this appendix is to briefly discuss certain technical aspects of the computer programs used to calculate $H_{c2}(T)$ using the various theories discussed in the main text and in Appendix C. All of these calculations have been carried out on a Digital PDP 11/03 computer using programs written in Fortran.

All of the relevant microscopic theoretical formulas for $H_{c2}(T)$ can be written in the general form $\ln(t) = F(H,t,\alpha)$. Here F is some complicated function (an integral or an infinite series), and α stands for all relevant parameters, e.g., the electron lifetime, the Fermi surface shape, and v_F. These equations can be solved iteratively by selecting a temperature t and iterating until H is determined with sufficient accuracy. The same basic computer program has been used for all the theories, the only signifigant differences being the forms of $F(H,t,\alpha)$. The programs require an initial guess for H at the first temperature point as an input parameter (the programs start at t = 0.99 and t is subsequently decreased), but generate initial guesses for H at all subsequent temperatures internally.* The iteration proceeds as follows. Starting with some guess H, the program calculates F at H and at $H\pm\Delta H$, ΔH being an incremental field. By comparison with ln(t), it can be determined which of these three fields provides the best fit. This field replaces the initial guess and this procedure is iterated until

---

* This is done using an extrapolation based on a quadratic fit to the last three H, t points. (For the second point to be calculated, a linear relationship based on the first point calculated and the point t = 1, H = 0 must be used.)

some H' provides a better fit than either of the fields H'±ΔH do. At this point ΔH is replaced by ΔH/10 and the entire procedure is repeated until ΔH has been reduced to some previously set final value. At this point the solution for this value of t is complete. The final value of ΔH (which is controlled by an input parameter) gives a measure of the uncertainty in the result, assuming that $F(H,t,\alpha)$ has been calculated with sufficient accuracy.

Except for the isotropic, dirty-limit WHH theory, $F(H,t,\alpha)$ always involves one or more integrals which are sufficiently complicated that they must be done numerically. All these integrals have been calculated using a fourth-order Newton-Cotes technique.[215] Using this formalism, the integral of a function $f(x)$ from x_a to x_b can be written as

$$I = \frac{2h}{45}\left[7f(x_a) + 7f(x_b) + 32 \sum_{i=1,3,5}^{m-1} f(x_i)\right. \tag{G.1}$$

$$\left. + 12 \sum_{i=2,6,10}^{m-2} f(x_i) + 14 \sum_{i=4,8,12}^{m-4} f(x_i)\right]$$

where

$$x_i = x_a + hi \tag{G.2}$$

and

$$h = \frac{x_b - x_a}{m} \,. \tag{G.3}$$

The various Fermi surface averages used in the H_{c2} calculations involve surface integrals. These have been done using the technique described by Kreyzig.[216]

As discussed in Chapter VII, the calculation of H_{c2} for the $NbSe_2$

Fermi surface proposed by Wexler and Woolley[19] uses some unpublished data provided by Professor Woolley. As described in Reference 19, the WW Fermi surface can be parametrized as two radial Fourier series expansions (one for each Fermi surface cylinder). Given the energy dependence of the coefficients in these expansions, the Fermi velocity can be calculated since the energy dependence of the constant energy surfaces in the vicinity of the Fermi energy can be calculated. The table below lists the coefficients as a function of energy as provided by Professor Woolley (using the notation of Reference 19 with energy in Ryd; E_F = -0.6268 Ryd).

E	C001	C101	C111	C002	C102	C112
-0.622	1.3536	0.1883	0.0850	1.4637	-0.1622	-0.0484
-0.626	1.4784	0.2059	0.0587	1.5798	-0.1361	-0.0954
-0.6268	1.5035	0.2096	0.0545	1.6112	-0.1405	-0.0865
-0.630	1.6116	0.2243	0.0351	1.7278	-0.1569	-0.0673

Table 6-1

$Nb_{1-x}Ta_xSe_2$ Transition Temperatures

Composition	T_m		Other Results*	
(at. % Ta)	2H	4H	2H	4H
0.0	7.01	6.31	7.29	6.30
0.5	7.05	--	--	--
1.0	7.17	--	--	--
2.0	7.22	--	--	--
3.0	7.12	--	--	--
4.0	6.99	6.24	--	--
5.0	6.85	--	6.88	--
6.0	6.69	6.14	--	--
8.0	6.46	--	--	--
10.0	6.21	5.81	6.42	--
12.0	6.03	5.61	--	--
15.0	5.90	5.42	--	--
17.0	--	5.28	--	--
20.0	5.55	5.12	5.37	5.37
25.0	5.22	4.91	--	--
30.0	--	--	--	4.61

* From Reference 75, except 4H $NbSe_2$ from Reference 166.

Table 6-2

Comparison of $NbSe_2$ $H_{c2}(T)$ Data

Reference	T_c	perpendicular slope*	parallel slope*
This work	7.01	6.60±0.17	21.5±1.2
Schwall et al.[85]	7.1	6.45	25.7
Toyota et al.[133]	7.18	6.96	16.43
	7.29	7.27	18.24
	7.34	6.54	16.35
	7.39	7.04	16.91
Prober et al.[14]	7.1	8.0	23
Foner and McNiff[171]	7.0-7.4	7.9±0.3	25.7±0.8
Leupold et al.[174]	7.14	7.82	23.3
	7.27	8.73	30.0
Ikebe et al.[75]	7.29	7.7	27.5
de Tray et al.[217]	---	7.3	25
Garoche et al.[38]	7.11	6.9	---

* These slopes are for the main linear section of the $H_{c2}(T)$ curves.

Table 6-3

The Slope $-dH_{c2}/dT$ For $Nb_{1-x}Ta_xSe_2$

$H_{c2\perp}$

Composition (x in %)	This Work* Main Linear Section	This Work* Just Below T_c	Ikebe et al.[75] t = 0.95
0.0	6.60±0.17	5.00±0.89	7.7
0.5	6.79		
1.0	8.00	5.68	
2.0	8.39±0.23	7.11±0.19	
3.0	8.58	7.42	
4.0	8.64±0.08	7.38±0.15	
5.0	8.49±0.07	7.17±0.58	8.1
6.0	8.54±0.15	6.68±0.48	
8.0	8.56	7.25	
10.0	8.38	5.96±0.06	8.3
15.0	8.28±0.23	6.43±0.23	
20.0	8.03	6.54	8.0

$H_{c2\parallel}$

Composition (x in %)	This Work* Main Linear Section	This Work* Just Below T_c	Ikebe et al.[75] t = 0.6	Ikebe et al.[75] t = 0.95
0.0	21.5±1.2	9.2±3.6	27.5	18.2
0.5	22.2	9.7		
1.0	26.5±0.4	11.8		
2.0	27.6±0.2	13.0		
3.0	29.4	12.7±0.9		
4.0	29.2	14.1		
5.0	29.4±0.6	15.7	30.4	18.2
10.0	29.2±0.1	16.7	40.7	24.7
15.0	30.0±0.5	14.9		
20.0	30.0		34.2	25.9

* Where several values have been measured for a particular composition, the mean value is shown ± one standard deviation.

Table 6-4

Properties of $NbSe_2$

Quanity	Comments
$\tau_{opt} = 2.5\times10^{-15}$ sec	Room-temperature electron lifetime from Drude analysis of the reflectivity. The average of two similar values.[202,203]
$\tau_{\rho} = 2.52\times10^{-15}$ sec	Room-temperature electron lifetime from the resistivity, Equation F.7.
$\tau = 2.57\times10^{-13}$ sec	Low-temperature electron lifetime (assuming RRR = 41 and $\lambda_{ep} = 1.5$), Equation 6.7.
$m_{opt} = 1.6m_e$	From a Drude analysis of the room-temperature reflectivity. The average of two similar values.[202,203]
$n = 1.55\times10^{22}$ cm^{-3}	Conduction electron density.[203]
$\lambda_{ep} = 0.75$	From the McMillan equation, Equation F.5.
$\lambda_{ep} = 1.61$	From the room-temperature resisitivity, Equation F.6.
$\lambda_{ep} = 1.62$	From the room-temperature optical lifetime, Equation F.8.
$\lambda_{ep} > 1.3$	From the jump in heat capacity at T_c, Equations E.3, E.6, E.7.
$\lambda_{ep} = 1.5$	Value arbitrarily chosen for use in other calculations.
$v_F^{BS} = 3.8\times10^7$ cm/sec	From the plasma frequency, Equation F.11.
$v_F^{BS} = 2.82\times10^7$ cm/sec	From the room-temperature resistivity, Equation F.12.
$v_F^{BS} = 2.31\times10^7$ cm/sec	Calculated from the Wexler and Woolley band structure calculation, Chapter VII.
$v_F = 1.32\times10^7$ cm/sec	Renormalized (low-temperature) electron velocity, obtained from an average of the values estimated from

	the plasma frequency and the room-temperature resistivity.
$v_F = 7.3 \times 10^6$ cm/sec	Renormalized electron velocity obtained from the experimental perpendicular critical field slope, BCS theory, Equation 6.12, assuming $\lambda_{tr} = 0.67$.
$v_F = 5.8 \times 10^6$ cm/sec	Renormalized electron velocity obtained from the experimental perpendicular critical field slope BCS theory, Equation 6.12, assuming $\lambda_{tr} = 0$.
$\lambda_{tr} = 0.67$	Equation 6.8
$\chi^{-1}(\lambda_{tr}) = 1.58$	Gor'kov function, with $\lambda_{tr} = 0.67$.
$\xi_0 = 26$ nm	Equation 6.3 with $v_F = 1.32 \times 10^7$ cm/sec.
$\xi_0 = 14.4$ nm	Equation 6.3 with $v_F = 7.3 \times 10^6$ cm/sec.
$\xi_0 = 16.4$ nm	From a Ginzburg-Landau analysis of the perpendicular critical field slope at T_c, Equation 6.11.
$\eta_{Hc2} = 1.14$	Masharov's model result, Appendix E.

Table 6-5

$Nb_{1-x}Ta_xSe_2$ Residual-Resistance Ratios

Composition	This work	Ikebe, et al.[75]
$NbSe_2$	41	32
$Nb_{.95}Ta_{.05}Se_2$	16.4 19.8	9.3
$Nb_{.90}Ta_{.10}Se_2$	7.56	6.9
$Nb_{.80}Ta_{.20}Se_2$	--	4.9

Table E-1

Experimental Data for λ_{ep}, $\Delta C/\gamma T_c$, and $\Delta/k_B T_c$

Material	λ_{ep}	$\Delta C/\gamma T_c$	$\Delta/k_B T_c$
Hg	1.61 [200,212]	2.37 [218]	2.30 [218,219] 1.98 [218,201]
V	0.64 [200]	1.50 [218]	1.76 [210,218]
Mo	0.42 [200]	1.27 [218]	1.70 [210]
In	0.805 [200]	1.73 [218]	1.82 [218]
Zn	0.40 [144,218]	1.26 [218]	1.60 [218]
Cd	0.39 [144,219]	1.32 [218,221]	1.65 [218,219]
Al	0.39 [144,219]	1.40 [218,221]	1.75 [219,222]
Tl	0.795 [200]	1.50 [218]	1.82 [218,201,219]
Ta	0.69 [200]	1.57 [218]	1.80 [218,221,223]
Nb	0.95 [200,224,225]	1.87 [218]	1.80 [210,218] 1.90 [210,218]
Re	0.46 [200]	--	1.80 [219]
Pb	1.55 [200]	2.71 [218,226]	2.15 [218,219,222]
Ga	0.41 [144,219]	1.42 [218]	1.75 [218,219,221]
Sn	0.72 [200]	1.60 [218]	1.78 [218,221]
$In_{.9}Tl_{.1}$	0.85 [200]	1.54 [227]	--
$Pb_{.6}Tl_{.4}$	1.38 [200]	--	2.05 [219,228]
$Pb_{.4}Tl_{.6}$	1.15 [200]	--	1.72 [228] 2.03 [219]
$Pb_{.8}Tl_{.2}$	1.53 [200]	--	2.18 [219,229]

Material	λ_{ep}	$\Delta C/\gamma T_c$	Δ/kT_c
$Pb_{.7}Bi_{.3}$	2.01 [200] 2.34 [229]	--	2.43 [219,229]
$Pb_{.9}Bi_{.1}$	1.66 [200]	--	2.35 [219,230]
$Pb_{.65}Bi_{.35}$	2.13 [200]	--	2.39 [219]
$Pb_{.8}Bi_{.2}$	1.88 [200]	--	2.35 [219]
$Pb_{.6}Tl_{.2}Bi_{.2}$	1.81 [200]	--	2.40 [219]
Nb_3Sn	1.7 [200,220,219]	2.4 [220,231,232]	2.40 [232] 2.15 [219]
$Tl_{.9}Bi_{.1}$	0.78 [200]	--	1.78 [219,228]
$Nb_{.75}Zr_{.25}$	1.3 [224]	--	2.14 [224]

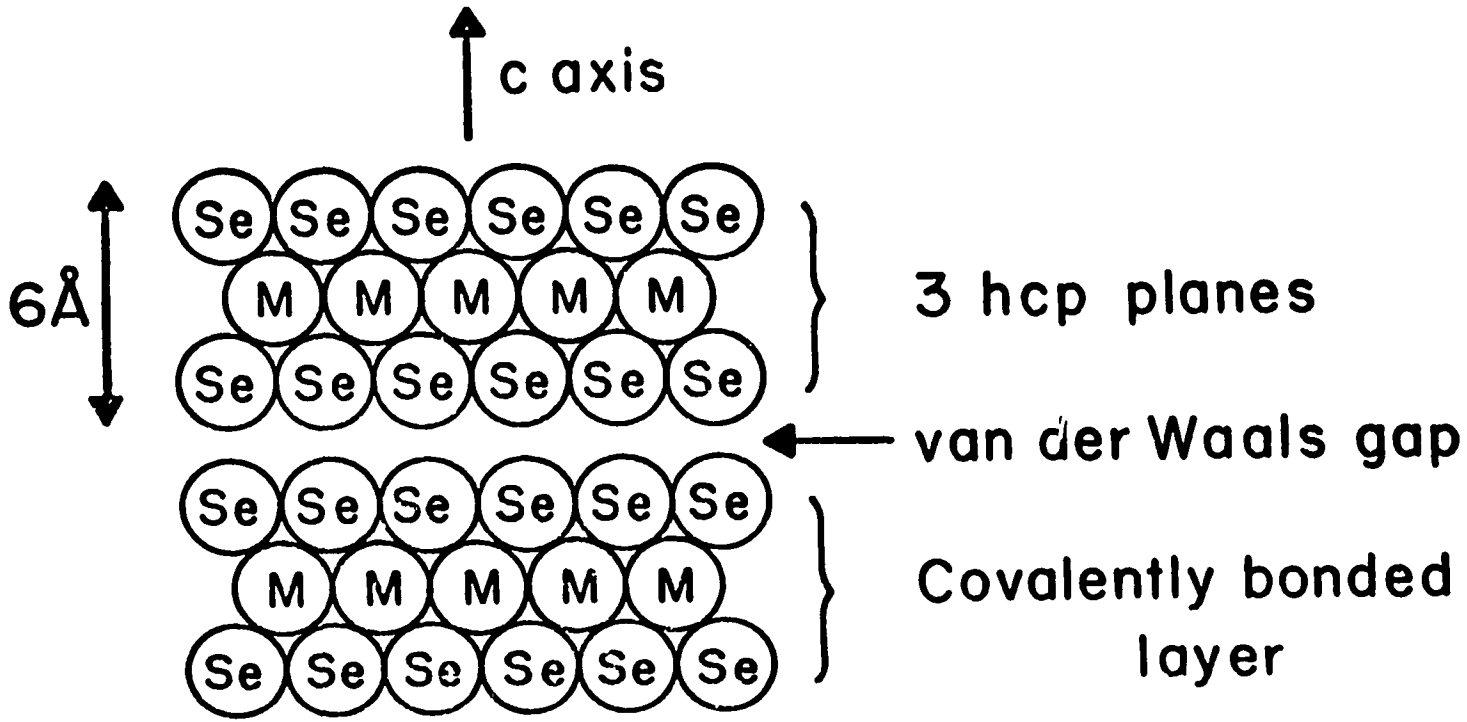

Fig. 2-1 Schematic diagram of the TDMC crystal structure. Here M stands for either of the the two metals Nb and Ta.

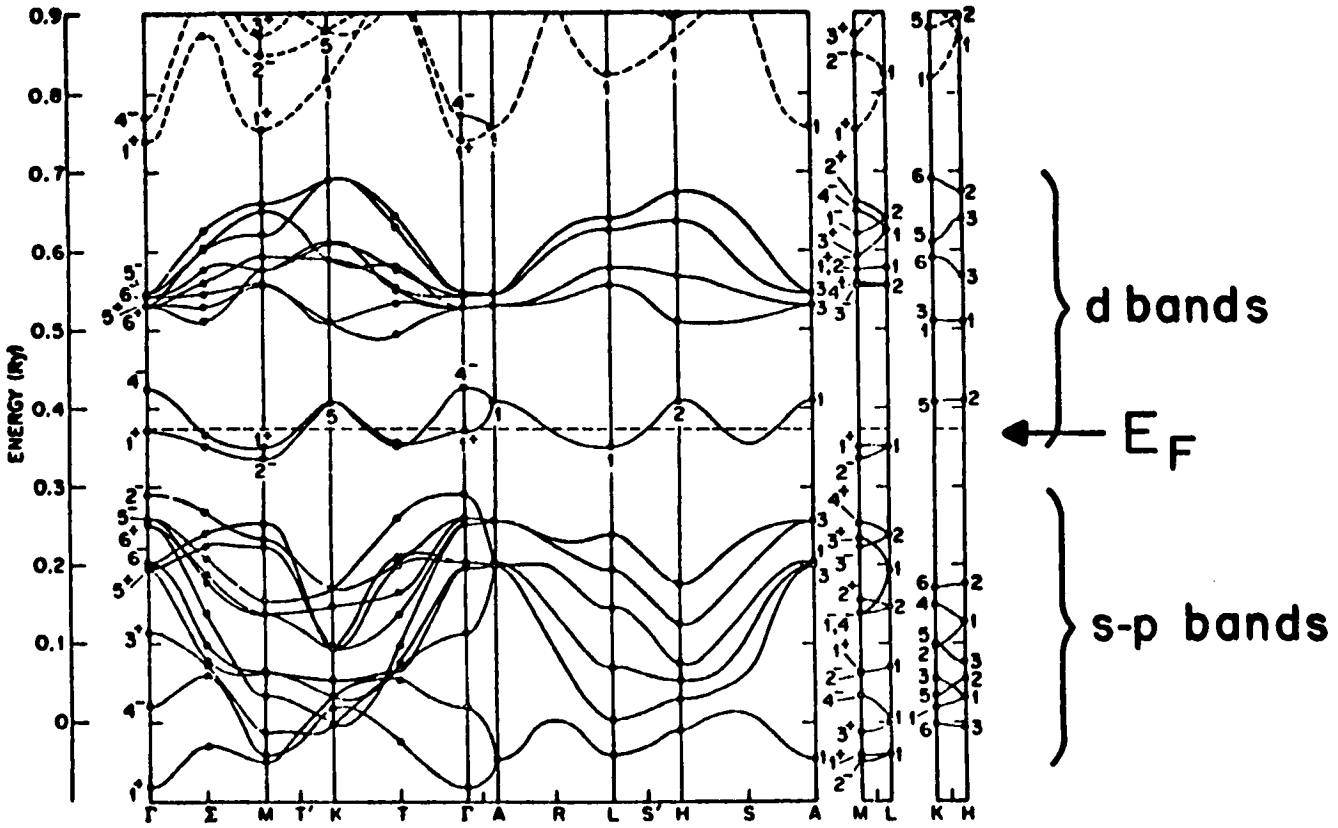

Fig. 2-2 $NbSe_2$ band structure as calculated by Mattheiss. The Fermi level passes through the lower, split-off pair of d-bands. From Reference 18.

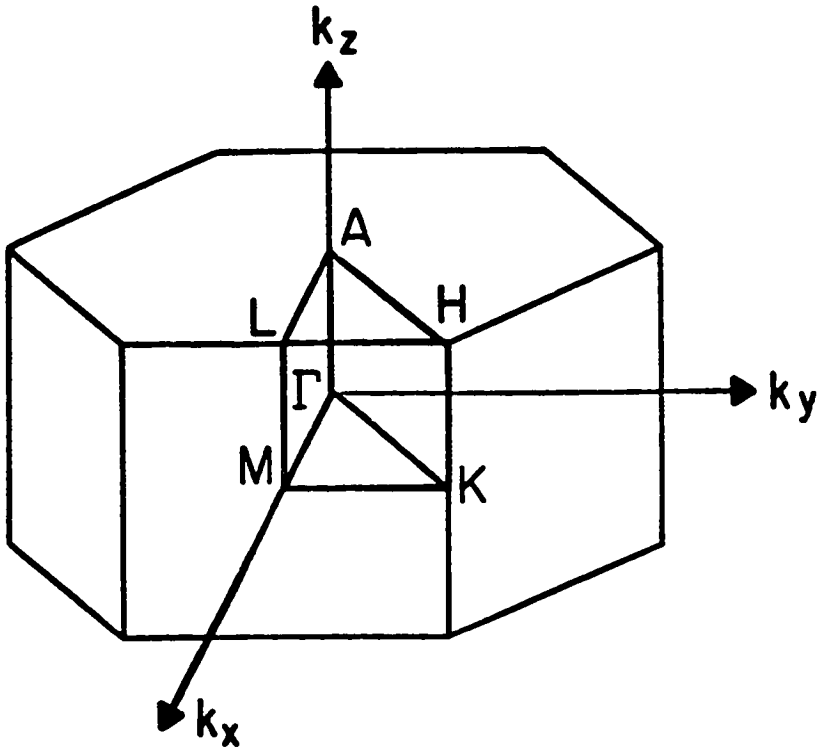

Fig. 2-3 The Brillouin zone of a hexagonal crystal, itself hexagonal, showing the standard notation for several high-symmetry points.

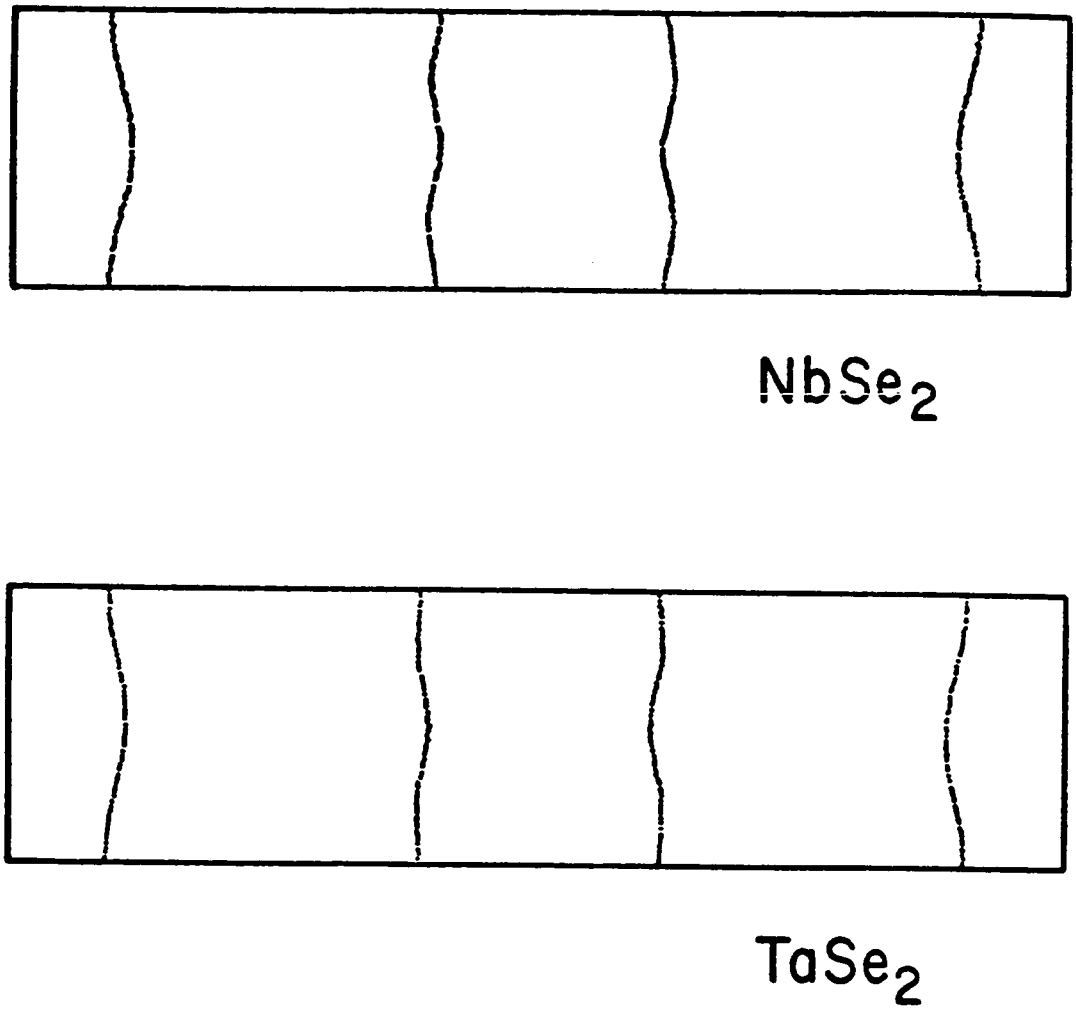

Fig. 2-4 A side view of the Wexler and Woolley Fermi surfaces for $NbSe_2$ and $TaSe_2$, in the plane defined by the points ΓKHA. The box shows the Brillouin-zone boundary in the doubled-zone scheme.

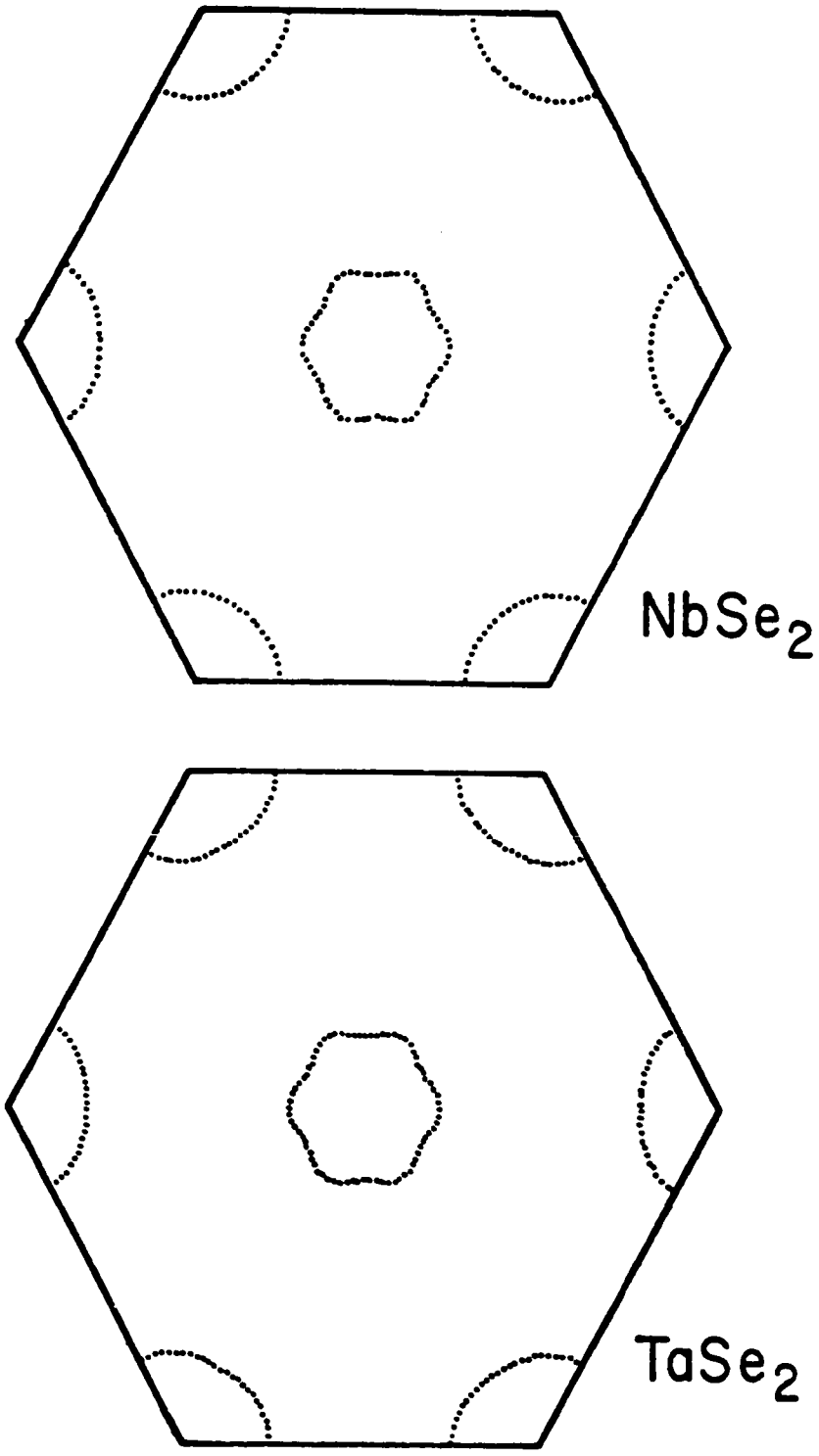

Fig. 2-5 A top view of the Wexler and Woolley Fermi surfaces for $NbSe_2$ and $TaSe_2$, in a plane passing through the center of the doubled zone. The box shows the Brillouin-zone boundry in the doubled-zone scheme.

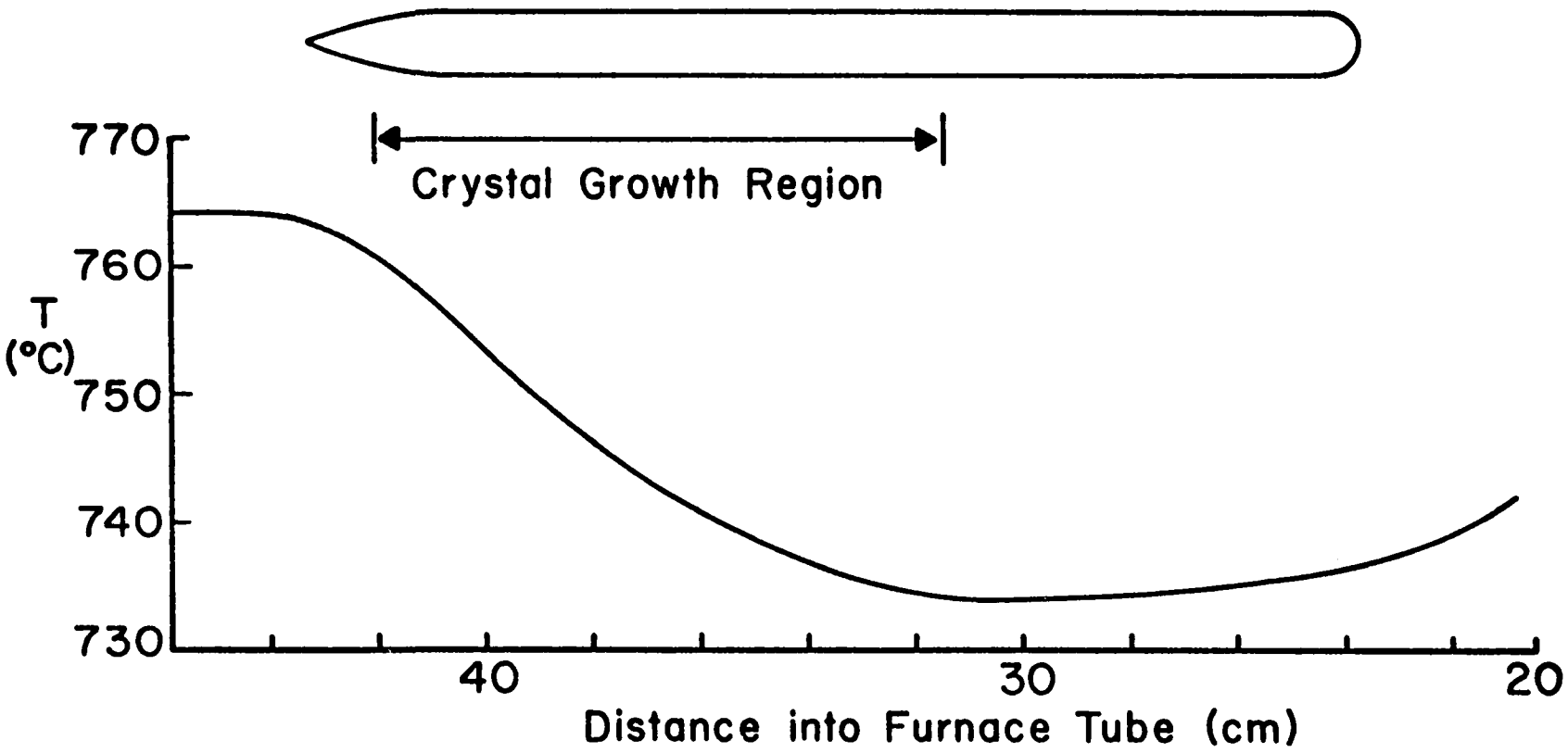

Fig. 3-1 The temperature profile used for crystal growth Batch 20 (iodine-vapor transport). The position of the tube is shown and the region over which transported crystals were found is noted.

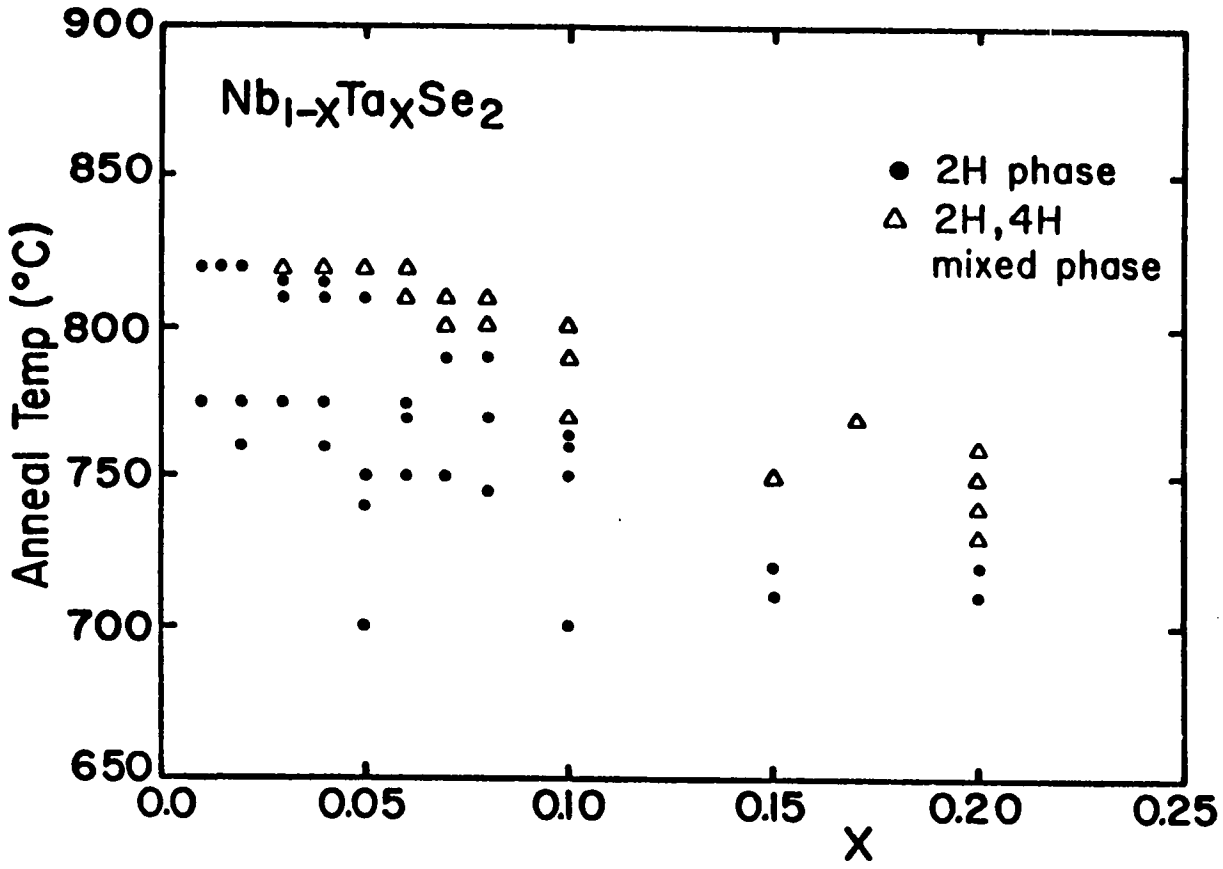

Fig. 3-2 The relevant portion of the $Nb_{1-x}Ta_xSe_2$ phase diagram as determined by powder x-ray and transition temperature measurements.

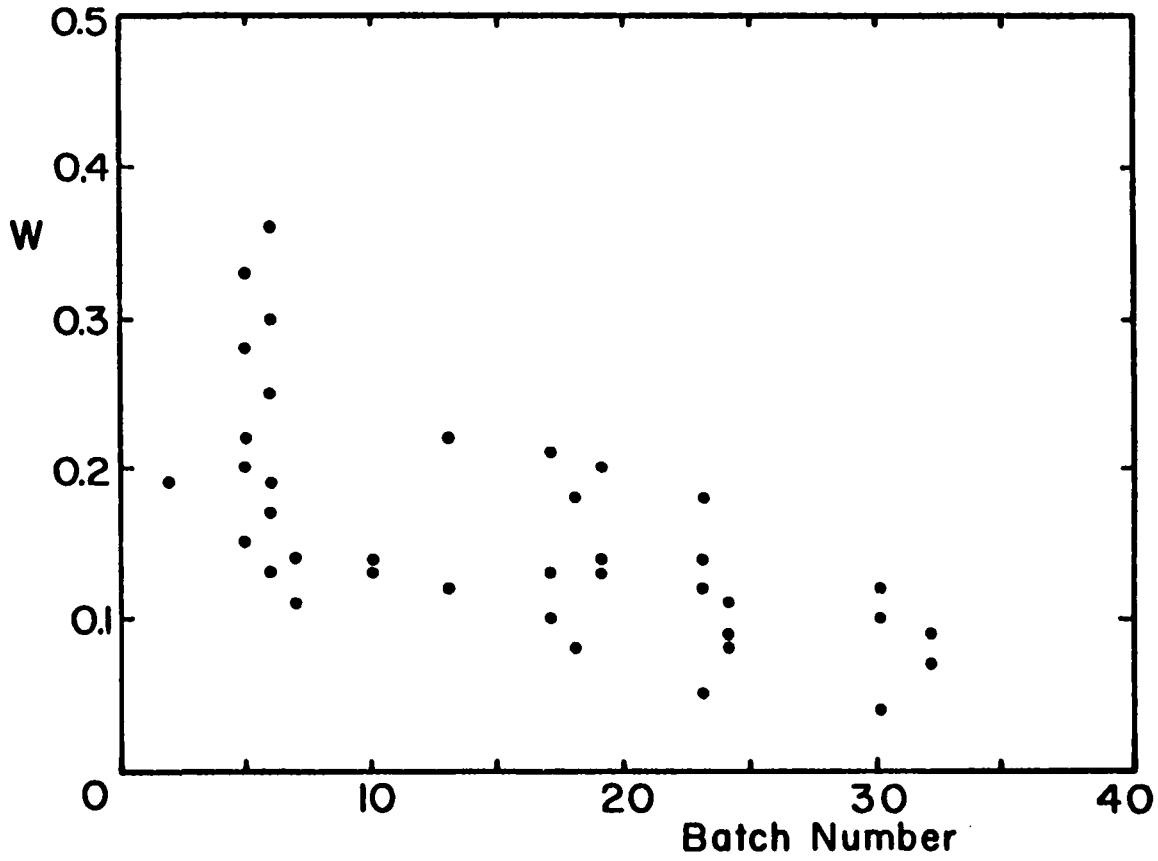

Fig. 3-3 The width W of the superconducting transition of bulk samples from various batches.

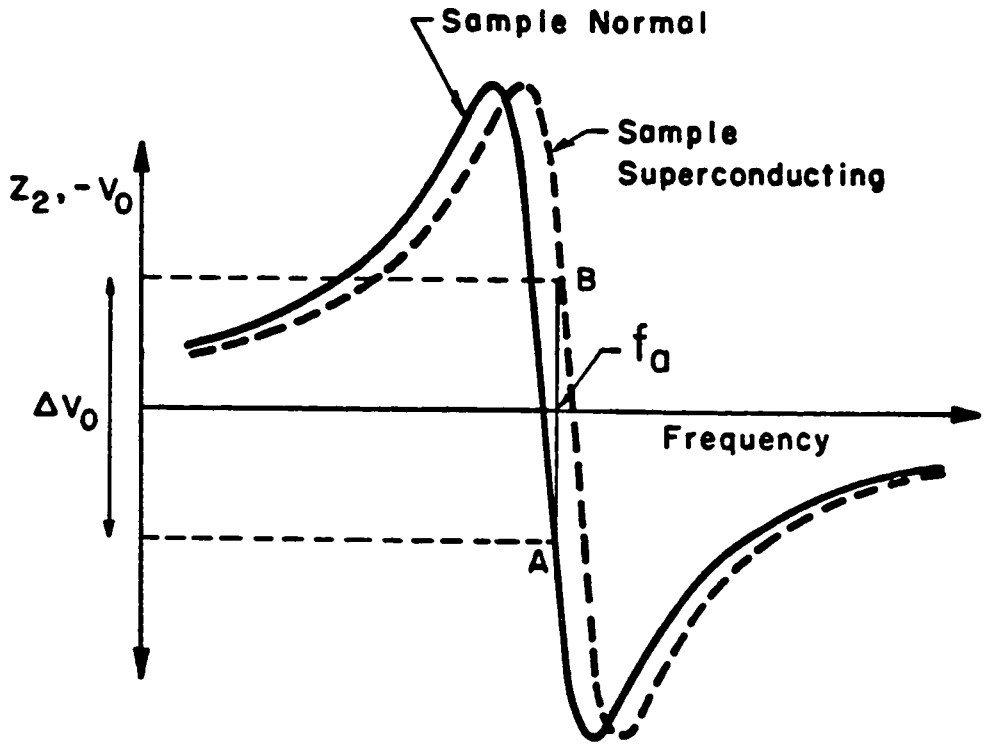

Fig. 4-1 The frequency-shift detector output voltage as a function of frequency with the sample in both the normal and superconducting states. If the circuit is driven at a fixed frequency f_a, the output voltage will change as shown at the superconducting-to-normal transition.

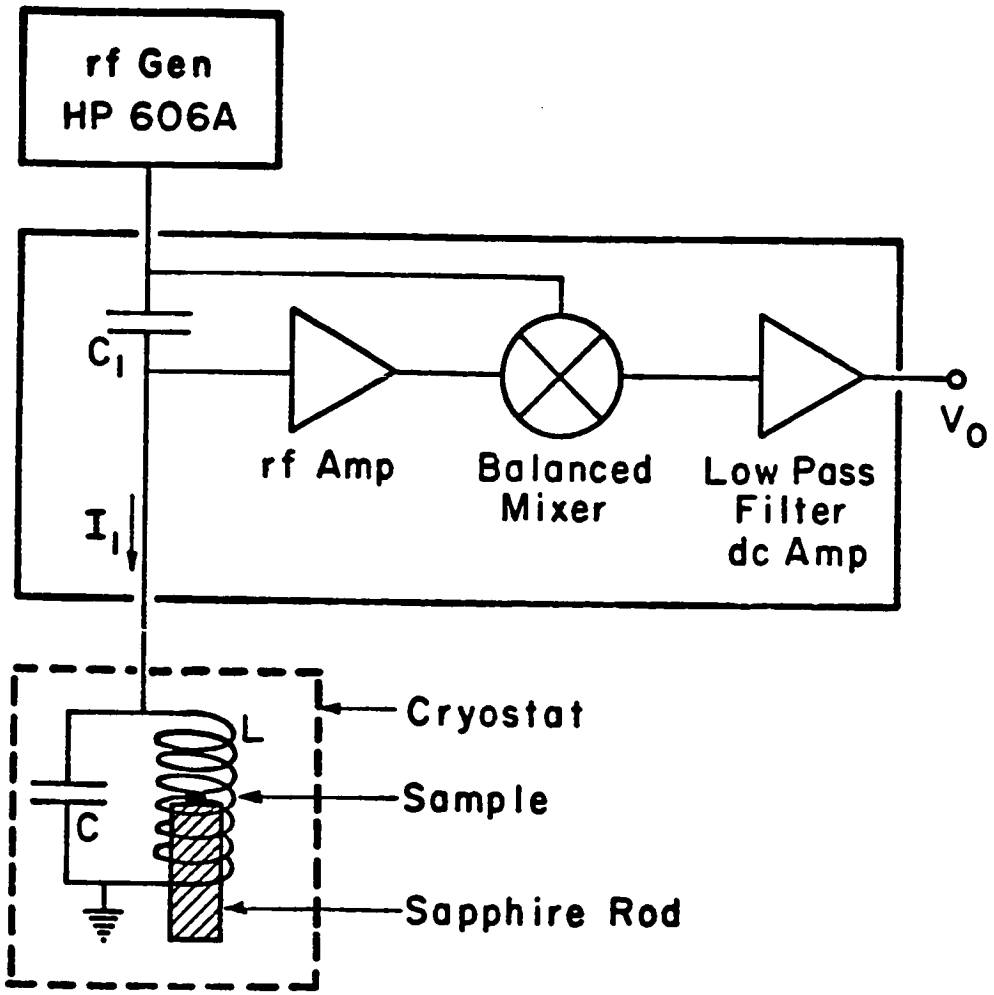

Fig. 4-2 Block diagram of the phase-sensitive detector used to measure shifts in the resonant frequency of the LC circuit.

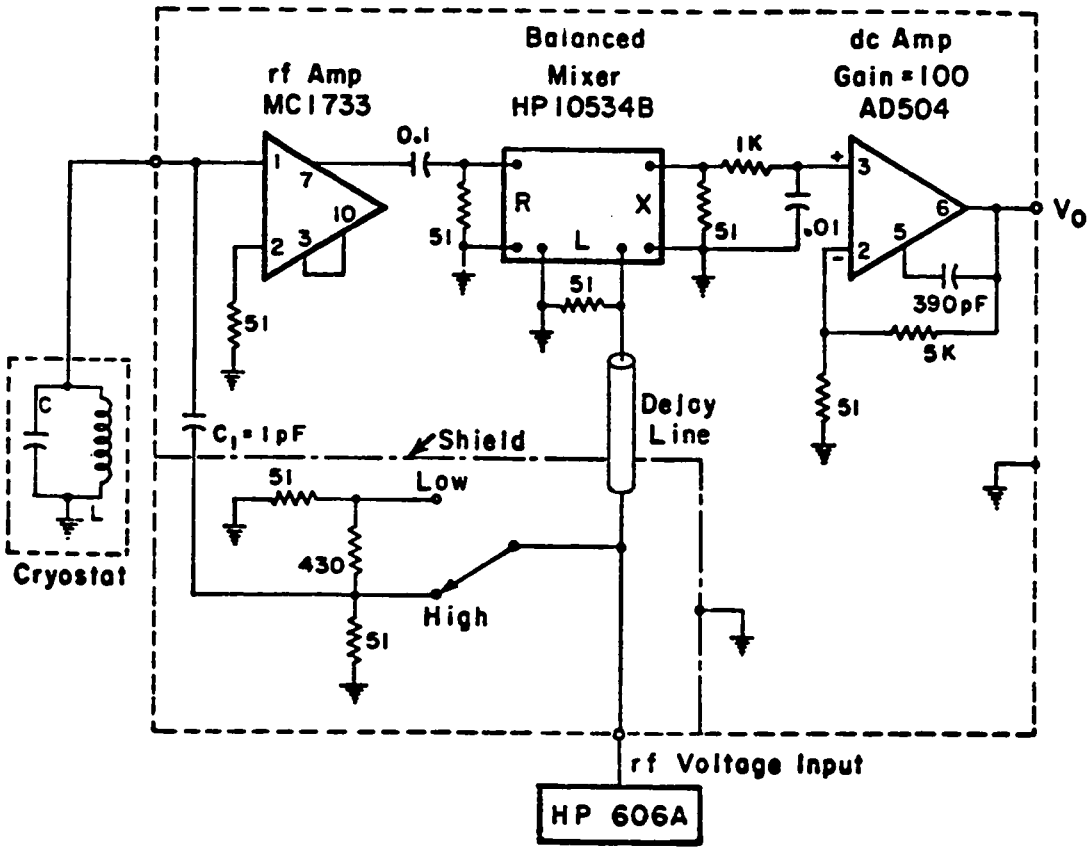

Fig. 4-3 Detailed schematic of the frequency-shift detector electronics. All the components inside the larger dashed box are mounted on a single circuit board inside a small aluminum box. The high-low switch allows the rf current supplied to the LC circuit to be reduced by a factor of 10. The two amplifiers are powered by a modular ±15 volt power supply (not shown). Resistances are in ohms and capacitances in μF, unless otherwise noted.

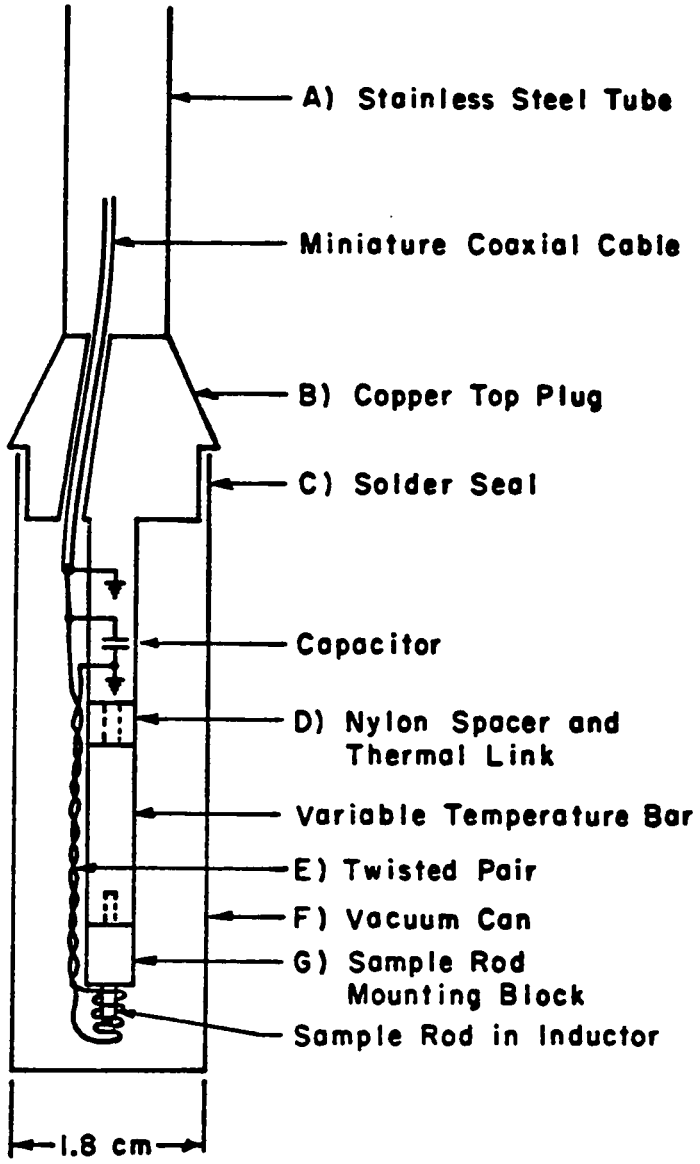

Fig. 4-4 Schematic diagram of the bottom of the dipstick cryostat (not to scale). The thermometers and heater (not shown) are mounted in holes in the variable-temperature bar. Also not shown are two small terminal strips on the top plug and the variable-temperature bar. For clarity, only one capacitor, coil, sample rod, ect. are shown although two sets actually exist.

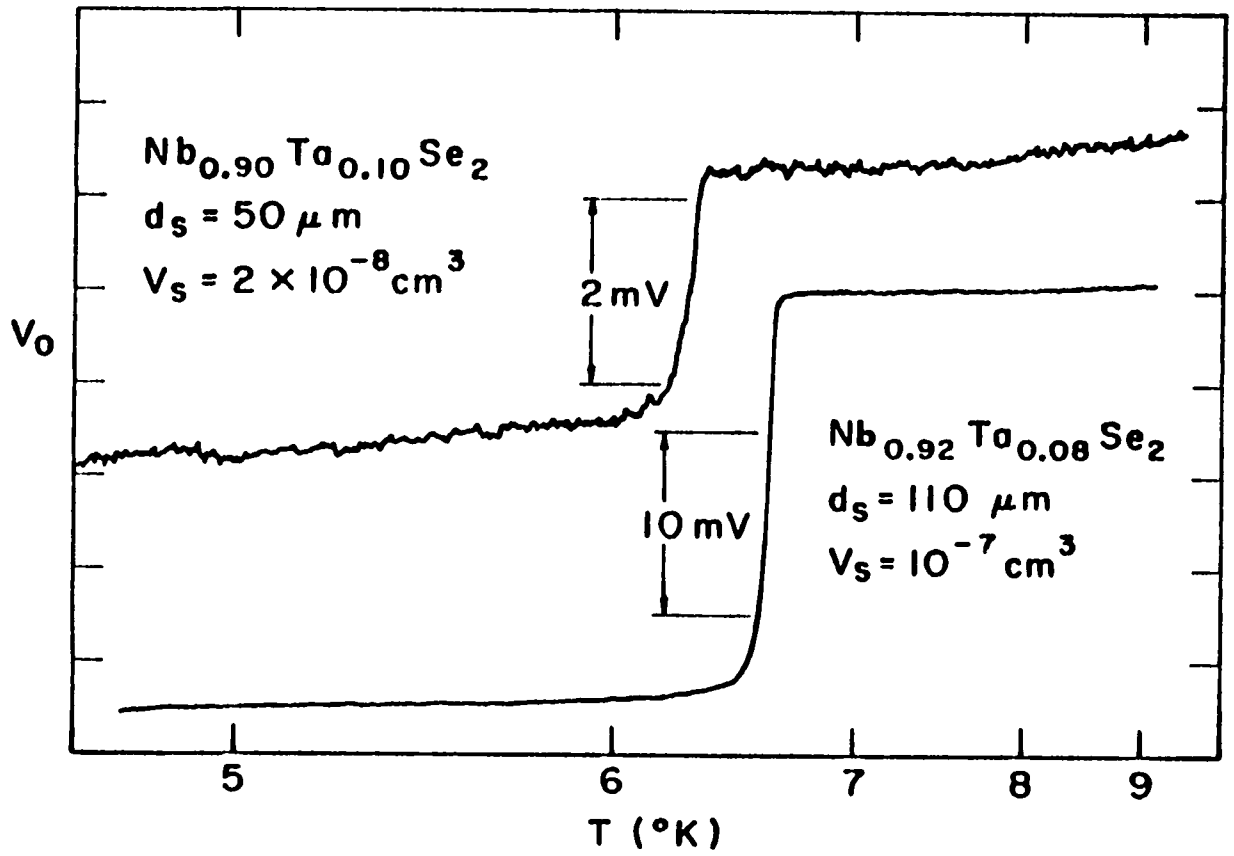

Fig. 4-5 The zero-field transitions as a function of temperature for two samples as recorded on an XY recorder. Both are thin hexagonal platelets approximately 10 μm thick. The mass of the smaller sample is approximately 0.13 μgm.

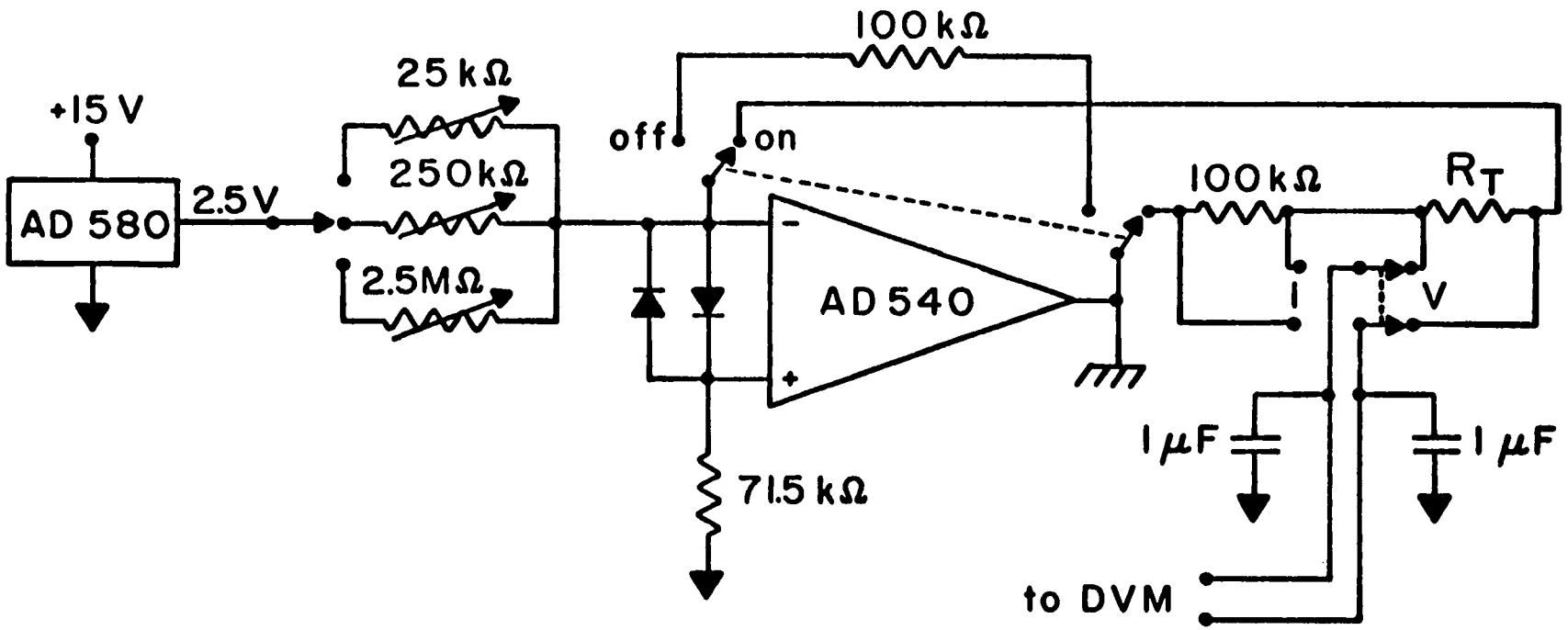

Fig. 4-6 Schematic diagram of the resistance thermometer current source. The AD 580 and the AD 540 are powered by a +15 volt power supply. The thermometer is shown here as R_T. The two diodes are small signal types (1N4446). The circuit is connected to the rack ground at the op-amp output. The other ground points shown are to the circuit-board ground (the common terminal of the power supply output).

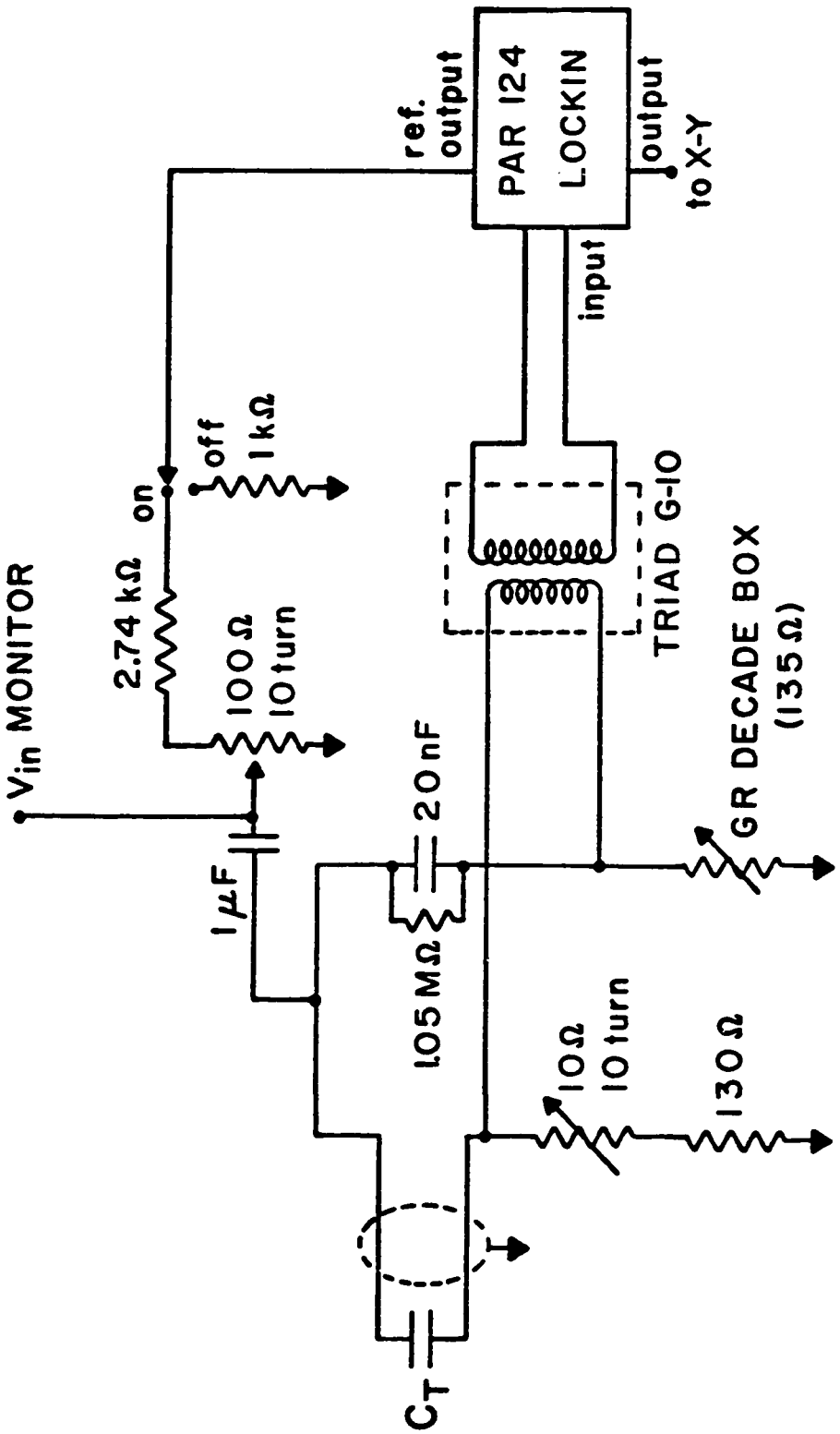

Fig. 4-7 Schematic diagram of the capacitance thermometer bridge circuit. The capacitance thermometer is shown here as C_T.

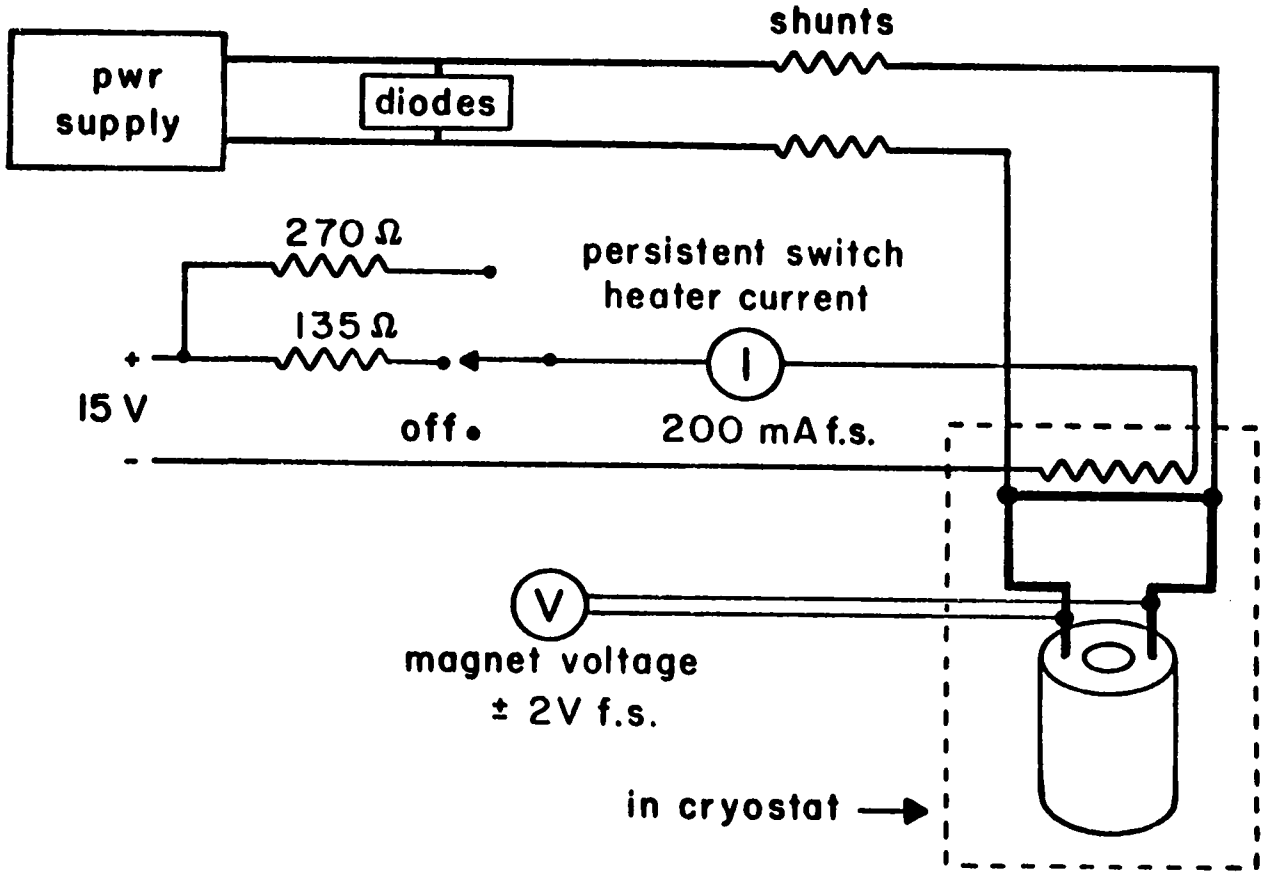

Fig. 4-8 Schematic diagram of the superconducting magnet control circuitry. The details of the diode array and the shunts are discussed in the text. The 15 volts for the persistent switch heater are supplied by a modular supply (not shown).

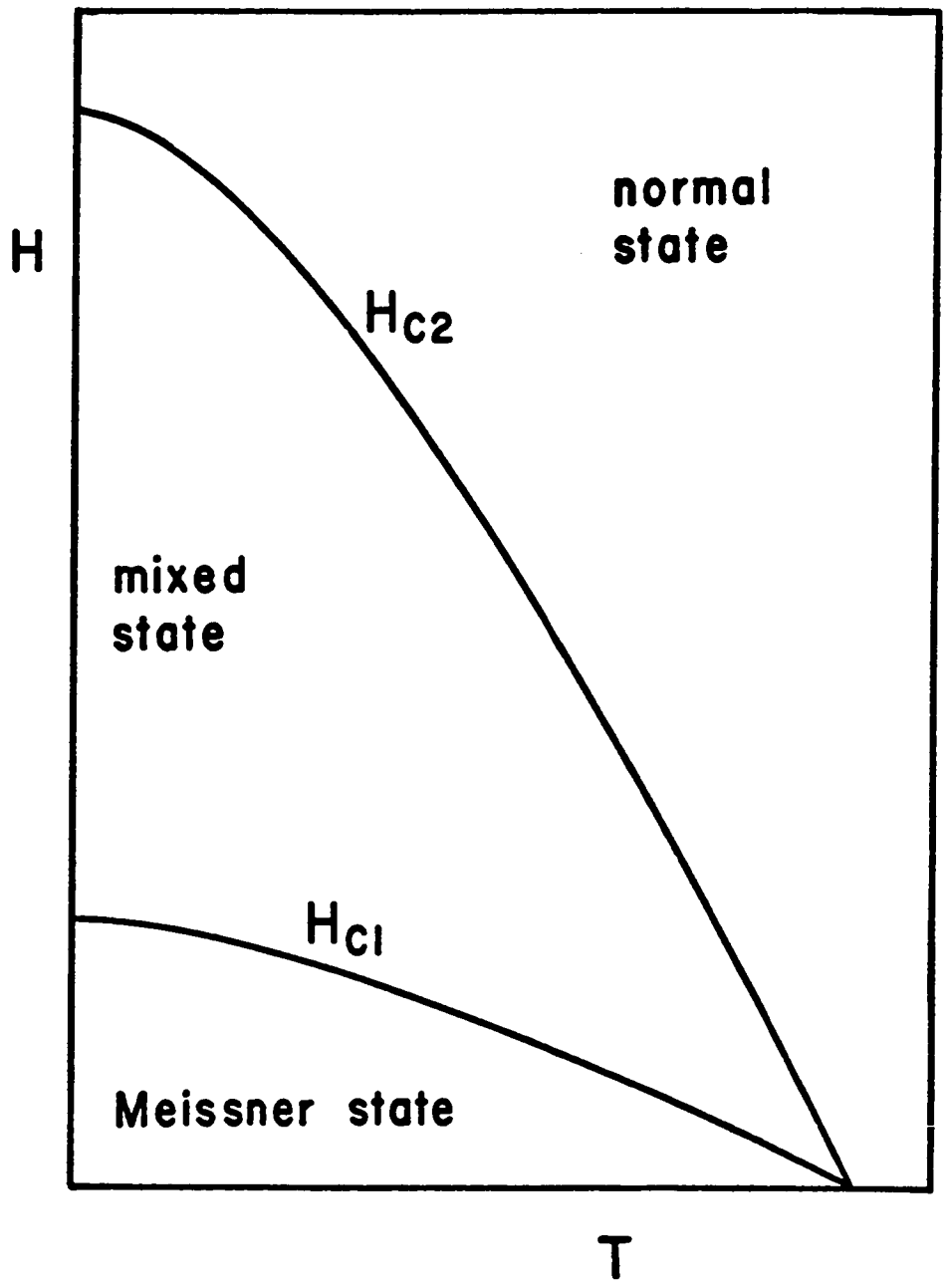

Fig. 5-1 The two critical fields $H_{c1}(T)$ and $H_{c2}(T)$ of a type II superconductor (schematic).

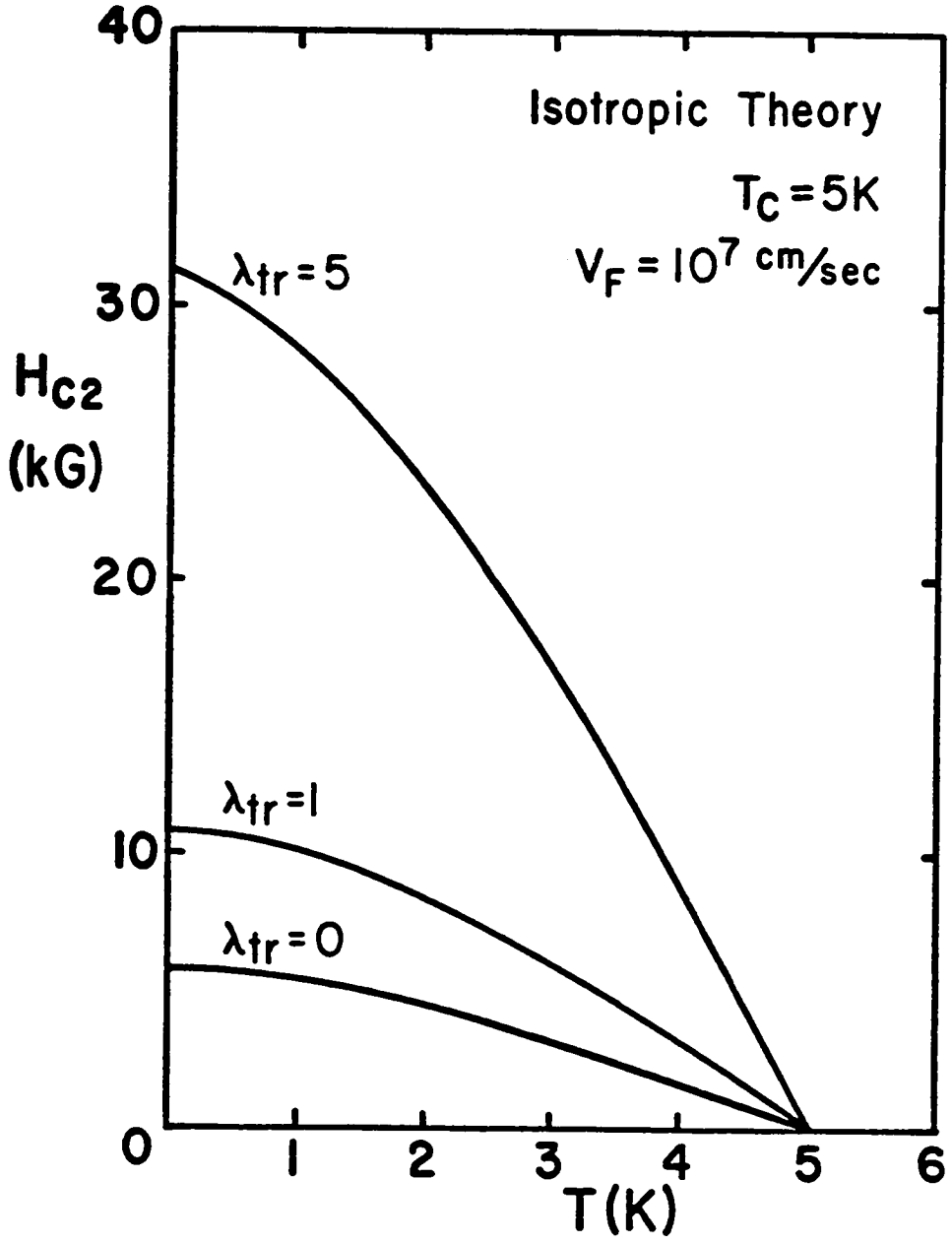

Fig. 5-2 The upper critical field for several values of the normalized scattering rate λ_{tr}, HW theory.

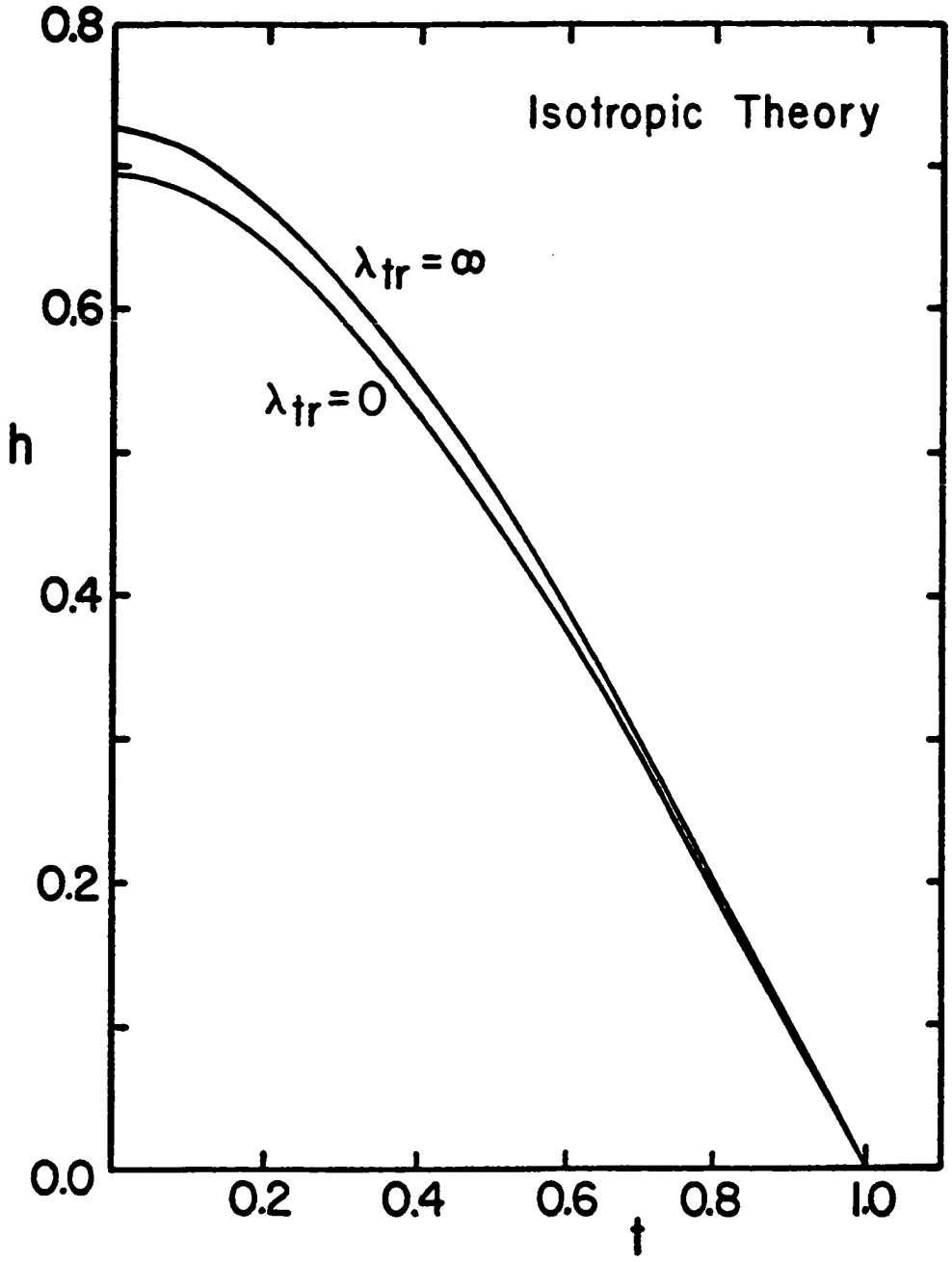

Fig. 5-3 The normalized upper critical field h as a function of the reduced temperature t for the clean and dirty limits, HW theory.

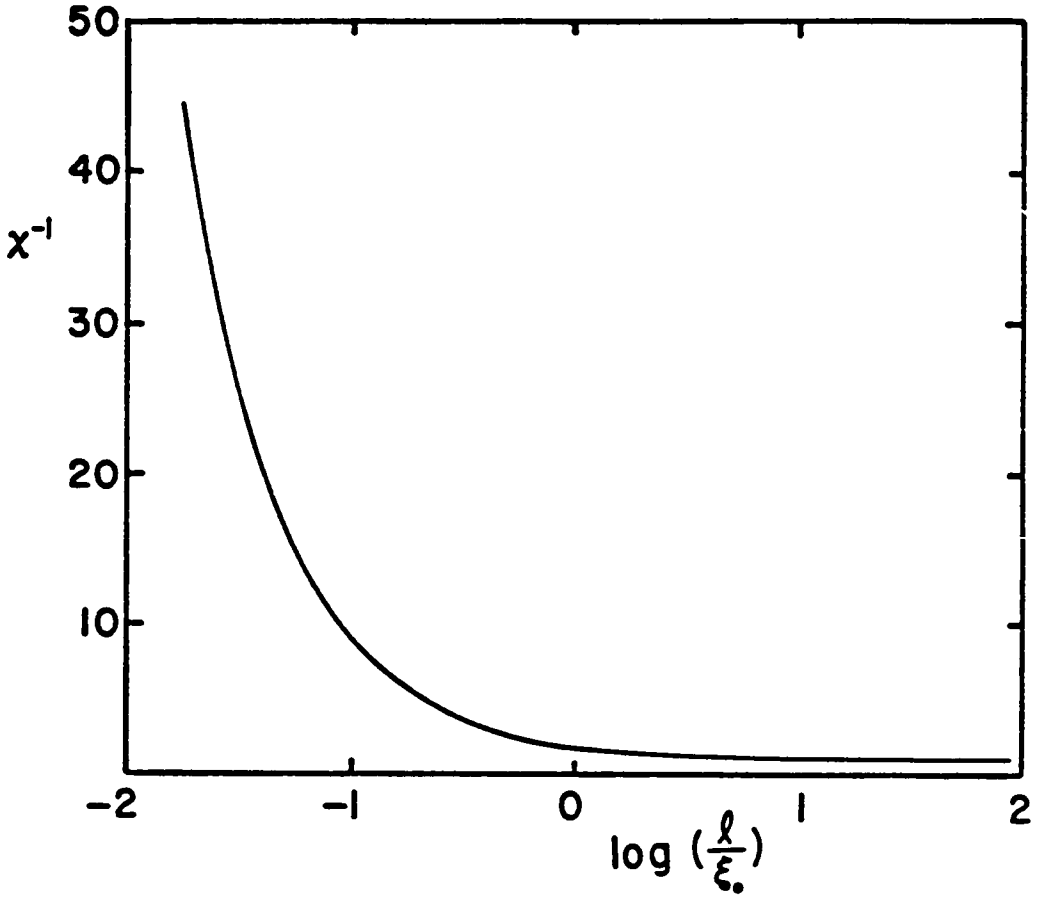

Fig. 5-4 The inverse Gor'kov function as a function of the electronic mean free path ℓ. Within the isotropic, weak-coupling theory this function gives the dependence of the upper critical field on ℓ. Mean free path effects become increasingly less important for cleaner materials, where ℓ is large relative to the coherence length.

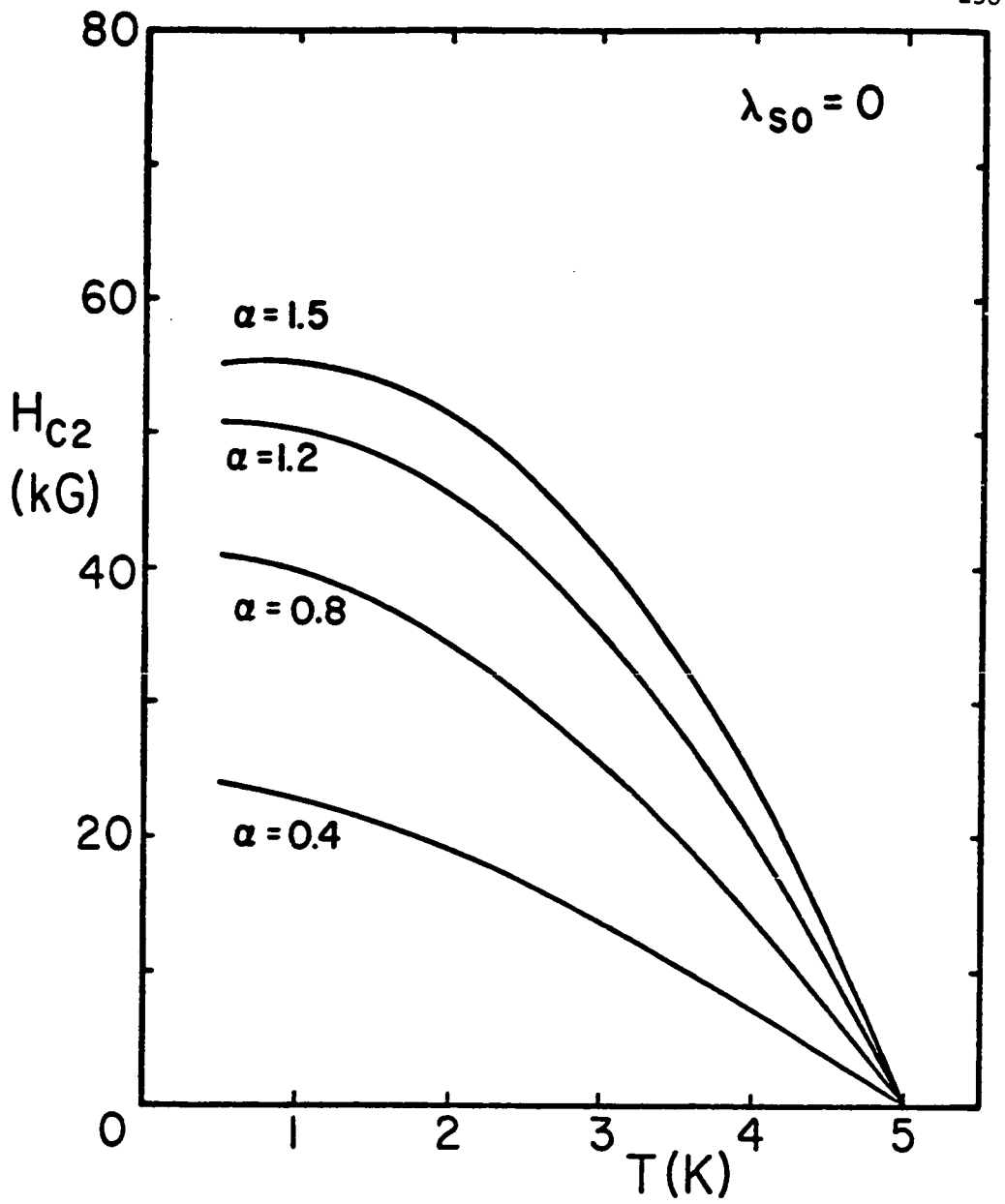

Fig. 5-5 Several upper critical field curves with no spin-orbit scattering, WHH theory. The higher α curves bend toward the field axis more rapidly at low temperatures because of the field-spin interaction, important only in large fields. The simple Pauli limiting field $18.6T_c$ = 91 kG here.

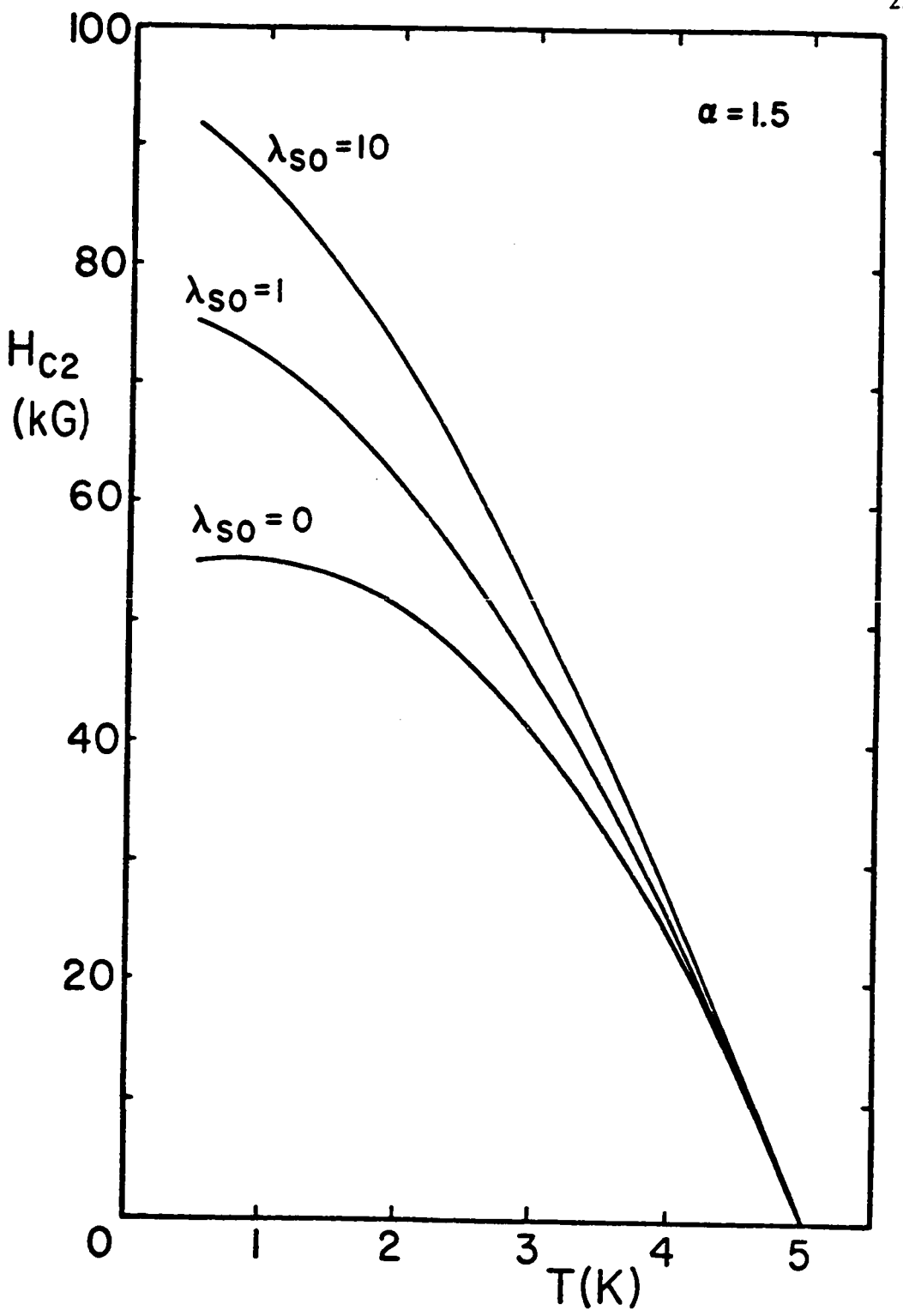

Fig. 5-6 $H_{c2}(T)$ for several values of λ_{tr}, WHH theory. Increasing the spin-orbit scattering rate negates the inhibiting effects of the field-spin interaction. $18.6T_c$ = 91 kG here.

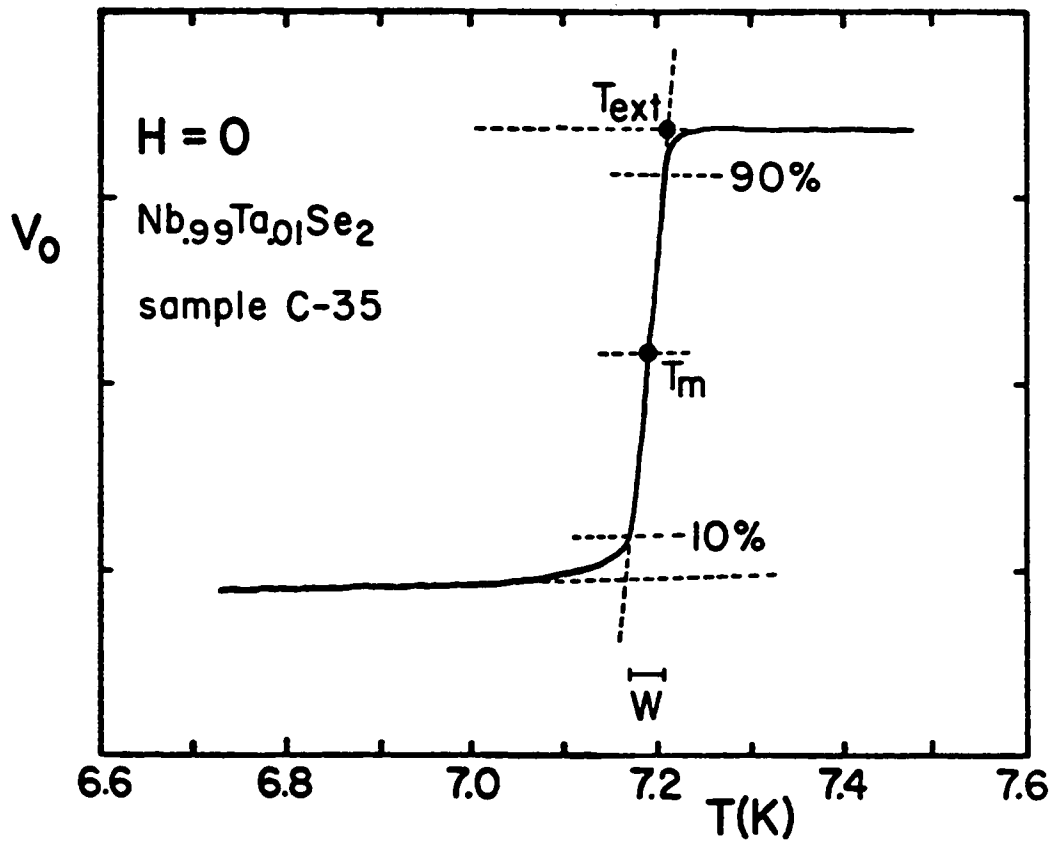

Fig. 6-1 The zero-field transition curve, sample C-35, showing the definitions of T_m, T_{ext}, W.

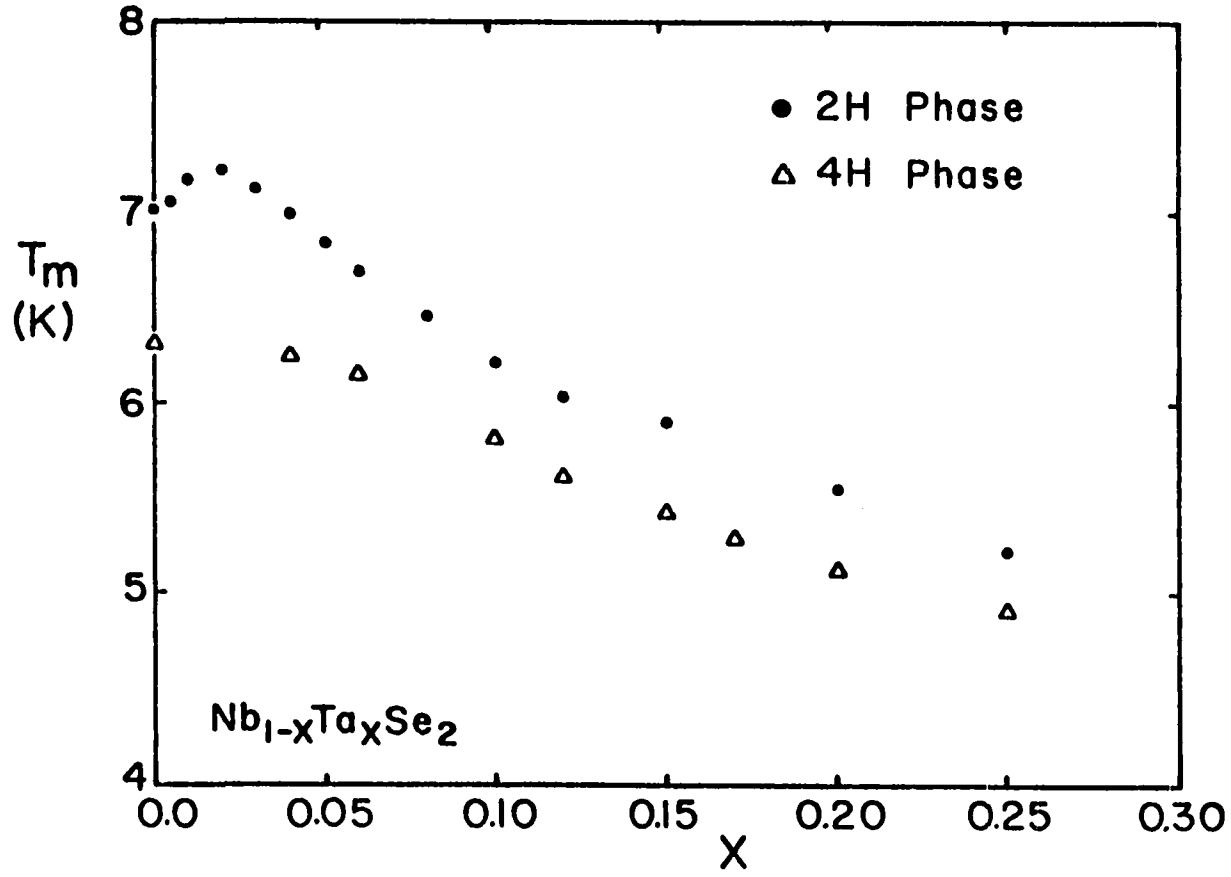

Fig. 6-2 The midpoint transition temperature T_m as a function of composition for the 2H and 4H phases. This data is a composite of a large number of measurements made on samples from many different crystal growth batches.

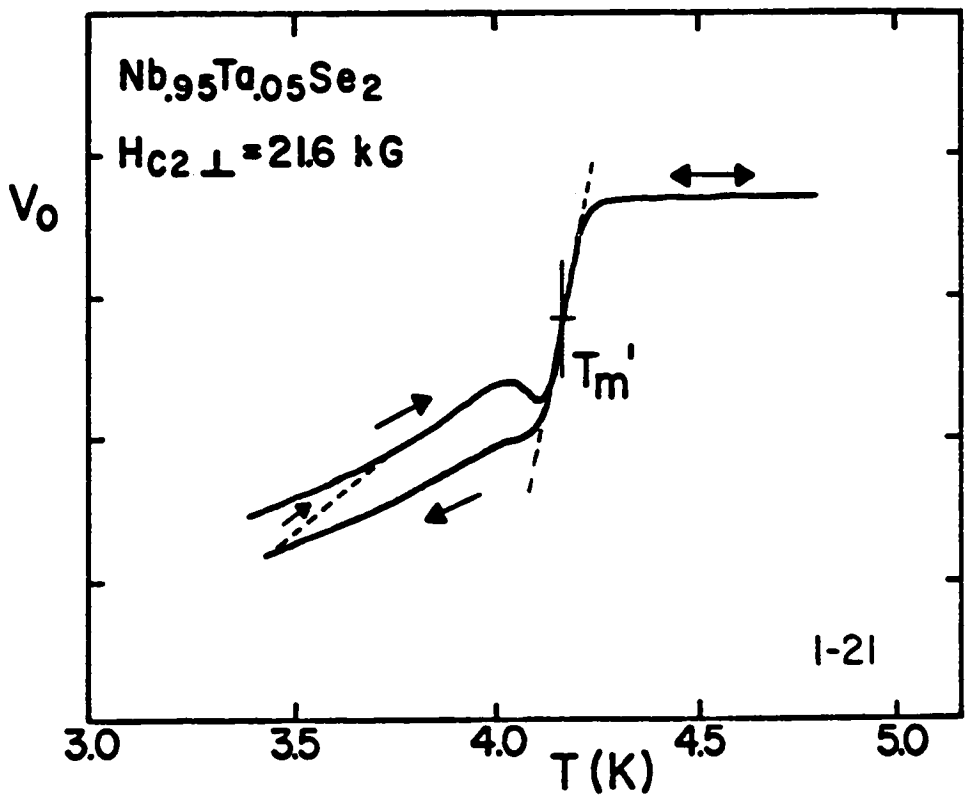

Fig. 6-3 A transition curve in a 21.6 kG magnetic field oriented perpendicular to the layer plane. The arrows indicate the direction of the temperature sweep corresponding to the various parts of the output trace. Also shown is the definition of the midpoint temperature T_m'.

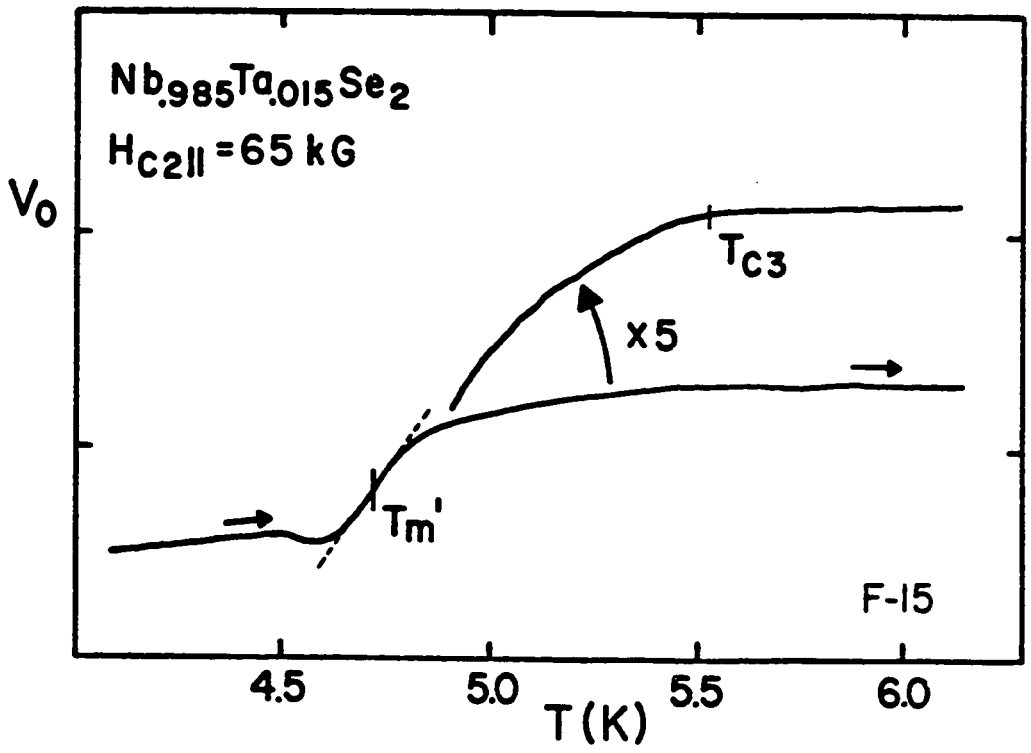

Fig. 6-4 A transition curve in a 65 kG field oriented parallel to the layer plane, sample F-15. Only one direction of temperature sweep is shown here. The output above the main transition is also shown on an enlarged scale showing the evidence for surface superconductivity. Only data taken in an increasing temperature sweep are shown here, thus no hysteresis is seen below the main transition.

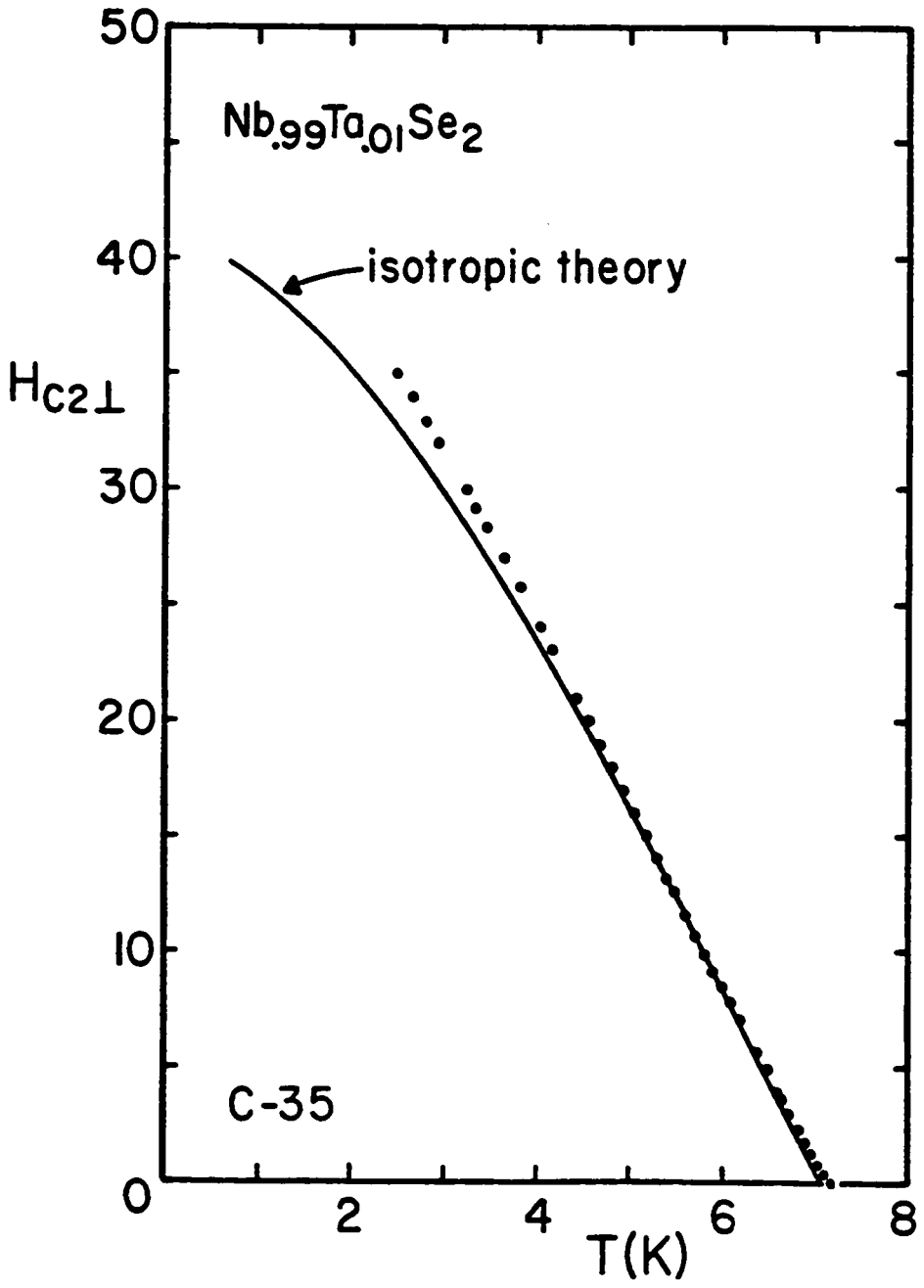

Fig. 6-5 The perpendicular critical field of sample C-35. Also shown is the temperature dependence of the isotropic, clean-limit theoretical result scaled by an arbitrary factor to obtain a best fit at intermediate temperatures.

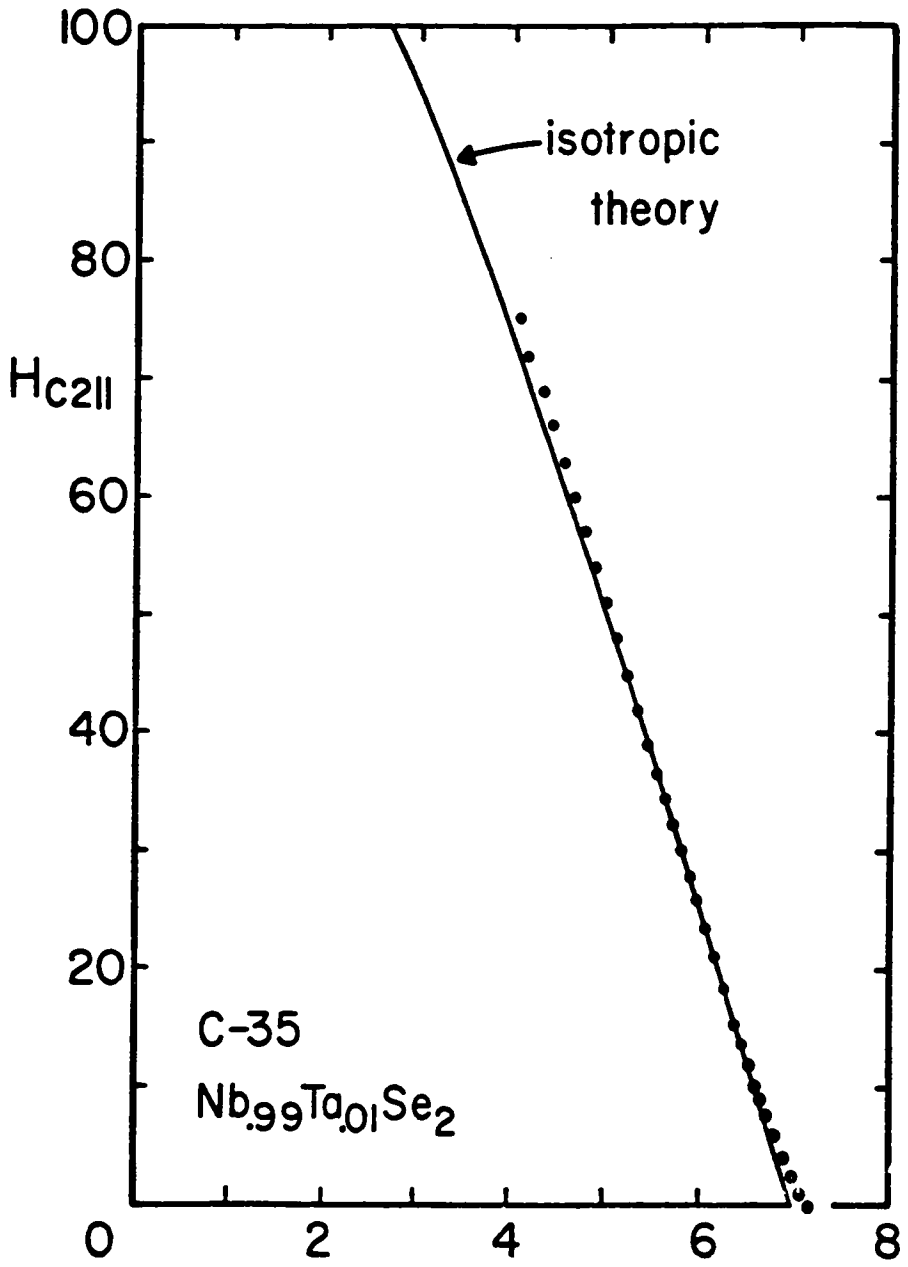

Fig. 6-6 The parallel critical field of sample C-35. Also shown is the temperature dependence of the isotropic, clean-limit theoretical result scaled by an arbitrary factor to obtain a best fit at intermediate temperatures.

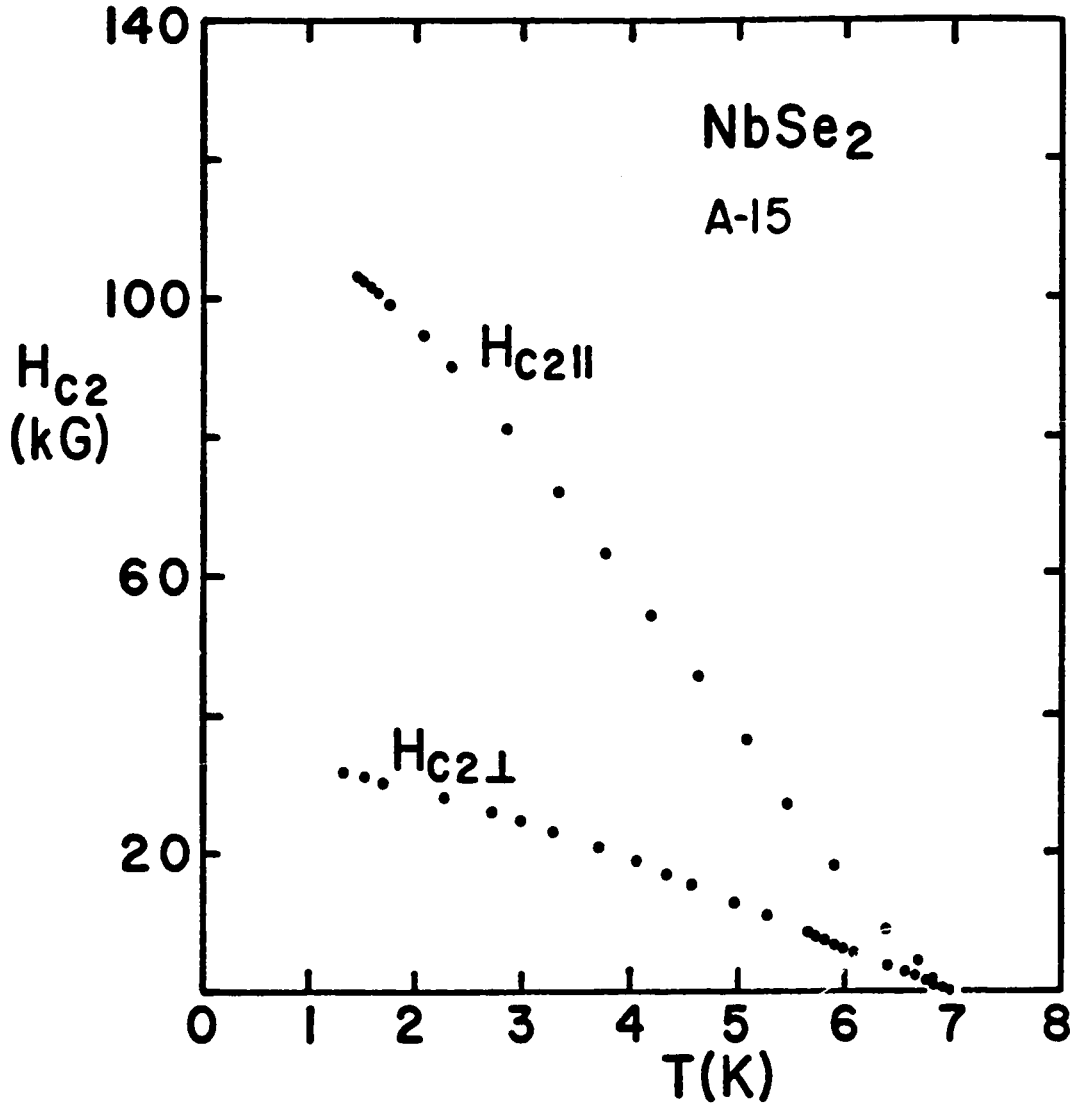

Fig. 6-7 The perpendicular and parallel critical fields of $NbSe_2$, sample A-15.

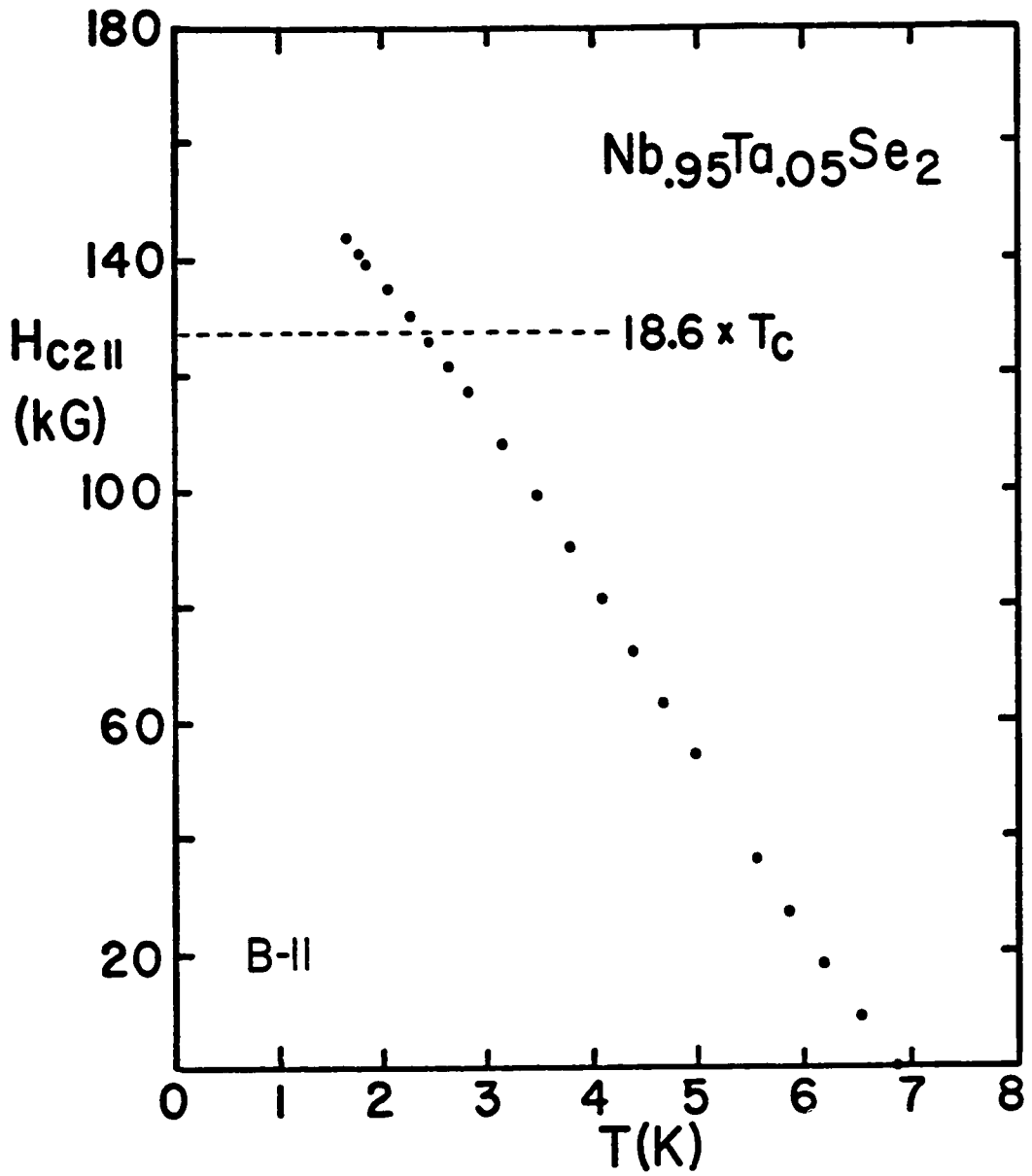

Fig. 6-8 An example of the apparent lack of Pauli paramagnetic limiting in these materials; the parallel critical field of $Nb_{.95}Ta_{.05}Se_2$, sample B-11. A dashed line has been drawn at a field equal to $18.6T_c$, the simple Pauli paramagnetic limiting value.

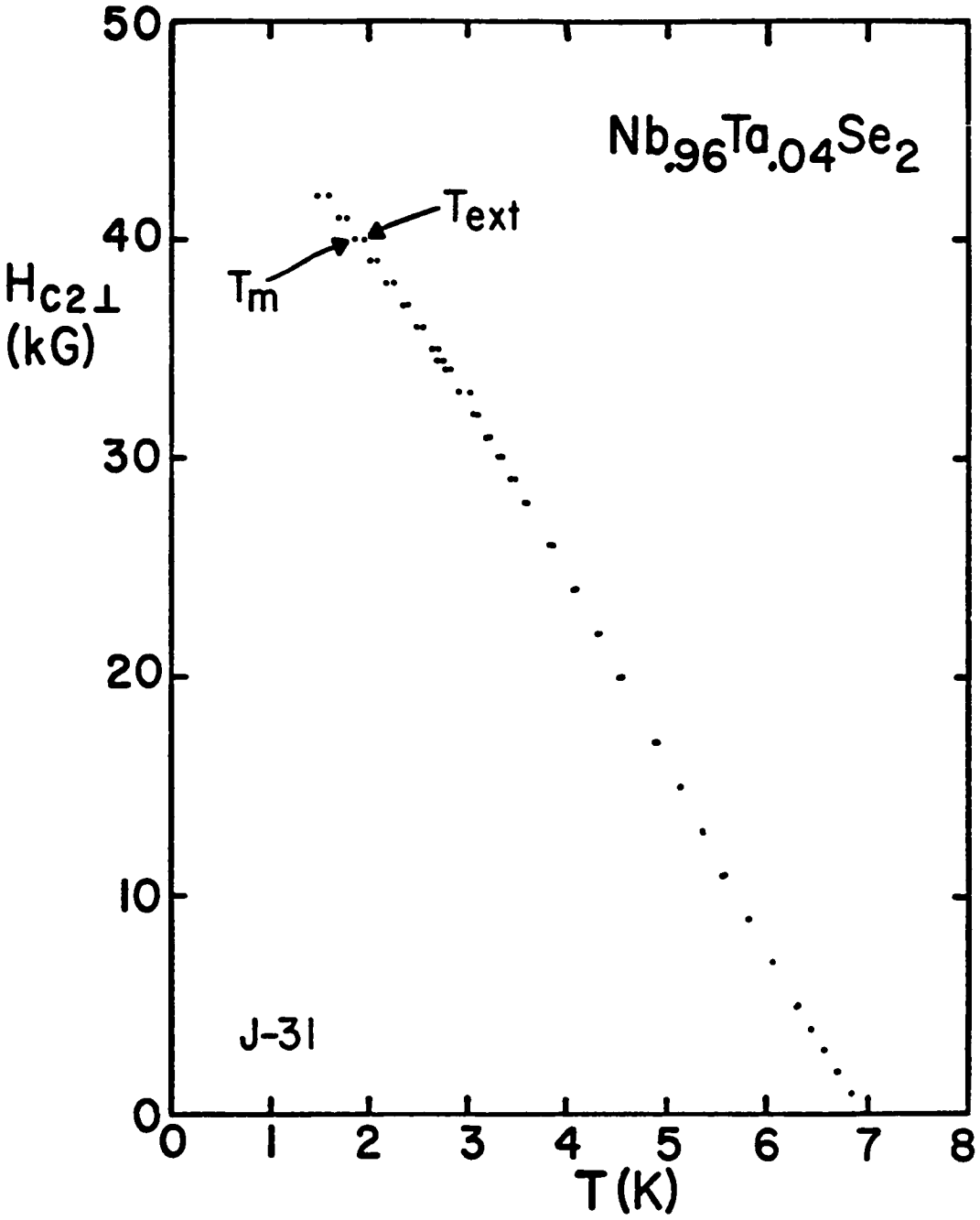

Fig. 6-9 The perpendicular critical field defined both by T_{ext} and by T_m', sample J-31. The two temperatures separate slightly at higher fields as the transition width increases.

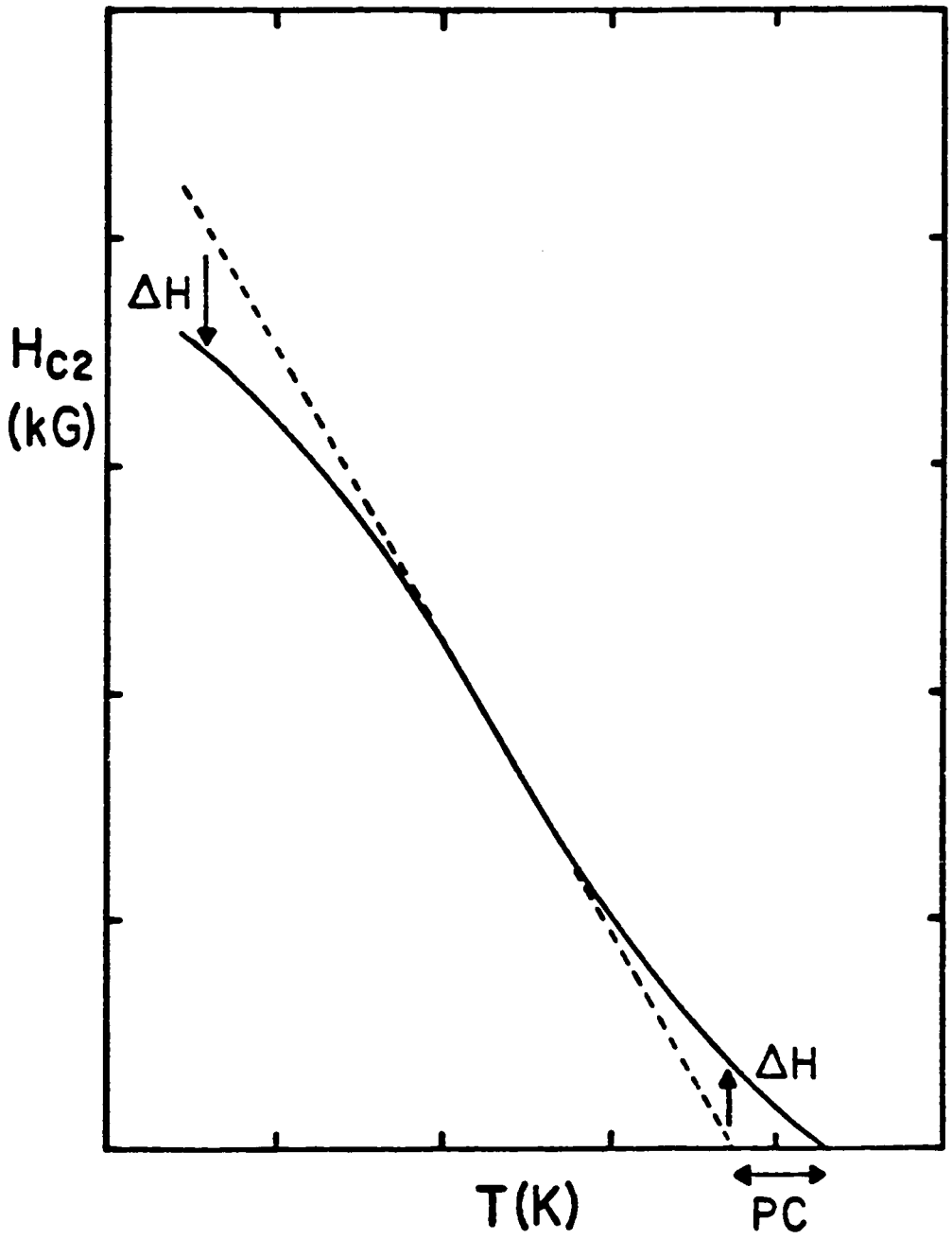

Fig. 6-10 A schematic illustration of how ΔH and the amount of positive curvature (PC) are defined. The experimental data are represented here by the solid line. The straight line fit to the data is shown by the dashed line.

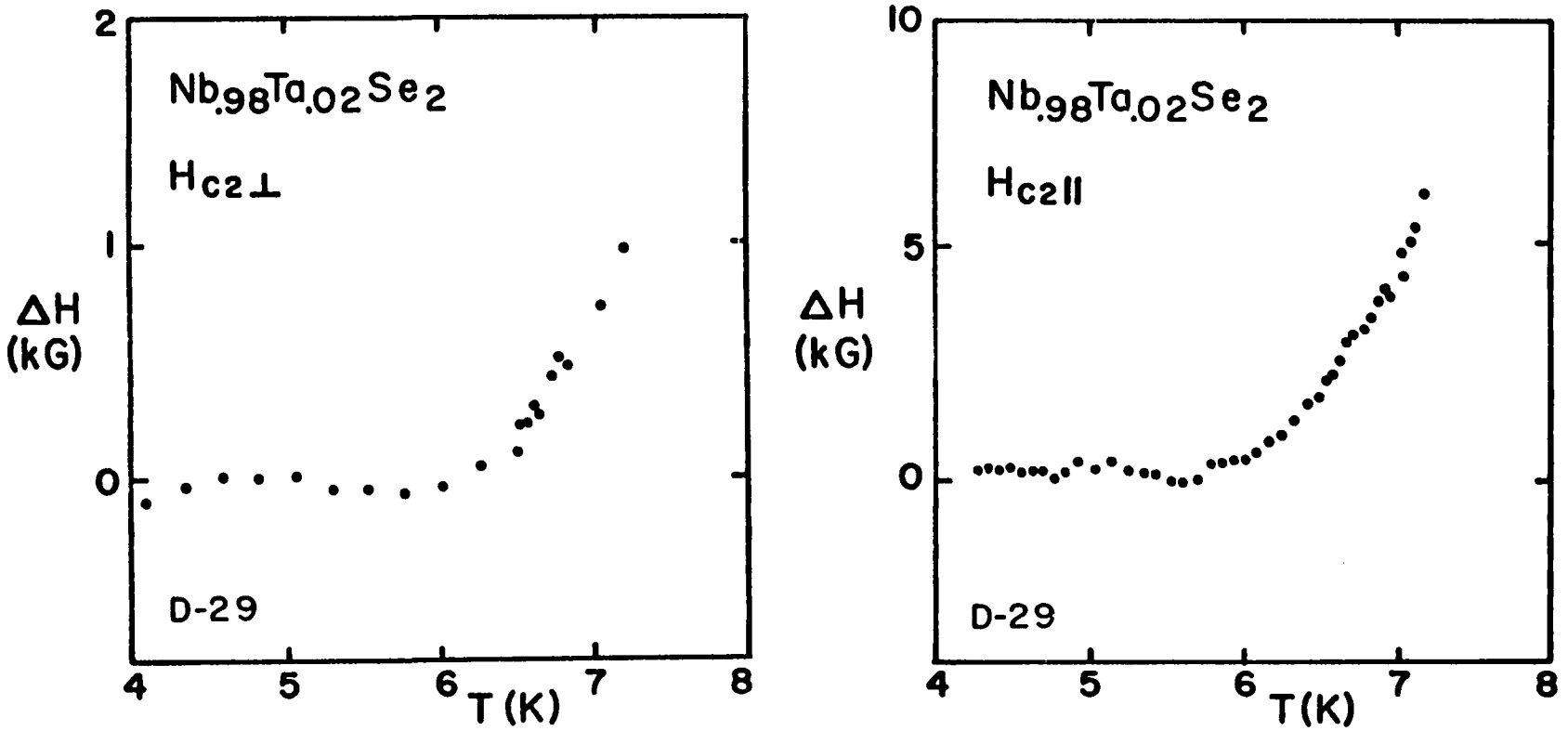

Fig. 6-11 ΔH for sample D-29. Only the higher-temperature points are shown. ΔH becomes negative at lower temperatures as $H_{c2}(T)$ bends toward the field axis.

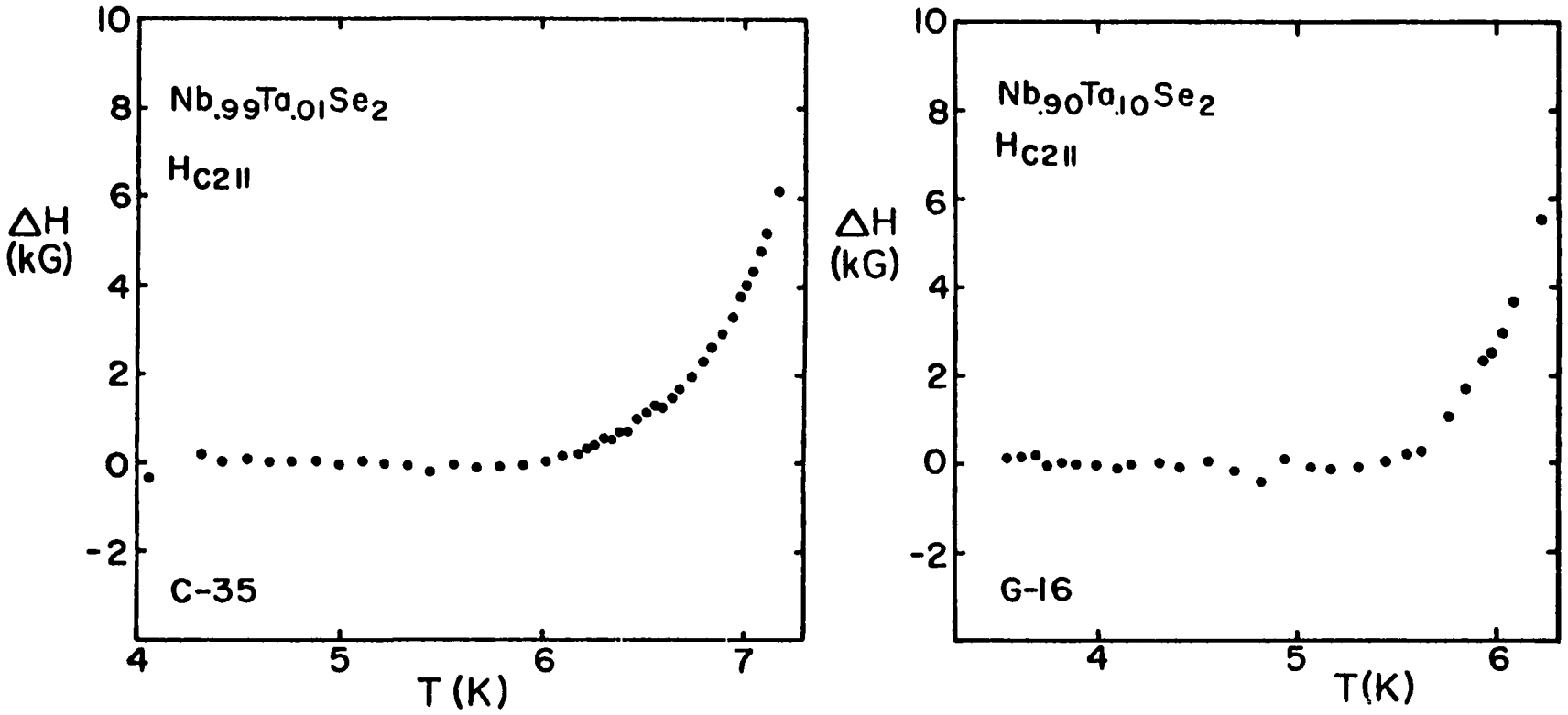

Fig. 6-12 ΔH for the parallel critical field data for 1% and 10% alloys. Only the higher-temperature points are shown.

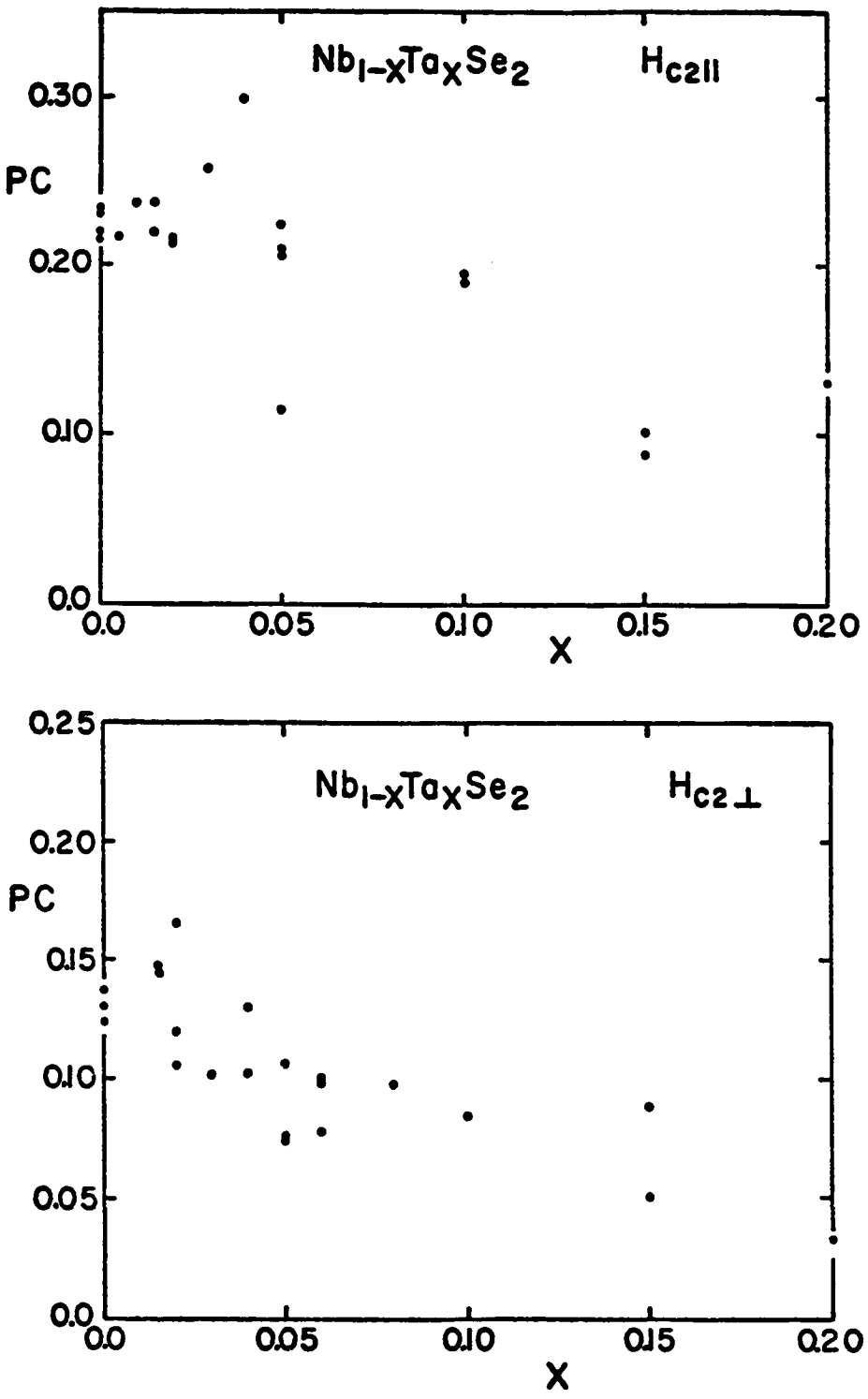

Fig. 6-13 The amount of positive curvature (PC) seen in the parallel and perpendicular critical field data as a function of composition.

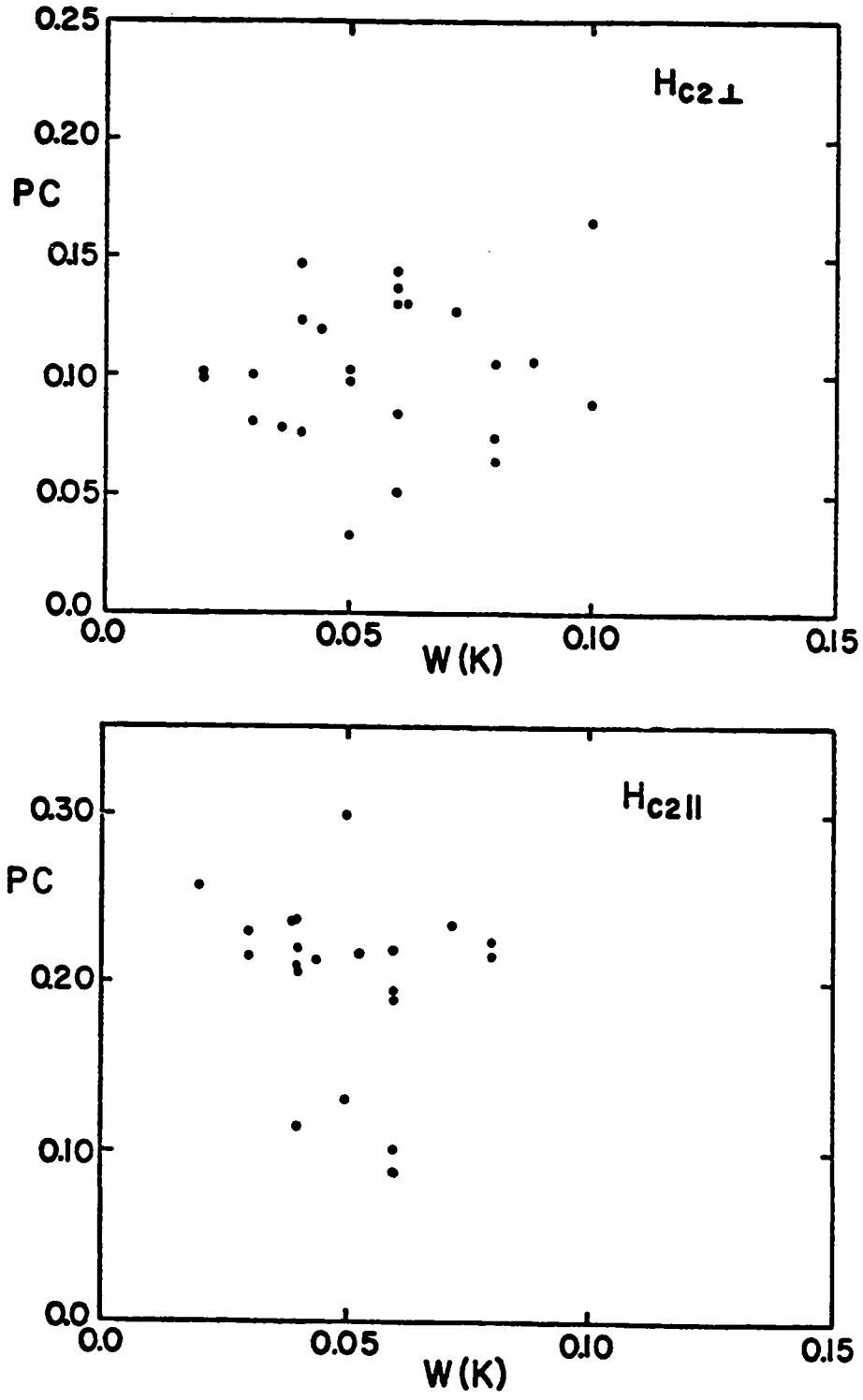

Fig. 6-14 The amount of positive curvature seen in $H_{c2\perp}(T)$ and $H_{c2\parallel}(T)$ as a function of the zero-field transition width W. W may be taken as a simple measure of crystal quality.

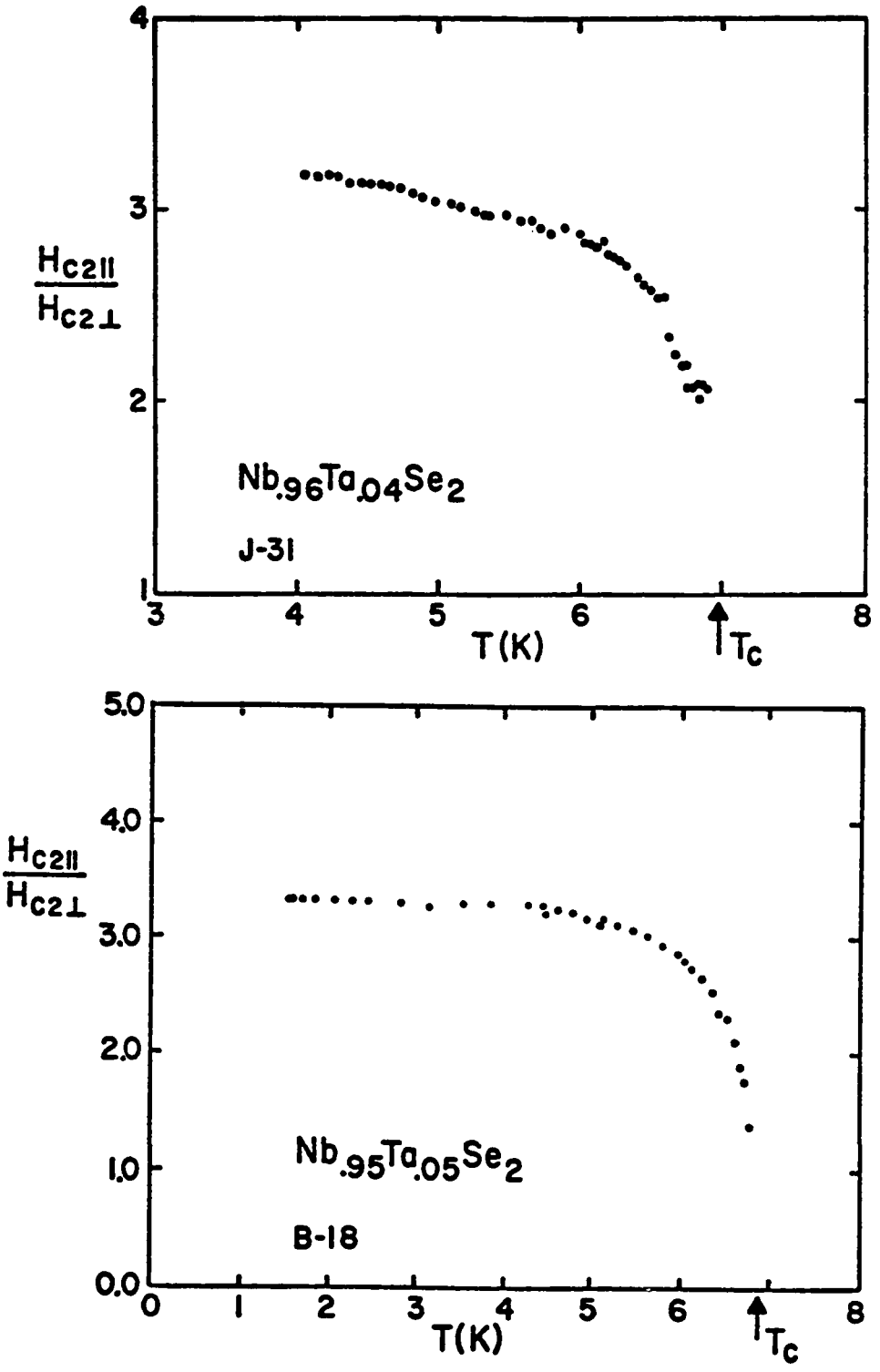

Fig. 6-15 The anisotropy in the critical fields as a function of temperature for two samples.

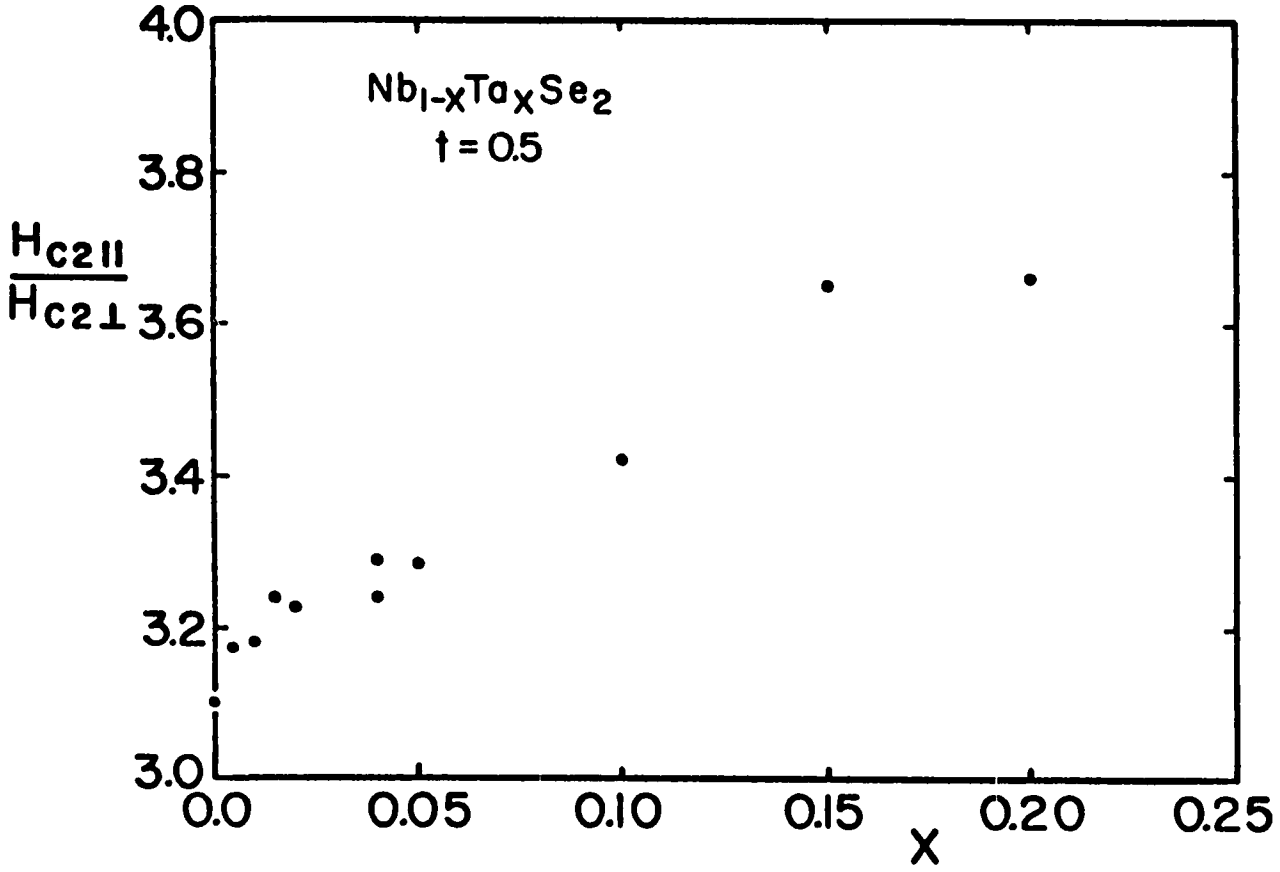

Fig. 6-16 The anisotropy in the critical fields as a function of composition at t = 0.5.

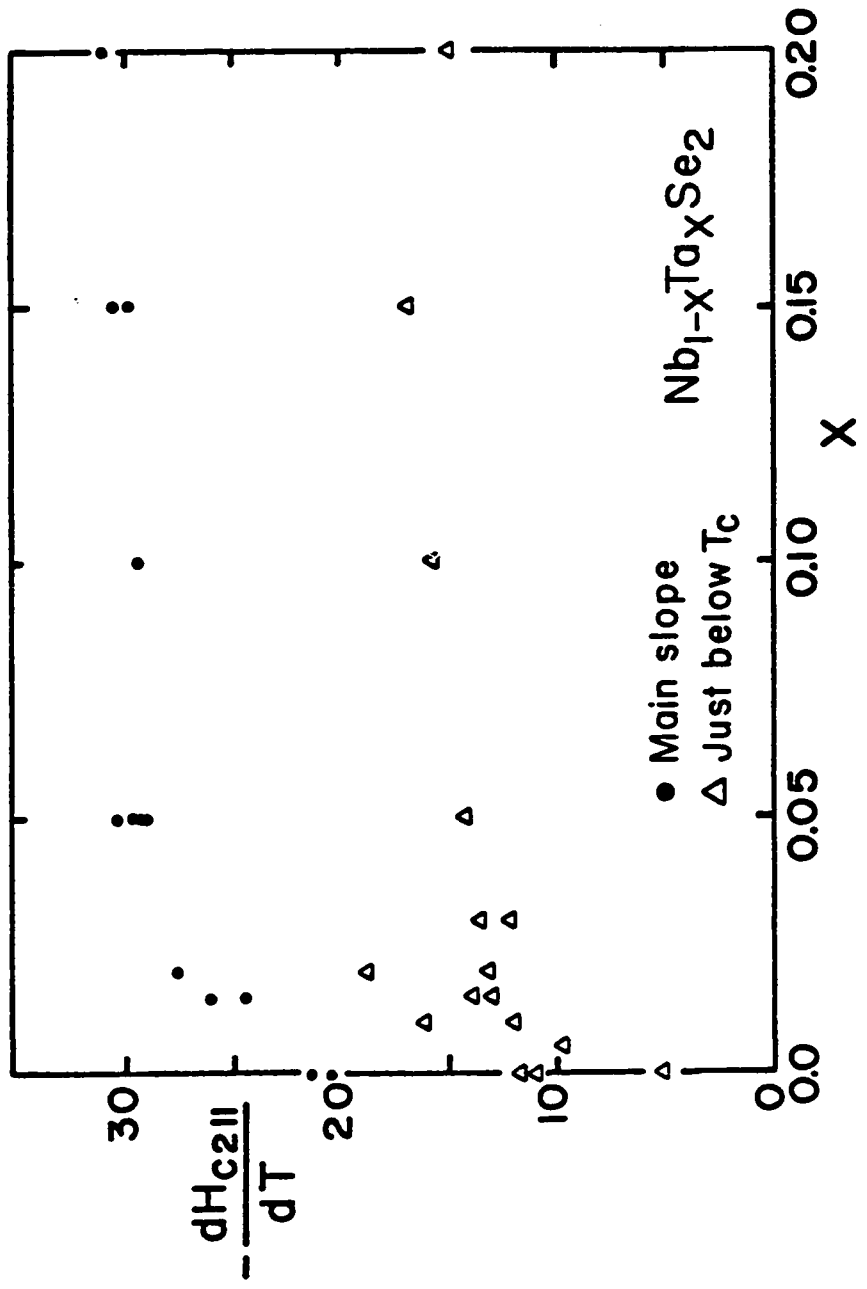

Fig. 6-17 The parallel critical field slope as a function of composition.

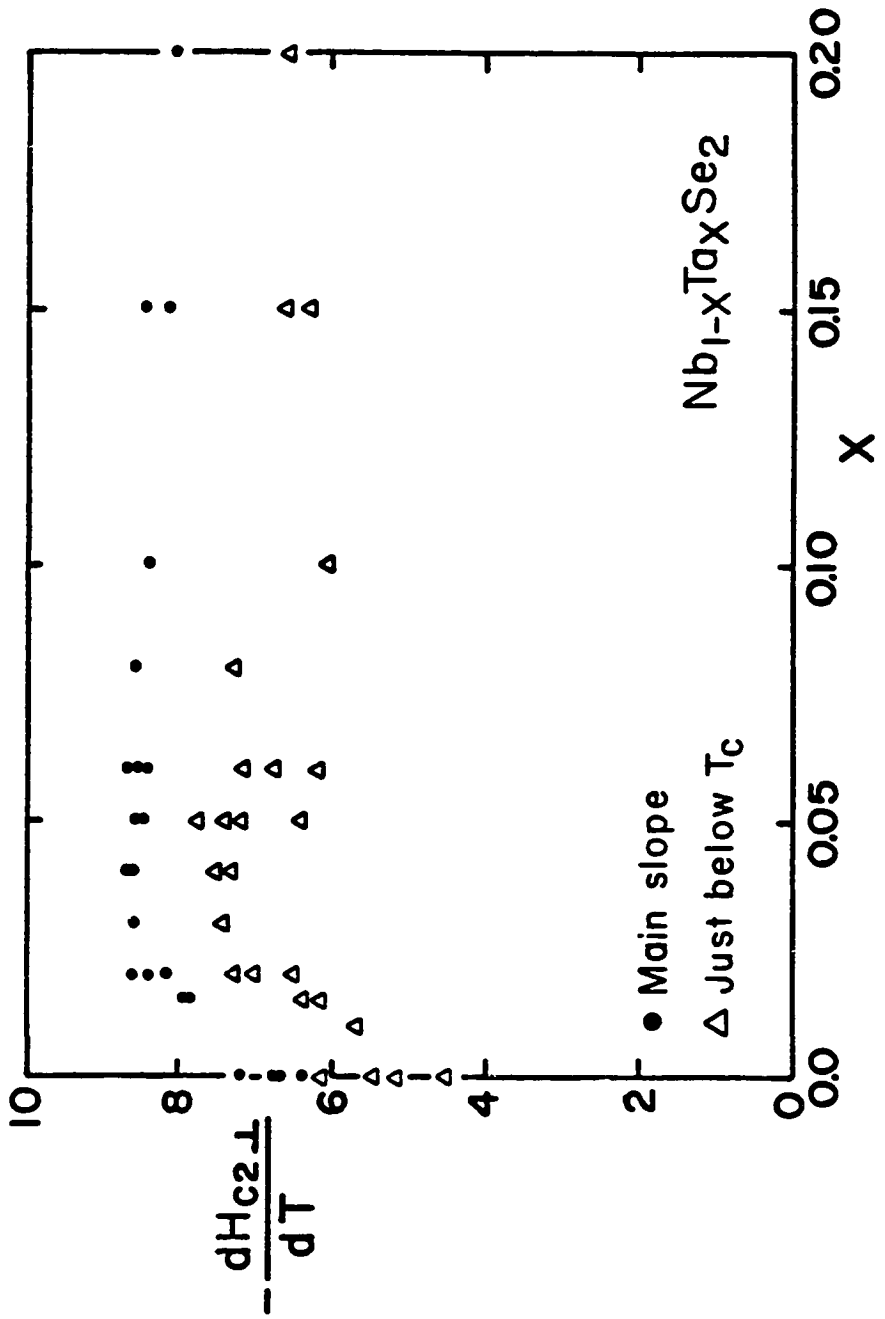

Fig. 6-18 The perpendicular critical field slope as a function of composition.

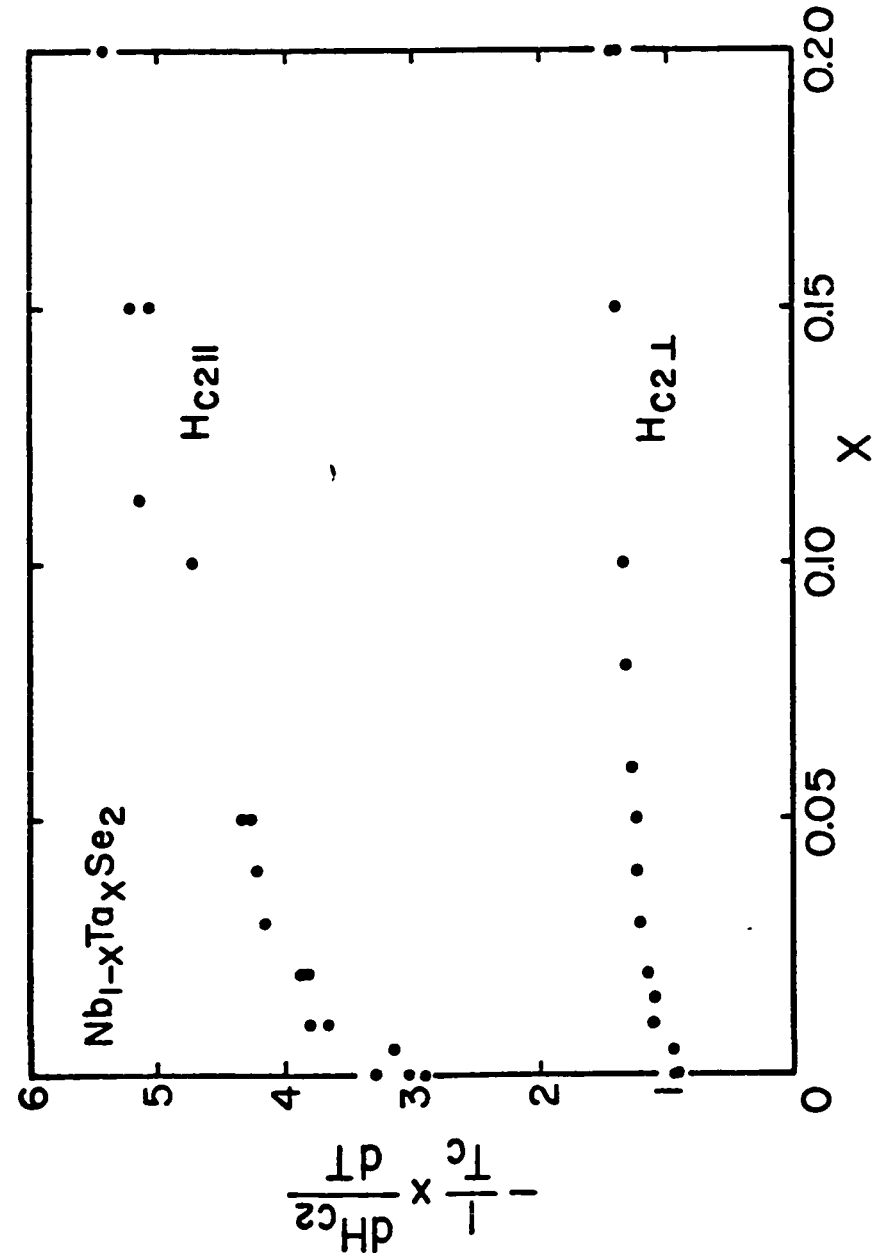

Fig. 6-19 The slopes of the main linear sections of the critical field curves for both field orientations with the T_c dependence normalized out.

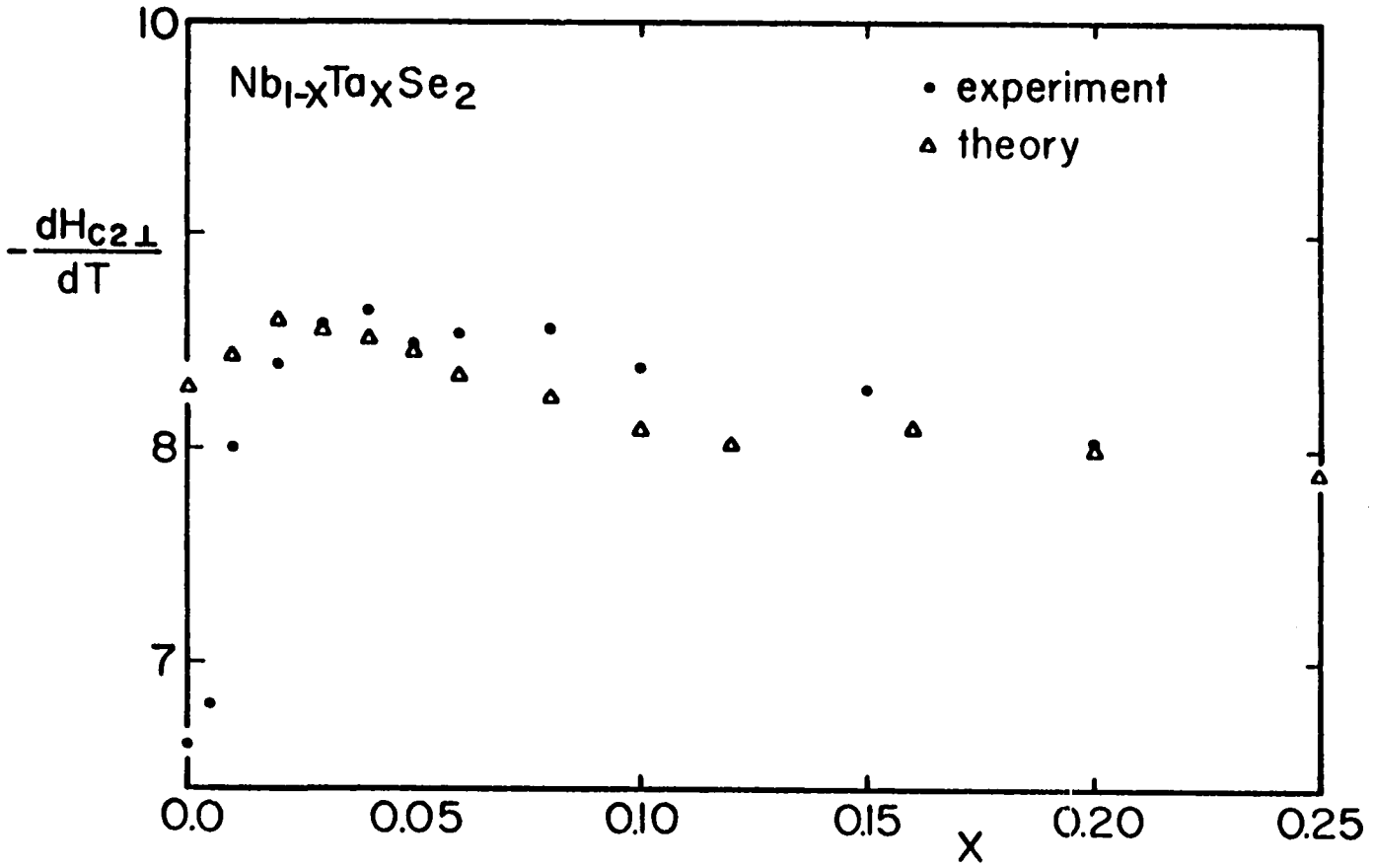

Fig. 6-20 The slope of the main linear section of H_{c2} (T) as a function of composition. Also shown is a theoretical result incorporating T_c and mfp effects. The disagreement at small x is caused by band structure changes associated with suppression of the CDW.

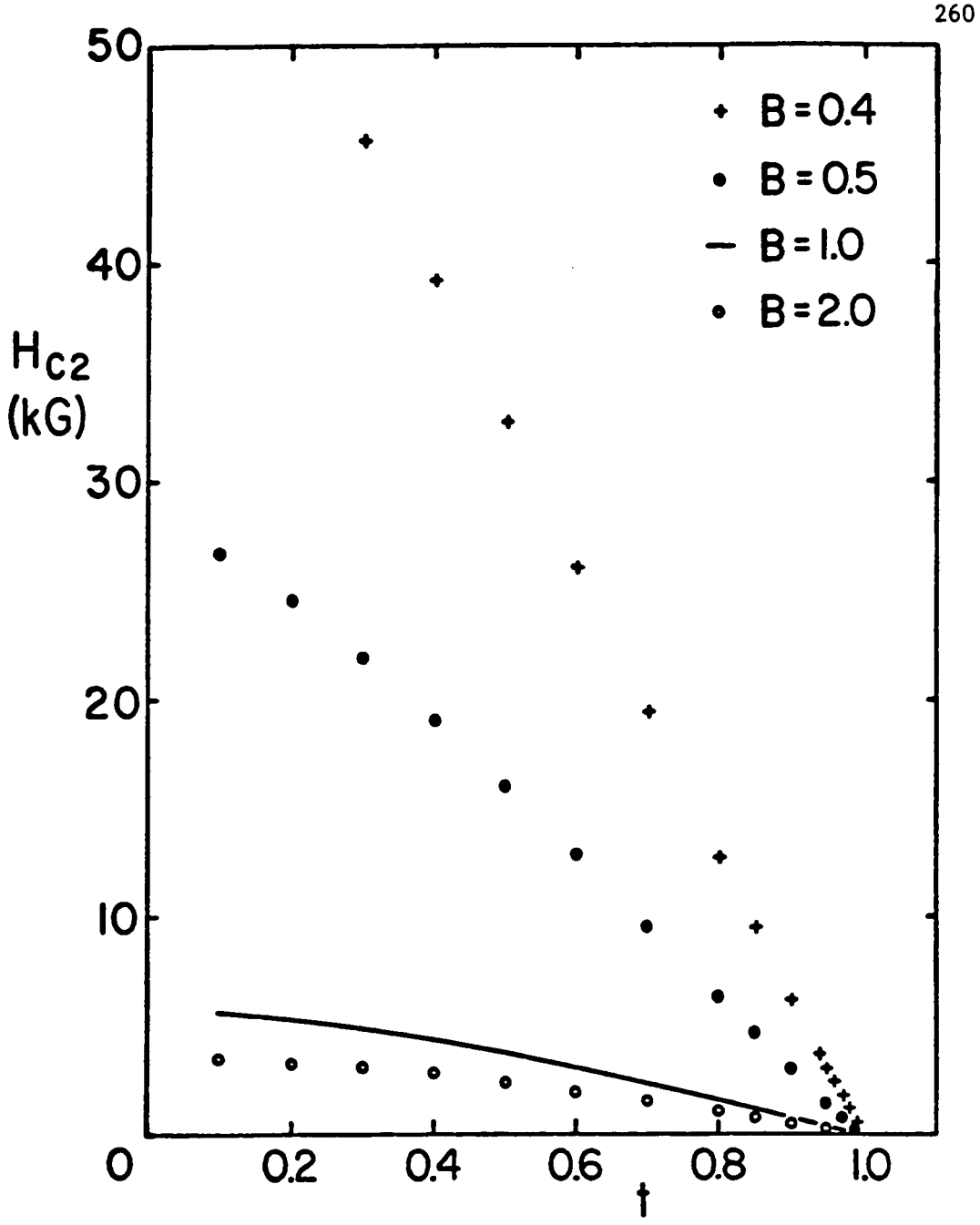

Fig. 7-1 Critical field curves for the ellipsoidal Fermi surface model for various values of the Fermi surface shape parameter B. Here T_c = 5 K and $v_F = 10^7$ cm/sec.

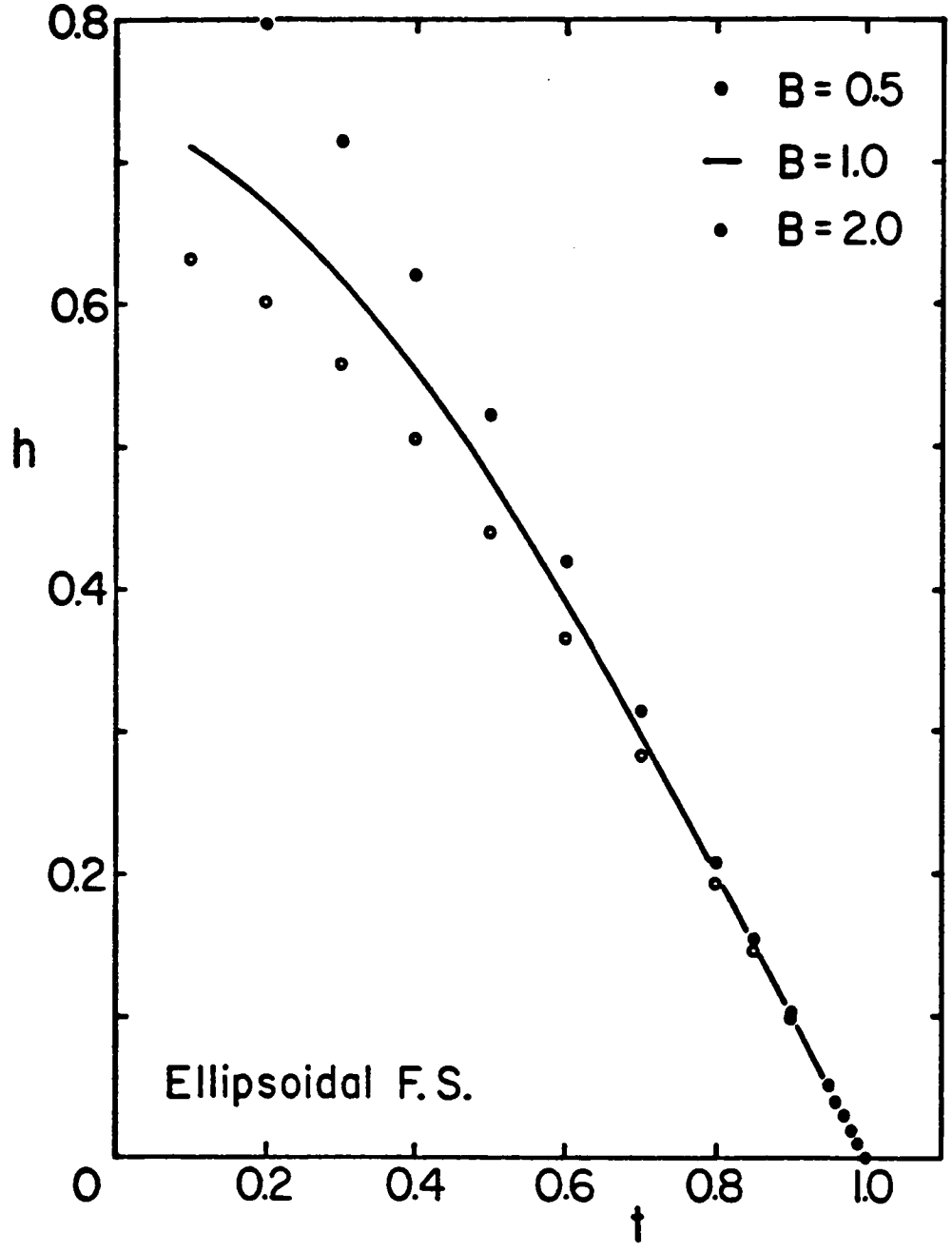

Fig. 7-2 The reduced field h for the ellipsoidal Fermi surface model for several values of B.

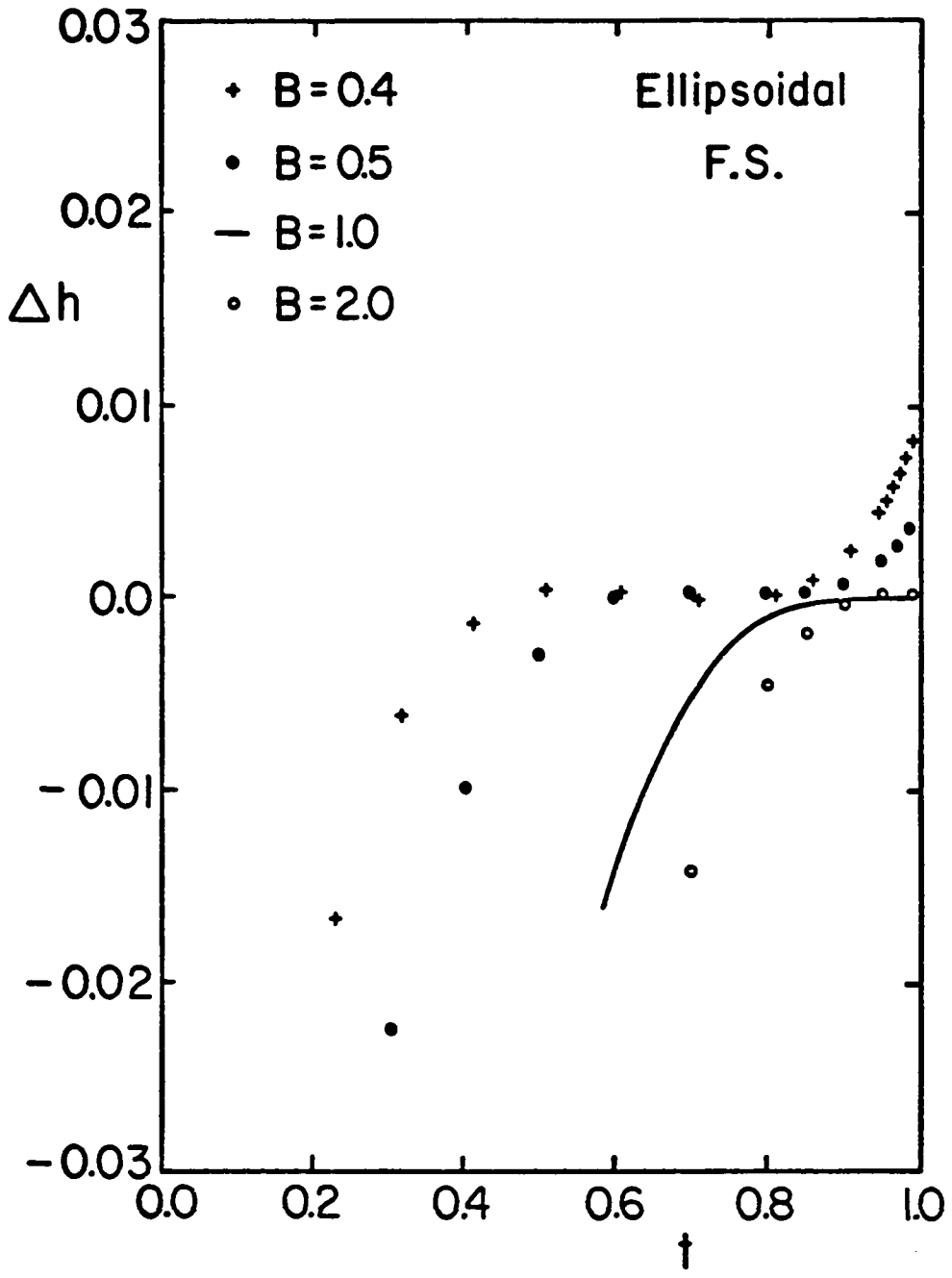

Fig. 7-3 Δh for the ellipsoidal Fermi surface model, showing how the shape of the critical field curve changes as the Fermi surface geometry is altered.

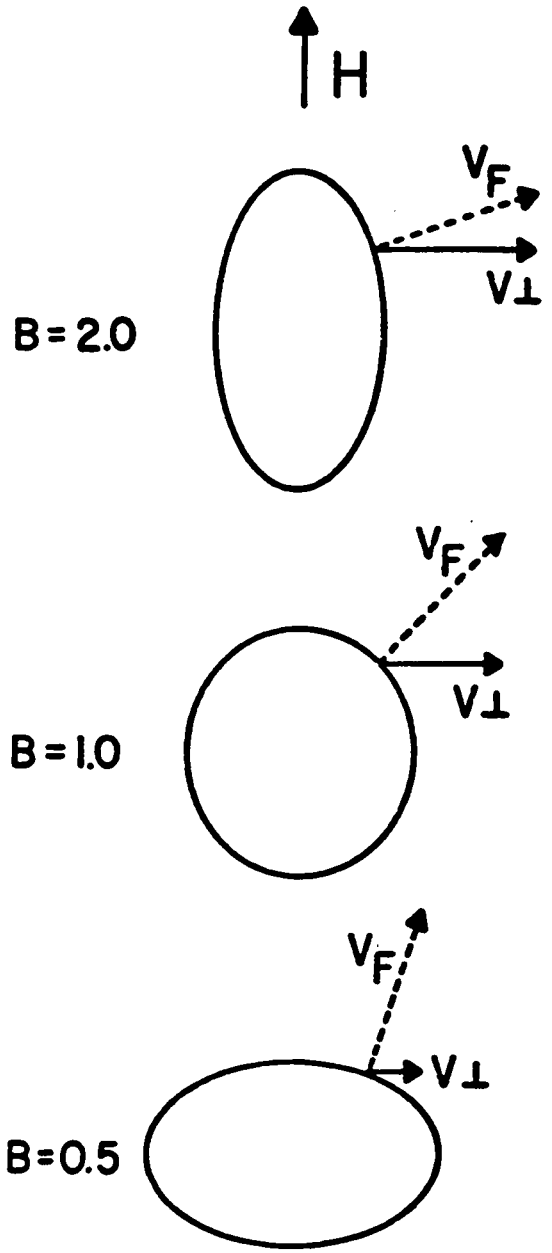

Fig. 7-4 Schematic illustration of how the component of the electron velocity perpendicular to the field direction is affected by the Fermi surface shape. The Fermi surfaces shown here are intended to be ellipsoids of rotation about the field axis.

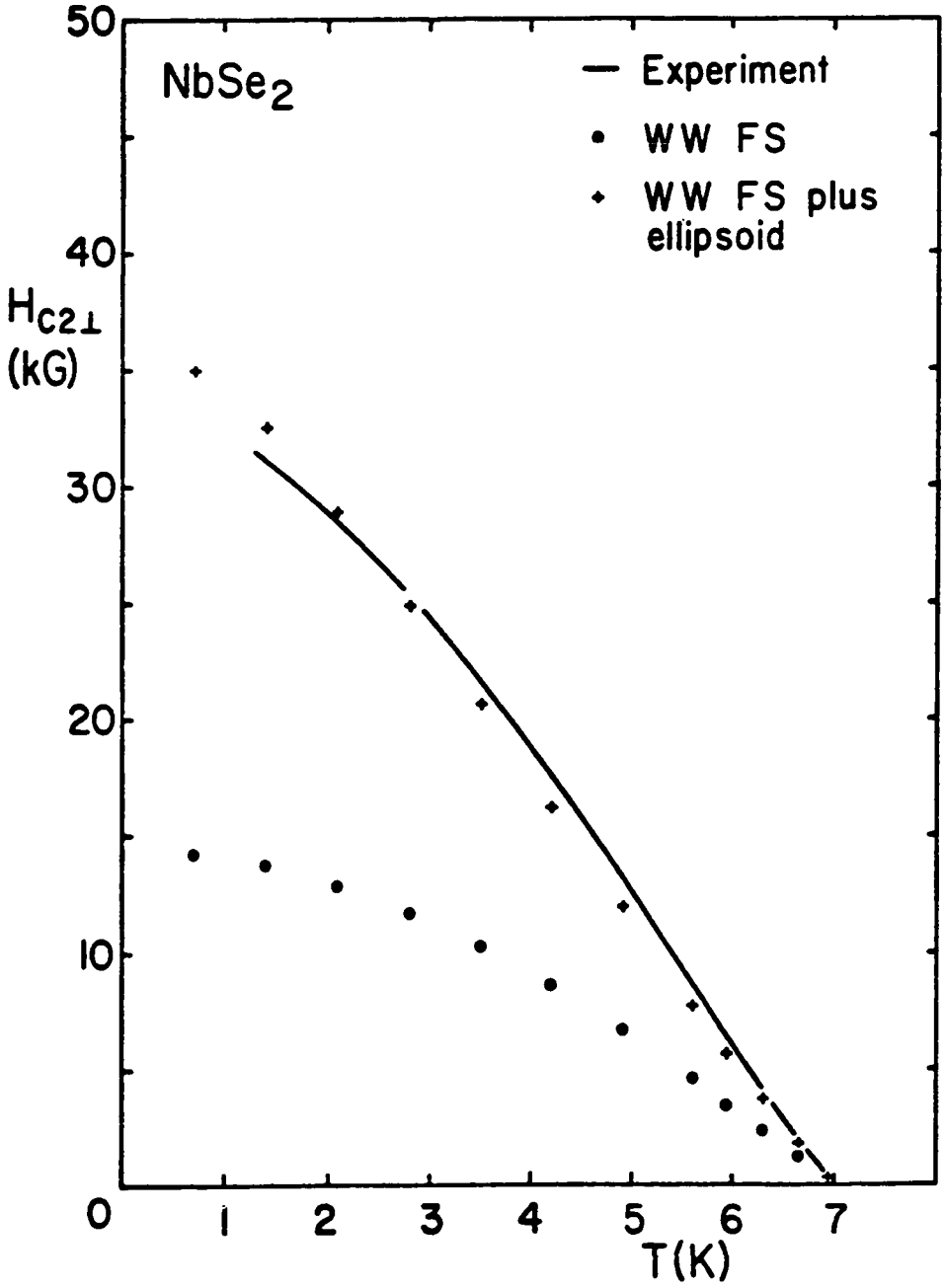

Fig. 7-5 The perpendicular critical field of $NbSe_2$, along with $H_{c2}(T)$ calculated using both the WW Fermi surface model and WW Fermi surface augmented by an ellipsoidal piece.

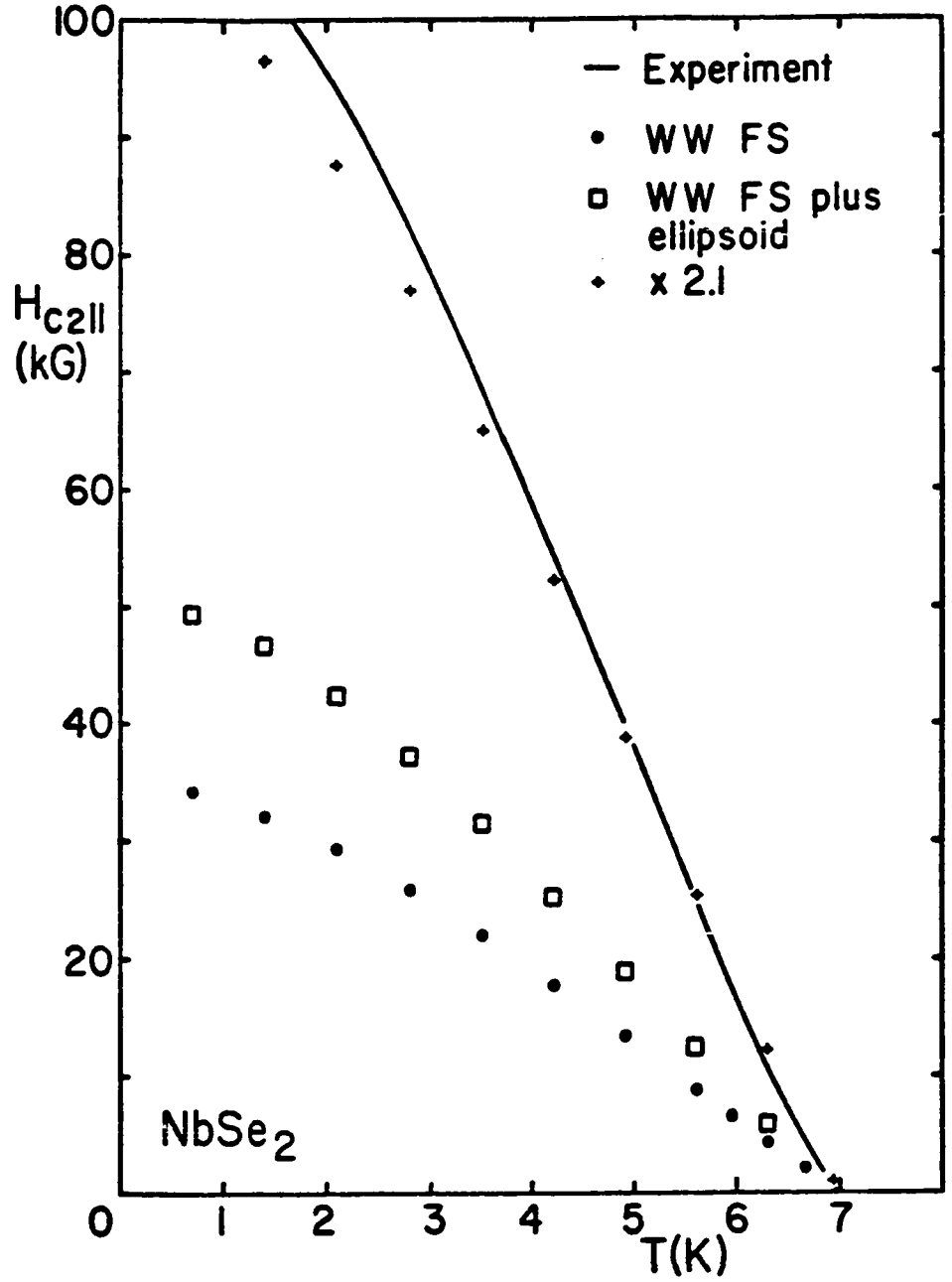

Fig. 7-6 The parallel critical field of $NbSe_2$, along with $H_{c2}(T)$ calculated for the same two models used for Fig. 7-5. The results for the model including the ellipsoid are shown twice; the scaling is discussed in the text.

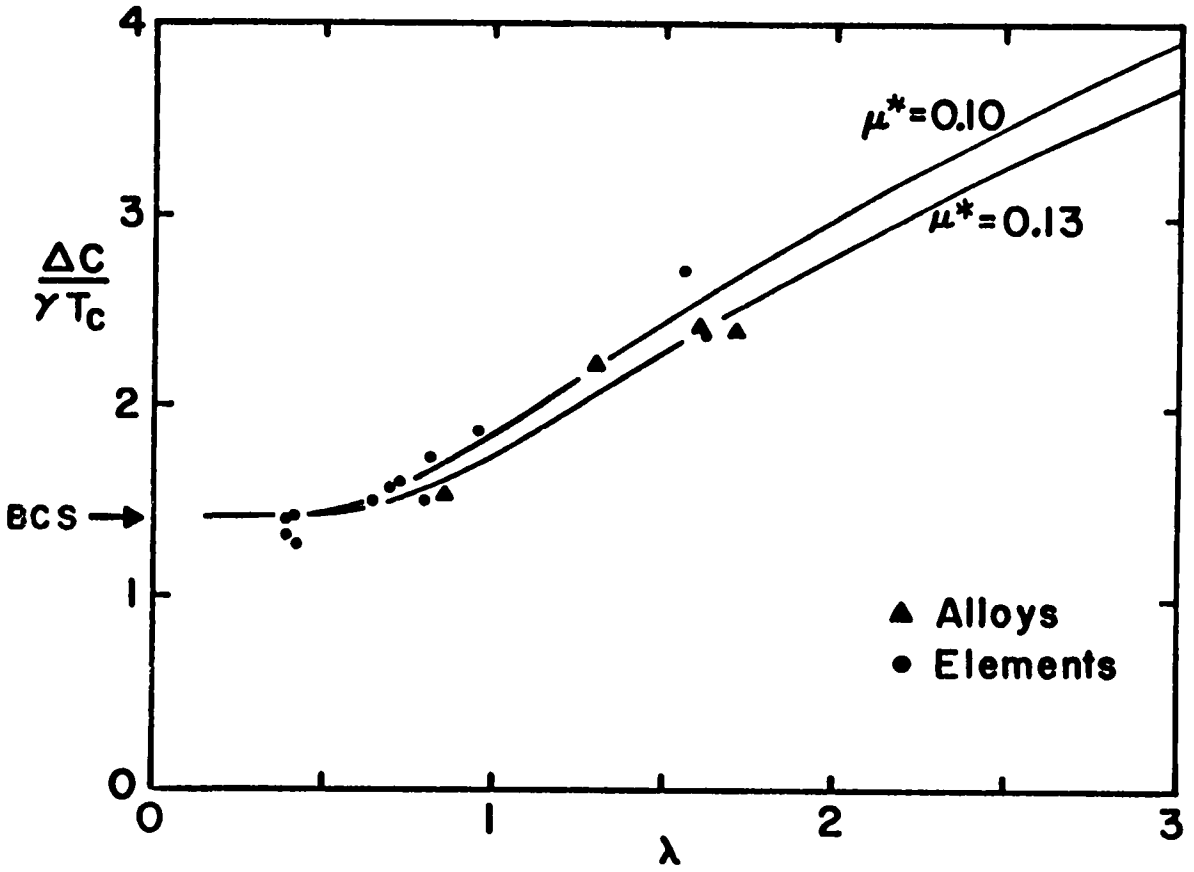

Fig. E-1 The normalized jump in the heat capacity at the superconducting transition (zero-field) as a function of the electron-phonon coupling constant. Experimental points from the literature are shown along with the simple theoretical prediction discussed in the text.

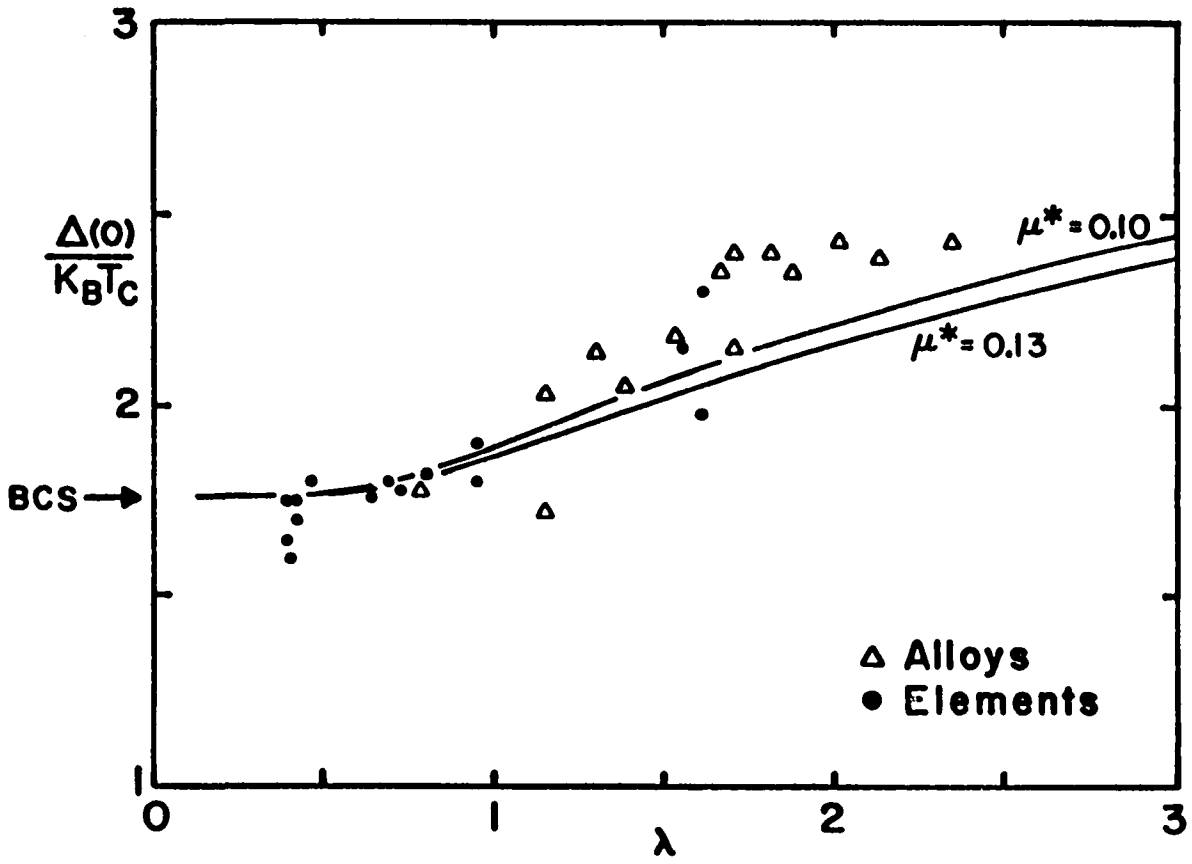

Fig. E-2 The normalized zero-temperature energy gap as a function of the electron-phonon coupling constant. Experimental points from the literature are shown along with the simple theoretical prediction discussed in the text.

References

1 J. A. Wilson, F. J. DiSalvo, and S. Mahajan, Adv. Phys. 24, 117 (1975).

2 J. A. Wilson and A. D. Yoffe, Adv. Phys. 18, 193 (1969).

3 F. J. DiSalvo, in Low Temp. Physics (LT-13), edited by K. D. Timmerhaus, W. T. O'Sullivan, and E. F. Hammel (Plenum Press, 1974), p. 417.

4 N. P. Ong and P. Monceau, Phys. Rev. B 16, 3443 (1977).

5 S. Kagoshima, Jpn. J. Appl. Phys. 20, 1617 (1981).

6 F. J. DiSalvo, Jr., Ph.D. Thesis, Stanford University, 1971.

7 J. F. Revelli, Jr., Ph.D. Thesis, Stanford University, 1973.

8 J. F. Revelli, Jr. and W. A. Phillips, J. Solid State Chem. 9, 176 (1974).

9 E. Revolinsky, B. E. Brown, D. J. Beerntsen, and C. H. Armitage, J. Less-Common Metals 8, 63 (1965).

10 F. Kadijk and F. Jellinek, J. Less-Common Metals 23, 437 (1971).

11 American Instute of Physics Handbook, third ed., edited by D. E. Gray (McGraw-Hill, 1972).

12 J. Edwards and R. F. Frindt, J. Phys. Chem. Solids 32, 2217 (1971).

13 F. R. Gamble, F. J. DiSalvo, R. A. Klemm, and T. H. Geballe, Science 168, 568 (1970).

14 D. E. Prober, R. E. Schwall, and M. R. Beasley, Phys. Rev B 21, 2717 (1980) and D. E. Prober, Ph.D. Thesis, Harvard University, 1975.

15 J. L. Vicent, S. J. Hillenius, R. V. Coleman, Phys. Rev. Lett. 44, 892 (1980).

16 S. T. Ruggiero, T. W. Barbee, Jr., and M. R. Beasley, Phys. Rev. Lett. 45, 1299 (1980), Phys. Rev. B 26, 4894 (1982).

17 R. A. Bromley, Phys. Rev. Lett. 29, 357 (1972).

18 L. F. Mattheiss, Phys. Rev. B 8, 3719 (1973).

19 G. Wexler and A. M. Woolley, J. Phys. C 9, 1185 (1976).

20 C. Y. Fong and M. L. Cohen, Phys. Rev. Lett. 32, 720 (1974).

21 D. W. Bullet, J. Phys. C 11, 4501 (1978).

22 J. L. Calais, Adv. Phys. 26, 847 (1977).

23 N. J. Doran, Physica 99B, 227 (1980).

24 D. D. Koelling, Rep. Prog. Phys. 44, 139 (1981).

25 N. W. Ashcroft and N. D. Mermin, Solid State Physics (Holt, Rinehart, and Winston, 1976).

26 F. Minami, M. Sekita, M. Aono, and N. Tsuda, Solid State Comm. 29, 459 (1979).

27 J. C. McMenamin and W. E. Spicer, Phys. Rev. Lett. 29, 1501 (1972).

28 F. J. DiSalvo, Jr. and T. M. Rice, Phys. Today 32, 32 (1979).

29 R. Pynn, Nature 281, 433 (1979).

30 R. H. Friend, in Solitons and Condensed Matter Physics, edited by A. R. Bishop and T. Schneider (Springer-Verlag, 1978), p. 199.

31 P. Bak, in Solitons and Condensed Matter Physics, edited by A. R. Bishop and T. Schneider (Springer-Verlag, 1978), p. 216.

32 F. J. DiSalvo, in Chemistry and Physics of One-Dimensional Metals, edited by H. J. Keller (Plenum Press, 1977), p. 369.

33 R. E. Peierls, Quantum Theory of Solids (Clarendon Press, Oxford, 1965).

34 W. L. McMillan, Phys. Rev. B 14, 1496 (1976).

35 D. E. Moncton, J. D. Axe, and F. J. DiSalvo. Phys. Rev. B 16, 801 (1977).

36 J. A. Wilson, F. J. DiSalvo, and S. Mahajan, Phys. Rev. Lett. 32, 882 (1974).

37 P. M. Willams, C. B. Scruby, and G. J. Tatlock, Solid State Comm. 17, 1197 (1975).

38 P. Garoche, J. J. Veyssie, P. Manuel, and P. Molinie, Solid State Comm. 19, 455 (1976).

39 J. M. E. Harper, T. H. Geballe, and F. J. DiSalvo, Phys. Rev. B 15, 2943 (1977).

40 J. R. Long, S. P. Bowen, and N. E. Lewis, Solid State Comm. 22, 363 (1977).

41 C. Berthier, D. Jerome, and P. Molinie, J. Phys. C 11, 797 (1978).

42 D. J. Huntley and R. F. Frindt, Can. J. Phys. 52, 861 (1974).

43 H. N. S. Lee, H. McKinzie, D. S. Tannhauser, and A. Wold, J. Appl. Phys. 40, 602 (1969).

44 T. H. Geballe, in Superconductivity in d- and f-Band Metals, edited by D. H. Douglas (American Instute of Physics, 1972), p. 237.

45 T. M. Rice and G. K. Scott, Phys. Rev. Lett. 35, 120 (1975).

46 J. A. Wilson, Phys. Rev. B 15, 5748 (1977).

47 J. E. Graebner and M. Robbins, Phys. Rev. Lett. 36, 422 (1976).

48 P. D. Hambourger and N. E. Lewis, Solid State Comm. 28, 187 (1978).

49 H. Schafer, in Preparative Methods in Solid State Chemistry, edited by P. Hagenmuller (Academic Press, 1972), p. 251 and H. Schafer, in Crystal Growth: An Introduction, edited by P. Hartman (North Holland, 1973) p. 143.

50 R. Nitsche, H. U. Bolsterli, and M. Lichtensteiger, J. Phys. Chem. Solids 21, 199 (1961).

51 R. Kershaw, M. Vlasse, and A. Wold, Inorg. Chem. 6, 1599 (1967).

52 N. E. Lewis, T. E. Leinhardt, and J. G. Dillard, Mat. Res. Bull. 10, 967 (1975).

53 M. Saeki, Mat. Res. Bull, 12, 773 (1977).

54 R. Nitsche, in Crystal Growth 1967, Suppliment to J. Phys. Chem. Solids C1, 215 (1967).

55 G. E. Meyers and G. L. Monet, J. Phys. Chem. Solids 32, 2645 (1971).

56 C. Berthier, P. Molinie, and J. Jerome, Solid State Comm. 18, 1393 (1976).

57 R. M. Fleming and R. V. Coleman, Phys. Rev. B 16, 302 (1977).

58 K. Onabe, M. Naito, and S. Tanaka, J. Phys. Soc. Jpn. 45, 50 (1978).

59 M. K. Agarwal and P. A. Wani, Mat. Res. Bull. 14, 825 (1979).

60 L. E. Conroy and K. R. Pisharody, in Solid State Chemistry, Procedings of the Fifth Mat. Res. Symposium, edited by R. S. Roth and S. J. Schneider (NBS Special Publication No. 364, 1972), p. 663.

61 F. J. DiSalvo, B. G. Bagley, J. M. Voorhoeve, and J. V. Waszczak, J. Phys. Chem. Solids 34, 1357 (1973).

62 Lindberg, Inc., 304 Hart St., Watertown, WI 53094.

63 Bruce Industrial Controls, Inc., Esquire Road, North Billerica, MA 01862 .

64 Omega Engineering, Inc., One Omega Drive, P.O. Box 4047, Stamford, CT 06907.

65 J. J. Murray, R. F. Pottie, and R. L. Sander, J. Mat. Sci. 8, 37 (1973) and G. J. Russell and J. Woods, J. Cryst. Growth 46, 323 (1979).

66 Atomergic Chemetals Corp., 100 Fairchild Ave., Plainview, NY 11803.

67 N. I. Sax, Dangerous Properties of Industrial Materials, forth ed. (Van Nostrand Rienhold, 1975).

68 Johnson Matthey and Co., Ltd. Products obtained through United Minerals and Chemical Corp., 129 Hudson St., NY, NY 10013.

69 E. Revolinsky, G. A. Spiering, and D. J. Beerntsen, J. Phys. Chem. Solids 26, 1029 (1965).

70 A. A. Al-Hilli and B. L. Evans, J. Cryst. Growth 15, 93 (1972).

71 B. E. Brown and D. J. Beerntsen, Acta Cryst. 18, 31 (1965).

72 E. A. Woods, Crystal Orientation Manual (Columbia University Press, 1963).

73 M. Yamamoto and T. Sambongi, J. Phys. Soc. Jpn. 41, 1146 (1976).

74 T. F. Smith, R. N. Shelton, and R. E. Schwall, J. Phys. F 4, 2009 (1974).

75 M. Ikebe, K. Katagiri, K. Noto, and Y. Muto, Physica 99B, 209 (1980).

76 R. Bachmann, F. J. DiSalvo, Jr., T. H. Geballe, R. L. Greene, R. E. Howard, C. N. King, H. C. Kirsch, K. N. Lee, R. E. Schwall, H. U. Thomas, and R. B. Zubeck, Rev. Sci. Instrum. 43, 205 (1972), R. E. Schwall, R. E. Howard, and G. R. Stewart, Rev. Sci. Instrum. 46, 1054 (1975), and R. L. Greene, C. N. King, R. B. Zubeck, and J. J. Hauser, Phys. Rev B 6, 3297 (1972).

77 N. A. H. K. Rao, E. D. Dahlberg, A. M. Goldman, L. E. Toth, and C. Umbach, Phys. Rev. Lett. 44, 98 (1980). and G. D. Zally and J. M. Mochel, Phys. Rev. Lett. 27, 1710 (1971), Phys. Rev. B 6, 4142 (1972).

78 G. R. Stewart, Rev. Sci. Instrum. 54, 1 (1983) and R. F. R. Pereira, E. Mayer, and M. F. DaSilveira, Rev. Sci. Instrum. 54, 899 (1983).

79 M. Strongin, D. G. Schweitzer, A. Paskin, and P. P. Craig, Phys.

Rev. 136, A926 (1964).

80 D. S. McLachlan and J. Feder, Rev. Sci. Instrum. 39, 1340 (1968).

81 A. L. Schawlow and G. E. Devlin, Phys. Rev. 113, 120 (1959).

82 D. M. Gualtieri, Rev. Sci. Instrum. 49, 1716 (1978).

83 A. T. Skjeltorp and W. P. Wolf, Phys. Rev. B 8, 215 (1973), W. I. Kinney, Ph.D. Thesis, Yale University, 1979 (available from University Microfilms, P. O. Box 1764, Ann Arbor, Michigan 48106, document number 7927631), and F. Rothwarf, D. Ford, and L. W. Dubeck, Rev. Sci. Instrum. 43, 317 (1972).

84 C. T. Van Degrift, Rev. Sci. Instum. 46, 599 (1975).

85 R. E. Schwall, G. R. Stewart, and T. H. Geballe, J. Low Temp. Phys. 22, 557 (1976).

86 J. J. Finley and B. S. Deaver, Jr., Solid State Comm. 36, 493 (1980).

87 Cerro Copper and Brass Co., Belefonte, PA 16823.

88 Superior Supersafe No. 30 Flux; The Superior Flux and Mfg. Co., 95 Alpha Drive, Cleveland, OH 44143.

89 Cryocal, Inc., 2457 University Ave., St. Paul, MN 55114.

90 Lake Shore Cryotronics, Inc., 64 E. Walnut St., Westerville, OH 43081.

91 Tyco Saphikon Division, Milford, NH 03055.

92 American Technical Ceramics, One Norden Lane, Huntington Station, NY 11746.

93 Type M ultraminiature coaxial cable, Lake Shore Cryotronics (Reference 90).

94 A. J. Bevolo and H. R. Shanks, J. Appl. Phys. 45, 4644 (1974).

95 G. K. White, Experimental Techniques in Low Temperature Physics, third ed. (Clarendon Press, Oxford, 1979).

96 H. H. Sample and L. G. Rubin, Cryogenics 17, 597 (1977).

97 L. J. Neuringer, A. J. Perlman, L. G. Rubin, and Y. Shapira, Rev. Sci. Instrum. 42, 9 (1971).

98 W. N. Lawless, Rev. Sci. Instrum. 42, 561 (1971) and W. N. Lawless, R. Radebaugh, and R. J. Soulen, Rev. Sci. Instrum. 42, 567 (1971).

99 L. G. Rubin and W. N. Lawless, Rev. Sci. Instrum. 42, 571 (1971).

100 W. N. Lawless, Rev. Sci. Instrum. 46, 625 (1975).

101 D. E. Prober, Rev. Sci. Instrum. 50, 387 (1979).

102 Magnetic Corp. of America, 179 Bear Hill Road, Waltham, MA 02154.

103 H. H. Sample and L. G. Rubin, IEEE Trans. Mag. MAG-12, 810 (1976) and L. G. Rubin, D. R. Nelson, and H. H. Sample, Rev. Sci. Instrum. 46, 1624 (1975).

104 D. L. Dector, D. E. Mapother, and R. W. Shaw, Phys. Rev. 112, 1888 (1958).

105 The critical field data recorded at the National Magnet Laboratory are not important for the quantitative conclusions drawn in Chapter VI. None of the results shown in Tables 6-1 through 6-5 involve NML data. Figure 6-8 displays NML data to illustrate the linearity of the parallel critical field data at low temperatures and the apparent lack of Pauli paramagnetic limiting. These conclusions would be unaffected by an 11% rescaling of the field axis. Figure 6-15 (the lower figure) displays NML data to illustrate the temperature independence of the anisotropy at low temperatures. Again, rescaling the field data would not alter this conclusion, although it would produce an unphysical jump in the anisotropy at the temperature at which a transition is made from high-field (NML) data to low-field (Yale) data. Figure 6-16 involves some NML data. However, the same qualitative behavior would be seen if the anisotropy were determined at a slightly higher temperature where only parallel critical field data recorded at Yale would be required. Only qualitative conclusions are drawn in the text concerning Figure 6-16. The fact that parallel critical field data recorded at both Yale and at NML can be plotted together with no apparent discrepancies (as in Figures 6-15 and 6-16) indicates that a simple rescaling solution to the calibration problem is acceptable. Thus, although this problem is unfortunate, it does not compromise any of the qualitative or quantitative conclusions which have been drawn from the critical field data.

106 M. Tinkham, Introduction to Superconductivity (McGraw-Hill, 1975).

107 D. Saint-James, G. Sarma, and E. J. Thomas, Type II Superconductivity (Pergamon Press, 1969).

108 R. P. Huebener, Magnetic Flux Structures in Superconductors (Springer-Verlag, 1979).

109 S. J. Williamson, Phys. Rev. B 2, 3545 (1970).

110 G. Kostorz, L. L. Isaacs, R. L. Panosh, and C. C. Koch, Phys. Rev. Lett. 27, 304 (1971).

111 J. Auer and H. Ullmaier, Phys. Rev. B 7, 136 (1973).

112 P. M. Tedrow, R. Meservey, and B. B. Schwartz, Phys. Rev. Lett. 24, 1004 (1970).

113 M. W. Denhoff and S. Gygax, Phys. Rev. B 25, 4479 (1982).

114 V. L. Ginzburg and L. D. Landau, Zh. Eksperim. i Theor. Fiz. 20, 1064 (1950).

115 J. Bardeen, L. N. Cooper, and J. R. Schrieffer, Phys. Rev. 108, 1175 (1957).

116 A. A. Abrikosov, Sov. Phys. JETP 5, 1174 (1957).

117 D. J. Scalapino, in Superconductivity, edited by R. D. Parks (Marcel Dekker, 1969), p. 449.

118 D. Rainer and G. Bergmann, J. Low Temp. Phys. 14, 501 (1974).

119 W. H. Butler, Phys. Rev. Lett. 44, 1516 (1980).

120 V. Z. Kresin and V. P. Parkhomenko, Sov. Phys. Solid State 16, 2180 (1975).

121 N. F. Masharov, Sov. Phys. Solid State 16, 1524 (1975).

122 G. Bergmann, in Low Temp. Physics (LT-13), edited by K. D. Timmerhaus, W. T. O'Sullivan, and E. F. Hammel (Plenum Press, 1974), Vol. 3, p. 552.

123 D. Rainer, G. Bergmann, and U. Eckhardt, Phys. Rev. B 8, 5324 (1973).

124 L. P. Gor'kov, Sov. Phys. JETP 9, 1364 (1959).

125 S. Foner and E. J. McNiff Jr., Solid State Comm. 39, 959 (1981).

126 O. Fisher, Appl. Phys. 16, 1 (1978).

127 C. Caroli, P. G. deGennes, and J. Matricon, Phys. Kondens. Materie 1, 176 (1963).

128 H. Teichler, in Anisotropy Effects in Superconductors, edited by H. W. Weber (Plenum Press, 1977), p. 7.

129 P. C. Hohenberg and N. R. Werthamer, Phys. Rev. 153, 493 (1967).

130 M. R. Skokan, R. C. Morris, and W. G. Moulton, Phys. Rev. B 13, 1077 (1976).

131 R. C. Morris and R. V. Coleman, Phys. Rev. B 7, 991 (1973).

132 J. A. Woollam and R. B. Somoamo, Phys. Rev. B 13, 3843 (1976).

133 N. Toyota, H. Nakatsuji, K. Noto, A. Hoshi, N. Kobayashi, Y. Muto, and Y. Onodera, J. Low Temp. Phys. 25, 485 (1976).

134 R. C. Morris, R. V. Coleman, and R. Bhandari, Phys. Rev. B 5, 895 (1972).

135 L. P. Gor'kov, Sov. Phys. JETP 7, 505 (1958).

136 E. Helfand and N. R. Werthamer, Phys. Rev. 147, 288 (1966).

137 L. W. Gruenberg and L. Gunther, Phys. Rev. 176, 606 (1968).

138 A. M. Clogston, Phys. Rev. Lett. 9, 266 (1962).

139 B. S. Chandrasekhar, Appl. Phys. Lett. 1, 7 (1962).

140 P. W. Anderson, J. Phys. Chem. Solids 11, 26 (1959).

141 P. W. Anderson, Phys. Rev. Lett. 3, 325 (1959).

142 G. Grimvall, Physica Scripta, 14, 63 (1976).

143 W. H. Butler, in Treatise on Material Science and Technology, Vol. 21, edited by F. Y. Fradin (Academic Press, 1981), p. 165.

144 G. Grimval, The Electron-Phonon Interaction in Metals, (North Holland, 1981).

145 T. P. Orlando, E. J. McNiff, Jr., S. Foner, and M. R. Beasley, Phys. Rev. B 19, 4545 (1979).

146 T. P. Orlando and M. R. Beasley, Phys. Rev. Lett. 46, 1598 (1981).

147 N. R. Werthamer, E. Helfand, and P. C. Hohenberg, Phys. Rev. 147, 295 (1966).

148 A. A. Abrikosov and L. P. Gor'kov, Sov. Phys. JETP 15, 752 (1962).

149 R. Meservey and P. M. Tedrow, Phys. Rev. Lett. 41, 805 (1978) and J. R. Samples and J. E. Cousins, Solid State Comm. 32, 1021 (1979).

150 L. J. Neuringer and Y. Shapiro, Phys. Rev. Lett. 17, 81 (1966).

151 S. Foner and E. J. McNiff Jr., Appl. Phys. Lett. 32, 122 (1978).

152 M. Decroux, O. Fischer, R. Flukiger, B. Seeber, R. Delesclefs, and M. Sergent, Solid State Comm. 25, 393 (1978).

153 L. J. Azevedo, W. G. Clark, G. Deutscher, R. L. Greene, G. B. Street, and L. J. Suter, Solid State Comm. 19, 197 (1976).

154 W. Biberacher and H. Schwenk, Solid State Comm. 33, 385 (1980) and W. Zacharko, R. Kubiak, and J. Mazur, Phys. Stat. Sol. (b) 76, K1 (1976).

155 L.Dobrosavljevic and M. Kulic, J. Low Temp. Phys. 32, 505 (1978) and W. L. Carter, S. J. Poon, G. W. Hull, Jr., and T. H. Geballe, Solid State Comm. 39, 41 (1981).

156 K. Machida, T Koyama, and T Matsubara, Phys. Rev. B 23, 99 (1981).

157 G. S. Grest, K. Levin, and M. J. Nass, Phys. Rev. B 25, 4562 (1982).

158 W. E. Lawrence and S. Doniach, in Low Temp. Physics (LT-12), edited by E. Kanda (Academic Press of Japan, 1971), p. 361.

159 R. A. Klemm, A. Luther, and M. R. Beasley, Phys. Rev. B 12, 877 (1975).

160 D. W. Youngner and R. A. Klemm, Phys. Rev. B 21, 3890 (1980).

161 D. W. Youngner (private communication).

162 K. H. Berthel, and B. Pietrass, J. Low Temp. Phys. 33, 127 (1978).

163 V. Ambegaokar, in Many-Body Physics, edited by C. Dewitt and R. Balin (Gordon and Breach, 1967) p. 299.

164 B. Serin, in Superconductivity, edited by R. D. Parks (Marcel Dekker, 1969), p. 925.

165 M. Tinkham, Phys. Lett. 9, 217 (1964).

166 S. F. Meyer, R. E. Howard, G. R. Stewart, J. V. Acrivos, and T. H. Geballe, J. Chem. Phys. 62, 4411 (1975).

167 T. F. Smith, L. E. Delong, A. R. Moonbeam, T. H. Geballe, and R. E. Schwall, J. Phys. C., 5, L230 (1972).

168 J. L. Feldman, J. Phys. Chem. Solids, 37, 1141 (1976).

169 R. E.Jones, Jr., H. R. Shanks, D. K. Finnemore, and B. Morosin, Phys. Rev. B 6, 835 (1972).

170 N. Kobayashi, K. Noto, and Y. Muto, J. Low Temp. Phys. 27, 217 (1977).

171 S. Foner and E. J. McNiff Jr., Phys. Lett. 45A, 429 (1973).

172 B. P. Clayman and R. F. Frindt, Solid State Comm. 9, 1881 (1971).

173 F. Roeske, Jr., H. R. Shanks, and D. K. Finnemore, Phys. Rev. B 16, 3929 (1977).

174 H. A. Leupold, F. Rothwarf, J. J. Winter, J. T. Breslin, R. L. Ross, and T. R. AuCoin, J. Appl. Phys. 45, 5399 (1974).

175 C. P. Bean and J. D. Livingston, Phys. Rev. Lett. 12, 14 (1964).

176 J. R. Clem, in Low Temp. Physics (LT-13), edited by K. D. Timmerhaus, W. T. O'Sullivan, and E. F. Hammel (Plenum Press, 1974), Vol. 3, p. 102.

177 R. W. DeBois and W. DeSorbo, Phys. Rev. Lett. 12, 499 (1964), A. S. Joseph and W. J. Tomach, Phys. Rev. Lett. 12, 219 (1964).

178 H. A. Ullmaier and W. F. Gauster, J. Appl. Phys. 37, 4519 (1966)

179 J. F. Bussiere, Phys. Lett. 58A, 343 (1976).

180 P. S. Swartz and H. R. Hart, Jr., Phys. Rev. 137, A818 (1965).

181 T. Matsushita, T. Tanaka, and K. Yamafuji, J. Phys. Soc. Jpn 46, 756 (1979).

182 A. B. Pippard, Phil. Mag. 19, 217 (1969).

183 J. le G. Gilchrist and P. Monceau, Phil. Mag. 18, 237 (1968).

184 D. F. Moore and M. R. Beasley, Appl. Phys. Lett. 30, 494 (1977).

185 Microwave surface resistance measurements have been carried out using a Pb-17at.%In alloy by M. Cardona, J. Gittleman, and B. Rosenblum [Phys. Lett. 17, 92 (1965)]. In the mixed state a hysteresis was observed, the sample being more lossy in a decreasing field.This result is not in accord with our explaination of the hysteresis seen in Figure 6-3. However, copper plating the sample was found to change the sign of the hysteresis [J. I. Gittleman and B. Rosenblum, Phys. Lett. 20, 453 (1966)]. In larger fields, the sample was more lossy when the field was being increased.

186 S. E. Lambert, M. B. Maple, A. R. Sweedler, and S. Moehlecke, J. Low Temp. Phys. 41, 653 (1980).

187 P. B. Allen, Phys. Rev. B 17, 3725 (1978).

188 J. J. Hopfield, in Superconductivity in d- and f-Band Metals, edited by D. H. Douglas (American Institute of Physics, 1972) p. 358.

189 M. H. Van Maaren and H. B. Harland, Phys. Lett. 29A, 571 (1969).

190 D. E. Farrell, B. S. Chandrasekhar, and H. V. Culbert, Phys. Rev. 177, 694 (1969).

191 S. T. Sekula and R. H. Kernohan, J. Phys. Chem. Solids 27, 1863 (1966).

192 R. Koepke and G. Bergmann, Z. Physik 242, 31 (1971).

193 L. P. Gor'kov, Sov. Phys. JETP 10, 593 (1960).

194 P. G. deGennes, Phys. Kondens. Materie 3, 79 (1964).

195 K. Maki, Phys. Rev. 148, 362 (1966).

196 A. L. Fetter and P. C. Hohenberg, in Superconductivity, edited by R. D. Parks (Marcel Dekker, 1969), p. 881.

197 I. S. Gradshteyn and I. M. Ryzhik, Table of Integrals, Series, and Products, fourth ed. (Academic Press, 1965).

198 N. V. Zavaritskii, Sov. Phys. Usp. 15, 608 (1973).

199 J. R. Clem, Ann. Phys. 40, 268 (1966)

200 P. B. Allen and R. C. Dynes, Phys. Rev. B 12, 905 (1975).

201 A. G. Shepelev, Sov. Phys. Usp. 11, 690 (1969).

202 S. S. P. Parkin and A. R. Beal, Phil. Mag. B 42, 627 (1980).

203 R. Buchmann, H. C. Kirsch, and T. H. Geballe, Solid State Comm. 9, 57 (1971) and J. A. Benda, R. E. Howard, and W. A. Phillips, J. Phys. Chem. Solids 35, 937 (1974).

204 N. Noto, S. Morohashi, K. Arikawa, Y. Muto, Physica 99B, 204 (1980).

205 J. M. Ziman, Electrons and Phonons, (Clarendon Press, Oxford, 1960).

206 J. H. Mooij, Phys. Status Solidi A 17, 521 (1973).

207 W. L. McMillan, Phys. Rev. 167, 331 (1968).

208 B. P. Clayman, Can. J. Phys. 50, 3193 (1972).

209 R. C. Morris and R. V. Coleman, Phys. Lett. 43A, 11 (1973).

210 G. Gladstone, M. A. Jensen, and J. R. Schrieffer, in Superconductivity, edited by R. D. Parks (Marcel Dekker, 1969), p. 665.

211 J. M. Daams and J. P. Carbotte, Solid State Comm. 29, 501 (1979).

212 G. Bergmann and D. Rainer, Z. Physik 263, 59 (1973).

213 P. B. Allen, W. E. Pickett, K. M. Ho, and M. L. Cohen, Phys. Rev. Lett. 40, 1532 (1978).

214 B. M. Klein, D. A. Papaconstantopoulos, and L. L. Boyer, in Superconductivity in d- and f-band Metals, edited by H. L. Suhl and M. B. Maple (Academic Press, 1980), p. 455.

215 R. W. Hamming, Numerical Methods for Scientists and Engineers (McGraw-Hill, 1962).

216 E. Kreyszig, Advanced Engineering Mathematics, third ed., (Wiley, 1972), Chapter 8.

217 P. deTray, S. Gygax, and J. P. Jan, J. Low Temp. Phys. 11, 421 (1973).

218 R. Meservey and B. B. Schwartz, in Superconductivity, edited by R. D. Parks (Marcel Dekker, 1969), p. 117.

219 E. L. Wolf, Rep. Prog. Phys. 41, 1439 (1978).

220 J. M. Daams and J. P. Carbotte, Solid State Commun. 29, 501 (1979).

221 E. Bucher, F. Heiniger, J. Muller, and J. L. Olsen, in Low Temp. Physics (LT-9), edited by J. G. Daunt, D. O. Edwards, E. J. Milford, and M. Yaqub (Plenum Press, 1965), p. 616.

222 J. C. Swihart, D. J. Scalapino, and Y. Wada, in Low Temp. Physics (LT-9), edited by J. G. Daunt, D. O. Edwards, E. J. Milford, and M. Yaqub (Plenum Press, 1965), p.607.

223 R. W. Rollins and L. C. Clune, Phys. Rev. B 6, 2609 (1972).

224 E. L. Wolf and R. J. Noer, Solid State Comm. 30, 391 (1979).

225 W. H. Butler, in Superconductivity in d- and f-Band Metals, edited by H. L. Suhl and M. B. Maple (Academic Press, 1980) p. 443.

226 J. E. Neighbor, J. F. Cochran, and C. A. Shiffman, Phys. Rev. 155, 384 (1967).

227 L. V. Munukutla and R. L. Cappelletti, Phys. Rev. B 21, 5111 (1980).

228 R. C. Dynes, J. P. Carbotte, D. W. Taylor, and C. K. Campbell, Phys. Rev. 178, 713 (1969).

229 J. G. Adler and T. T. Chen, Solid State Comm. 9, 1961 (1971).

230 P. Vashishta and J. P. Carbotte, Phys. Rev. B 7, 1874 (1973).

231 G. R. Stewart, A. L. Giorgi, and M. C. Krupka, Solid State Comm. 27, 413 (1978).

232 L. J. Vieland and A. W. Wickland, Phys. Rev. 166, 424 (1968).

233 R. C. Dynes, Solid State Comm. 10, 615 (1972).